UNIVERSITY OF SOUTHAMPTON

FACULTY OF ENGINEERING AND THE ENVIRONMENT

Engineering Materials

National Centre for Advanced Tribology at Southampton (NCATS)

Tribological Behaviour of Ultrafine-Grained Alloys Formed by Severe Plastic Deformation

by

Chuan Ting Wang

Thesis for the degree of Doctor of Philosophy

June_2013

UNIVERSITY OF SOUTHAMPTON

<u>ABSTRACT</u>

FACULTY OF ENGINEERING AND THE ENVIRONMENT

<u>Engineering Materials</u>

<u>National Centre for Advanced Tribology at Southampton (nCATS)</u>

Thesis for the degree of Doctor of Philosophy

TRIBOLOGICAL BEHAVIOUR OF ULTRAFINE-GRAINED ALLOYS FORMED BY SEVERE PLASTIC DEFORMATION

Chuan Ting Wang

This thesis presents a study on wear behaviour of materials processed by severe plastic deformation (SPD). Al-1050 alloy and commercial purity Ti have been processed via different SPD methods. Wear tests of different contact size were employed to compare the wear performance between ultrafine grained (UFG) alloys and their as-received state. The aim of this study is to understand the effect of SPD processing on wear behaviour of materials, to seek a way to use SPD processing to improve the mechanical properties of materials and their wear resistance at the same time.

Al-1050 was processed using equal-channel angular pressing (ECAP) and high-pressure torsion (HPT), respectively. Microhardness evolution was analysed by Vickers hardness testing. The results showed clear evidence of strength improvement by SPD. Afterwards, dry sliding testing was performed on a TE77 tribometer against different counter materials. The results showed that both ECAP and HPT led to a decrease to the wear resistance to Al-1050. Scanning electron microscopy, energy dispersion spectroscopy and surface profile meter were used to examine the worn surface and debris. The transition from severe platelet wear to oxidation wear was observed during the wear tests. The decrease of wear resistance of Al-1050 after SPD processing is attributed to a lack of work hardening capacity during the severe wear stage and a higher oxidation rate during the oxidation wear stage.

In addition, commercial purity Ti was processed via HPT and heat treatment. Mechanical testing and a microstructure study demonstrated the trend of increasing strength with decreasing grain size. In this study, the micro-tribological behaviour of UFG Ti was studied for the first time via microscratch testing. The results showed that HPT-processing of Ti inhibited operation of adhesion and ploughing during wear tests and led to better wear resistance.

Based on the results from the above studies and a comprehensive review of published research on wear of UFG alloys, a conclusion was drawn that when the wear process is dominated by adhesion and oxidation wear, SPD processing decreases the wear resistance of materials. However, when wear is dominated by mechanical wear mechanisms (plastic deformation, abrasion and ploughing), the strengthening of SPD processing brings better wear performance to the material.

To enhance the wear resistance of UFG Ti as bio-implant materials, TiN and DLC coatings were deposited on to Ti substrates via physical vapour deposition methods. Wear tests indicated a significant improvement of wear resistance after coating deposition. Adhesion tests showed that the thin coatings had much enhanced load bearing capacity with UFG Ti as the substrate compared to coarse-grained Ti, which is explained by a modified composite hardness model. This model showed good accuracy in predicting the critical load of a wide range of thin coatings on different substrates.

Finally, an improved bio-implant design was proposed for total joint replacement applications. This design involves fabricating the main body of the bio-implant from UFG pure Ti processed by SPD and subsequently applying a hard thin coating to protect the head of the implant. It is anticipated this design will provide the implant with high strength, good fatigue life, good corrosion resistance, together with good wear and tribo-corrosion resistance from the coating and a non-toxic ion release. The product is aimed to replace the toxic bio-metals in total joint replacement use, such as SS316, Co-Cr alloy and Ti-6Al-4V. Therefore, the design has a very strong application prospect.

List of Contents

List of Figures

IX

X

List of Tables

Declaration of Authorship

I, Chuan Ting Wang, declare that the thesis entitled:

Tribological Behaviour of Ultrafine-Grained Alloys Formed by Severe Plastic
Deformation
and the work presented in the thesis are both my own, and have been generated by
me as the result of my own original research. I confirm that:

- this work was done wholly or mainly while in candidature for a research degree
  at this University;

- where any part of this thesis has previously been submitted for a degree or any
  other qualification at this University or any other institution, this has been clearly
  stated;

- where I have consulted the published work of others, this is always clearly
  attributed;

- where I have quoted from the work of others, the source is always given. With
  the exception of such quotations, this thesis is entirely my own work;

- I have acknowledged all main sources of help;

- where the thesis is based on work done by myself jointly with others, I have
  made clear exactly what was done by others and what I have contributed myself;

- parts of this work have been published as:

1.   **C.T. Wang**, N. Gao, M.G. Gee, R.J.K. Wood and T.G. Langdon (2013)
*Tribology testing of ultrafine-grained Ti processed by high pressure torsion with
subsequent coating*. Journal of Materials Science, 48, 4742-4748.

2.   **C.T. Wang**, N. Gao, M.G. Gee, R.J.K. Wood and T.G. Langdon (2013)
*Processing of an ultrafine-grained titanium by high-pressure torsion: An evaluation
of the wear properties with and without a TiN coating*. Journal of the Mechanical
Behaviour of Biomedical Materials, 17, 166-175.
3.   **C.T. Wang**, A. Escudeiro, T. Polcar, A. Cavaleiro, R.J.K. Wood, N. Gao and
T.G. Langdon (2013) *Indentation and scratch testing of DLC-Zr coatings on
ultrafine-grained titanium processed by high-pressure torsion*. Wear, in press.
4.   **C.T. Wang**, N. Gao, M.G. Gee, R.J.K. Wood and T.G. Langdon (2012)
*Effect of grain size on the micro-tribological behaviour of pure titanium processed
by high-pressure torsion*. Wear, 280-281, 28-35.

5.   N. Gao, **C.T. Wang**, R.J.K. Wood and T.G. Langdon (2012) *Tribological properties of ultrafine-grained materials processed by severe plastic deformation*. Journal of Materials Science, 47, 4779–4797.

6.   **C.T. Wang**, N. Gao, R.J.K. Wood and T.G. Langdon (2011) *Wear behaviour of an aluminium alloy processed by equal-channel angular pressing*. Journal of Materials Science, 46, (1), 123-130.

7.   N. Gao, **C.T. Wang**, R.J.K. Wood and T.G. Langdon (2011) *Wear resistance of SPD-processed alloys*. Materials Science Forum, 667-669, 1095-1100.

8.   **C.T. Wang**, N. Gao, R.J.K. Wood and T.G. Langdon (2010) *Wear behaviour of Al-1050 alloy processed by severe plastic deformation*. Materials Science Forum, 667-669, 1101-1106.

Signed: …………………   ………………

Date:………………………04/04/2013………………………………………

Acknowledgement

I would like to express my sincere appreciation to the following people, without whose support this thesis would not have been possible.

Firstly, a huge thanks to my supervisors Dr. Nong Gao, Professor Robert J K Wood and Professor Terence G. Langdon for their valuable guidance, support and encouragement throughout my PhD research. I am also very grateful to Professor Mark G Gee and Dr. John Nunn (National Physical Laboratory) for their valuable discussion and stimulation with micro-wear testing.

My sincere acknowledgment is due to Dr. Shun Cai Wang and Ms. Chao Ma for training on SEM, TEM, EBSD. I specially thank Dr. Tomas Polcar and Ms. Ana Escudeiro (University of Coimbra, Portugal) for the successful cooperation and discussion on DLC coatings. I appreciate Dr. Meng Yan Nie and Dr. John Low for the related experiments on Ti. I want to thank Prof. J.T. Wang, Dr. Y. Zhang, Dr. A.P. Zhilyaev, Dr. Y. Huang, Dr. X.G. Qiao, Ms. Y. Chen, Mr. A. Al-Zubaydi, Ms. N. Hu, Mr. N.X. Zhang, Mr R. Jiang, Ms Y.K. Wang, Ms B.Y. He, Mr Y. He and Ms F. Zhang for all the valuable discussion on SPD processing and material characterization. Also thanks to Dr. T.J. Harvey, Dr. R. Cook and Dr. J.C. Walker for the help with wear testing.

I sincerely acknowledge all the staff and students in the Engineering Materials Research Group and nCATS at the University of Southampton for their support and help during my study.

I would like to thank University of Southampton and China Scholarship Council for their financial support throughout the duration of my study.

Finally, I would like to thank my parents, my wife and little son for always believing in me. Without their support and love I would have never achieved this.

Definitions and Abbreviations

AE	acoustic emission
AFM	atomic force microscopy
ARB	accumulative roll bonding
BL	boundary lubrication
C2S2	continuous confined strip shearing
CG	coarse-grained
CGP	constrained groove pressing
CP	commercial pure
CR	cold rolling
CRSS	critical resolved shear stress
CVD	chemical vapour deposition
DLC	diamond-like carbon
DP	dual phase
EBSD	electron back-scatter diffraction
ECAP	equal-channel angular pressing
EDS	energy disperse spectroscopy
EHL	elasto-hydrodynamic lubrication
FCC	face-centered cubic
FIB	focused ion beam
GBS	grain boundary sliding
GND	geometrically necessary dislocations
HCP	hexagonal close-packed
HPT	high-pressure torsion
HT	hydrothermal treatment
IFM	infinite focused optical microscopy
IO	internal oxidation
MAO	micro-arc oxidation
MEMS	microelectromechanical systems
MML	mechanically mixed layers
OM	optical microscopy
PBS	phosphate buffer solution

PVD	physical vapour deposition
RCS	repetitive corrugation and straightening
SEM	scanning electron microscopy
SMAT	surface mechanical attrition treatment
SPD	severe plastic deformation
SSD	statistically stored dislocations
TE	twist Extrusion
TEM	transmission electron microscopy
TJR	total joint replacements
UFG	ultrafine-grained
UTS	ultimate tensile stress
XRD	X-ray diffraction
a	contact radius of Archard law
a_1	constant
a_{att}	the attack angle
a_{therm}	the thermal diffusivity
A_n	the nominal contact area
b	Burgers vector
d	the width of the subgrain bands
d_0	original grain size
d_{GS}	grain size
d_r	grain refinement of metal via straining
D_p	degree of penetration
E_C	Young's Modulus of the coating
E_S	Young's Modulus of the substrate
E^*	reduced Modulus
F	tangential force needed to move the two bodies
$\tilde{F}$	the normalized pressure at the sliding interface
G	shear modulus
h	the disc thickness
h_{dep}	depth of penetration
H	hardness of the softer surface
H_o	the room temperature hardness

H_C	hardness of the coating
$H_{C,S}$	hardness of the coating-substrate system
H_S	hardness of the substrate
k_1	constant
k_2	constant
k_{SWR}	specific wear rate
K	dimensionless wear coefficient
k_{HP}	Hall-Petch constant
k_{SS}	shear flow stress
l	mean free path for dislocation moving
L	normal load
L'	load per unit length
M	Taylor factor
p	contact pressure
P_m	mean contact pressure
P_0	maximum contact pressure
Q	volume loss of the whole area per sliding distance
r	the radius of the HPT disc
r_{cont}	the contact radius during indentation or sliding
r_{GEO}	the geometrical length of the indentation volume
R_C	the radius of deformation zone of coating
R_S	the radius of deformation zone of substrate
R_{ind}	radius of the indenter
S	total sliding distance
S_{GB}	the area of grain boundaries per unit volume
t	thickness of coating
v	sliding speed
$\tilde{V}$	the normalized velocity
V	volume worn away during testing
V_C	deformation volume of the coating
V_g	volume of worn groove below unworn surface
V_r	volume of ridge formed above the mean surface
V_S	deformation volume of the substrate

V_{total}	total deformation volume
W	track width at the critical load point
R_a	mean surface roughness
R_q	root mean square roughness parameter
β	indentation depth
χ	factor by which the plastic zone changes
ε	equivalent strain
ε_N	equivalent strain after N passes
ϕ	the shear angle.
Φ	the channel angle
γ	shear strain
η	the total angular range of the various slip systems
μ_{COF}	the coefficient of friction
θ_2	slop of the tensile curve
$\bar{\theta}$	average misorientation angle after straining
ρ_0	initial dislocation density
ρ_g	SSD generated via straining
ρ_{gb}	dislocation density which formed grain boundary
ρ_{ig}	volume dislocation density stored inside grains
ρ_{SSD}	density of SSD
ρ_{GND}	density of GND
σ_y	yield strength
$\Delta\sigma_{gb}$	grain boundary strengthening
τ	critical resolved shear stress
τ_0	intrinsic stress
τ_{int}	shear strength of the interface
τ_{weak}	shear strength of the weaker material
τ_{max}	maximum shear stress
$\Delta\tau_{ss}$	solid solution strengthening
$\Delta\tau_{prec}$	precipitate strengthening

$\Delta\tau_d$	dislocation strengthening
Ψ	the angle subtended by the arc of curvature
ξ	total strain
ε_{gbs}	the strain due to grain boundary sliding
ε_t	the total strain

1. Introduction

Producing ultrafine-grained (UFG) materials by severe plastic deformation (SPD) has been widely studied as an effective tool to improve properties of materials over the last two decades. Processing by SPD refers to various experimental procedures of metal forming that can apply very high strains on materials leading to exceptional grain refinement. A unique feature of SPD processing is that the strain is imposed without any significant change in the overall dimensions of the work piece. Therefore, it is possible to impose a large strain to the samples by repeating SPD processing. Another feature is that the shape is retained by using special tool geometries that prevent free flow of the material and thereby produce a significant hydrostatic pressure. Currently, many SPD technologies have been developed, including equal-channel angular pressing (ECAP) [1], high-pressure torsion (HPT) [2], accumulative roll bonding (ARB) [3, 4] and other techniques. Processing by SPD leads to very small grain sizes and the processed metals are usually termed UFG materials where the average grain sizes are typically less than 1 μm [1]. So far, extensive studies have been performed on microstructural evolution, tensile properties, and thermal stability of the SPD-processed UFG materials. It has been found that UFG materials possess superior mechanical properties, including high strength [5], enhanced fatigue property and excellent superplasticity [6].

Most of the previous studies focused on the microstructure evolution during SPD and/or the mechanical properties of metals obtained [7, 8]. With the novel and often extraordinary properties provided by SPD process, these materials have potential to be used in many applications, especially for precision instruments, microelectromechanical systems (MEMS) [9] and biomedical implants [10].

In order to make better use of SPD-processed materials, it is necessary to study their tribological behaviour of them, including friction and wear. Coefficients of friction (COF) and wear resistance are parameters describing the state of contact of bodies in a tribo-system, and they are not material constants of the bodies in contact. Friction between contacting surfaces leads to surface temperature raise and energy waste. A lower coefficient of friction is desirable to reduce the energy wasting. Meanwhile,

materials should demonstrate good wear resistance for use in structural materials application because most of machine components involve relative motion between two surfaces [7]. Wear of sliding surfaces can occur by one or more wear mechanisms, including adhesion, abrasion, fatigue wear, corrosive wear and fretting. As wear leads to increase of clearance and loss of precision for moving structural components, a higher wear resistance can yield a longer service life. Especially, as the dimensions of components and loads used continue to decrease as in MEMS, wear property on the micro-scale becomes crucial. Wear resistance of engineering materials have significant effects on the serviceability and durability of their components. Hence, the wear resistance must be taken into account in the design of engineering parts, especially for UFG materials.

However, there are only limited papers available reporting wear properties of SPD-processed materials. Until now, it is still in controversial whether the SPD process can improve wear resistance of the materials, which depend on many factors and particularly depend on experimental materials and testing conditions. This topic needs to receive more attention and studies.

In this study, Al-1050 alloy and pure Ti were processed by ECAP and HPT. Various tests were conducted to characterize how SPD affects wear resistance. Various coatings were deposited on to UFG Ti to enhance its wear resistance in an effective way. The wear mechanism was correlated to microstructure and surface morphology change through transmission electron microscopy (TEM), scanning electron microscopy (SEM) and energy disperse spectroscopy (EDS).

The aims of the present project are to investigate the tribological behaviour of UFG alloys formed by SPD; study the effect of different grain sizes on wear behaviour of materials, including coefficient of friction and wear resistance; to compare the different wear performance of SPD-processed materials and the as-received materials; to determine the key factors which affect the wear behaviour of materials with different grain sizes; to study the microstructure evolution of SPD materials during wear. To explore a method to enhance the wear resistance of UFG alloys, to

enhance the service ability of UFG alloys in contact applications. The main objectives of this research are as follows:

- Process UFG alloys (Al and Ti) using ECAP and HPT, evaluate the change of microstructure and mechanical properties of Al and Ti after SPD processing. Perform wear tests on both coarse-grained (CG) and UFG Al and Ti, study the different wear behaviour caused by SPD processing, including coefficient of friction and wear rate. Investigate the wear surface and debris after wear test, to determine the effect of grain size on deformation behaviour of materials during wear. Discuss the operated wear mechanisms and the interaction between several wear mechanisms during wear.

- Deposit thin coatings on SPD processed alloys, in order to achieve superior wear resistance and mechanical properties by combining SPD and coating technology. Study the wear behaviour and adhesion of coatings on top of substrates with different grain sizes, and explore the effect of mechanical properties of substrate on the adhesion and wear behaviour of thin coatings. Study the deformation behaviour of coatings during wear and adhesion testing by employing theory modelling methods.

The structure of this thesis is as follows. After this introduction, literature reviews of SPD technology and tribology are described in Chapter 2. Information about the materials, testing and analysis are demonstrated in Chapter 3. Reciprocating wear test of Al-1050 alloy processed by ECAP is presented in Chapter 4. Chapter 5 describes the reciprocating wear test of Al-1050 alloy processed by HPT. In Chapter 6, micro-scratch testing of pure titanium processed by HPT is analysed. Chapter 7 investigates the tribological behaviour and adhesion of TiN coating on Ti substrates processed by HPT. Chapter 8 studies the adhesion of DLC-Zr coatings on Ti substrates processed by HPT. Chapter 9 contains the general discussion and theory modelling work. Chapter 10 presents the conclusions. And Chapter 11 lists the future work. Several journal papers published during the period of this PhD study are attached as appendix in the end of this thesis.

2. Literature review

2.1 Severe plastic deformation

2.1.1 Principle of severe plastic deformation (SPD)

The mechanical and physical properties of crystalline materials are determined by many factors, and the average grain size of the material generally plays a very significant role. It is well known that the strength of crystalline materials can be improved by reducing the grain size. Materials with fine microstructure often possess extraordinary properties, including very high strength, good toughness, long fatigue life [7]. For this reason, there is much current interest in producing metals with a very small grain size.

The technologies being used to produce UFG materials can be roughly divided into two categories: the 'bottom-up' and 'top-down' approaches [11]. The 'bottom-up' approach focuses on assembling individual atoms or consolidating nano-particulate solids. These technologies such as inert gas condensation [12] and high energy ball milling [13] are possible to produce ultrafine grains down to 10 nm. Limitations of these technologies are obvious, such as small dimension of samples and high degree of residual porosity.

The 'top-down' approach emphasizes on refining grain size of the existing coarse-grained (CG) materials through large straining or shock loading. This approach can be used to produce large bulk solids. SPD processing are methods involving extensive hydrostatic pressure in which a high strain is imposed onto the material without any significant change in the overall dimensions of the solid. Therefore, SPD processing introduces a high density of dislocations, these dislocations may further re-arrange to form new grain boundaries inside the former grains. In this way, bulk UFG materials are produced [14]. UFG materials obtained by SPD processing contain lattice defects such as large fraction of high angle grain boundaries with high energy (or called non-equilibrium boundary), and high density of dislocations [15].

5

These factors have significant contribution to the improvement of properties of UFG materials.

2.1.2 SPD techniques

Many different SPD techniques have been designed to impose large plastic straining to the materials without reducing the cross-sectional dimensions of the work pieces. These techniques include ECAP [1], HPT [2], accumulative ARB [3, 4], continuous confined strip shearing (C2S2) [16], constrained groove pressing (CGP) [17]. These techniques are fundamentally different, but all of them can refine grains of materials to the submicrometer level. So far, most attention currently has been devoted to the first two techniques: ECAP and HPT.

2.1.3 Equal-channel angular pressing (ECAP)

2.1.3.1 Principle of ECAP

ECAP was invented by Segal and his co-workers in 1981 [18]. This technique had the ability to introduce high strain into metal billets by simple shear. Since 1990s, ECAP started to draw attentions, and it was regarded as an ideal method to produce ultrafine-grained or nanostructured materials. By now, ECAP has been successfully applied to various materials such as copper [5], Al alloys [19] and Ti alloys [20], etc.
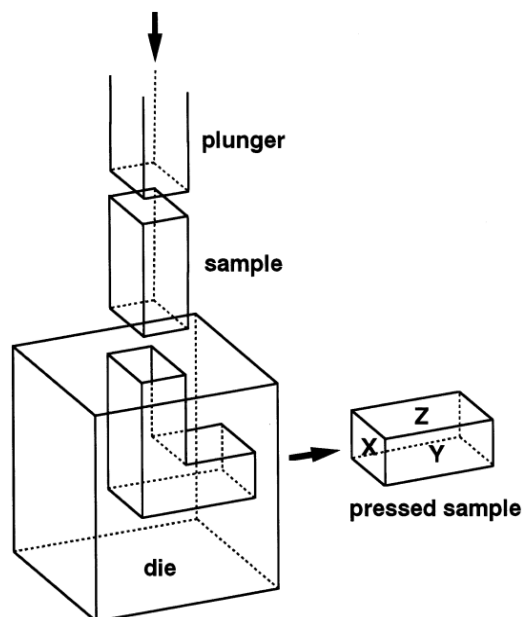
Figure 2-1 Schematic illustration of ECAP [21].

6

As shown in Figure 2-1, the die of ECAP is a block with two intersecting channels inside [21]. A lubricated sample of the same cross-section size with the channel is inserted into the die. As the plunger presses the sample into the channel, the deformation is achieved by simple shear (in theory, if there is no friction between the sample and the side walls) through the corner of two channels. So the whole sample is deformed in a uniform manner. Larger strain can be imposed to the sample by re-inserting the sample back into the die and pressing it out again in several cycles.

2.1.3.2 Estimation of strain imposed during ECAP
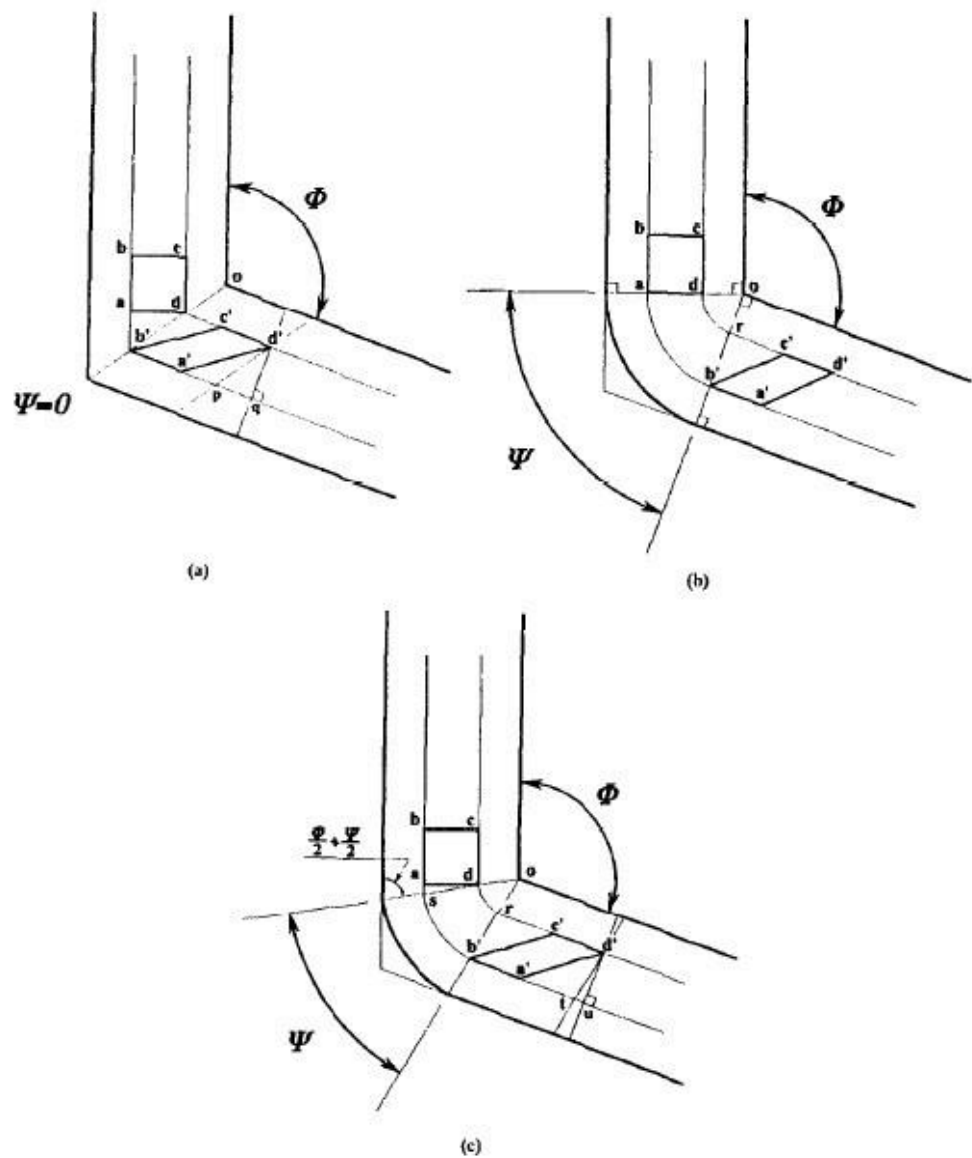
Figure 2-2 Principle of ECAP where Φ is the angle of intersection and Ψ is the angle of the arc of curvature: (a) $\Psi = 0$, (b) $\Psi = \pi - \Phi$, (c) an arbitrary value of Ψ lying between $\Psi = 0$ and $\Psi = \pi - \Phi$ [22].

7

It is believed that the strain imposed by ECAP each pass is determined by two angles of the die, Φ and Ψ. Where Φ is the channel angle, Ψ is the angle of the arc of curvature. Changes of the two angles lead to three main types of dies, shown in Figure 2-2 [22]. The three types of ECAP die designing was considered by Segal et al. when they invented this technique, and they associated the angle Ψ with the magnitude of friction between the sample and the channel wall [18]. The frictional effects were avoided by using appropriate lubricants. Wang et al. took an early step to estimate the strain by considering various factors [23]. Subsequently, Iwahashi et al. derived an equation which can be applied for all three types of dies [22]. The equivalent strain, ε, after each pass of ECAP is

$$\varepsilon = \frac{1}{\sqrt{3}}\left[2\cot(\frac{\Phi}{2}+\frac{\Psi}{2})+\Psi\cos ec(\frac{\Phi}{2}+\frac{\Psi}{2})\right] \qquad \text{(Eq.2-1)}$$

Equal strain will be imposed to the material by each pass ECAP, so the equivalent strain after N passes, ε_N, is presented by

$$\varepsilon_N = \frac{N}{\sqrt{3}}\left[2\cot(\frac{\Phi}{2}+\frac{\Psi}{2})+\Psi\cos ec(\frac{\Phi}{2}+\frac{\Psi}{2})\right] \qquad \text{(Eq.2-2)}$$

These equations provide basic principles when designing new ECAP dies.

2.1.3.3 Different routes of ECAP and their corresponding shear patterns

Since the ECAP technique was invented, Segal noted that different microstructures can be developed in any selected material by rotating the sample between each presses since any rotation changes the operative shear plane and shear direction when the sample passes through the corner [24]. After that, different routes of ECAP were widely studied [25-27], and four typical processing routes were finally published, shown in Figure 2-3 [21]. In route A, samples are pressed with no rotations between passes; in route B_A and B_C, samples are rotated by 90º in alternate directions or the same direction between each pass; in route C, samples are rotated by 180º between passes.

Shearing characters of these ECAP routes are shown in Figure 2-4 [27]. Each face of the cube gives a square before ECAP. After ECAP the cubic element is distorted. It is apparent from Figure 2-4 that during route A, continues deformation happens to the X plane and Y plane, but no change happens to the Z plane; During route B_A, continues changes happens to all three planes. The cubic element is retorted every 4 passes during route B_C and every 2 passes during route C. There is no deformation in the Z plane when processing with route A or C. Route A and B_A have the similar shear pattern, while route B_C and C have the similar shear pattern.
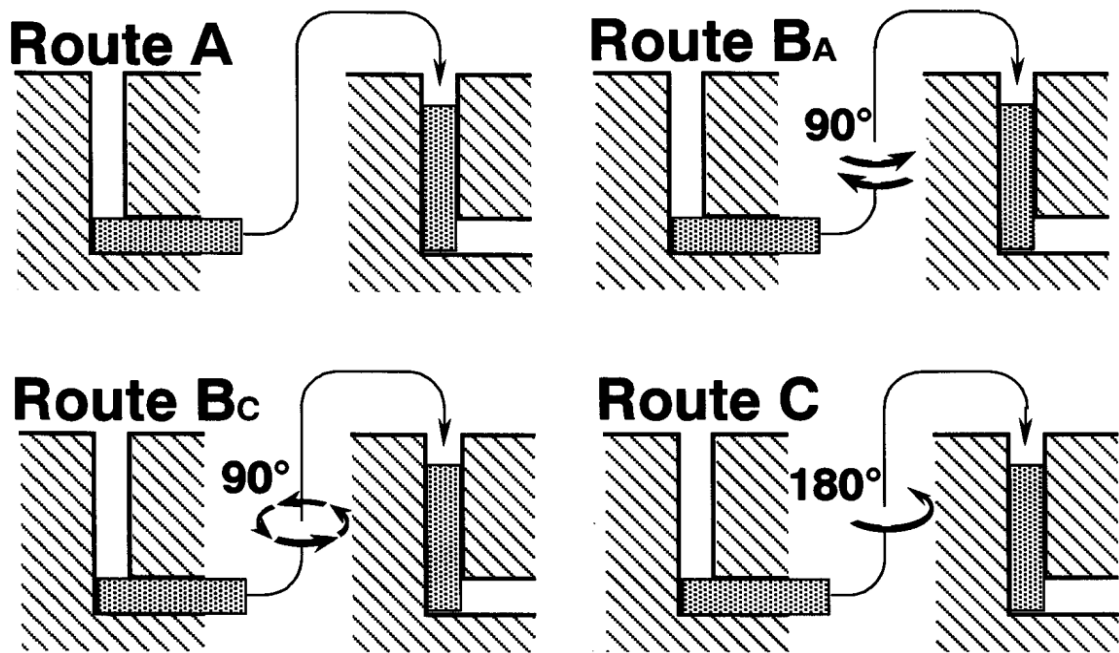
Figure 2-3 The four routes of ECAP [21].

With information from Figure 2-4, and also experimental observations using samples of high purity aluminium [26, 28], it is believed that route B_C refines the microstructure of material most effective, route C does less effective, route A and B_A are the least effective to refine microstructure.

Some complex combination routes were also studied, such as route B_A-A and route B_C-A. Results showed that these complex routes did not lead to additional improvement to the microstructure refinement [29].
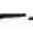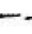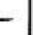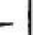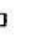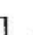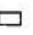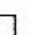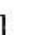
Figure 2-4 Shearing characters of the four ECAP routes [27].

2.1.3.4 Models of grain refinement during ECAP

Valiev proposed a model incorporated the continuous formation of new grain boundary through introduction of dislocations during the straining process [14]. However, Xu et al [30] claimed this model is not consistent with the observations that after 1 pass of ECAP the grain size of pure Al is ~1.3μm, the ultimate grain size of pure Al is also ~1.3μm after 12 passes of ECAP [25, 26, 31, 32]. Terhune et al. produced a new model for grain refinement of aluminium when processed by ECAP [32]. This model based on the inter-relationship between the formation of subgrain boundaries and slip, it also included estimates of the fractions of high angle grain boundaries (HAGB).

Later, the Terhune model was further developed by Langdon [33], as shown in Figure 2-5. In this model, the width of the subgrain bands is set as *d* for each pass of ECAP. The symbol η in Figure 2-5 represents the total angular range of the various

slip systems. During route B_C, the present of several intersecting slip systems introduces high density of dislocations. After 4 passes, the microstructure shows equiaxed grains on the Y plane. During route C, the shear plane lies consistently at 45º with the X direction when viewed on the Y plane. During Route A, the shear planes lies at 8º, 11º, 18º and 45º after 1, 2, 3 and 4 passes, respectively [34]. The angular ranges, η, of routes A and C are small, which causes these two routes are less effective in grain refining.

Recently, a new model was produced by Starink et al. [35], which can be used to predict grain size after SPD using volume averaged number of dislocations.
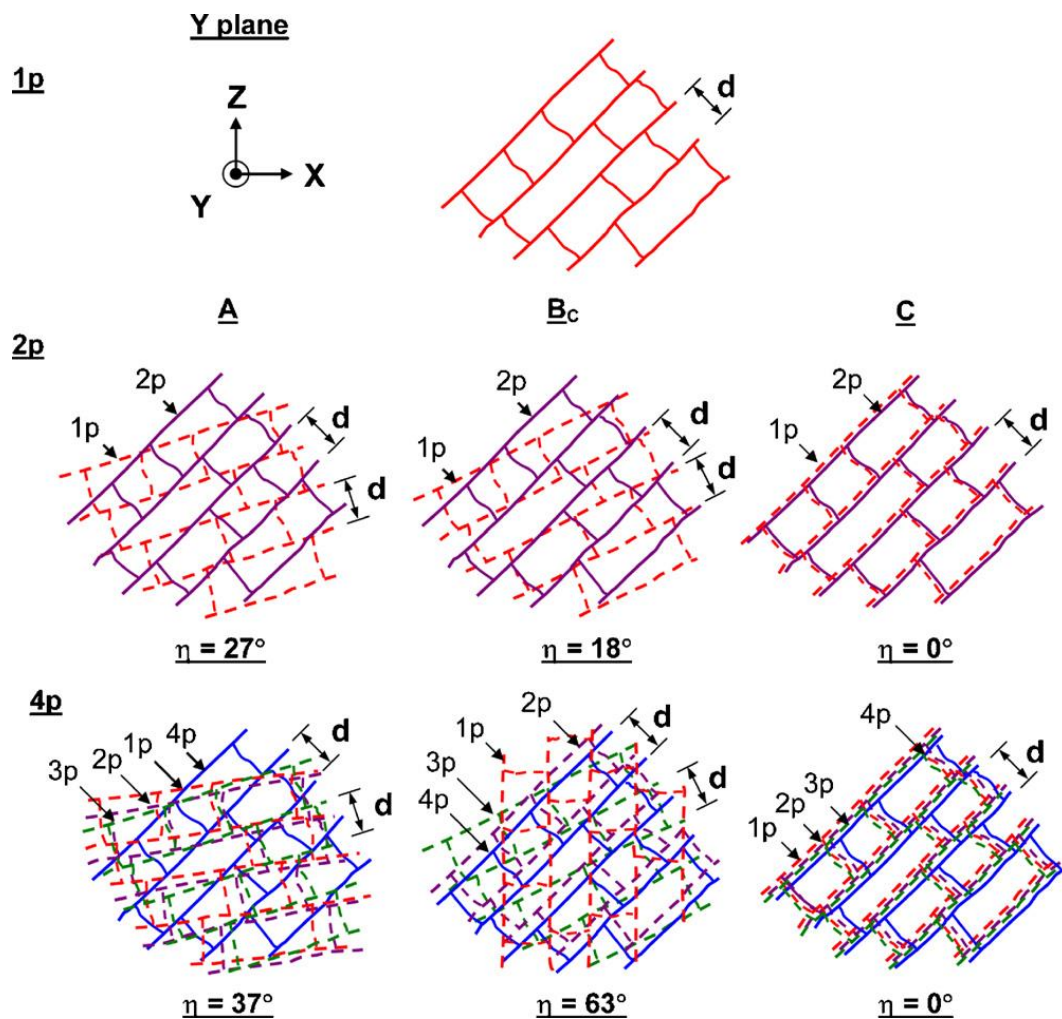
Figure 2-5 A model for grain refinement during ECAP where subgrain bands are formed after different number of ECAP passes [33].

2.1.4 High-pressure torsion (HPT)

2.1.4.1 Principle of HPT

HPT refers to the processing of metals in which samples are subjected to a compressive force and torsional straining [2]. Fundamental principles of HPT was first proposed by Bridgman around 1943 [36], these early studies from Bridgman successfully applied compression pressure up to 1 GPa and increased the torsional strength of samples, Figure 2-6 [36].
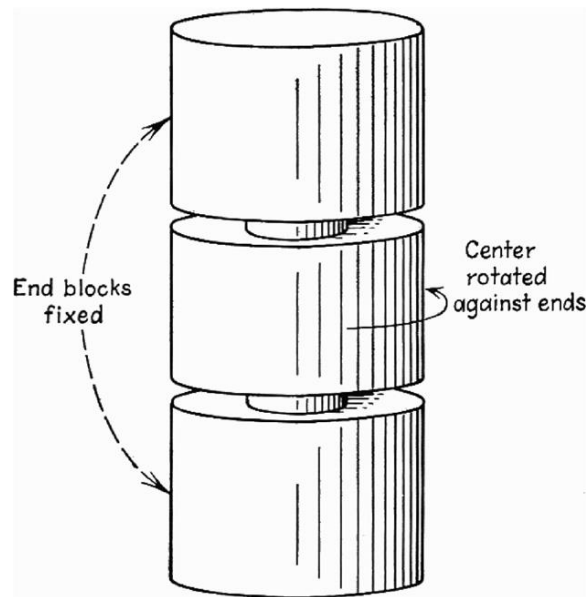
Figure 2-6 The Schematic illustration of apparatus proposed by Bridgman in which torsional straining is combined with longitudinal compression [36].

As shown in Figure 2-7, a sample in the form of a disc is put in the middle of two anvils applied with high compressive pressure, and a torsion strain was imposed through friction forces between the anvil and sample as the lower anvil rotating [37].

In practise, there are two main types of HPT processing depending on the shape of anvils: the unconstrained HPT and constrained HPT. In unconstrained HPT, samples are placed between two anvils as shown in Figure 2-8(a) and subjected to HPT processing. In such case, the material of sample is free to flow outwards when high presser is applied, samples are mostly much thinner after HPT processing [38].
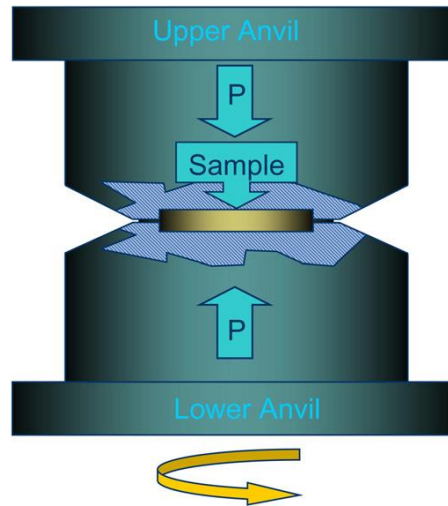
Figure 2-7 The Schematic illustration of HPT processing [37].

In constrained HPT, samples are placed into a cavity of the lower anvil or both anvils, as shown in Figure 2-8 (b) and (c) [39]. This designing can prevent material flowing outwards, so that the HPT processed samples have slightly smaller thickness than before processing. Normally, the constrained HPT is more popular method for metal processing, as this designing conducts a more effective back-pressure to the samples [40-42].
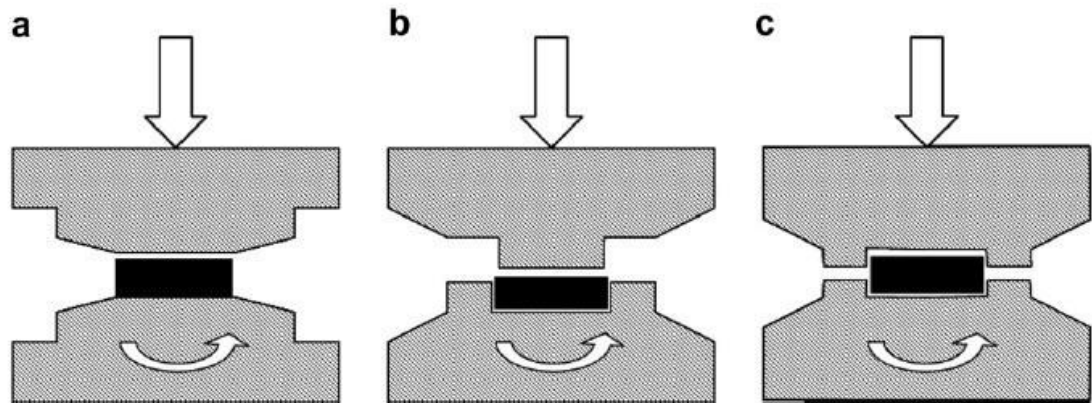
Figure 2-8 Schematic illustration for unconstrained HPT (a) and constrained HPT (b,c) [2, 39]

2.1.4.2 Estimation of strain imposed during HPT

Figure 2-9 shows the parameters used to estimate the strain imposed during HPT processing, given by equation [38]:

$$dγ = \frac{dl}{H} = r\frac{dθ}{h} \tag{Eq.2-3}$$

Where h is the disc thickness, r is the radius of the disc, $d\theta$ is the infinitely small rotation, dl is the infinitely small displacement, $d\gamma$ is the incremental shear strain.
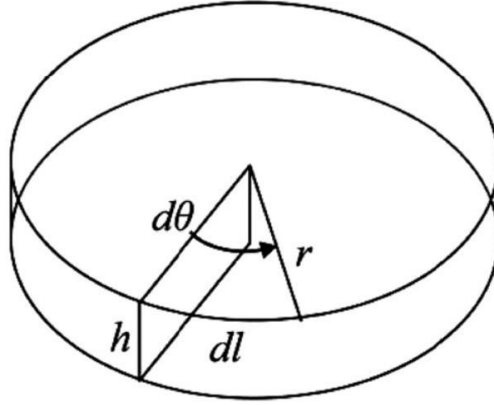
Figure 2-9 The parameters used to estimate the imposed strain in HPT [38].

When the imposed shear strain was very small, the equivalent strain ε was defined by [43]:

$$\varepsilon = \frac{\gamma}{\sqrt{3}} \qquad \text{(Eq.2-4)}$$

When the imposed shear strain was large, especially for the cases where $\gamma \geq 0.8$, the equivalent strain ε is given by :

$$\varepsilon = \frac{2}{\sqrt{3}} \ln \left[\left(1 + \frac{\gamma^2}{4} \right)^{\frac{1}{2}} - \frac{\gamma}{2} \right] \qquad \text{(Eq.2-5)}$$

2.1.4.3 Variation in homogeneity of disc samples during HPT

As shown in Eq.2-3, the strain imposed to the sample varies across the sample. Consequently, the microstructure and property produced by HPT processing is inhomogeneous, which has been regarded as a limitation of HPT processing. Microhardness measurement across the disc surface has been an efficient way to study homogeneity of HPT processed Al [44, 45], Cu [46, 47], Ni [48] and Ti. Most of the results show that a reasonable homogeneous microstructure can be achieved after a sufficient high torsion straining. As shown in Figure 2-10 [49], a commercial pure (CP) Al was processed via HPT under pressure of 1 GPa for several revolutions, it is clear to see that the microhardness across the disc sample is inhomogeneous during the initial period of torsion straining by showing the centre of disc sample has much lower microhardness than the edge of sample. However, the microhardness

across the sample becomes very homogeneous after 4 revolutions of torsion. Moreover, it is noticeable that the microhardness near the edge of sample keeps unchanged over 1 revolution of HPT, which indicates that a saturation of deformation and grain refinement are reached.
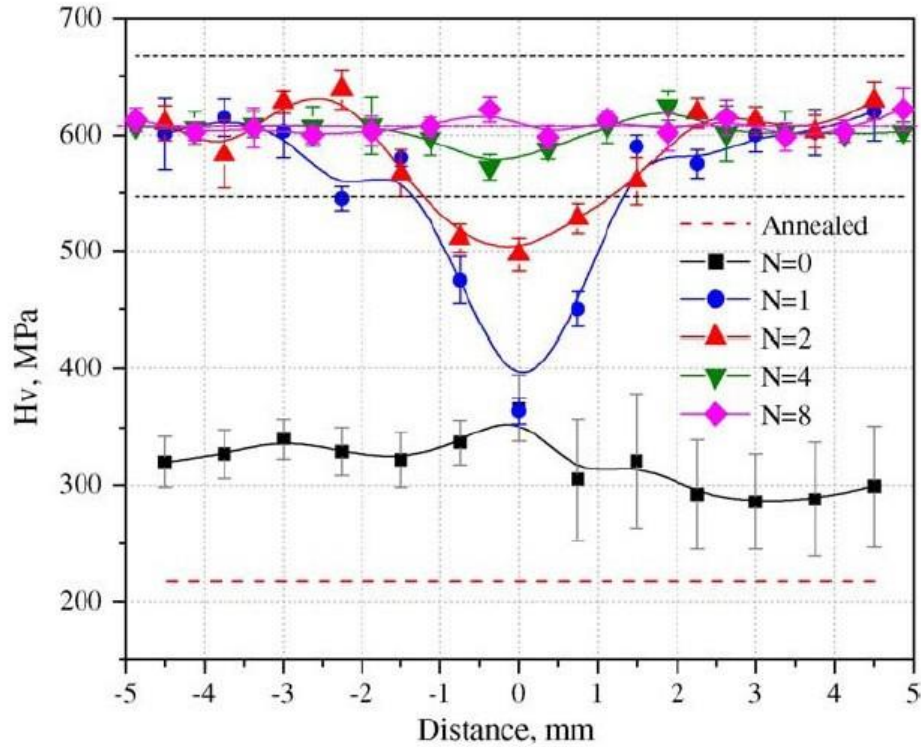
Figure 2-10 Microhardness distributions across the diameters of CP aluminium discs subjected to a pressure of 1GPa and up to eight whole numbers of revolutions: the lower broken line shows the initial annealed condition [49].

A recent report studied the effect of different HPT pressure on the microhardness of Al-3%Mg-0.2%Sc alloy [44]. As shown in Figure 2-11, microhardness increases with increasing distance from the centre of disc after the same number of torsion revolutions and the higher HPT pressure leads to a more homogeneous microhardness across the disc sample, which indicates that a higher HPT pressure prompts microhardness homogeneity of the disc sample.

Recently, a study investigated microhardness of a commercial magnesium AZ31 alloy processed by HPT at 453 K using three different rotation rates [50]. Results demonstrate the hardness and the homogeneity both exhibit a very small dependence on the local strain rate.

15
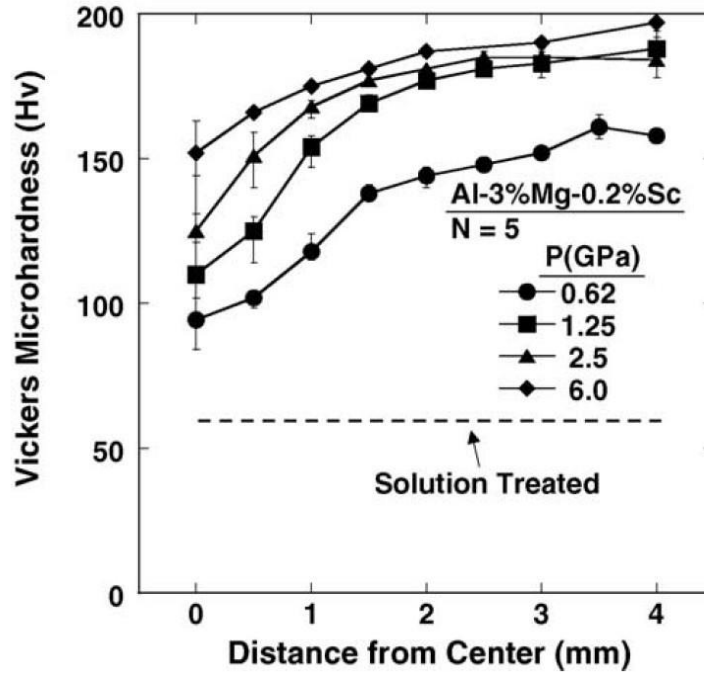
Figure 2-11 Microhardness according to distance from the centre of the disc for samples tested through five turns under various levels of the applied pressure [44].

2.1.5 Other SPD technologies

Along with ECAP and HPT processing, there are several other SPD methods which also can introduce ultrafine grains to materials by straining. Some of these SPD techniques have very good potential for industry applications, including ARB [3, 4], con-shearing process [51, 52], repetitive corrugation and straightening (RCS) [16, 53, 54] and Twist Extrusion (TE) [55, 56].

2.1.5.1 Accumulative roll bonding (ARB)

During ARB, two layers of materials (may be two different materials) are joined together by rolling like a roll-bonding process. Then, the length of rolled material is sectioned into two halves. The sectioned strips are roll-bonded again. As the process carry on in this way, high plastic strain are introduced to the material, shown in Figure 2-12 [57]. ARB process has been successfully used to produce UFG microstructures of Al [3], Mg [57] and steel [4]. It is believed that ARB process has high productivity and good feasibility for large-sized material production.
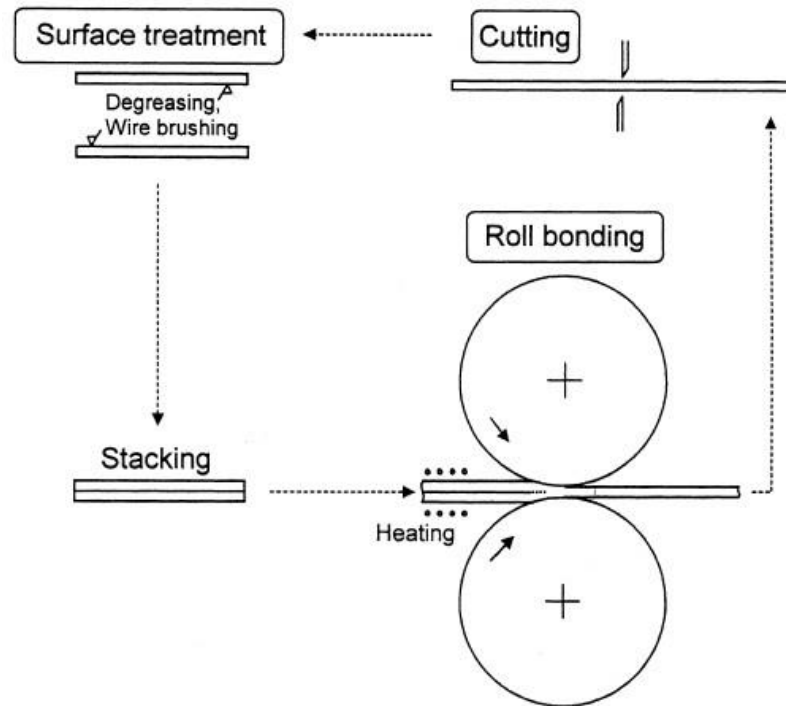
Figure 2-12 Principle of ARB [57].

2.1.5.2 Conshearing process
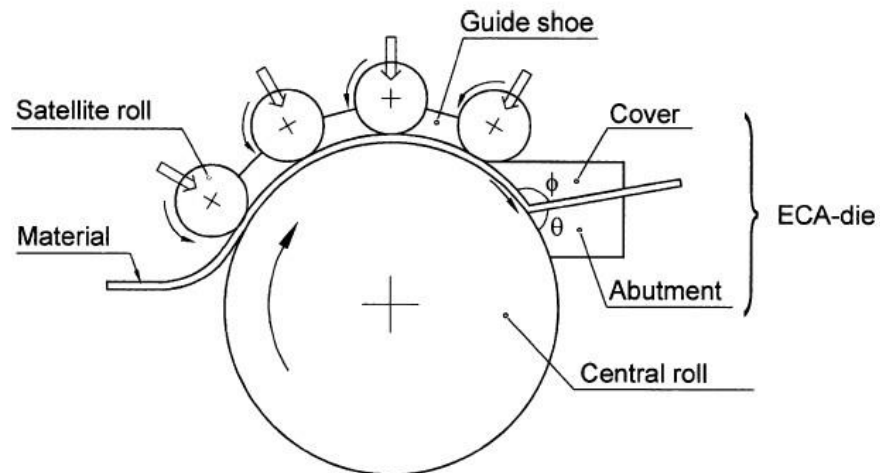
Figure 2-13 Principle of conshearing process [51, 52].

The conshearing process is a continuous version of ECAP processing. An ECA die was mounted at the exit of a satellite mill. Four small rolls and one large roll were used as feed rolls via friction force, shown in Figure 2-13 [51, 52]. Meanwhile, the inside of the ECAP die was coated by low friction coatings, and lubricated by mineral oil, all these designs were aimed to reduce the friction between material trips

and the die [51, 52]. The conshearing process is more efficient in productivity compared to traditional ECAP processing, however, new designs are still necessary to further reduce the friction inside ECAP die to make this process more applicable.

2.1.5.3 Repetitive corrugation and straightening (RCS)

Another SPD technology, RCS can not only create bulk nanostructured materials, but can also be easily adapted to large-scale industrial production. As shown in Figure 2-14, there are two steps in a RCS recycle: corrugation and straightening [16]. The corrugation is carried out in a die set as shown in Figure 2-14 (a), which is the discontinuous version of the RCS process. Figure 2-14 (b) demonstrates continuous version of the RCS process. It is obvious that the continuous RCS process can be easily adapted to a rolling mill for industrial production of nanostructured metals and alloys. After that, the corrugated work-piece is straightened using two flat platens [53].
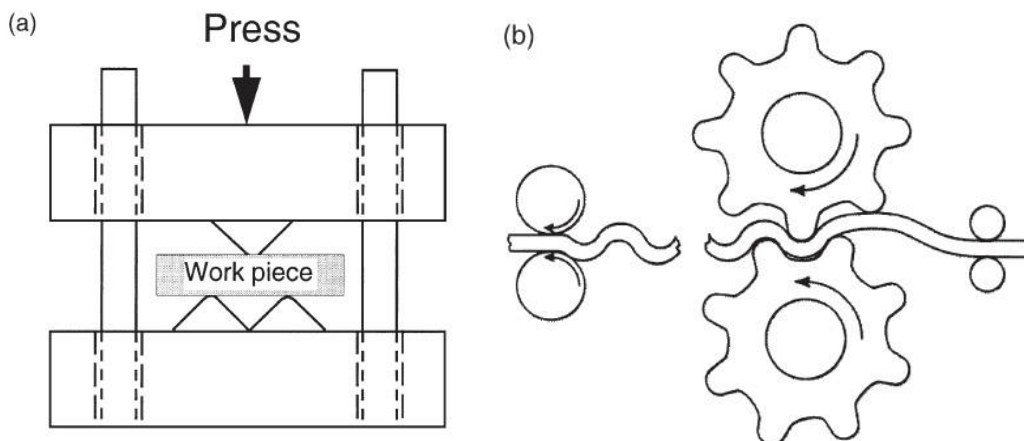
Figure 2-14 Principle of RCS: (a) discontinuous version and (b) continuous version [16].

2.1.5.4 Twist extrusion (TE)

Twist extrusion is carried out via pressing out a prism specimen through a die with a profile consisting of two prismatic regions separated by a twist part, as show in in Figure 2-15 [56]. As the specimen is pressed through the die, it undergoes severe deformation with two simple shear planes: one of them is perpendicular and the other is parallel to the specimen axis. At the same time, the cross-section of the work piece keeps unchanged after one pass of extrusion which indicates that more deformation

can also be introduced by repeating the same process. Like ECAP, TE is performed under high hydrostatic pressure in the centre of deformation. The pressure is created by applying backpressure to the specimen when it is pressed out from the die [58].
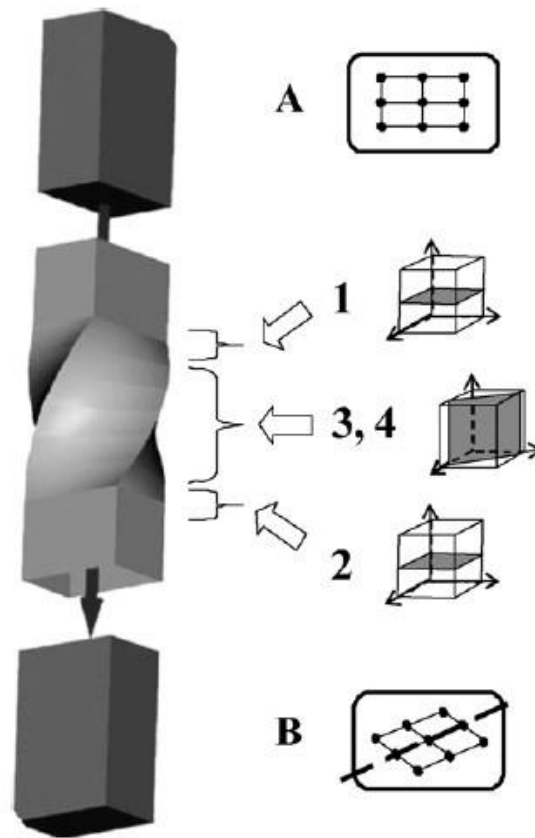
Figure 2-15 Principle of TE [56].

2.1.5.5 Latest developed SPD methods for industry

Recently, there have been attempts to develop SPD techniques with reduced cost and on a larger scale for industrial applications. For example, equal-channel angular pressing-conform is a new technique combining ECAP and the conform process [59]. At the same time, new procedures such as continuous high-pressure torsion [60, 61], tube high-pressure shearing [62] and high-pressure tube twisting [63] are starting to emerge. These new procedures make it possible to produce large scale UFG materials in a more efficient and less wasteful manner.

As illustrated by Figure 2-16, the facility of continuous high-pressure torsion consists two anvils, the upper anvil has a half ring-shaped groove, the lower anvil has a rough ring-shaped surface. A U-shaped specimen is placed in the groove between two anvils, and the pressure is applied on the sample by raising the lower anvil up to a

rigid contact with the upper anvil, which is very similar with HPT processing. The lower anvil is then rotated while the upper anvil is fixed in place, and shear strain is introduced to the sample under a high pressure [60, 61]. Tube high-pressure shearing [62] and high-pressure tube twisting [63] have similar facility design with continuous high-pressure torsion. Compared with conventional HPT processing, these new processing ensures the ability to produce a more homogeneous microstructure of samples, moreover, the open shape of these facilities can be used as a continuous process for producing metallic sheets and wires with very long product length.
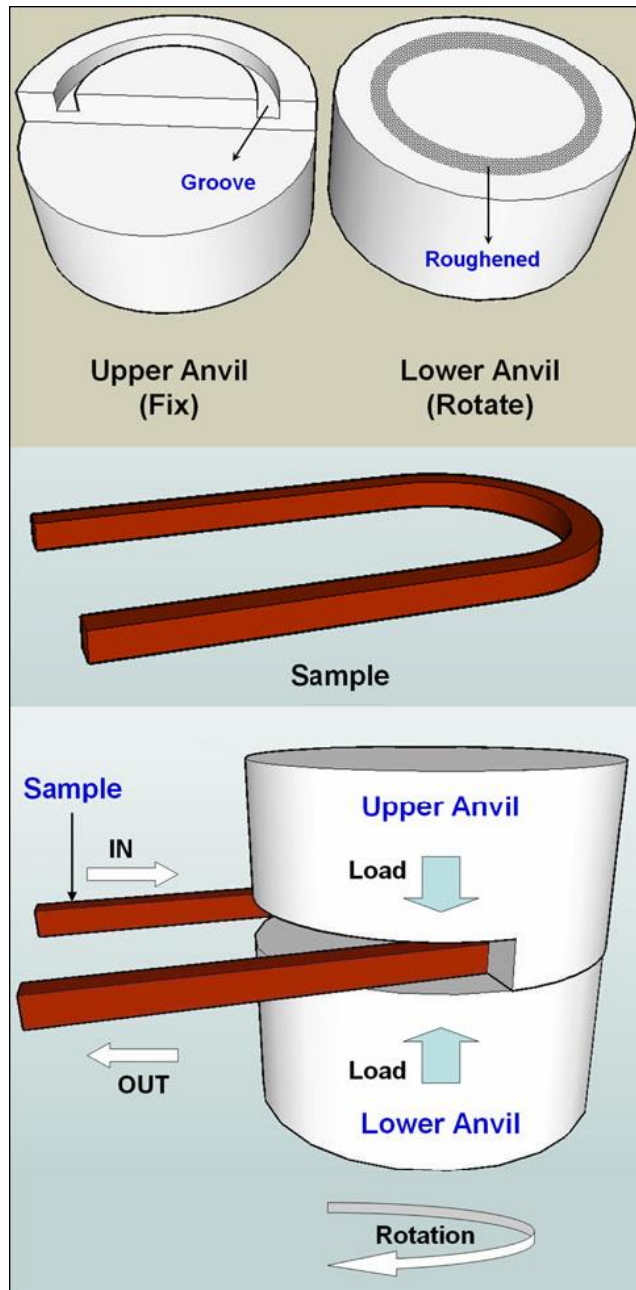
Figure 2-16 Schematic illustration of continuous high-pressure torsion [61].

2.1.6 Properties of SPD-processed materials

2.1.6.1 Strength and ductility

It is well known that grain refinement can significantly improve mechanical strength of materials [7, 64]. However, it is also observed that SPD process decrease the ductility of materials at the same time [5, 19]. As reported in an early study, strength of several Al alloys increases remarkably after equivalent strain of ~1 and followed by a gradual slow increase with further increase of imposed strain. On the other hand, the ductility of the Al alloys decrease remarkably after one pass of ECAP and remains similar with further increase of equivalent strain, as shown in Figure 2-17[19].
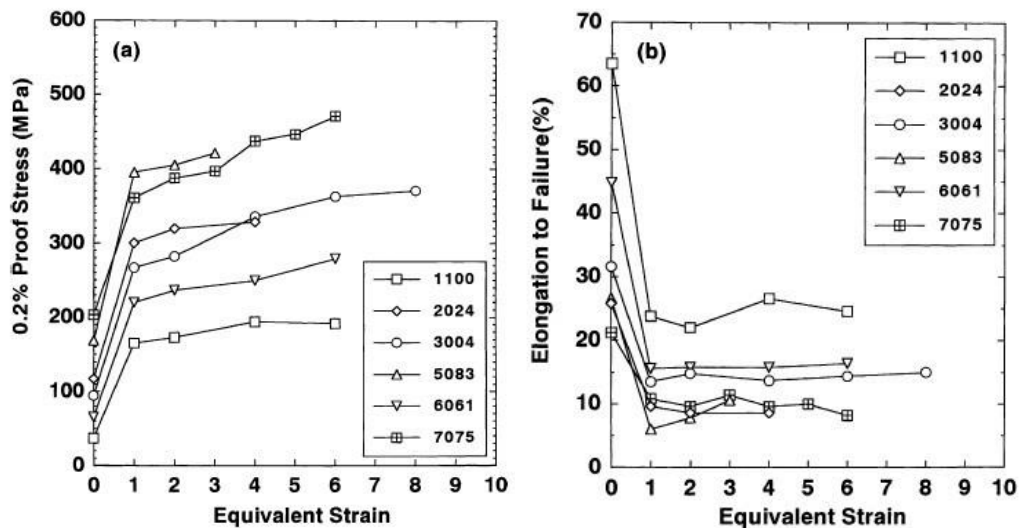
Figure 2-17 Plots of 0.2 proof stress (a) and elongation to failure (b) of several Al alloys according to equivalent strain [19].

Another study on Cu also reported the similar trend, in which Cu samples was processed by cold-rolling and ECAP, respectively. As shown in Figure 2-18, the strength of Cu was improved after cold-rolling but the ductility was decreased dramatically. The same trend was true for Cu processed by ECAP for 2 passes. However, as Cu was further processed by ECAP up to 16 passes, ductility rose back close to the as-received stage. It was believed the increasing fraction of high angle boundaries with increasing ECAP passes changed the dominating deformation mechanism during tensile test, in which grain boundary sliding and grain rotation became more important [5]. Additionally, it is very easy to form deformation twinning during SPD processing due to its low stack fault energy.

During recent years, several approaches have been taken to obtain a good combination of exceptionally strength and ductility, such as creating 'bimodal' structure [65, 66], inducing nanoscale twins [67, 68], and using transformation-induced plasticity [69].
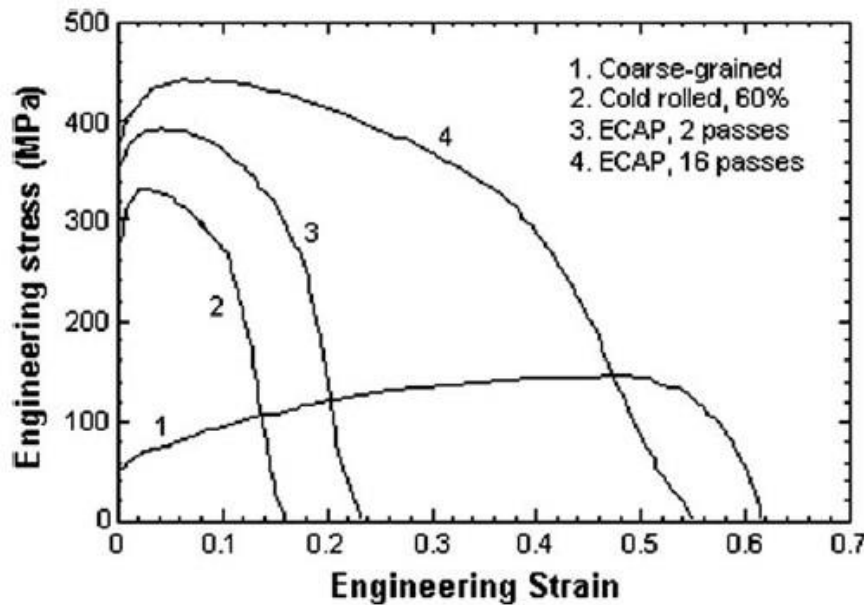
Figure 2-18 Tensile curves for Cu tested at room temperature [5].

Cu with a bimodal microstructure had similar strength to ultrafine-grained Cu and a comparable ductility of coarse-grained Cu [66]. Such a bimodal microstructure was obtained by a short annealing at 200 ℃ for 3 minutes after ECAP processing. TEM analysis showed that some micron sized grains were surrounded by ultra-fine grains, shown in Figure 2-19 [66]. The ultra-fine grains bring grain boundary strengthening to the material, while the micro grains stabilize the tensile deformation of the material. During the tensile testing of bimodal structures, the storage of geometrically necessary dislocations required for compatible plastic strains gradient at the interface between nano-grains and micro-grains. This strain-gradient plasticity is believed to play a significant role to bring ductility enhancement to the bimodal materials [70]. Similar behaviour was also observed on Zn [71] and Al-Mg alloy [72].

Another study on Al-10.8%Ag alloy processed by ECAP and subsequent aging showed that a further increase of hardness after ECAP processing was achieved after

aging at 373 K for 100 hours [73]. The TEM analysis showed that this increase was due to precipitation of spherical particles and elongated particles. Tensile test also showed that these precipitations increase the work hardening capacity and ductility of Al-Ag alloy, as shown in Figure 2-20 [73].
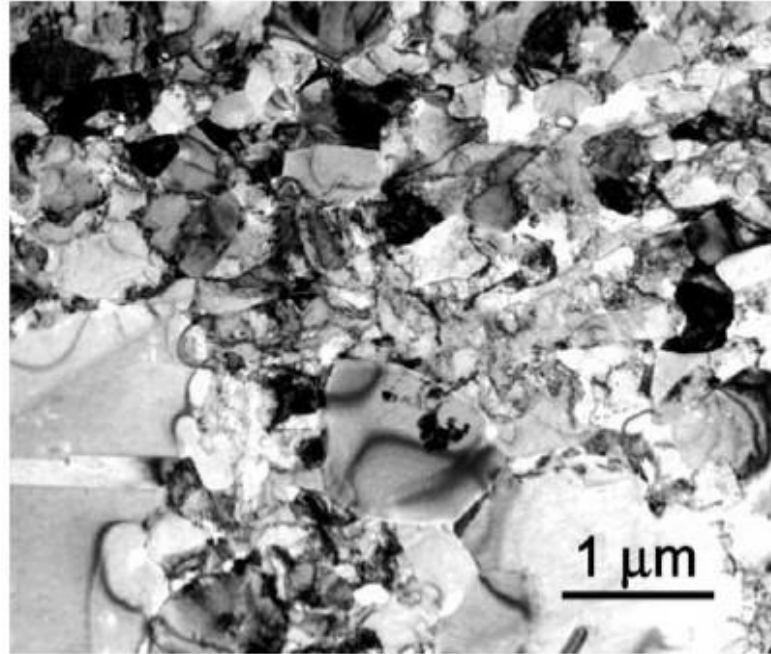
Figure 2-19 Microstructure of Cu which was processed by using ECAP and cold-rolled to 2300%, followed by annealing at 200 ℃ for 3 min [66].
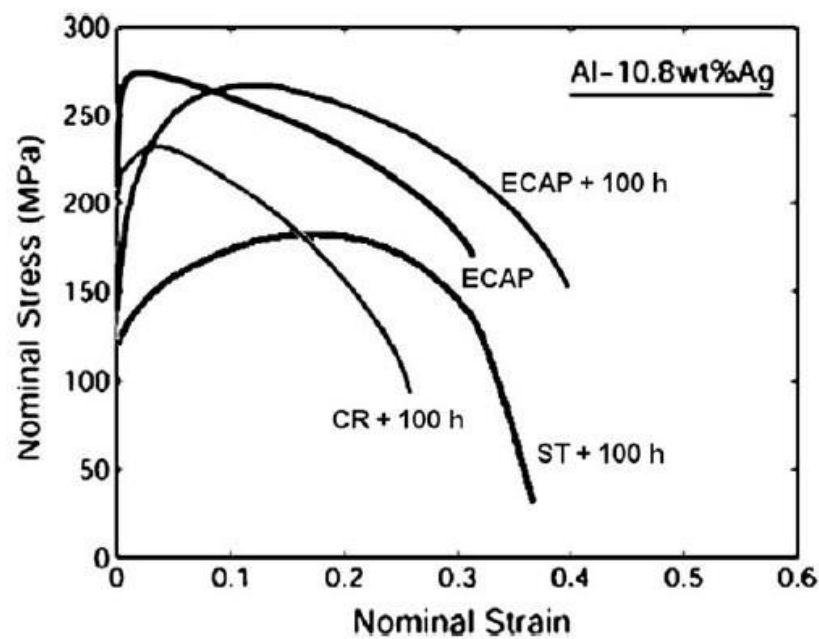
Figure 2-20 Tensile curves of Al-10.8%Ag after solution treatment (ST) or cold-rolling (CR) or ECAP with/without aging for 100 hours [73].

High strength and good ductility of Ti processed by HPT was also obtained by heat treatment following HPT. As shown in Figure 2-21, the short annealing at 300ºC and 350ºC after HPT processing both improved the strength of Ti significantly. Especially the annealing at 350 ºC brought yield strength of over 1200 MPa and a much improved ductility compared to that HPT processed Ti (Curve 1) [74]. As TEM investigation showed that the annealing at 300 ºC lead to the movement of defects from grain interiors to the near grain boundary region without grain growth. The grain boundary after annealing contained a highly disordered region and an ordered region made up by array of dislocations. It was assumed that the highly ordered structure of grain boundary enhanced ductility of Ti while the high dislocation density near grain boundaries brought higher strength. The grain boundary structure after annealing at 350 ºC still needs more investigations. However, these results showed the possibility of achieving good mechanical property of materials using SPD and heat treatments.

.
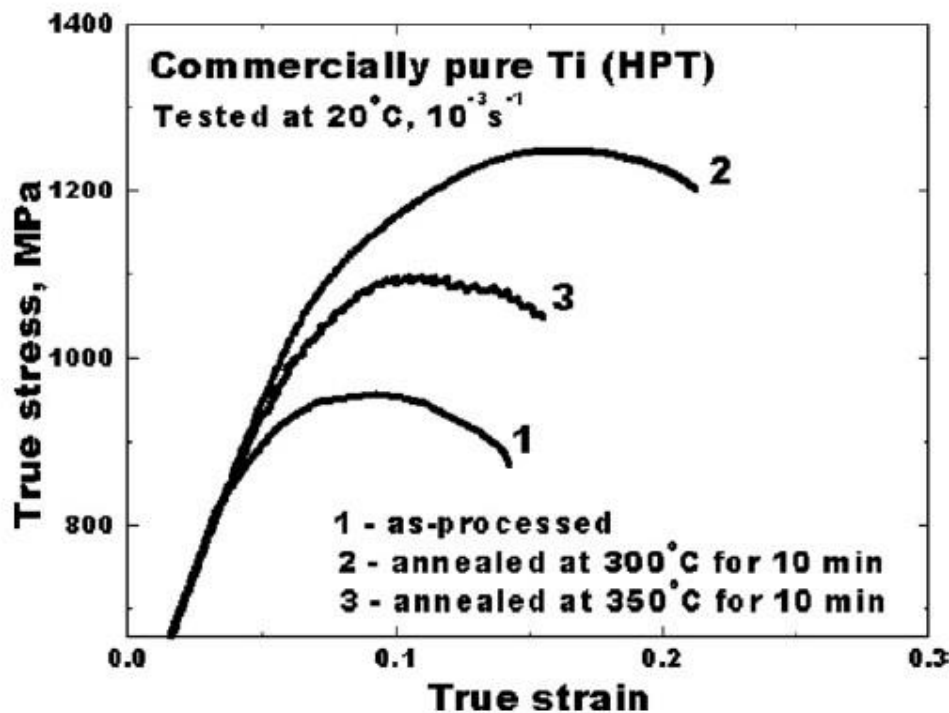
Figure 2-21 Tensile curves of pure Ti after HPT (Curve 1) and HPT plus annealing (Curve 2 and 3) [74].

2.1.6.2 Superplasticity

At elevated temperatures, grain boundary sliding (GBS) [75, 76] may have significant contribution to the total strain of superplasticity, the total strain, ξ, is given by

$$\xi = \frac{\varepsilon_{gbs}}{\varepsilon_t}$$
(Eq.2-6)

Where ε_{gbs} and ε_t are the strain due to grain boundary sliding and the total strain, respectively. It is reported that in some cases, the ξ can be as large as 50-70%. Therefore, achieving superplasticity by refining grain size has drawn attention of researchers recently. In practise, it is attractive to achieve superplastic ductility using SPD methods. These materials produced may be used in industrial superplastic forming operations, Figure 2-22 shows an example of superplastic forming for an Al–3% Mg–0.2% Sc alloy processed by ECAP [77].
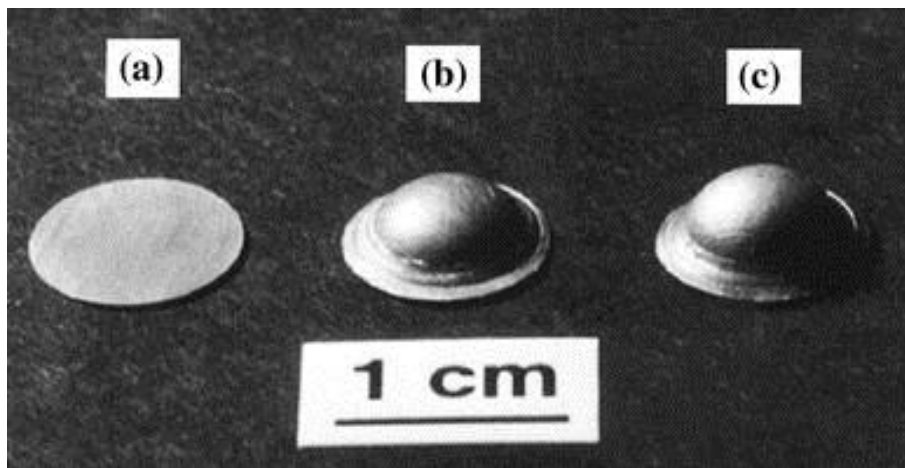
Figure 2-22 Superplastic forming at high strain rates in a gas-pressure facility of an Al–3% Mg–0.2% Sc alloy processed by ECAP [77].

The same Al–3% Mg–0.2% Sc alloy processed by HPT also exhibits the characteristics of true superplasticity and quasi-stable plastic flow. As shown in Figure 2-23, appearance of the horizontal specimen which was deformed to 1600% at failure, very uniform deformation with no evidence for the occurrence of any incipient necking within the gauge length was observed [78]. Furthermore, experiment which was conducted on a HPT-processed Mg–9%Al alloy at a temperature of 473K achieved elongation of 810% [79].

Figure 2-24 shows how SPD processing brings higher elongation to failure to AZ31 [80]. When the tensile test was performed at 473 K, ECAP processing for 4 passes successfully brought elongation to failure of 960% compared to 310% of the as-received AZ31. Furthermore, a clear trend of increasing elongation to failure of material with increasing ECAP passes was observed.
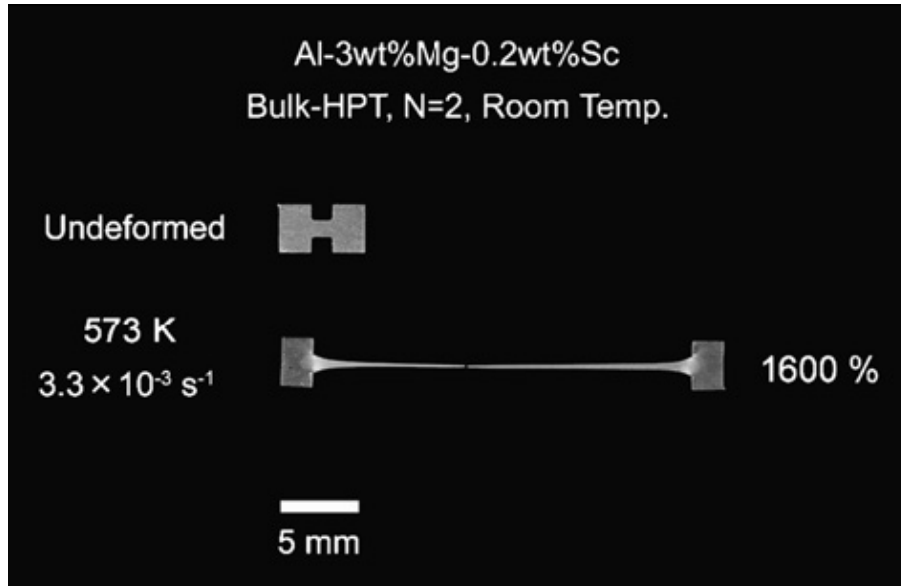
Figure 2-23 Appearance of extruded specimen with elongation to failure up to 1600% processed by HPT [78].
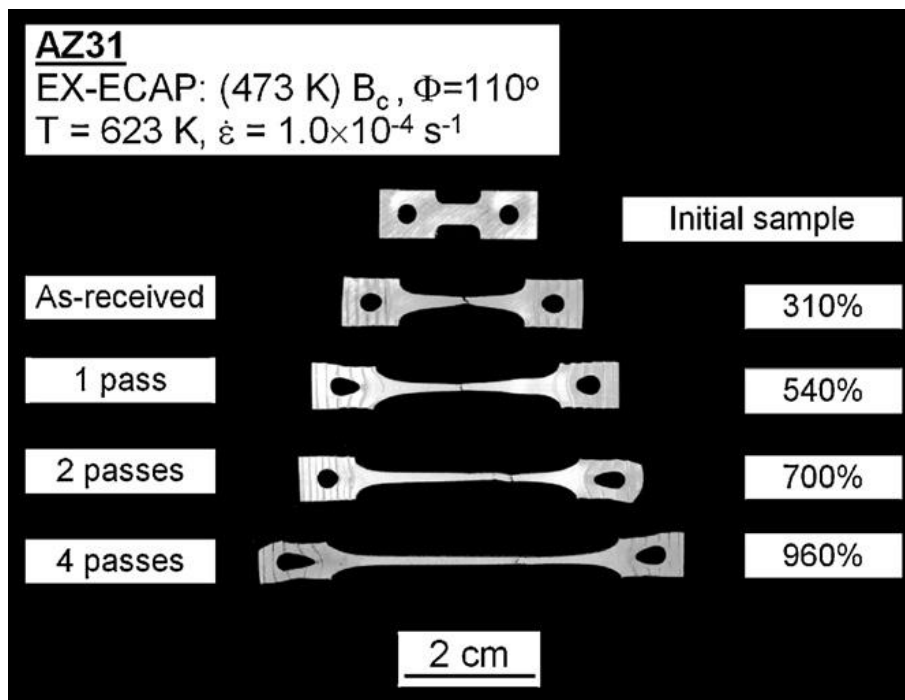
Figure 2-24 Appearance specimens of the extruded AZ31 alloy after testing to failure at 623K with an initial strain rate of 1.0×10^{-4} s^{-1} before and after processing by ECAP for different numbers of passes of ECAP [80].

2.1.7 Applications of SPD processed materials

With higher strength, especially higher strength-to-weight ratio, those bulk SPD-processed materials have advantages for structural and functional applications.

2.1.7.1 UFG Ti for bio-medical applications

Total joint replacements (TJR) are now applied worldwide to alleviate the functional deteriorations in human joints caused by aging, degenerative diseases and accidents [81]. In England in 2011 there were >80,000 total knee replacements and >75,000 total hip replacements [82]. Predictions suggest that these numbers will increase substantially in future years [83]. Based on these reports, it is anticipated there will be an ever increasing demand for bio-implants.

Metallic biomaterials such as stainless steels, Co-Cr alloys and titanium alloys are used extensively in orthopaedic applications due to their high strength, bio-tolerance and excellent corrosion resistance. Nevertheless, there are numerous reports documenting the toxicity of these metal implants. As the metal ions (Ni, Cr, Co, Al, V, etc) are released from the implants, there are potential health problems such as skin diseases due to Ni toxicity and carcinogenicity due to Co and Cr [84-87]. Therefore, there is now an urgent need for exploring the potential for developing other bio-metals. This problem may be avoided through the use of CP titanium but procedures are then required for improving the strength of the material [88, 89]. Recent reports have demonstrated that UFG CP Ti, having a comparable high strength to Ti-6Al-4V and a much improved biocompatibility, may be produced using several metal forming procedures based on the imposition of SPD [20, 90-94]. To date, bulk UFG CP Ti was successfully produced using SPD methods such as ECAP and HPT and processing both at high temperatures and room temperature.

The results available to date show that processing by HPT generally produces greater grain refinement and improved strengthening by comparison with ECAP [95-98]. For example, a high ultimate tensile stress (UTS) of ~1400 MPa was achieved in Grade 4 Ti using HPT but with a corresponding significant loss in ductility [99]. A corrosion study reported superior corrosion resistance in UFG Ti due to rapid passivation along

the grain boundaries [100]. The fatigue life of Ti is enhanced by SPD so that in Grade 4 Ti the fatigue limit after 10^7 cycles was increased to ~590 MPa using ECAP compared with ~350 MPa in the CG condition [101-103]. Recent research on biocompatibility has documented improved pre-osteoblast attachment and rate of growth on UFG pure Ti compared with CG pure Ti and Ti-6Al-4V substrates, where this is attributed to the presence of surface discontinuities, the surface energy, a higher wettability and the presence of stable TiO_2 films which improve the protein adsorption on the surface [104-106].
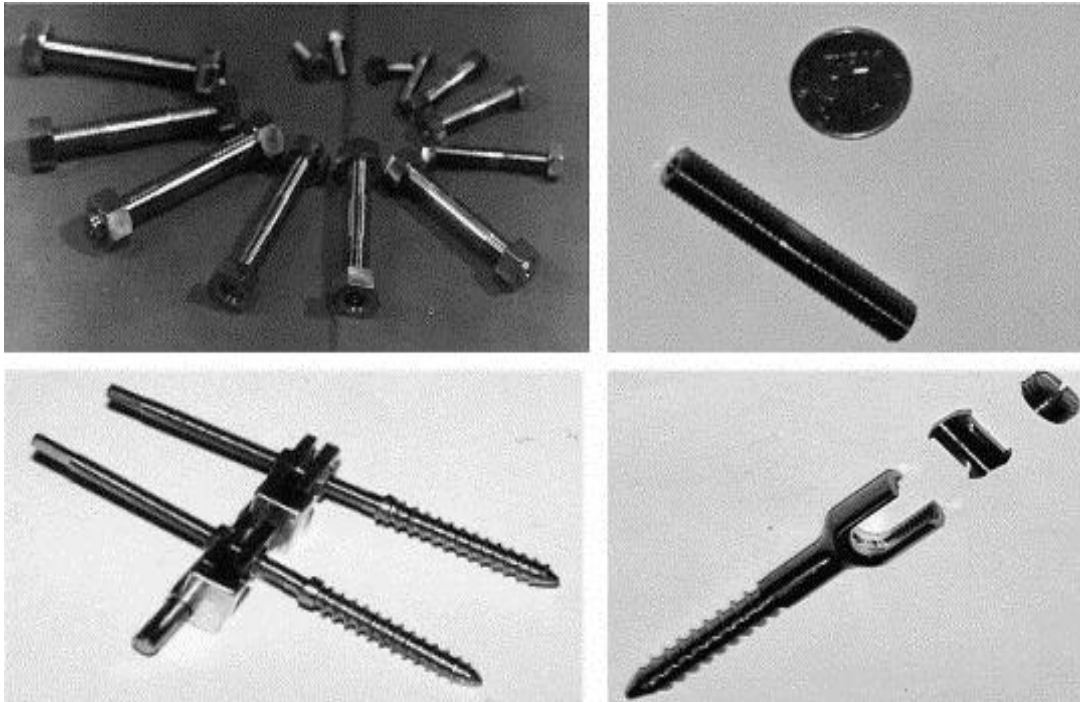
Figure 2-25 Screw implanted items made of UFG pure titanium [10].

With all the favourable properties as addressed above, it is widely expected that high strength pure Ti items processed by SPD can be used to substitute Ti-6Al-4V in biomedical area [10, 107]. As shown in Figure 2-25, these bio-medical products made of pure titanium with UFG structure have high mechanical properties, together with complete lack of intoxication of the organism and corrosion of metal. Therefore, these products can be widely used for medical devices and implants [10]. Besides, dental implants with a smaller diameter 2.4 mm were successfully manufactured from UFG pure titanium. These implants can withstand the same load as conventional titanium implants with a diameter of 3.5 mm, they can be installed to thinner jawbones and introduce less damage during surgery [107]. After scaling up of

SPD processing, larger components made of UFG pure Ti can also be applied as total joint replacements.

Despite these merits, questions remain concerning the long term durability of UFG Ti and specifically the wear resistance. In practice, the sliding motion between the femoral and acetabular metal components will generate metallic debris that may cause pain in the patient and lead ultimately to mechanical failure of the device [108, 109]. To address this problem, studies are very necessary to evaluate the wear behaviour of UFG Ti.

2.1.7.2 Other applications of SPD materials

Al has very good thermo conductivity and work ability, which makes it good candidate as microparts of heat exchanger. Thermal embossing was conducted on Al-1050 and Al–Mg–Cu–Mn alloys using a micro silicon mould fabricated by deep reactive ion etching after processing with SPD. Micro channels were successfully created on top surfaces of Al alloys and hot embossing of UFG Al–Mg–Cu–Mn processed by SPD, as shown in Figure 2-26 [110, 111]. The UFG Al alloys had much smoother surface and better channel shape after embossing compared to CG Al, which ensures UFG Al a good potential for fabrication of MEMS components.
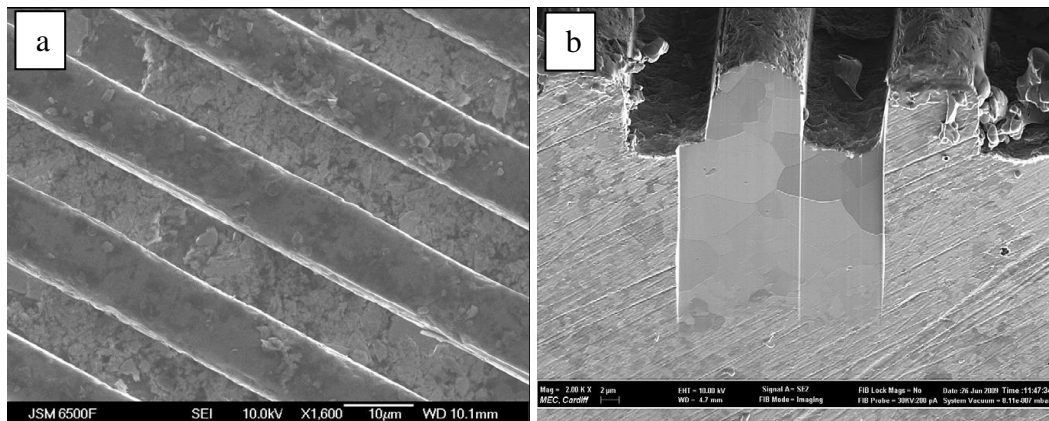
Figure 2-26 300 ℃ embossed UFG Al-1050 produced by eight passes of ECAP, (*a*) Secondary electron SEM image of the top surface; (*b*) secondary electron FIB image of the cross-section [110].

SPD materials also have potential application in other areas such as strong light weight gears for motor industry and aviation engines [112]. Figure 2-27 shows a micro gear shaft extruded from the ECAP processed Mg alloy [9]. Grain refining of

Cu and Al via SPD significantly improves their mechanical properties with very little or no reduction of their electrical conductivity, the long Cu and Al rods fabricated by ECAP-confirm supply important materials for electrical industry use. Reports showed that SPD processing can be used to improve the hydrogen storage capacity of Mg, and nano-sized Mg powders produced via ball milling were consolidated by ECAP and HPT. These Mg cylinders and discs can be widely used as hydrogen carriers in batteries [113].
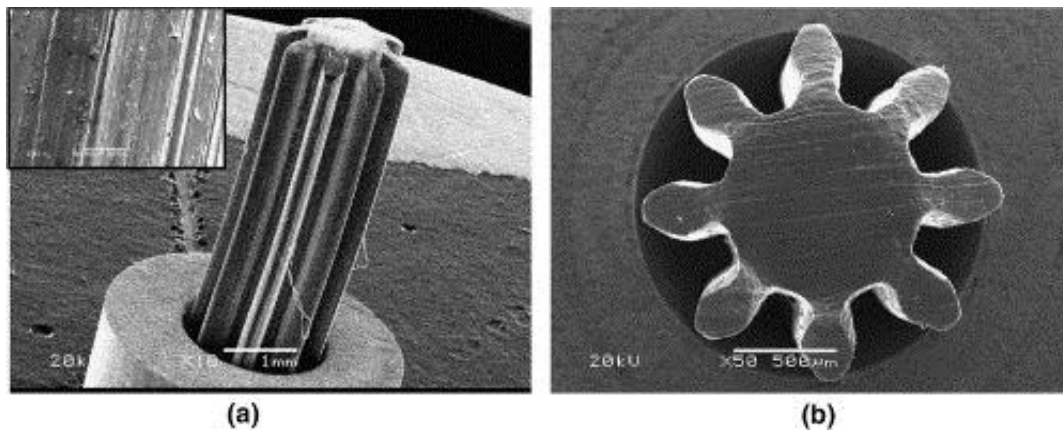
Figure 2-27 A micro-gear shaft extruded from the ECAP processed Mg alloy [9].

The development of bulk UFG metals has now extended beyond laboratory research and has entered the industrial area for potential commercialization. Therefore, related research on functional properties of UFG materials provides very important information for their wide applications in transition towards the commercial manufacturing for a range of promising products.

2.2 Tribology

2.2.1 Introduction of Tribology

Tribology is defined as 'the science and technology of interacting surfaces in relative motion and of related subjects and practices' [114]. And the word 'Tribology' was coined in 1966. The government committee of UK reported that annual savings of more than £500,000,000 could be made by UK industry if known tribological principles were widely applied (at 1966 levels) [115].

Tribology is an interdisciplinary subject which draws on the expertise of the chemist, the mechanical engineer, the materials scientist and the physicist. This topic embraces the study of friction, wear and lubrication.

When examined at a sufficiently high magnification, all surfaces are found to be rough. So when two such surfaces are loaded together, the highest tips of the surface roughness must first carry the applied load by touching each other. Up to now, there is no single numerical parameter which can be used to adequately describe surface topography. The two most widely used parameters are the R_a value and R_q value. R_a value is defined as the arithmetic mean deviation of the surface height from the mean through the profile [115].

$$R_a = \frac{1}{L} \int_0^L |y(x)| dx \qquad \text{(Eq.2-7)}$$

Where y is the height of the surface above the mean line at a distance x from the origin, and L is the overall length of the profile under examination.

In many cases, R_a fails to distinguish between a relatively gently undulating surface and a spikier profile surface. The root mean square roughness parameter R_q overcomes this difficulty as the squared term gives greater significance to surface variations some way from the mean [115]. R_q is defined by

$$R_q = \sqrt{\frac{1}{L} \int_0^L Z^2 dx} \qquad \text{(Eq.2-8)}$$

For many cases, the R_a value and R_q value are similar, $R_q = 1.25\ R_a$. R_a and R_q cannot describe the information on the shapes or spacing of the surface irregularities, and cannot covey indication of the probability of finding surface heights within certain limits. For a fuller description of topography of the surface, other values including amplitude density function and bearing ratio curve are also employed sometimes.

As two engineering surfaces are brought gently together, deformation will initially occur at a few points. As the load increases, more asperities of the surfaces come into contacts, these asperities support the normal load and generate the frictional forces. In 1881, Heinrich Hertz was the first to describe an elasticity theory to determine the finite area when two elastic surfaces touch each other [116]. Hertz assumed that:

1. The size of the contact area is small compared with the other dimensions of the bodies. The deformation between two surfaces is elastic.

2. Both contacting surfaces are smooth and frictionless.

3. The resulting deflections are much less than the dimensions of the contact area.
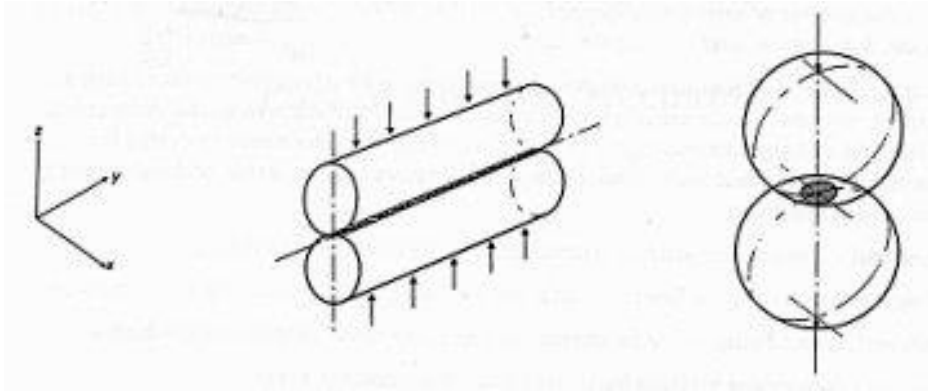
Figure 2-28 Schematic of line contact (left) and point contact (right) [117].

Table 2-1 Dimensions of the area of contact in line and circular point contacts [117].

	Parallel Cylinders – Line contact	Spheres – Circular point contact
Dimensions of the contact	$b = \sqrt{\dfrac{4L'R}{\pi E^*}}$	$a = \sqrt[3]{\dfrac{3LR}{4E^*}}$
Relative radius of curvature R^*	$\dfrac{1}{R^*} = \dfrac{1}{R_1} + \dfrac{1}{R_2}$	
Reduced Modulus E^*	$\dfrac{1}{E^*} = \dfrac{1-v_1^2}{E_1} + \dfrac{1-v_2^2}{E_2}$	
Contact pressure distribution, p	$p(x) = p_0\sqrt{1 - \dfrac{x^2}{b^2}}$	$p(r) = p_0\sqrt{1 - \dfrac{r^2}{a^2}}$
Mean contact pressure, p_m Maximum contact pressure, p_0	$p_m = \dfrac{\pi p_0}{4} = \dfrac{L'}{2b}$	$p_m = \dfrac{2p_0}{3} = \dfrac{L}{\pi a^2}$

When two cylinders are loaded together with a load L' per unit length, a line contact of width $2b$ is produced. When two spheres are loaded together with a load L, a point contact with radius of a is produced, shown in Figure 2-28 [117]. When a cylinder or a sphere is contacting with a concave surface, that produces line contact or point contact by assuming the radius of a concave surface $R_2 = \infty$, respectively. Information of the two contact types is listed in Table 2-1 [117].

The stress under a surface is very inhomogeneous, the stress ratio σ/P_0 depends on Poisson's ratio of the material. The maximum shear stress occurs on the z-axis at a sub-surface location, for steel which has a Poisson's ratio of 0.3:

For a line contact $\qquad \tau_{max} \approx 0.30P_0 \quad$ at z=0.79b $\qquad$ (Eq.2-9)

For a circular point contact $\quad \tau_{max} \approx 0.31\,P_0 \quad$ at z=0.4a $\qquad$ (Eq.2-10)

Z is the depth of place where first yield would occur. The Tresca yield criterion shows that yield occurs when:

$$\tau_{max} = \frac{\sigma_y}{2} \qquad\qquad\qquad \text{(Eq.2-11)}$$

Where σ_y is the yield stress in tension. Yield will occur at a sub-surface. The region of plasticity is initially contained by an elastic region. If the load increased further then the plastic region grows. The state of 'full plasticity' is defined when the plastic region reaches the surface.

2.2.2 Friction and wear

Friction is defined as the resistance encountered when two bodies moving against each other [118]. The friction force is expressed by the equation:

$$F = \mu_{COF}L \qquad\qquad\qquad \text{(Eq.2-12)}$$

Where F is the tangential force needed to move the two bodies, L is the normal component of the load, the constant of proportionality μ_{COF} is called the coefficient of friction.

Bowden and Tabor [119] proposed a model by assuming that frictional forces arise from adhesive forces and deformation forces. The adhesive force is linked to the attractive forces which are assumed to operate at the asperity contacts. The deformation forces are made up by the force raised through local displacement of the

opposing asperities by squashing them and the ploughing force which is raised from macroscopic interaction between the asperities resulting the harder material ploughing grooves in the softer material.

Wear is the progressive damage which occurs when two surfaces in contact slide over each other. Wear is the almost inevitable companion of friction [116]. However, the interrelationship between friction and wear is not fully understood. The assumption that low friction accompanies low wear and high friction accompanies high wear is not universally valid. For example, low friction can result from the high wear rate of solid lubricants such as silver or graphite.

Up to now, more than 200 wear equations have been proposed to predict wear [120]. However, none of the equations successes in predicting the wear performance even if all their physical and chemical properties have been considered [121]. A simple theory for describing the severity of wear is produced by Archard, the Archard equation is given by [122]:

$$V = K \frac{SL}{H} \qquad \qquad \text{(Eq.2-13)}$$

Where V is the volume worn away during testing (m^3), S is the total sliding distance (m), L is the normal load (N), H is the hardness of the softer surface (N/m^2) and K is the dimensionless wear coefficient specific to the sample under test. Details of this equation are given in section 2.2.3.1 and 2.2.3.2.

2.2.3 Wear mechanisms

During sliding, materials may show different wear behaviour under different sliding conditions. In fact, there are several wear mechanisms which change as the sliding conditions are varied, such as adhesive wear, abrasive wear, corrosive wear, fretting wear, erosive wear, and delamination wear. Each wear mechanism produces debris with particular shape and chemical composite, and consequently leaves worn surface with particular morphology [123]. Hence, studying the worn surface and debris with experimental methods can provide important information to know which wear mechanism operated. In practise, more than one wear mechanism may be operating in one typical engineering contact [124]. In most cases, wear is initially dominated

by one wear mechanism and then by another wear mechanism which makes the post analysis even more complicated [125].

2.2.3.1 Adhesive wear

Adhesive wear occurs when two flat surfaces are in sliding contact which involves the detachment of flake debris and attachment to the counter surface. High spots of the both surfaces, no matter how perfectly the surfaces are prepared, initially contact at the interface which leads to an extremely high contact pressure. These high spots tend to adhere to each other and normally the upper surface of the softer material is dragged away during sliding, this phenomenon is mostly called 'material transfer'. The transferred debris may directly drop off and cause mass loss or transfer back to the soft surface, shown in Figure 2-29 [126].
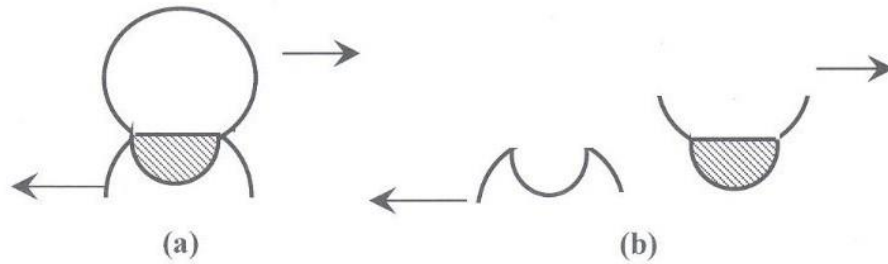
Figure 2-29 Principle of adhesive wear [126].

Based on experimental data, a general law of adhesive wear was proposed as:

$$V \propto \frac{SL}{H}$$ (Eq.2-14)

Where V is the volume worn away during testing (m^3), S is the total sliding distance (m), L is the normal load (N).

The model above was improved by Archard by considering the asperities on both contact surfaces [122]. Assume that the contact between two surfaces is made up of circle asperities with diameter of 2a, as shown in Figure 2-30. When the two asperities are fully contacted as shown in Figure 2-30 (a), the load at this point dL is distributed on an area of πa^2. If the load causes yield of the asperity,

$$dL = \pi a^2 H$$ (Eq.2-15)

Where H is the hardness of the softer material. Therefore, the total load of the whole area L is:

$$L = \sum dL = \sum \pi a^2 H \qquad \text{(Eq.2-16)}$$

Furthermore, yield of the soft material lead to production of wear debris, and as most examinations observed that the wear debris has almost hemisphere shape. Thus, it is assumed that the wear volume taken from an asperity dV is:

$$dV = \frac{2}{3}\pi a^3 \qquad \text{(Eq.2-17)}$$
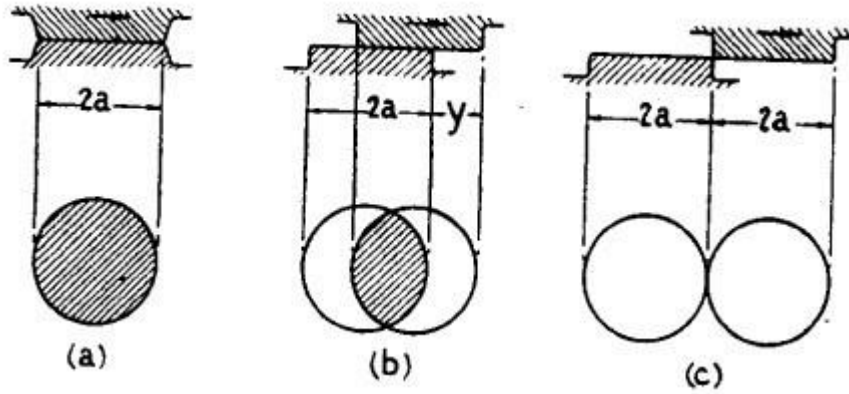
Figure 2-30 Schematic diagram showing evolution of a single contact area as two asperities move over each other, proposed by Archard [122].

As shown in Figure 2-30 (a) to (c), the contact surfaces slide for a distance of 2a, so the average volume loss of material per unit sliding distance dQ is:

$$dQ = \frac{dV}{2a} = \frac{1}{3}\pi a^2 \qquad \text{(Eq.2-18)}$$

Considered that only small proportion, δ, of contacted asperities produce wear debris, thus the volume loss of the whole area per sliding distance Q is:

$$Q = \delta \sum \frac{1}{3}\pi a^2 \qquad \text{(Eq.2-19)}$$

Therefore, it is concluded

$$Q = \frac{\delta L}{3H} \qquad \text{(Eq.2-20)}$$

As defined in (Eq.2-20), the volume loss of worn material per unit sliding distance is proportional to the load and the inverse of hardness of the soft material [122]. The dimensionless wear coefficient, K, which was assumed to be $\delta/3$, provides a valuable means of comparing the severity of wear processes. While, the dimensional wear coefficient which is known as specific wear rate (m^2/N), k_{SWR}, is widely used to compare wear resistance in different classes of materials. As defined by:

$$k_{SWR} = \frac{V}{SL}$$ (Eq.2-21)

2.2.3.2 Abrasive wear
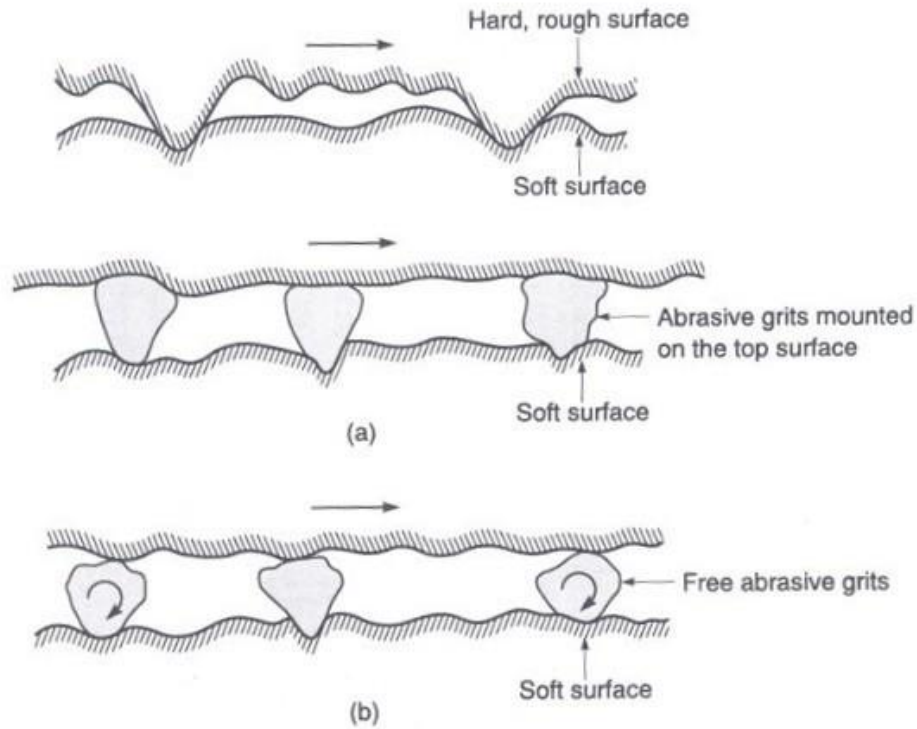
Figure 2-31 Schematics of (a) a rough, hard surface or a surface mounted with abrasive grits sliding on a softer surface, and (b) free abrasive grits caught between the surface with at least one of the surfaces softer than the abrasive grits [118].

Generally, abrasive wear is supposed to occur on a soft material surface when asperities of a hard material or hard particles sliding on it [127]. Abrasive wear also happens in the case of sliding between two similar materials as hard particle may be formed [128]. There are two situations of abrasion wear, two-body abrasion as shown in Figure 2-31(a) and three-body abrasion illustrated in Figure 2-31(b) [118]. Normally, wear rates of three-body abrasion are generally lower than those generated by two-body abrasion. Mostly, abrasive wear leaves a series of grooves parallel to the sliding direction of sliding on the worn surface.

In order to understand the process of surface deformation and wear debris generation, two abrasive wear modes were proposed by Challen and Oxley [129, 130]. In their slip line field model, wave removal mode as shown in Figure 2-32(left) and chip

formation mode as shown in Figure 2-32(right). Wear rate of the wave removal mode is:

$$\frac{V}{SL} = \frac{1}{2k_{SS}} \cdot \frac{\sin^2 a_{att} + \frac{1}{2}\sin 2a_{att}}{1 + \sin 2a_{att}} \tag{Eq.2-22}$$

Where V is the wear volume, S is the sliding distance, L is the load, k_{SS} is the shear flow stress and a_{att} is the attack angle. Wear rate of the chip formation mode is:

$$\frac{V}{SL} = \frac{1}{k_{SS}\left\{\left[1 + 2\left(\frac{1}{4}\pi - \phi\right)\right]\cot\phi - 1\right\}} \tag{Eq.2-23}$$

Where ϕ is the shear angle.
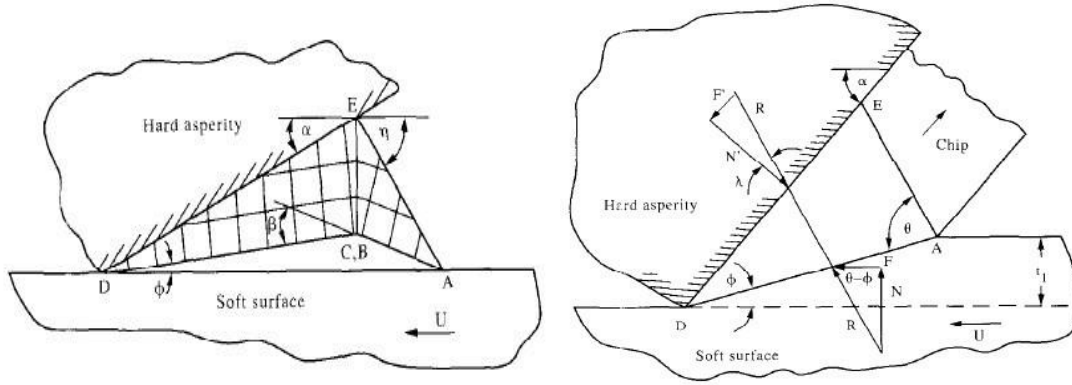
Figure 2-32 Slip-line field model of wave removal mode (left) and chip formation mode (right) [129, 130].

Different wear modes of abrasive were also observed via in-situ SEM wear studies [131]. Abrasive wear was devised into three modes depending on severity of contact, shown in Figure 2-33 [131]. In the ploughing mode, ridges form along the sides of grooves and not many wear particles are formed. In the wedge forming mode, the hard tip pushes the soft material and forms a wedge and the wedge will detach off when the soft material reach its plastic limit. Cutting mode is more like chip formation mode in which large chips of the soft material are removed when the attack angle is large.
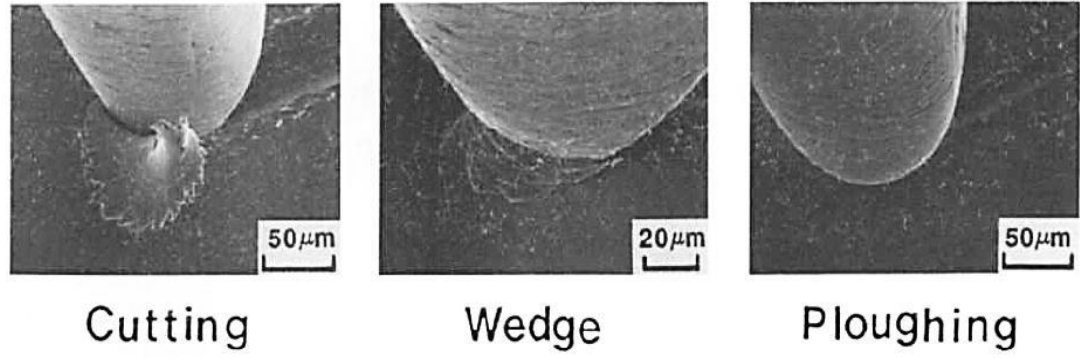
Figure 2-33 Three mode of abrasive [131].

The index called degree of penetration D_p is introduced to describe the severity of contact [131-134]. D_p is defined by equation:

$$D_p = \frac{h_{dep}}{r_{cont}} = R \left(\frac{\pi H}{2L} \right)^{\frac{1}{2}} - \left(\frac{\pi R^2 H}{2L} - 1 \right)^{\frac{1}{2}} \qquad \text{(Eq.2-24)}$$

Here r_{cont} is the contact radius, h_{dep} is the depth of penetration, R_{ind} is the radius of the spherical asperity, H is the hardness of soft material, L is the load. It is believed that the wear mode transfers from ploughing to wedge forming and cutting while the degree of penetration D_p is increasing. In addition, the degree of penetration D_p is related to attack angle a via equation:

$$D_p = 0.8 \tan \left(\frac{a_{att}}{2} \right) \qquad \text{(Eq.2-25)}$$

Normally, a larger attack angle yields to larger degree of penetration, and also corresponds to higher severity of contact.

2.2.3.3 Corrosive wear

Corrosive wear involves the removal of chemical layer on top of material during sliding process. The most common corrosive wear is oxidation-dominated wear which happen when materials are sliding in the air environment [135-137]. Corrosive wear involves two stages: formation of chemical layer and rubbing. Sometimes, the real situation may be more complicated as the worn surface has no time to be re-corrosive before rubbing off. After corrosion, the real contact normally changes from metal-metal contact to film-film contact, which changes the whole wear process [136].

Experiments conducted on several different passive metals (Ti, stainless steel) to wear in aqueous solutions at controlled anodic or catholic potentials demonstrate that, the electrochemical metal removal rate is strongly influenced by mechanical parameters and, prevailing electrochemical conditions. In order to understand the interactions between mechanical and electrochemical parameters under tribocorrosion conditions, it is necessary to look at the tribocorrosion system as a whole, including the behaviour of the rubbing pin and the possible role of wear debris [138].

Electrochemical methods are suggested for the study of tribocorrosion phenomena because they allow one to simulate the corrosive effect of the environment by imposing a fixed potential. Furthermore, the measurement of the anodic current permits one to determine the amount of material removed by oxidation as opposed to mechanical wear [139]. A recent study has investigated the relationship between applied interfacial electrical potentials and friction for steel/steel contacts in alkaline aqueous-based solutions. The results showed corresponding change of coefficient of friction (COF) when the environment varied between -1.0 and +1.0 V potential [140].

2.2.3.4 Fretting wear

Fretting wear occurs where there is cyclic motion with very small amplitude between two surfaces. Wear debris is produced by combination of adhesion between asperities and the crack nucleation [141]. Fretting wear happens when machines are subjected to vibration [142]. A three-stage mechanism of fretting wear was presented, and adhesive process was believed to be dominating for the initial accumulation of wear debris between the contact surfaces [143]. Additional fretting cycles introduces more wear debris and plastic deformation, and the sub-surface plastic deformation results in nucleation of micro cracks. Then wear debris is formed when these cracks growth and propagation.

2.2.3.5 Erosive wear

Erosion involves generation of wear debris and the debris strikes the surface of material with a high speed which results in more damage and material loss. Erosive

wear is classified into three types: cavitation erosion, solid particle erosion and liquid impingement erosion.

Cavitation erosion occurs when a solid is in relative motion with liquid, bubbles formed in the fluid implode against the surface of the solid. The bubbles firstly nuclear near the impurities of the liquid, and they will collapse when the liquid is subjected to a sufficient high compressive pressure [144].
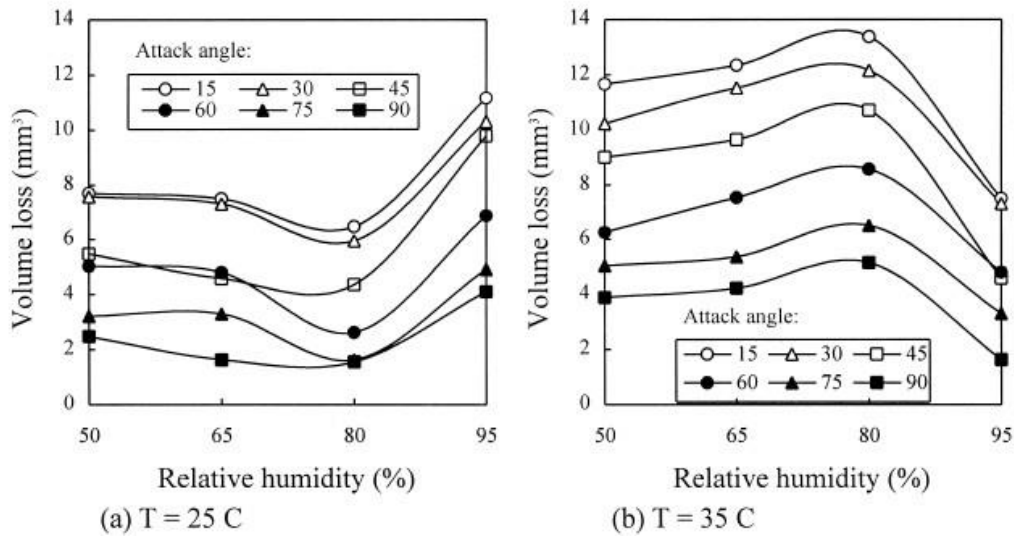
Figure 2-34 Effect of humidity on erosion damage depending on test temperature [148].

Solid particle erosion occurs when material surface is impacted by particles. Wear debris formed as a result of repeated impact [145]. For ductile materials, the impact of particles causes plastic deformation to the surface. For brittle materials, the impact introduces cracks to the material and leads to loss of eroded debris. The velocity, size and even impact angle of hard particles are important parameters determining the wear rate [146]. Moreover, the shape the impact particle also turned out to be essential for the wear rate by showing that sharper impact particles lead to higher wear rate than rounded particles [147]. The effect of relative humidity on the erosion of 6063 aluminium alloy subjected to sandblasting of silicon carbide was studied. The results showed that the effect of humidity on the erosion damage depends on the testing temperature, as shown in Figure 2-34 [148].

When a solid surface is stroke by small liquid drops at high speed (more than 300m/s), this may result in damage to the solid surface [149]. Liquid jet impingement

technique is preferred for coatings, elastomers and brittle materials because various jet sizes can be used to evaluate materials [150].

2.2.3.6 Delamination wear

When a hard rough surface is sliding repeatedly on a softer component under a high load, protective residual stresses may be developed in the subsurface of the softer material, and form a thin work hardened layer. This work hardened region increases the shear strength of the material and reduces the yield region. After thousands to millions of loading cycles, more and more deformation is introduced to the surface region. For brittle materials, micro cracks are formed in the subsurface of material and grow parallel or at an angle to the surface; For ductile materials, it is more likely that ductile failure results from an accumulation of plastic strain close to the contact surface [121]. The wear debris in form of thin sheet is formed, leading to the introduction of delamination wear [151].

2.2.3.7 Wear maps

As mechanical stresses, temperature and oxidation phenomena are the main factors controlling the underlying mechanisms. All these three factors may be influenced by load and sliding velocity. Lim and Ashby started to produce a very useful load-speed based wear map for dry sliding steel in 1987 [152]. They successfully made a dry sliding wear map for steel by using the following relationships for the normalized pressure at the sliding interface, $\tilde{F}$, and the normalized velocity, $\tilde{V}$, where the latter corresponds to the sliding velocity in wear divided by the velocity of heat flow [124], shown in Figure 2-35:

$$\tilde{F} = \frac{L}{A_n H_0} \qquad\qquad (Eq.2\text{-}26)$$

and

$$\tilde{V} = \frac{v \times r_{cont}}{a_{therm}} \qquad\qquad (Eq.2\text{-}27)$$

Where L is the normal force (N), A_n is the nominal contact area (m^2); H_o is the room temperature hardness (N m^{-2}), v is the sliding speed (m s^{-1}), r_{cont} is the radius of the nominal contact area and a_{therm} is the thermal diffusivity.

In the left part of the wear map, wear is dominated by essentially mechanical processes. The wear rate depends on the normalized pressure other than normalized velocity, so the wear rate contour line appears to be horizontal in this area; In the right part of the wear map, wear process is more affected by thermal and chemical effects (melting wear and oxidation wear). The wear rate depends on both normalized pressure and velocity; In the upper part of the wear map where the seizure works, the normalized pressure is so high that it brings very severe damage to the working piece, such a work condition should be prohibited for all wear systems.
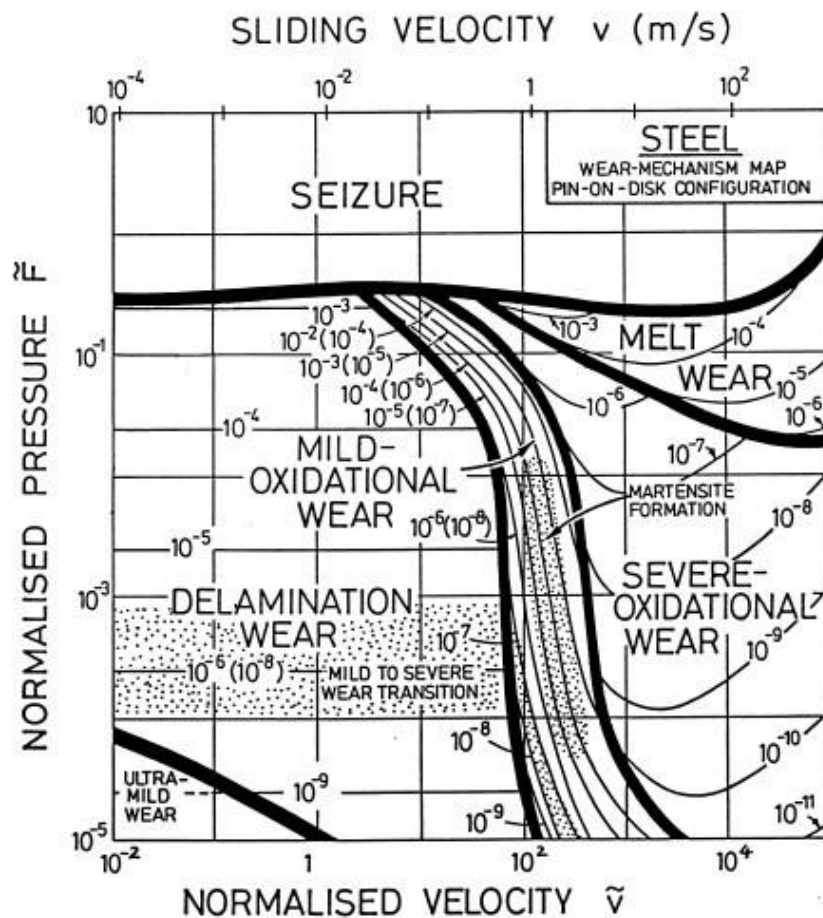
Figure 2-35 Wear map for the dry sliding of steel on steel [124].

Although the map above is specific for steels, the general form is similar for the dry sliding of most metals in air. This wear map has been further improved several times afterwards [153, 154]. A more comprehensive form of wear map provides an important design guide to dry sliding by considering the 'pv' value, as shown in Figure 2-36 [121]. The 'pv' factor refers to energy input per unit area per second, where p is the contact pressure and v is the sliding velocity. Generally, the contact pressure and sliding speed are particularly required by the application, so the

machine designers have little control on them. However, they can recommend a secondary operation condition to try and ensure the wear mechanism of initial stage of wear in a mild stage [121].
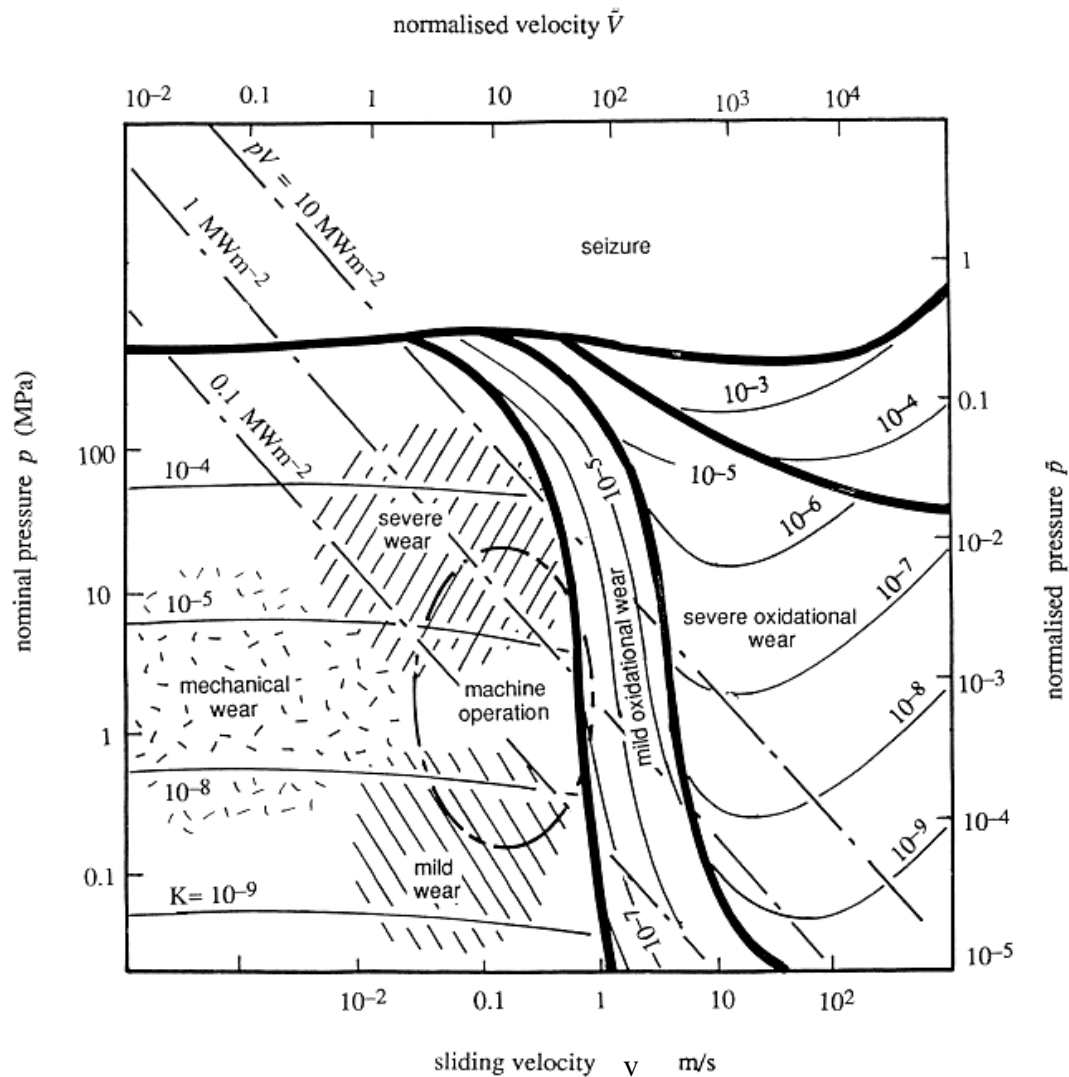
Figure 2-36 Load-speed wear map for the dry sliding of steel on steel, with chain line representing constant value of *pv* factor [121].

Based on the physical modelling approach suggested by Lim and Ashby [152], wear maps for aluminium alloys [155], magnesium alloy [156], and even metal matrix composites are presented. These maps can provide basic guidance about wear behaviour of materials under different conditions, and can also be conducted to encompass new-generation tailor-made engineering materials which have potential superior wear resistance.

An alternative map was suggested which emphasis to the mechanical aspects of the surface damage, as shown in Figure 2-37 [157]. This map was plotted τ_{int}/τ_{weak} (shear strength of the interface τ_{int} divided by shear strength of the weaker material, τ_{weak}) versus attack angle a_{att}, which is defined by Eq. (2-25). In this map, abrasive wear was further divided into several modes: Rigid-plastic wave, in which the surface morphology of material was changed a lot, but not much debris was formed; Micro cutting, in which a much higher proportion of deformed material was detached from the surface and formed debris; Abrasive machining, which combines the effect of polishing, grinding and lapping. Other wear mechanisms which normally produced thin plate-like debris (such as pitting fatigue and ratchetting) were also considered. As shown in Figure 2-37, high wear rate is related to a large attach angle.
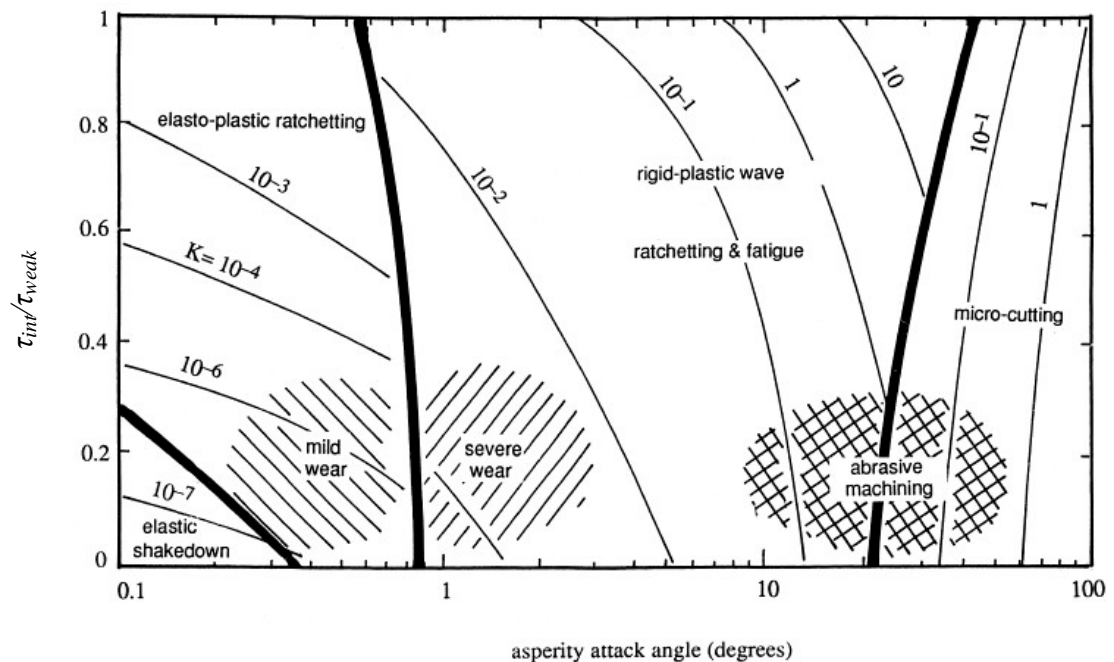
Figure 2-37 Wear map for a soft surface abraded by a hard asperity [157].

As wear causes a series of problems including loss of precision of instruments, expenses involved in machine downtime, costs of replacement parts and pollution, so researches on wear issue are purposed to reduce wear damage or produce materials with good wear resistance.

2.2.4 Surface treatments for wear control

Surface engineering is widely applied to improve wear resistance and modify friction behaviour of materials in an effective manner. Various technics have been developed

to produce wear resistant coatings and films, including semi molten methods and vapour processing routes. Semi-molten processing methods such as plasma spraying and thermal spraying tend to produce porous thick coatings. Coatings produced by these methods are often as thick as several hundred micro meters. However, these coatings have rough surface which limits the scope of applications [158, 159]. For plasma spraying, the plasma discharges can result in high temperature conversion in a localized area [160].

Vapour processing techniques such as chemical vapour deposition (CVD) and physical vapour deposition (PVD) are capable of producing highly pure coatings with structural control at the atomic level or nanometer level and at low processing temperatures. The processing temperature is of great importance for UFG alloys. As if the ultrafine grains introduced via SPD straining are lost through grain growth during the coating processing, the superior mechanical properties achieved by SPD are lost as well. The deposition temperature of thermal activated CVD is around 900 to 1100 ºC, which is too high for almost all the UFG alloys [161]. Plasma enhanced CVD methods have much lower deposition temperature of 450–550 ºC. It is reported that this deposition temperatures may be reduced to about 140 ºC via using metal-organic compounds as precursor in the plasma enhanced CVD process [162]. PVD may be a better approach for UFG alloys because this permits the use of a lower processing temperature and easier control over the surface roughness. It is important to note that PVD methods such as magnetron sputtering can be controlled even at room temperature which leads to a much lower internal stress at the interface.

As addressed in section 2.1.7.1, pure titanium has excellent properties including high corrosion resistance, low electronic conductivity, a low ion-formation tendency and very good biocompatibility. All of these characteristics make it a very good candidate as an implant material. Nevertheless, pure titanium has a very poor wear resistance when it is subjected to sliding and abrasion. Thus, it is generally not suitable for use in artificial joints which seek materials with high strength and good tribological properties. As an alternative approach, it appears that surface treatments or coatings may be necessary to enhance the service durability of titanium as implant components.

The idea of improving wear resistance of Ti alloys via surface treatment has been reported extensively. In recent years, some attentions have been moved to surface engineering of ultrafine-grained Ti. High-current-density nitrogen ion implantation was used to enhance the wear resistance of ultrafine-grained Ti and the results demonstrated the potential for forming a hard layer with good wear and corrosion resistance on the surface of ultrafine-grained Ti via ion implantation [163]. However, this method required that the samples were held at the relatively high temperature of 820 K, which may lead to recrystallization of the ultrafine grains. As shown by the microhardness measurement, the hardness of Ti was improved from 163 Hv to 250 Hv after ECAP processing, and this hardness dropped to 170 Hv after a further ion-implantation processing.
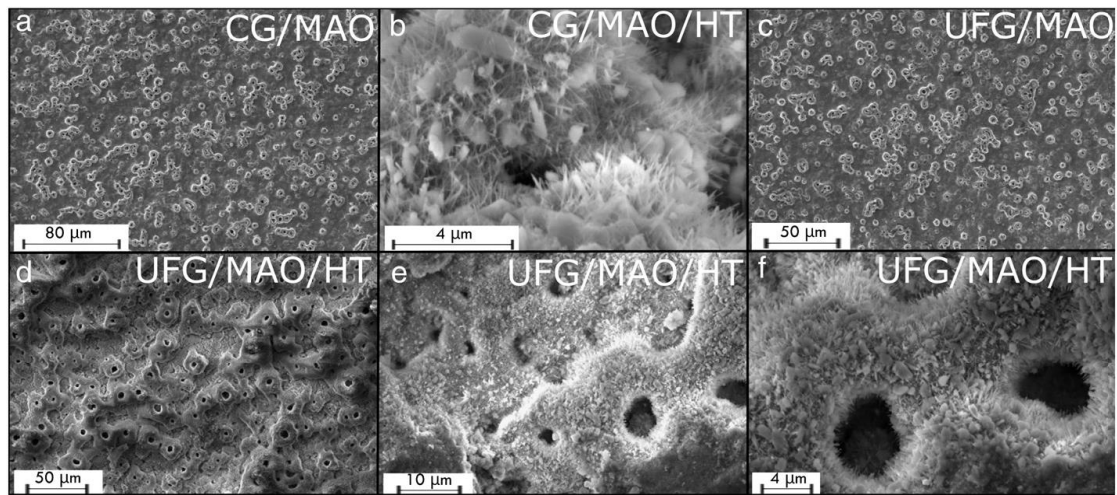
Figure 2-38 Surface topographies of treated CG and UFG Ti: (a) CG/MAO, (b) CG/MAO/HT, (c) UFG/MAO and (d)–(f) UFG/MAO/HT [164].

Another study showed that the wear resistance of UFG pure Ti may be improved significantly by using a micro-arc oxidation (MAO) and hydrothermal treatment (HT) to form a porous oxide layer with a thickness of ~10 μm on the surface of UFG Ti [164]. CP Ti was recently processed by ECAP, and then subjected to micro arc oxidation and hydrothermal treatment with hydroxyapatite-containing titania coating. As shown in Figure 2-38, a surface layer of porous and rough circular shapes was obtained after MAO processing (Figure 2-38 (a)–(c)). Porous coating was homogeneously dispersed on the surface of both CG and UFG Ti samples. After HT processing, dendritic hydroxyapatite crystals were observed around or inside the pores and throughout the surface (Figure 2-38 (b) and (f)). The wear behaviour of

UFG Ti was systematically investigated before and after surface modification. The results showed that the application of MAO resulted in a considerable increase in its wear resistance and osseointegration due to the formation of hard and adhered hydroxyapatite-containing TiO_2 coating on the surface. Therefore, it has been concluded that the use of ECAP plus MAO/HT coating can provide a simple and effective procedure to obtain pure Ti with high strength and high wear resistance. Moreover, with higher hardness and reduced ductility, the SPD processed Ti was regarded as better substrate to support the hard brittle coatings. This suggests the possibility of combining SPD processing and coating technology to fabricate a coated UFG Ti having high strength and excellent corrosion and wear resistance for use in bio-medical applications.

Some research have demonstrated that a TiN coating, introduced via PVD, is effective as a cutting tool coating and biomedical coating due to the dense structure, good interface bonding, high hardness and biocompatibility [165, 166]. In addition, TiN coatings have excellent bonding with the Ti substrate and good ductility when subjected to impact and scratching and they are widely recognized as good candidate materials for introducing protective layers on bio-implants [167-170].

Diamond-like carbon (DLC) coatings are regarded as other good candidates for the purpose of wear protection because of their excellent mechanical and tribological properties such as high hardness, good wear and corrosion resistance. Moreover, DLC coatings also have a much lower COF which can also reduce the wear of the counter surface during sliding [171]. To date, several studies have explored DLC coatings for bio-implant use [172-174].

2.3 Tribological performances of SPD-processed materials

SPD process leads to significant influence to the microstructure (grain size, second phase, texture, deformation twinning) and mechanical properties of the materials (strength, ductility, fracture toughness, fatigue performance). Wear is a system property, it can be affected by lots of factors, including load level, sliding velocity, lubricants, the counter materials, different wear rigs, and most importantly, mechanical properties of the material tested. Moreover, under different wear

conditions, it is possible that different wear mechanism works. When abrasive wear is the main wear mechanism, hardness of the material is crucial to the wear rate; when the wear is dominated by delamination wear, formation and growth of the cracks under surface are important; while the chemical activity of surface may be vital when oxidation wear works.

As a result, the study of wear behaviour of SPD-processed materials needs a comprehensive understanding about every aspect SPD caused to the material, also needs a systemic observation during the wear test.

2.3.1 Improved wear resistance by SPD
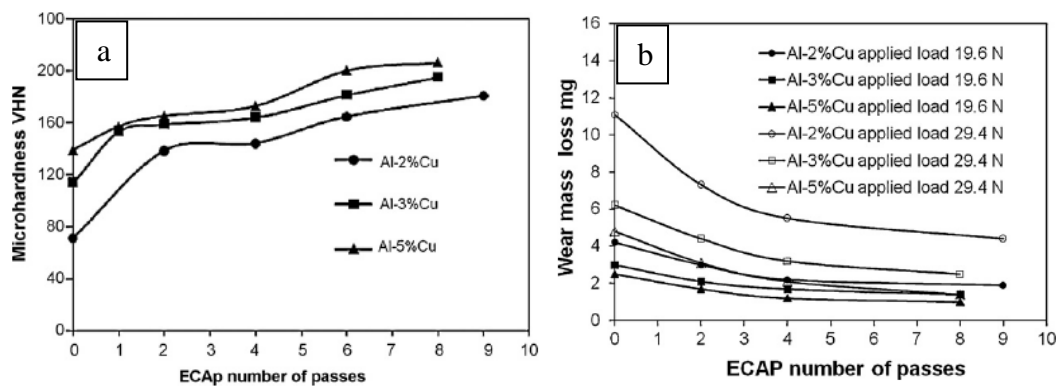
Figure 2-39 The effect of ECAP and copper content on (a) microhardness and (b) wear mass loss of Al–Cu alloys [175].

A number of studies have showed the benefit effect on wear resistance by ECAP [175-180]. The wear properties of ECAP-processed Al–2, 3 and 5% Cu alloys under dry sliding conditions using different sliding distances and loads were investigated [175]. The work showed that the increase in the microhardness with the increase of the number of ECAP passes and the Cu content (Figure 2-39 (a)), due to the decreased grain size and the increased strength. The wear mass loss decreased remarkably as the number of ECAP passes and Cu content increased (Figure 2-39 (b)).

Figure 2-40 shows that increasing ECAP up to 15 passes to Al-5%Ti grain refiners considerably decreases the wear values of Al and Al-12.6Si-5Ti [176]. This corresponded to the changing trends of the mean size of α-Al grains and the Al–Si

49

eutectic structures, in which the samples with small grain sizes and high hardness obtained a small wear volume. The effect of grain size (1, 30 and 60 μm) on the friction and wear behaviour of a copper samples before and after ECAP under different lubrication regimes was studied [177]. It demonstrated that the transition from the elasto-hydrodynamic lubrication (EHL), in which the two surfaces were separated by lubricate film only interacted at some asperities, to boundary lubrication (BL) regions, in which the load between two surfaces were carried by surface asperities rather than lubrication film depended on the grain size. Larger grain sizes gave a lower load of transition to the BL region as the soft surface asperities were much easier to be deformed and flattened. The wear rate increased remarkably with growth of the grain size in the BL region.
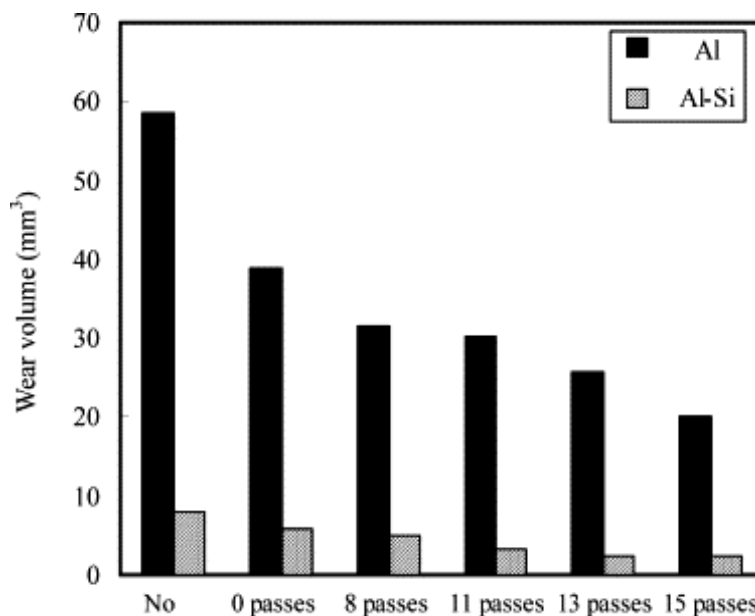
Figure 2-40 Wear volume of the pure Al and Al–12.6% Si alloys before and after ECAP [176].

The coefficient of friction and wear rate of the ECAP-processed aluminium bronze alloy (Cu–10Al–4Fe) have been investigated [178-180]. The coefficient of friction of the alloy decreased considerably with increasing ECAP passes (Figure 2-41 (a)). A reduction of the coefficient of friction due to the increase of the hardness indicates the increase of the load bearing capability. Although the wear rate of all specimens increased with increasing load, the specimen with six ECAP passes showed the lowest-wear rate (Figure 2-41 (b)). In particular, the seizure load for specimens increased from 160 N before ECAP to 253 N after six ECAP passes. These results

indicate that the wear resistance of the aluminium bronze alloy was improved by ECAP. Fretting wear studies of Cu-4.5%Cr alloys showed that the wear volume decreased with number of ECAP passes, indicating that the wear resistance of the alloy was improved by ECAP processing due to strengthening of grain refinement [181].
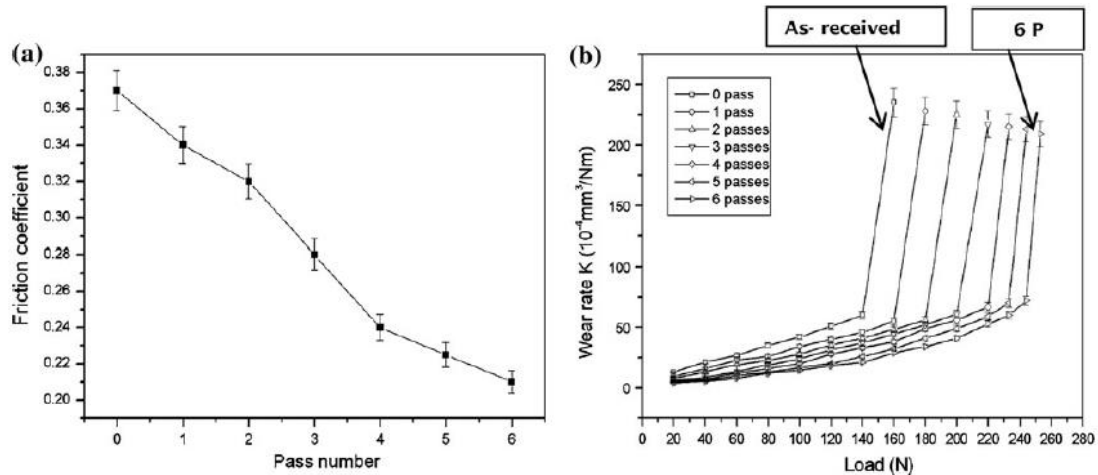
Figure 2-41 Effect of ECAP on (a) friction coefficient, and (b) wear rate of Cu-10Al-4Fe alloy [178].

Several studies on titanium alloys and most of them showed improved wear resistance by ECAP. The tribological properties of CP Ti prepared by ECAP have been investigated under dry sliding at varying load and sliding speed [182]. Although the coefficient of friction of the UFG Ti and the CG Ti were similar in the range of 0.45–0.60 (Figure 2-42 (a)), the wear rate of the UFG Ti was about 30% lower than that of the CG annealed Ti (Figure 2-42 (b)). It was observed that the wear mechanism of the UFG Ti was micro-ploughing and delamination, which was different from the adhesion and delamination mechanism of CG Ti. Similar result was also report on wear testing of fine rained surface layer of Ti processed by surface mechanical attrition treatment (SMAT) [183]. After SMAT processing, a thick fine grained layer of 160 μm was produced on pure Ti. The microhardness of this fine grained layer was around 320 Hv, which is much higher compared to 190 Hv of the CG substrate. Dry sliding tests showed that the COF of both CG Ti and the UFG surface layer was around 0.6. The wear rate loss of UFG Ti layer was lower than that of CG Ti under all load range from 1 to 5 N.
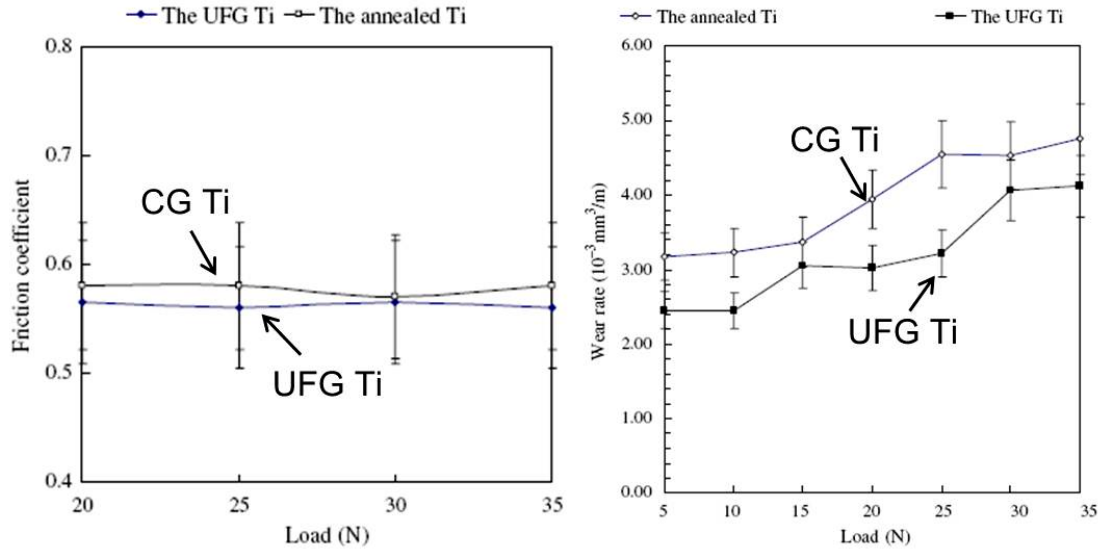
Figure 2-42 Variations of (a) friction coefficient and (b) wear rate of the UFG and the annealed Ti [182].

The coefficient of friction of commercial purity CG Ti, UFG Ti processed by 8 ECAP passes, and UFG Ti processed by 8 ECAP passes plus further cold rolling for 75% rolling strain were systematically investigated at different pressures and temperatures, which possessed with an average grain size of 15, 0.3 and 0.1 μm respectively [184]. It was found that the UFG Ti processed by ECAP plus cold rolling had the lowest coefficient of friction, especially at higher temperatures, which indicates that the finer grained UFG Ti has a lower tendency for seizure at higher temperatures and higher wear resistance than CG Ti.

In addition of aluminium, copper and titanium alloys, other alloys including magnesium alloys, titanium nitride and steels have also been investigated on their wear behaviour. The tribological behaviour of AZ91D magnesium alloy (Mg-9.0Al-0.68Zn-0.13Mn), hardened with SiC disperse powder filler and deformed by ECAP, was studied [185]. Results showed that two passes of ECAP considerably reduced the coefficient of friction. However, investigation of wear behaviour on UFG AZ61 Mg alloy processed by ECAP under dry sliding tests demonstrated that the refined microstructure after the ECAP almost had no effect on the wear rate [186].

The wear behaviour of TiNi alloy processed by two passes of ECAP was investigated [187]. The average grain size of the as-received TiNi alloy was 80 μm, while the ECAP-processed TiNi alloy had a fine equiaxed grain of 5 μm. Compared to the as-

received TiNi alloy, wear mass loss of the ECAP-processed TiNi alloy decreased 62.7% and 21.4% under loads of 50 N and 250 N, respectively. Detailed observation of the morphologies of worn surface found that the wear mechanism of the ECAP-processed TiNi alloy was micro-ploughing and delamination, which was different from the adhesion and delamination mechanism of the as-received TiNi alloy. Another study for TiNi in as-received and UFG conditions, with an average grain size of 20-30 and 0.2-0.3μm respectively [188]. It showed that the creation of an UFG microstructure in the alloy after ECAP had favourable effect of ECAP on the wear resistance of the TiNi alloy at temperatures from –25 to +70°C.

Dry sliding wear and friction characteristics of Zn–40Al–2Cu–2Si alloy were studied [189]. The results showed that ECAP processing led to decrease of the coefficient of friction and led to an improvement in wear resistance, especially at high contact pressures. The worn surface of the as-cast alloy revealed mainly scratches and deep grooves with large amounts of brittle failure, indicating the main wear mechanism as abrasion. However, the morphology of the worn surface of the ECAP-processed alloy showed adhesion and plastic deformation, which means that ECAP can inhibit certain wear mechanism.

The processing of UFG bulk materials by HPT is an especially attractive procedure because, by comparison with ECAP, it leads both to smaller grain sizes and to a higher fraction of high angle grain boundaries [44, 190]. On the other hand, the ARB process produces not only UFG structures but also it leads to specific deformation textures in various materials [191, 192]. Therefore, attention recently has been moved from studying the wear behaviour of alloyed processed by ECAP to HPT and ARB. Most of the results show both processing techniques more likely reduce wear resistance, and only one paper demonstrates that HPT could improve wear resistance.

The tribological behaviour of HPT-processed nanostructured Ti was investigated and compared with the coarse-grained samples [193]. The nanostructured samples showed much better wear resistance either in dry or wet wear tests. Figure 2-43 shows a cross-section profile of the wear tracks measured by the surface profile-meter for both dry and tribocorrosion wear tests, which demonstrates that the

nanostructured Ti has the lowest wear track volume, compared with untreated and annealed Ti. Signs of severe plastic deformation and inter granular fracture were found on the worn surfaces of these samples. On the other hand, there was less deformation and lower wear debris on the surface of the nanostructured Ti sample, indicating a mild abrasion wear mechanism.
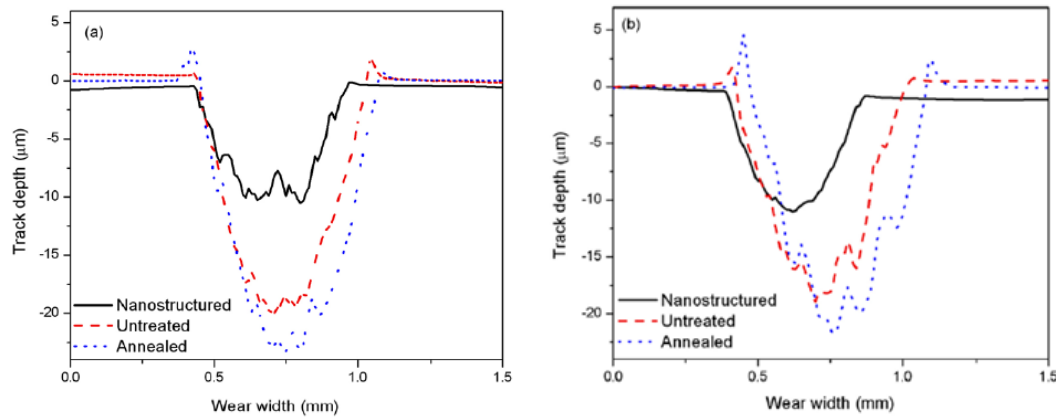
Figure 2-43 Wear track cross-sectional profile of titanium with different grain sizes. (a) Dry and (b) tribocorrosion experiment [193].

2.3.2 Reduced wear resistance by SPD

Some of the experimental results demonstrated negative effect of SPD on wear behaviour of materials. A comparison of study for the wear behaviour of the as-cast and ECAP-processed Al–12Si alloys showed that the weight loss increased with increasing applied pressure. Compared with the as-cast alloy, the wear resistance of the alloy decreased after 6 ECAP passes, especially for long sliding distance and high applied pressures [194]. SEM and X-ray diffraction (XRD) analysis indicated that the surfaces of the as-cast and the ECAP-processed alloy were covered with a thick oxide layer (Figure 2-44), mainly SiO_2 and Al_2O_3. Therefore, it was concluded that the tribochemical reaction in formation of the oxide layer played a dominant role in determining the wear resistance of the alloy in both cases, and it masked the effect of strengthening of the alloy structure on the wear resistance. In addition, the oxidation rate of ECAP-processed alloy was faster than that of as-cast alloy, which led to high weight loss.

The effect of SPD on the corrosion and wear behaviour of Al-Cu composites have been studied [195]. The composites processed by powder metallurgy were severely

plastically deformed using ECAP to produce an UFG microstructure. Al_2O_3 or SiC particles in two different fractions (5 or 15 vol.%) as well as sizes (fine or nano) were used as reinforcements. The wear behaviour was evaluated by oscillating friction and wear as well as scratch tests. The results showed that the reinforced non-ECAP composites were more wear-resistant against an oscillating friction movement, whereas under abrasive load the ECAP processed composites had a batter wear resistance.
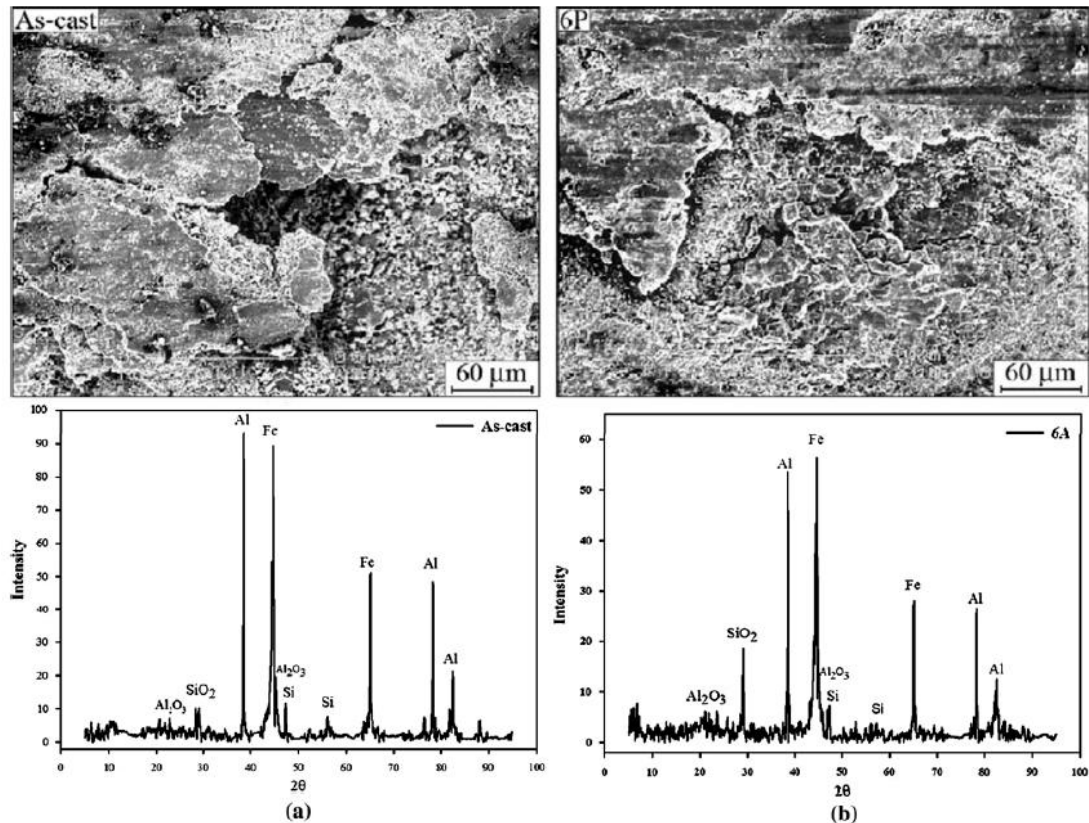
Figure 2-44 SEM micrographs of the worn surface and XRD spectra for as-cast and ECAP-processed Al-12Si alloy [194].

Figure 2-45 shows the wear rates of the UFG dual phase (DP) steel and coarse-grained counterpart (CG-DP) as a function of the applied load [196]. The UFG steel had a higher wear rate than the CG steel. The lower wear-resistance of the UFG steel at high loads was partly associated with a relatively low strain hardening of the UFG steel. During the wear of the UFG steel, numerous shear bands were formed beneath the wearing surface along the sliding direction, and cracks were initiated along the shear bands at interfaces between martensite and ferrite phases.
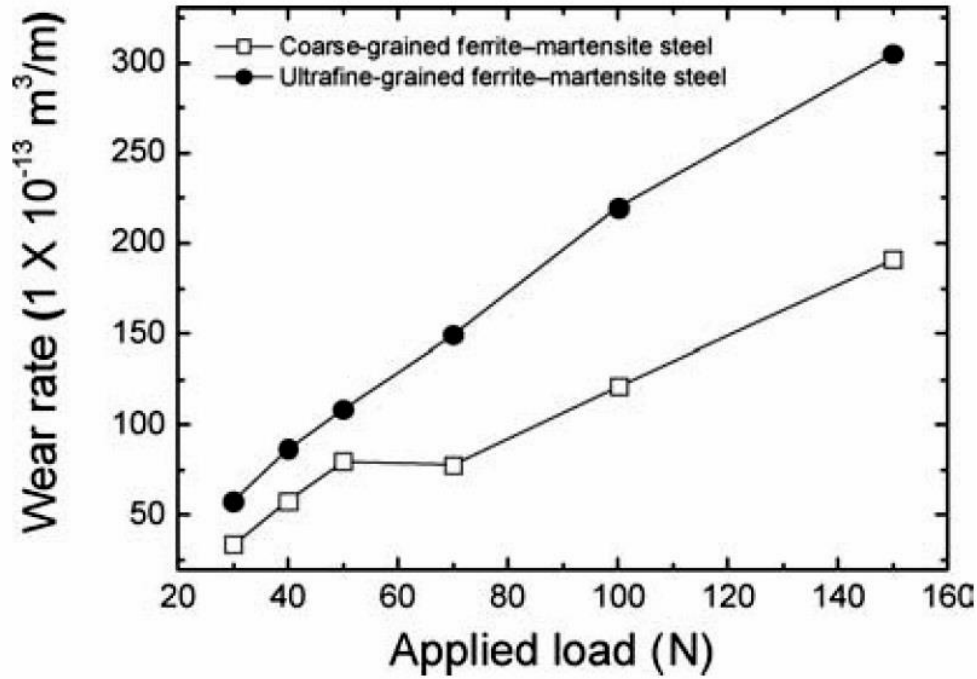
Figure 2-45 Wear rates of UFG and CG dual phase steel as a function of applied load [196].
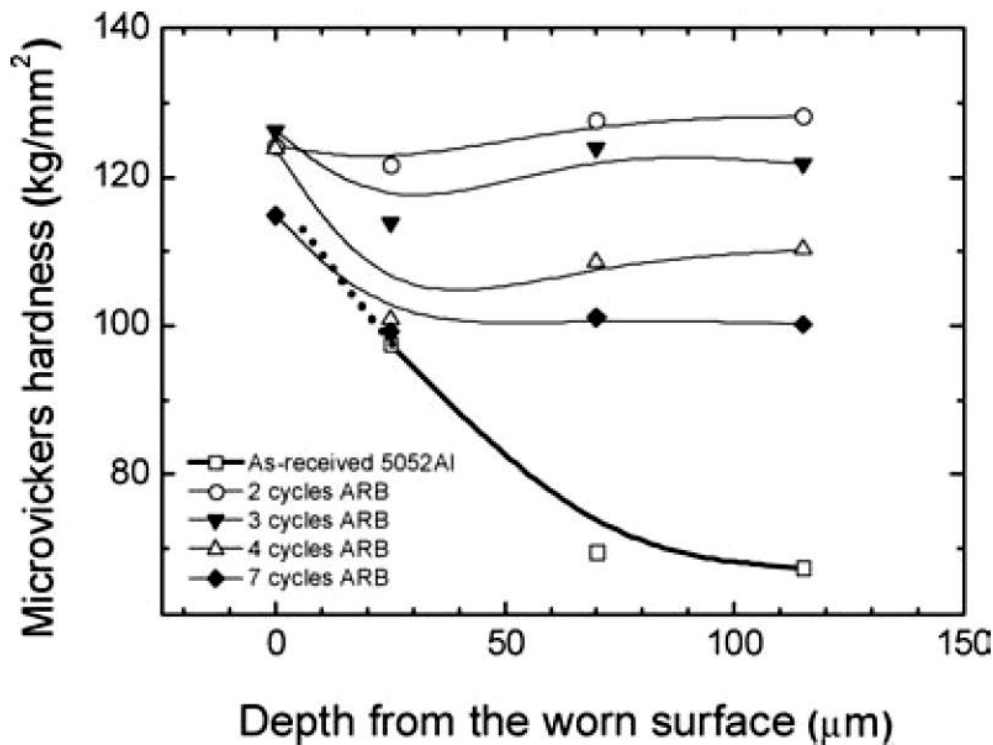
Figure 2-46 Variation of HV of ARB-processed UFG and CG Al-5052 alloys as a function of depth from the worn surface [196].

Wear behaviour of accumulative roll bonding (ARB) processed commercial pure aluminium was investigated under dry and immersion lubrication, and different

56

rotation speeds [197, 198]. The wear resistance of the ARB-processed Al samples was less than the non-processed samples. Dry sliding wear characteristics of ARB-processed UFG Al-1100 and Al-5052 alloys were also investigated [196, 199]. The UFG alloy showed higher wear rate than the as-received alloy in spite of its higher hardness and strength. Figure 2-46 shows the variation of micro Vickers hardness of the Al-5052 alloy as a function of depth from the worn surface. Different degrees of surface strain hardening occurred during the wear among the tested specimens. The low wear resistance of UFG Al-5052 alloy was attributed to its lower strain hardening capability. Similar studies have also been carried out for ARB-processed Al-5052, 5083 and 6061 alloys and all results demonstrated that the increased hardness did not enhance wear resistance of the ARB-processed Al alloys [186, 198, 199].

Because of the complex nature of the wear behaviour of SPD-processed materials, it is difficult to accurately model the process and mechanism. Only one report is attempted to explain why ARB-processed alloy has a lower wear resistance, compared with as-received alloy [198]. It is believed that the strain incompatibility due to recrystallization of grains occurs in the plastic deformation region ($2 - 5$ μm below surface) during the wear test. Figure 2-47 illustrates a schematic of recrystallization and delamination stages in the plastic deformation region. It seems that after the beginning of the wearing process due to high temperature at the contact surfaces between the pin and the worn surface, growth of the grains occurs within the plastically deformed region. The growth is more rapid in the subsurface zone than the middle thickness. Therefore, a coarse grain structure forms under subsurface which has a strain incompatibility regarding the fine grain structure and non-equilibrium ultrafine grains. As the subsurface of the wearing samples is always subjected to the Hertz shear stress, the strain incompatibility causes a delamination of coarse grains and as a result debris particles are formed. The recrystallization and delamination processes occur in repetitive cycles during ARB processing. According to the proposed deformation and recrystallization model, the high wear rate of the ARB-processed Al, therefore, is attributed to its non-equilibrium high energy and unstable grain boundary characteristics. During the wear test, subsurface grain growth caused by high flash temperature at interacted asperities and delamination of these coarse grain structures played a major role.

57
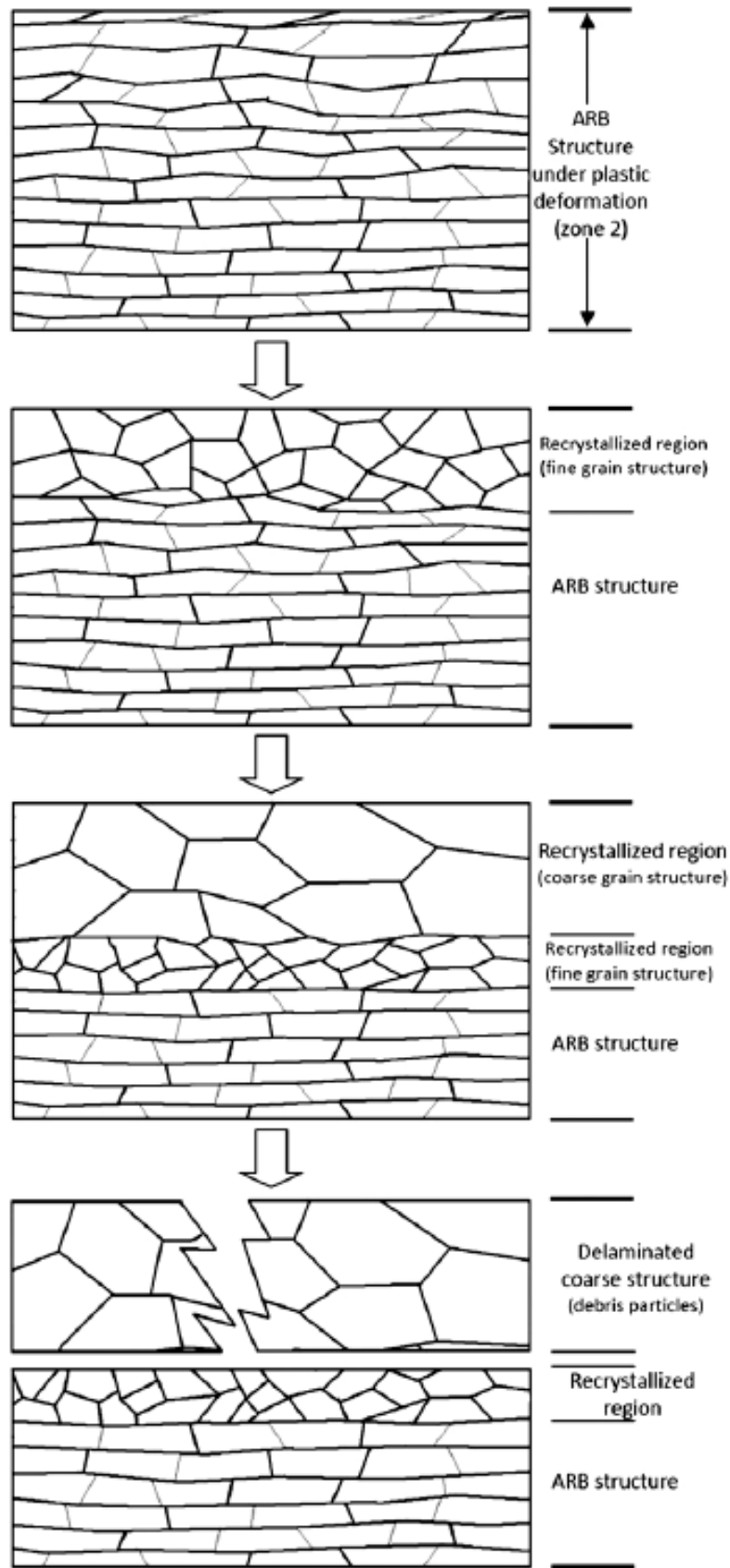
Figure 2-47 Schematics of different stages of recrystallization and deformation mechanism during the sliding wear of ARB-processed Al sheets [198].

2.3.3 No effect on wear resistance by SPD

Some studies also showed that SPD processing had no effect on wear resistance. Sato et al. [200] processed Al-Al$_3$Ti with route A and Bc ECAP, both the shape and distribution of Al$_3$Ti were changed by ECAP process, but they observed that wear property of the samples processed for different passes under different route was quite similar. They assumed that is because wear property of ECAP processed Al-Al$_3$Ti mostly depended on the shape of Al$_3$Ti phase. They also suggested that ECAP was an effective method to make homogeneous wear property for materials containing plate particles, like Al-Al$_3$Ti. Similar study for Al/Al$_3$Zr alloy has also showed that the change of processing routs had little influence on wear [201].
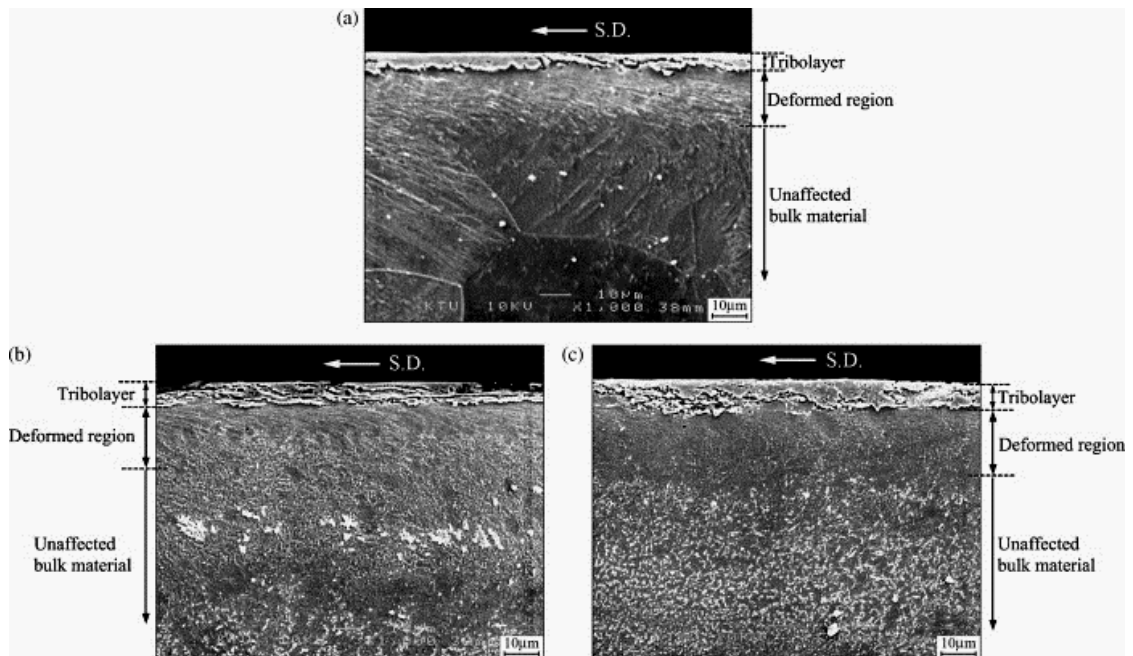
Figure 2-48 Subsurface regions of (a) CG Ti and UFG Ti processed by ECAP through (b) 8 passes and (c) 12 passes [202].

Dry sliding wear testing was conducted for CP Ti processed by ECAP for 8 and 12 passes in route-E [202]. This route is a combination of the standard routes of ECAE, in which the billet is rotated 180° and again 180° in subsequent passes (2C) followed by a 90° rotation and then another 2C extrusion [203]. A homogeneous UFG structure, with a mean grain sizes of about 0.3 and 0.25 µm respectively, was formed after 8 and 12 passes of ECAP, compared with the initial equiaxed coarse grains of 110 µm. The ECAP led to a considerable increase in strength values with sufficient ductility, but did not cause any considerable improvement in wear resistance.

Generally no qualitative differences in surface topography were observed among the worn surfaces of CG and UFG Ti after wear. The main wear mechanisms during friction of CG and UFG Ti were tribochemical reaction leading to oxidative wear with the abrasive effect, and adhesion by material transfer, suggesting that the UFG structure did not affect the wear products and wear mechanisms. Observation of the cross section of samples indicated that three distinct regions were formed on the subsurface of CG and UFG Ti after sliding wear (Figure 2-48), which were the tribolayer including titanium oxide with smeared wear material at the top, a deformed region having material structure oriented along the sliding direction in the middle, and the original unaffected bulk material at the bottom.
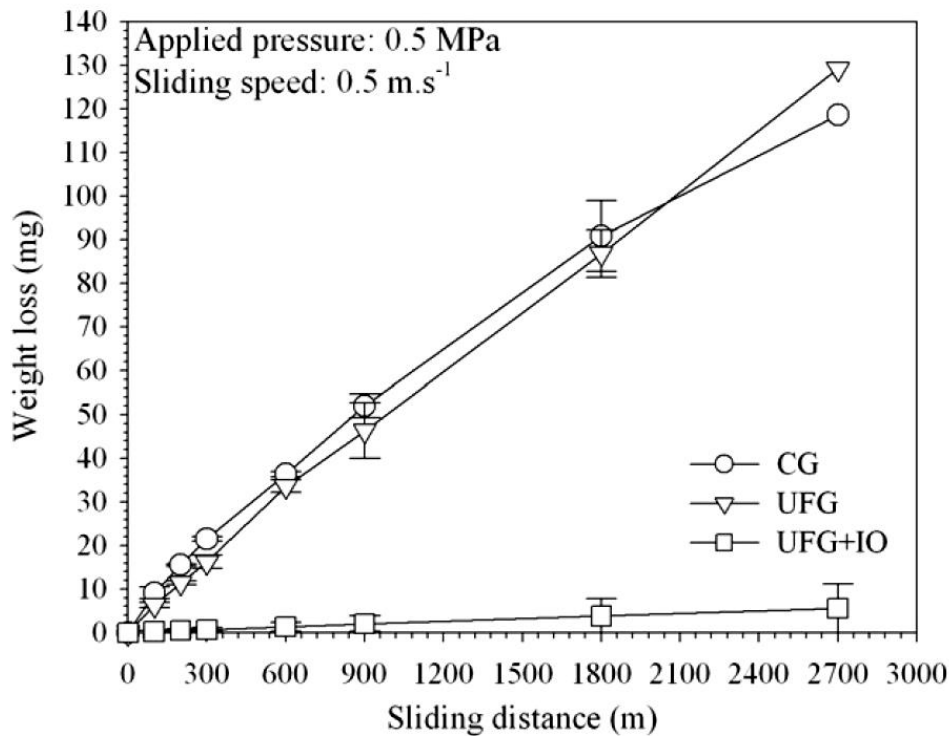
Figure 2-49 Mass loss of CG, UFG and internally oxidized UFG Nb–Zr samples versus sliding distance under 0.5 MPa pressure [204].

A biocompatible Nb-Zr alloy with very low modulus of 85 GPa was processed by ECAP using Route-E. The grain size of Nb-Zr was refined from 25 μm to 450 nm with large fraction of high angle grain boundaries after 8 passes of ECAP processing, consequently, the UTS of this alloy was increased fron 500 MPa to 750 MPa [204]. However, the CG and UFG Nb-Zr alloys showed very similar wear rate when the wear test was performed under a low contact pressure 0.5 MPa. Oxidized worn particles were widely observed on the worn surface which indicated the formation of

a thin passive oxide layer by the effect of a tribo-chemical reaction during sliding. Therefore, similar with Ti alloys, the effect of ECAP processing on wear resistance of Nb-Zr alloy was eliminated when oxidative wear was the dominate wear mechanism. After the UFG Nb-Zr was thermal treated under 560 ℃ for 6 hours, a 50 μm thick oxidation layer was formed on the top of the material. This oxidation layer had superior wear resistance under sliding due to its high hardness of 830 Hv. As shown in Figure 2-49, the thermal treated UFG Nb-Zr had a much reduced mass loss during sliding compared to Nb-Zr alloy without thermal treatment, this demonstrated that surface treatment could be an effective tool for wear control of SPD materials.

Till now, only limited works have been performed on wear of SPD-processed ultra-fine grained materials. Table 2-2 list all the wear tests currently available for a range of UFG materials processed by SPD, which include the details of SPD processing (technique used, temperature) and the wear testing (wear rig, counterpart of wear test, linear velocity, sliding distance, load, temperature). It can be seen from Table 2-2 that different SPD techniques were applied with varying processing parameters (such as, ECAP route A, B, C, and different ECAP passes). In addition, different wear testing facilities were used with also different counterparts, velocity loads and temperatures. Limited information available in friction levels and wear mechanism also are included. Most of the wear tests are related to ECAP-processed materials mainly tested at room temperature. A few available reports are related to ARB and HPT, and most of them show that both SPD techniques cause reduction of wear resistance. It is apparent from the Table 2-2 that there is no consistent effect of SPD processing on the wear properties of materials since in some experiments SPD leads to an increase in the wear resistance, and in others the wear resistance decreases or no significant effect, which likely to link with wear mechanism change.

Generally, when the wear process is dominated by abrasive wear mechanism, the improved strength of SPD mostly leads to a higher wear resistance, as the high hardness stops hard particles penetrating into the material [175-180]; when adhesive wear is the dominating mechanism, the wear resistance is more related to ductility and structure stabilization. In this case, SPD processing mostly leads to a worse wear resistance [197, 198]; When oxidation wear is dominating, the wear rate is decided by the oxidation rate and the property of the mechanical layer, mostly the SPD-

processed material has similar wear resistance with the as received material [202]. In some case, as the SPD-processed material has higher chemical activity which leads to a higher oxidation rate, the SPD-processed material has worse wear resistance [194]. Normally, wear is not only dominated by a single wear mechanism but several ones. The situation becomes even more complex when the material contains a second phase or the wear process is performed in a complex environment. Therefore, it is very difficult to simply forecast the effect of SPD on wear resistance, but have to exam the whole wear process and each wear mechanism carefully. Nevertheless, it is clear to see that the SPD processing surely changes the wear behaviour of material, either in a positive or negative way. It is important to seek the possibility of using SPD processing to achieve a better mechanical property of materials, and a better wear resistance at the same time.

Many of the above literatures showed evidence of severe wear mechanism such as adhesive and delamination, which indicates that the SPD materials (often soft materials such as Al, Mg and Ti) are still not good enough for wear applications. Therefore, more research works are necessary for seeking an improved good wear performance of SPD materials.

Table 2-2 Wear properties of materials processed by SPD.

Material	SPD method	SPD details	Wear rig	Counter part	Linear velocity m/s	Sliding distance (m)	Load (N) / Pressure (MPa)	Temp. (º C)	Lubrica-tion	COF	Effect of SPD on COF	Effect of SPD on wear resistance	Wear mechanism	Reference
Al	ARB	8C	Ball-on-disc	SS	0.035	500	N/A	RT	None	N/A	N/A	Decrease	N/A	Eizadjou et al. [197]
Al	ARB	8C	Ball-on-disc	SS	0.035-0.12	500	1.4-11.2	RT	Dry/Oil / water	N/A	N/A	Decrease	CG:Ploughing, deformation UFG: Delamination	Talachi et al. [198]
Al-1100	ARB	7C, 165ºC	Pin-on-disc	304 SS	0.05-0.1	N/A	0.5-12.0	RT	None	N/A	N/A	Decrease	Flake-let wear	Kim et al. [196, 199]
Al-5052	ARB	7C, 300ºC	Pin-on-disc	304 SS	0.05-0.1	N/A	0.5-4.0	RT	None	N/A	N/A	Decrease	Flake-let wear	Kim et al. [196, 205]
Al-6061	ARB	7C, 315ºC	Pin-on-disc	304 SS	N/A	N/A	1-7	RT	None	N/A	N/A	Decrease	N/A	Kim et al. [186]
Al-6061	ARB	5C	Pin-on-disc	SS	0.035-0.12	500	1.4-11.2	RT	None	N/A	N/A	Decrease	Delamination	Eizadjou et al. [206]
Al-5%Ti	ECAP	A/ Bc, RT, 8P	Block-on-disc	S45C	0.13	468	10	RT	None	N/A	N/A	No effect	N/A	Sato et at. [200]
Al-5%Zr	ECAP	A/ Bc, RT, 8P	Block-on-disc	S45C	0.13	468	10	RT	None	N/A	N/A	Decrease	Abrasive	El-Hadad et al. [201]
Al–2,3,5%Cu	ECAP	9P	Ball-on-disc	S45C	0.3	269-537	20-29	RT	None	N/A	N/A	Increase	Adhesion, delamination	Abd El Aal et al. [175]
Al-Cu composite	ECAP	1P, RT/ 180ºC	Ball-on-disc		0.03 0.4	360	10 10	RT RT	None None	N/A	N/A	Increase Decrease	N/A	Nickel et al. [195]
Al–12%Si	ECAP	A, 200ºC, 6P	Pin-on-disc	AISI 1045	1.1	10400	/ 0.5-3.0	RT	None	N/A	N/A	Decrease	Oxidative wear	Kucukomeroglu [194]
Al-13%Si-5%Ti	ECAP	Bc, RT, 15P	Block-on-disc	S45C	1.0	1000	/ 1.5	RT	None	N/A	N/A	Increase	N/A	Zhang et al. [176]

Cr-Si steel	SFPB		Ball-on-disc	Cr alloy	0.10	240	3-9	RT	None	CG: 0.8	Reduce	Increase	CG: Abrasion, adhesion	Ba et al. [207]
										UFG: 0.7			UFG:Abrasion	
Cu	ECAP		Block-on-ring	AISI 51100	0.1-1.2		90-620 / 5-35	RT	Synthetic oil	0.23-0.25	No effect	Increase	Ploughing	Moshkovich et at. [177]
Cu	SMAT		Ball-on-disc	WC-Co	0.2	72	5-60	RT	None	CG: 0.8 UFG: 0.7	Reduce	Increase	Delamination	Zhang et al. [208]
Cu–10%Al–4%Fe	ECAP	650ºC, 6P	Block-on-ring	GCr15	0.42	2400	20-260	RT	None	0.2-0.37	Reduce	Increase	CG: Adhesion	Gao et al. [178-180]
													UFG: Abrasion	
Cu-4.5Cr alloys	ECAP	RT, 12P	Fretting wear tester	N/A	0.02	72	20	RT	None	N/A	N/A	Increase	N/A	Bera et al. [181]
Mg AZ61	ECAP	Bc, 275ºC, 8P	Pin-on-disc	304 SS	N/A	N/A	1-7	RT	None	N/A	N/A	No effect	N/A	Kim et al. [186]
Mg AZ91	ECAP	2P	Block-on-disc	R18 steel	0.92-3.7	1650	10-50	20-300	None	0.25-0.8	Reduce	Increase	N/A	Semenov et al. [185]
Sn–11.5%Sb–5.5%Cu	ECAP	1P	Pin-on-disc	S45C	0.07-4.5	7850	256-980	RT	Dry	0.3	No effect	Decrease	Plastic deformation, adhesion	Korshunov et al. [209]
									MS-20	0.05-0.08	Reduce	Increase	Fatigue	
Zn–40%Al–2%Cu–2%Si	ECAP	Bc, 230ºC, 4P	Pin-on-disc	AISI 1045	1.1	1500-13860	/ 0.5-2.5	RT	None	CG: 0.5-0.7	Reduce	Increase	CG: Abrasion	Purcek et al. [189]
										UFG:0.4-0.6			UFG: Adhesion	
Low carbon steel	ECAP	C, 500ºC, 4P	Pin-on-disc	AISI 52100	0.05-0.1		10-150	RT	None	N/A	N/A	Decrease	N/A	Kim et al. [196]
Low carbon steel	HPT	RT, 5 GPa	Ball-on-disc	WC-Co	0.042	25.2	39.6 N	RT	None	CG: 0.7	Increase	Increase	Oxidative wear	Kato et al. [210]
										UFG:0.7-0.9				

Material	Process	Conditions	Test	Counterface			Load	Temp	Environment	COF		Wear	Wear mechanism	Reference
Low carbon steel	HPT	RT, 5 GPa	Ball-on-disc	carbon-chromium steel	0.042	25.2	39.6 N	RT	None	0.6	No effect	Decrease	Adhesion	Kato et al. [210]
Low carbon steel	SMAT		Ball-on-disc	Diamond	0.03	90	2-8	RT	None	CG: 0.2-0.35 UFG: 0.1-0.16	Reduce	Increase	Micro ploughing, micro cutting, fatigue	Wang et al. [211]
Nb-Zr	ECAP+ internal oxidation	E, RT, 8P	Ball-on-disc	Alumina	0.5	2700	/0.25-3	RT	None	N/A	N/A	None	Oxidative wear	Purcek et al. [204]
Ti	ECAP	Bc, 450ºC, 8P	Ball-on-disc	WCo8	0.13	7.9	480-2400	25-800	None	0.2-0.6	Reduce	N/A	N/A	Stolyarov et al. [184]
Ti	ECAP	Bc, 450ºC, 8P	Ball-on-disc	AISI 52100	0.05	30	5-35	RT	None	0.45-0.6	No effect	Increase	CG:Adhesion, delamination UFG:Micro-ploughing, delamination	La et al. [182]
Ti	ECAP	E, 300ºC, 12P	Pin-on-disc	AISI 1045	1.1	1520-10400	/ 0.5-2.5	RT	None	N/A	N/A	No effect	Oxidative wear	Purcek et al. [202]
Ti	ECAP + coating	E, 300ºC, 8P	Pin-on-disc	WC	0.052	84	2	RT	None	0.5	No effect	No effect	N/A	Alsaran et al. [212]
Ti	HPT	RT, 5T	Ball-on-disc	Alumina	0.1	18	5	RT	Dry / Phosphate solution	N/A	N/A	Increase	CG: Plastic deformation, Fracture UFG:Abrasion	Faghihi et al. [193]
Ti	HE		Pin-on-disc	X17CrNi 16-2	0.15	540	/ 0.28-2.0	RT	Dry	0.27-0.7	No effect	Decrease	Adhesion, corrosion wear	Garbacz et al. [213]
									0.9%NaCl / oil	N/A	No effect	Decrease		
Ti	SMAT	RT	Ball-on-disc	AISI 52100		30	1-5	RT	None	0.4-0.8	Decrease	Increase	Abrasion, adhesion	Wen et al. [183]

Ti-13Nb-13Zr	ECAP	Bc, 600ºC, 8P	Ball-on-disc	100Cr6	0.003	4.6	6	RT	Hanks solution	0.3	No effect	Decrease	Abrasion	Suresh et al. [214]
TiNi	ECAP	750ºC, 2P	Block-on-ring	GCr15	0.42	3000	50-250	RT	None	N/A	N/A	Increase	CG: Adhesion, delamnation UFG: Micro-ploughing, delamnation	Cheng et al. [187]
TiNi	ECAP	450ºC, 8P	Block-on-disc	Alumina	0.18	17.6	49-196	RT	None	0.4-0.6	N/A	No effect	Abrasion, adhesion	Korshunov et al [188]
			Pin-on-disc		0.015	14-20		-25-70	None		No effect	Increase		

Note: A- rout A; Bc- rout Bc; C- rout C; E- rout E; RT- room temperature; P –passes; C- cycles; T – turns; SS- stainless steel; COF-coefficient of friction

3. Materials and experimental procedures

In this chapter, details of the materials, SPD processing, wear test, analysis methods and experiment procedures are introduced. The main procedures of the study are as follows: Firstly, process the materials by using SPD methods (ECAP or HPT) with different strains. Secondly, measure the grain size and mechanical properties (microhardness or tensile testing) of each sample. Thirdly, wear testing of all the samples. Fourthly, examine the worn surface and wear debris to confirm the wear mechanism operated.

3.1 Materials

As during wear process, the impurities and second phase may have significant effect on wear rate which causes complication during discussion on the effect of SPD on wear resistance. Therefore, only relatively pure materials have been used as testing samples in this study. Currently, extensive literatures are available on the deformation mechanisms, property revolutions and microstructure refinement after SPD processing of Al and Ti. Therefore, wear testing of this study has been focused on pure Al and Ti.

Al-1050 alloy was chosen to investigate the effect of SPD processing on wear resistance of Al with different grain sizes. The Al-1050 has a simple face-centred cubic (FCC) crystal structure, it is single phase. Therefore, effect of texture and the second phase on wear property can be avoided by choosing Al-1050. The Al-1050 aluminium alloy has a composition shown in Table 3-1.

Table 3-1 Composition of Al-1050 alloy used in this study

Elements	Al	Cu	Fe	Mg	Mn	Si	Ti	Zn	Other
wt%	Balance	0.01	0.18	0.01	<0.01	0.12	0.02	<0.01	<0.01

In addition, a CP titanium alloy (Grade 2) was also used in this investigation which has impurities shown in Table 3-2. Pure Ti has a hexagonal close-packed (HCP) crystal structure. Therefore, it is possible to study the effect of SPD processing on wear of materials with different crystal structures.

Table 3-2 Composition of grade 2 Ti used in this study

Elements	Ti	C	Fe	H	N	O	Other
wt%	Balance	< 0.1	< 0.3	< 0.015	< 0.03	< 0.25	<0.1

3.2 ECAP processing

During the ECAP processing, the billets with diameter of 10 mm and length of 65 mm were inserted into a die which was made of H13 tool steel. As shown in Figure 3-1, the die and a plunger were fixed onto a hydraulic press. As the ECAP die was lifted up which was controlled by computer software, the billet was pressed out from the die by plunger. The pressed billet can be inserted back again into the ECAP die for more ECAP pressings. The ECAP die had an angle of 90° between the two channels and an outer arc of curvature of 20°, see Figure 2-2. These angles led to an imposed strain of ~1 on each passage through the die according to Eq. (2-1). The billets were lubricated with a suspension of MoS_2 in mineral oil ('ASO oil' supplied by Rocol) before each press in order to reduce the friction between the billets and the die walls.
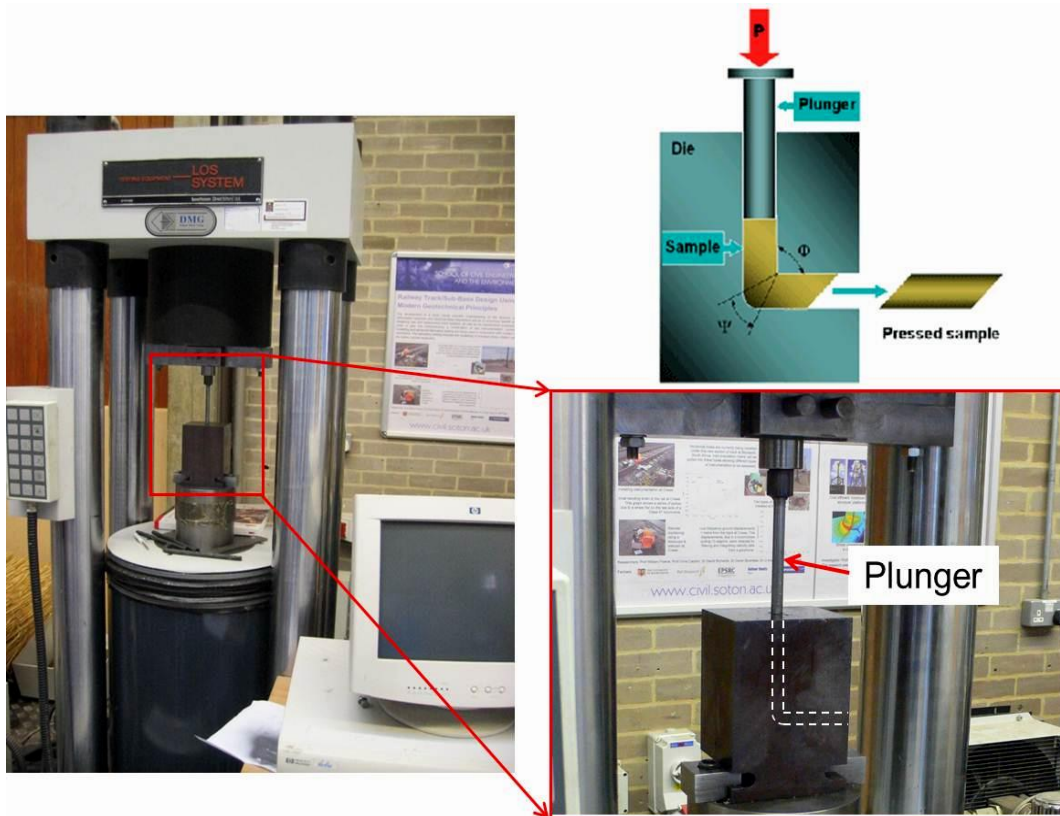
Figure 3-1 The ECAP facility.

The billets were pressed using processing route B_c in which each billet is rotated in the same direction by 90º around the longitudinal axis between each passage through the die [27], where route Bc was selected because it leads most expeditiously to a reasonably homogeneous array of ultrafine grains separated by a high fraction of high-angle boundaries [28].
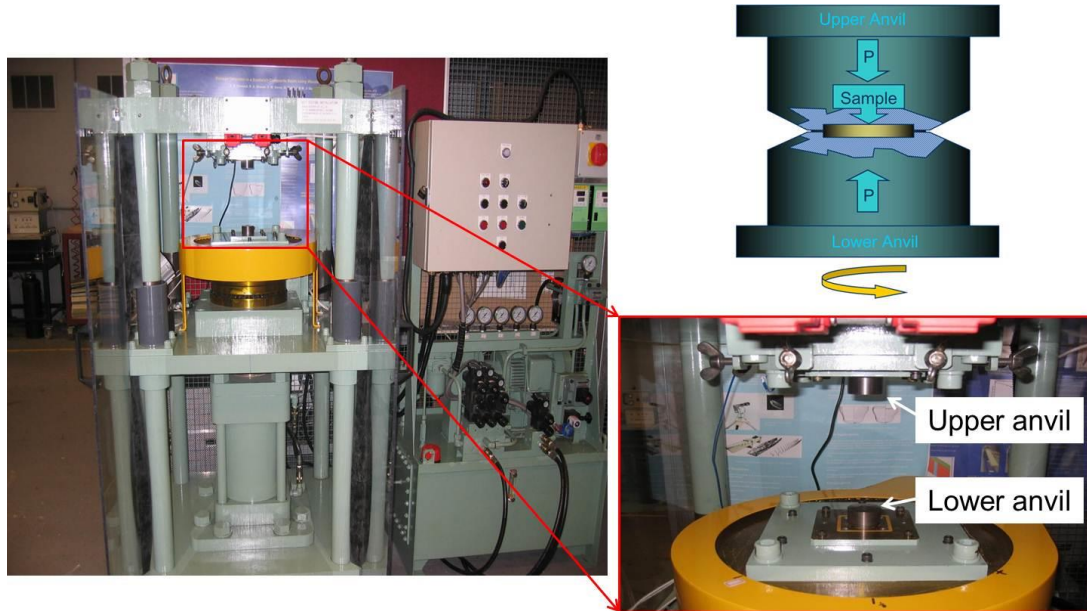
Figure 3-2 The HPT facility.

3.3 HPT processing

For HPT, specimens having a diameter of 10 mm were sliced from the as-received billets and ground with abrasive papers to a thickness of 0.8-0.85 mm. The HPT processing was conducted at room temperature on a facility with two anvils with circular flat-bottom depressions at the centres. The depression depth was 0.25 mm and the diameter was 10 mm. Details of the HPT facility is shown in Figure 3-2. After the disc sample was fitted in the cavity of the lower anvil, the lower anvil moved upward and imposed high pressure to the sample by pressing together with the upper anvil. Then the lower anvil rotated at a speed of 1 revolution per minute as well as maintaining the compression force, so that a high-pressure straining was imposed to the disc sample. Different pressures from 0 to 8 GPa can be chosen by setting the hydraulic pressures of the HPT machine. The edges of the anvils were lubricated by MoS_2 to reduce the friction between anvil edges.

In this study, high-pressure torsion processing was conducted under quasi-constrained conditions in which there is some restricted outflow of material around the periphery of the disc during the processing operation [36, 37]. Additional details on the principles of high-pressure torsion processing are given in earlier reports [38-40].

3.4 Mechanical properties testing

3.4.1 Microhardness testing
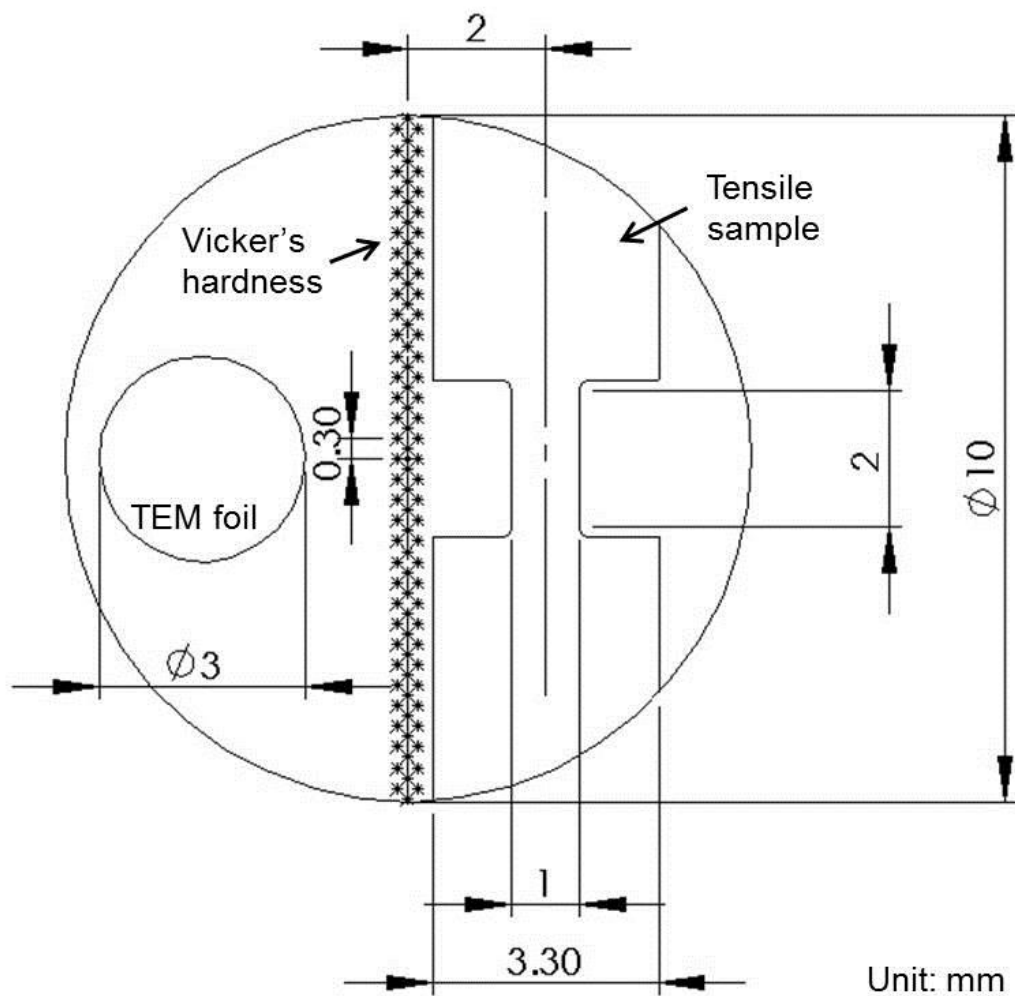
Figure 3-3 Illustration of an HPT disc showing the procedures for hardness testing at the black cross positions, examining microstructure using TEM foil with diameter of 3 mm, and tensile testing using specimens cut from the disc.

Prior to microhardness testing, the samples were polished with abrasive papers up to 1200 grid to give the samples good surface finish. Then the micrhardness was tested

using a Matsuzawa Seiki MHT-1 hardness tester. Microhardness of Al samples was tested using a load of 100 g and a dwell time of 15 s, while microhardness of Ti samples was tested using a load of 1000 g and a dwell time of 15 s.

As for HPT processed samples, the torsion strain is inhomogeneous along the diameter. Therefore, the microhadness measurements were performed at black crosses in Figure 3-3, these measurements have incremental distance of 0.3 mm. The hardness value of a position was determined by averaging four measurements around this position, to achieve a good accuracy of the measurements.

3.4.2 Tensile testing

Due to the small size of the samples processed by HPT, tensile testing was performed by machining mini-specimens from off-centre positions in the HPT discs shown in Figure 3-3. Tensile specimens were cut from the polished discs using electro-discharge machining with the specimens having gauge lengths of 2 mm and gauge widths of 1mm. A special sample holder was designed to fix the samples within the tensile testing machine.
.
These specimens were tested in tension using an Instron testing facility at room temperature operating under conditions of constant cross-head displacement with an initial strain rate of $1.0 \times 10^{-2} \text{ s}^{-1}$.

3.5 Physical vapour deposition

3.5.1 TiN coating

TiN coatings were deposited on the Ti substrates before and after HPT using PVD in a magnetron sputter ion plating system produced by Teer Coatings Ltd. Prior to the PVD process, all Ti substrates were ground to 1200 grit paper to give an average roughness, R_a, of 230 ± 20 nm. The Ti substrates were then cleaned by Ar plasma ion using a pulsed DC bias, followed by depositing a 100 nm thick Ti layer on the Ti substrates by DC magnetron sputtering. Finally, nitrogen with a carefully controlled flow was introduced into the PVD chamber to produce the TiN coating together with Ti ions from the Ti target. All of these processes were performed at a temperature

below 150ºC to avoid recrystallization of the Ti substrates. Following deposition, the coating had a thickness of ~2.5 μm.

3.5.2 DLC-Zr coatings

Prior to deposition, the Ti substrates were polished to a roughness less than 50 nm, cleaned in an ultrasonic bath in acetone, ethanol and distilled water for 15 min, and then etched using Ar^+ bombardment for 1 h at a substrate bias voltage of -650 V in order to remove all contaminants and oxides on the substrate surface. The coatings were deposited using dc dual magnetron sputtering in an Ar atmosphere (non-reactive process) and Ar+CH_4 (reactive process) to produce non-hydrogenated and hydrogenated coatings, respectively. Two targets were used: Titanium was used to deposit an interface layer and a graphite target was used with embedded Zr pellets to prepare functional film. Table 3-3 summarizes the deposition parameters. The work pressure was maintained constant for both reactive and non-reactive sputtering by adjusting the gas flow. A pulsed bias voltage of -50 V and a frequency of 250 kHz were applied.

Table 3-3 Deposition parameters of DLC-XZr and DLC:H-XZr coatings.

Parameters	DLC-XZr	DLC:H-XZr
Reactive gas flow (%)	---	5
Ar flow (%)	45	40
Base pressure (Pa)	1.5×10^{-3}	
Work Pressure (Pa)	0.4	
Substrate bias (V)	-50	
Graphite doped target (W/mm^2)	0.075	

A TiN/TiCN interlayer with a varying composite gradient and a thickness of 450 nm was deposited in order to improve adhesion. The thickness of the functional coating was approximately 1 μm so that the total film thickness was of the order of ~1.4 μm. To facilitate a detailed description of the results, the coatings were denoted as DLC-

XZr (non-hydrogenated) and DLC:H-XZr (hydrogenated), where X represents the zirconium content.

3.6 Coating adhesion testing

The coating adhesion to the Ti substrates was evaluated using Rockwell C indentation and scratch testing where these are standard techniques commonly used to quantify the interfacial strength of coating-substrate systems.

3.6.1 Rockwell C indentation test

During the Rockwell C indentation test, a cone-shaped diamond 120° tip (200 μm in radius) was indented perpendicularly onto the coating applying a normal load of 200N, thereby causing layer damage to the boundary of the indentation. The results of the test were qualitatively evaluated by comparing the optical microscope images of the crack network and the degree of delamination with an adhesion quality chart which classifies the images into six levels from HF1-HF6, shown in Figure 3-4 [215]. In this classification, HF1 is featured with only a few minor cracks after indentation which indicates a good bonding while at the other extreme HF6 denotes extensive delamination of the coating and very poor adhesion. Adhesion levels from HF1 to HF4 are typically considered as acceptable coating adhesions for use in commercial applications.
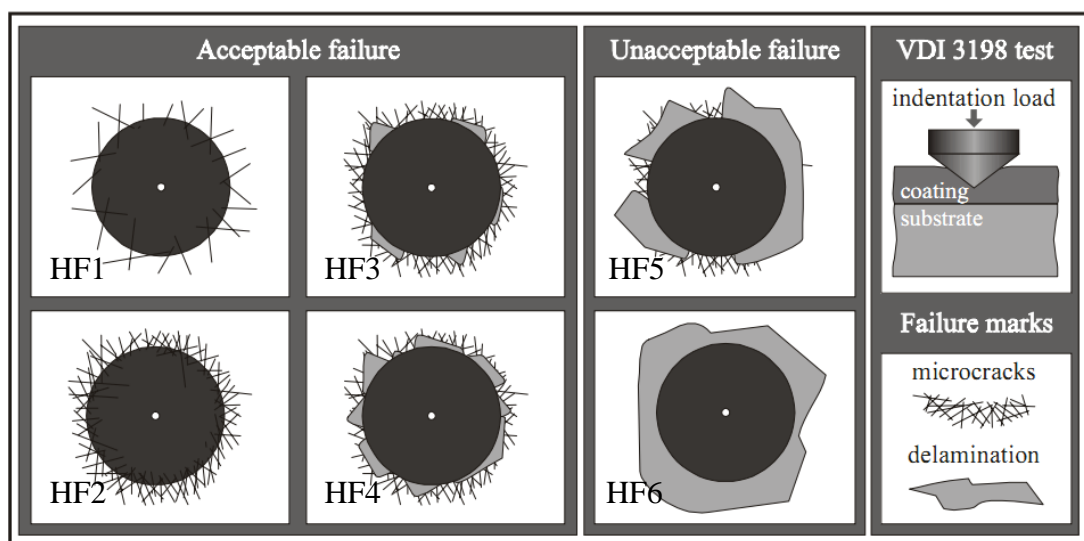
Figure 3-4 The reference chart to qualify the Rockwell C indentation test [215].

3.6.2 Scratch testing

Since thin coatings are now widely applied in many applications, various experimental methods have been proposed to measure the properties of these coatings. The scratch test is currently accepted as a standard testing method which can be used to provide extensive information on several features of the coatings: examples include the initial cracking load of the coating under which the coating initially cracks and the critical loads of the coating. The scratch test also reveals typical failure modes of the coatings which are mostly related to the property of the coating and the adhesion between the coating and the substrate [216].
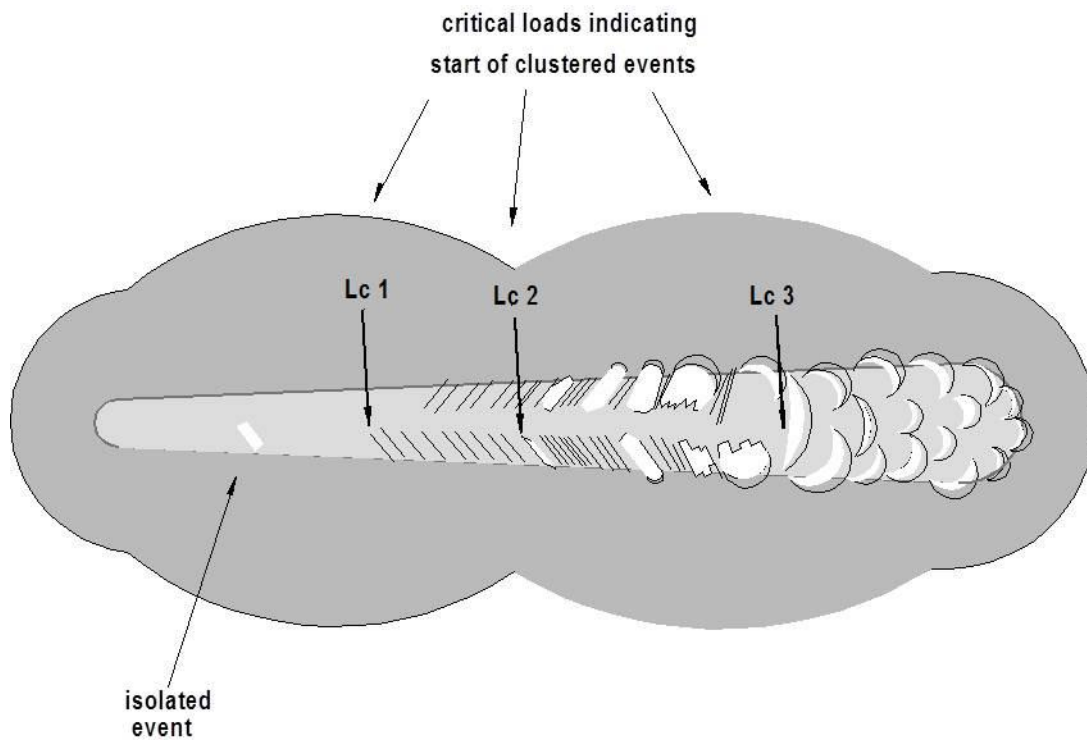
Figure 3-5 Schematic representation of typical critical loads present on scratch test [217].

The scratch test was performed by using a spherical Rockwell C diamond indenter (200 μm radius) according to standard testing methods [217]. The indenter was slid over the coating surface and the load increased from 2 to 50 N at a speed of 10 N/mm. Any failure event, such as a cracking of the coating or delamination, was detected and recorded using an acoustic emission (AE) detector. The scratch testing was repeated 5 times for each sample to obtain reliable results. As shown in Figure 3-5, the lower critical load, L_{c1}, was defined as the load where the first cracks occurred (representing cohesive failure) and the upper critical load, L_{c2}, was defined

74

as the load associated with the first delamination at the edge of the scratch track (representing adhesive failure). In addition, a load L_{c3} was defined as the load under which the coating was totally removed from the substrate.

3.7 Scanning electron microscopy

A JEOL JSM 6500 SEM with EDS was used to examine the morphology of debris and the wear surface of samples after wear testing, the energy dispersive X-ray spectrometry was conducted with an INCA EDX analyser to provide information of chemical composite of debris and wear surface.

3.8 Transmission electron microscopy

A JEOL 3010 TEM which has accelerating voltage 100 to 300 kV was used to analysis the microstructure of samples. This TEM has a revolution to 0.21 nm and it is connected with an energy dispersive X-ray microanalysis (Oxford Inca 100 TEM) to study the composite of sample during TEM imaging. Samples were polished with abrasive papers to reduce the thickness to around 50 μm. TEM foils with diameter of 3 mm were punched out from the samples, and the TEM foils were produced by twin-jet chemical polishing at a temperature of -30 ℃ in the solution of 5% perchloric, 35% butanol and 60% methanol.

3.9 Wear testing

3.9.1 TE77 high frequency friction machine

The TE77 high frequency friction machine is a versatile test system for the evaluation of the friction and wear properties of materials in dry and lubricated reciprocating rolling/sliding contact conditions. The control unit includes the SLIM 2000 Serial Link Interface Module and COMPEND 2000 software for sequence control and data acquisition on a host PC. As shown in Figure 3-6, the upper sample is fixed on to an arm which is connected to an eccentric cam. As the eccentric cam is rotating in the lubricate bath, the upper sample is doing a reciprocating movement against the fixed lower specimen. The load is applied to the moving samples through

a spring, linkage and roller cam follower. The spring is actuated through a geared servomotor and pulley which can provide a load of up to 1000 N.
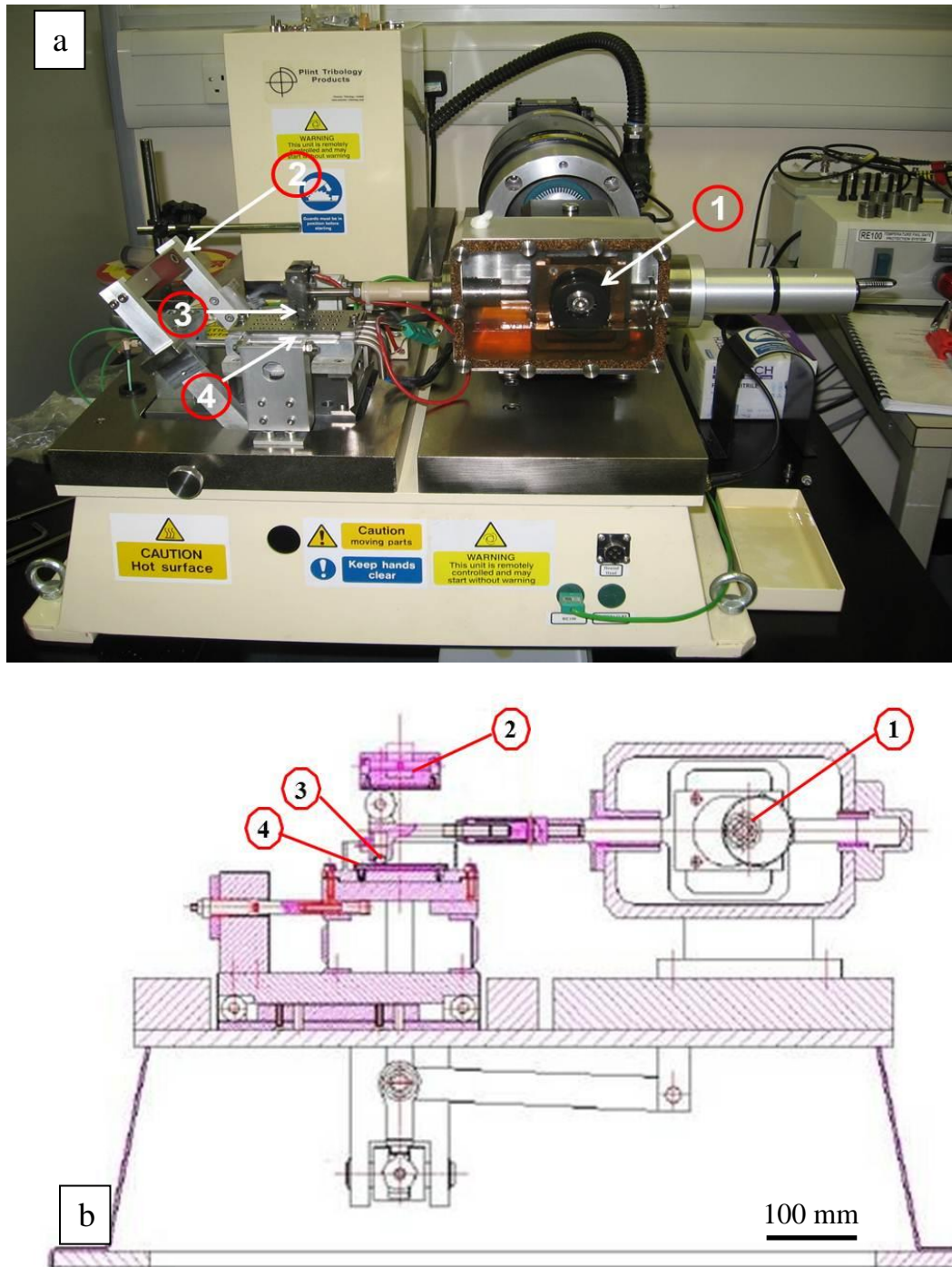
Figure 3-6 Overview (a) and illusion (b) of the TE77 system: 1, the eccentric cam; 2, the load linkage; 3, upper sample; 4, lower sample.

The friction force during wear test was measured by a piezo-electric transducer which has a Sensitivity of typically 45.7 pC/N and range of +/- 500 N. Other parameters such as contact potential and sample temperature are also measured by

corresponding sensors connected to the bench. The mass loss of each sample after the wear test was measured using a Mettler AE240 microbalance having an accuracy of 0.1 mg.

3.9.2 The microscratch system

During the service life of moving contacts, problems and damages are often caused by wear particles generated from the interface, especially in the field of electronic engineering and precision instruments. There has been some previous work focussed on trying to understand the nature of the microscopic wear mechanisms, and the generation of wear particles in micro or nano contacts [132]. In-situ SEM wear study via micro or nano tribology test systems has been one of the most effective methods. Several different types of micro or nano tribology test systems have been developed since 1974. An in-situ SEM video tape recording tribosystem was developed and used to study micro-wear mechanisms of steel, ceramic and coatings. Several different wear modes and the transitions between them were plotted on wear maps [132, 134, 218]. Atomic force microscopy (AFM) has also been used to scratch samples in a much lower load range.

Recently, a cost effective tribometer was developed, which was used to study micro-scratch behaviour of WC/Co hard metals and coatings [219-221]. This test system has now been further developed, and can perform wear tests with a load range between 10 mN and 0.3 N, filling the gap between AFM and traditional wear testers. The micorsratch system designed in National Physical Laboratory of UK can be used as a bench top system or SEM in situ system. The bench top system can carry out wear tests in air or controlled environment by setting atmospheres of the chamber. The SEM in situ system has the ability to observe the removal of materials during wear test to a reasonable high resolution.

As shown in Figure 3-7, the key feature of this microscratch system is the flexure design which was based on a three dimensional cage with eight bar kinematic chain [222]. When the probe is brought into contact with sample surface, compression force is generated by deflection of these eight bars. At the same time, the normal force capacitance plate measures the deflection of the bars which indicates how

much the bars are bended. The position of probe is adjusted by applying a feedback signal to a piezoelectric actuator mounted under the flexure to keep the compression force constant. Similarly, the friction force generated during wear test is measured by vertical capacitance plate. The microscratch system can carry out wear tests with load range of 5-250 mN, a stroke length of up to 8 mm and a speed range of 15-220 μms^{-1}.
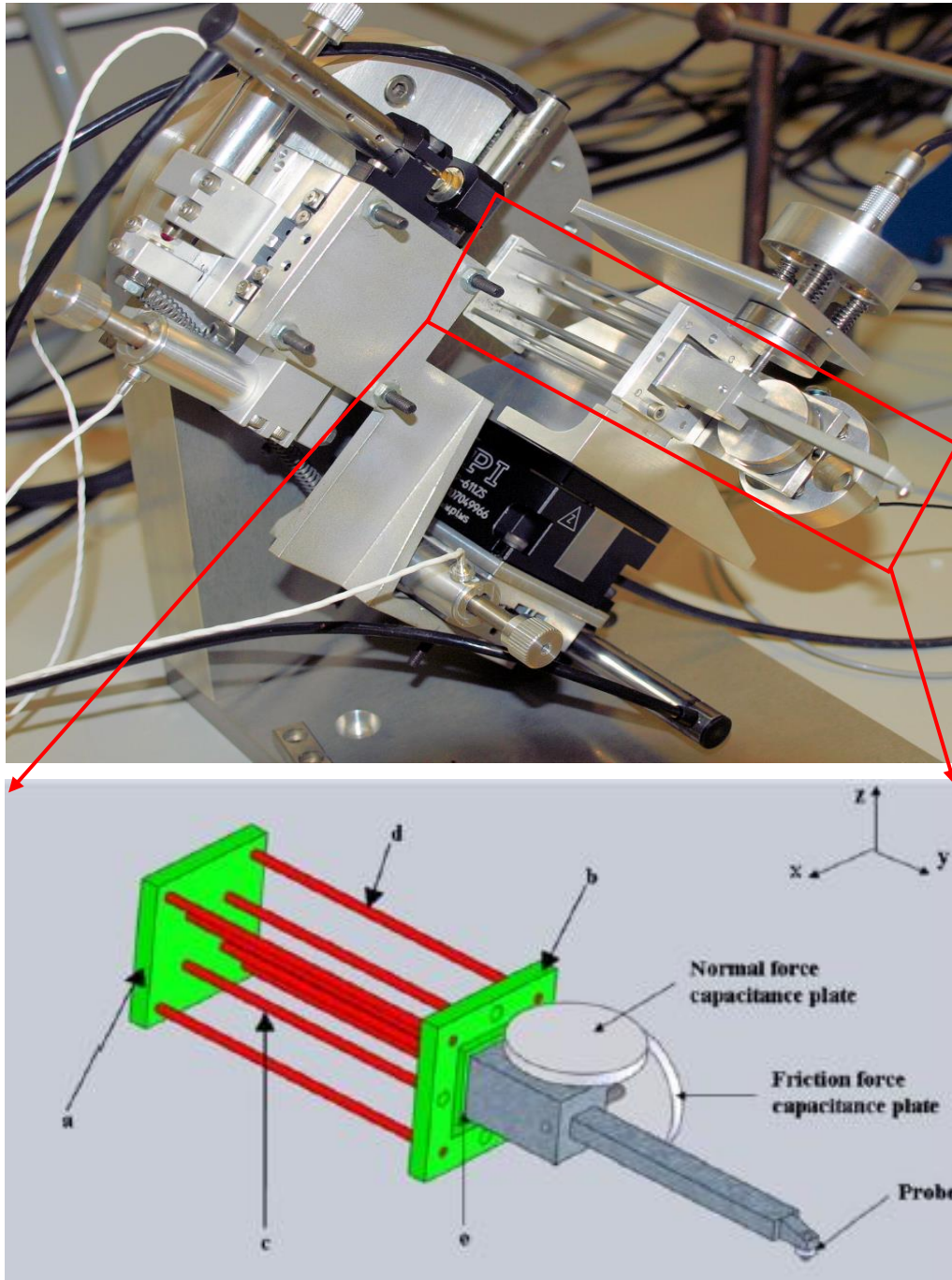
Figure 3-7 The overall schematic of micro-scratch test system: (a) the free plate in the flexure element; (b) the mounting plate supported on the piezoelectric actuator; (c) is inner flexure bars; (d) outer flexure bars; (e) the probe lever support [219, 222].

3.10 Surface profile meters

3.10.1 The XYRIS 2000 TL/CL metrology system

An XYRIS 2000 TL/CL metrology system produced by TAICAAN was used to study the topology of the surface roughness and 3-D surface profiles after wear tests. The XYRIS 2000 system is an advanced 3D metrology system which offers the users complete measurement solution for surfaces. It can be used in a high precision mode for 3D radius measurements of rough surfaces or as a 2D scanner for surface roughness properties. The XYRIS 2000 system is enhanced with a confocal laser and a triangular laser for a wide range of measurement and revolutions. Parameters of each laser system are shown in Table 3-4.

Table 3-4 Typical Sensor Specifications of XYRIS system

Typical Values	Confocal Laser	Triangular Laser
Gauge (mm)	0.6	10
Stand Off	6	15
Resolution (μm)	0.01	0.1
Spot Size (μm)	2	30
Sample Rate (Hz)	1.5k	100k
Angular Tolerance	17°	N/A

3.10.2 Infinite focus microscopy

Surface morphology of samples before and after wear testing was investigated using an infinite focus microscopy (IFM) produced by Alicona. Infinite focus microscopy is an optical 3D micro coordinate system for surface morphology measurement. The system based on an optical technology which delivers a measurement density of more than 100 million measurement points. The system has the capacity for measurement of even large measurement areas and volumes. The vertical resolution of infinite focus microscopy is up to 10 nm. The optical technology used in IFM is included in the most recent EN ISO standard 25178.

4. Reciprocating wear test of Al-1050 alloy processed by ECAP

In this chapter, an attempt was made to investigate the wear behaviour of Al-1050 alloy processed by ECAP, including coefficient of friction and mass loss. Wear tests were conducted on Al-1050 alloy after processing by ECAP. Coefficient of friction and wear rate of as-received Al-1050 and ECAP processed Al-1050 were compared. Morphology of wear surfaces and debris was studied using SEM and surface profile meter, and the composition of them was studied by EDX. Possible wear mechanisms and their interactions are discussed.

4.1 Experimental procedure
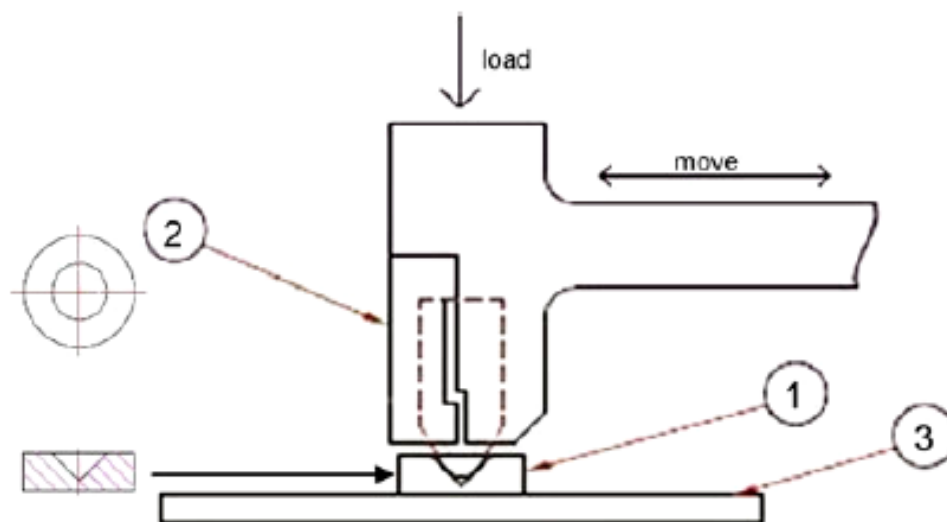
Figure 4-1 Schematic illustration of the high-frequency reciprocating test rig used for the wear tests: 1-counter surface; 2-holder; 3-sample fixed in position.

ECAP was performed at room temperature for 1, 2, 4 and 8 passes, respectively, using a pressing speed of 0.5 mm s^{-1}.

The reciprocating dry sliding wear test was chosen to avoid the effect of lubrication. Dry sliding wear tests were conducted on both the as-received alloy and the alloy after processing by ECAP using a Phoenix TE77 high-frequency reciprocating test rig as illustrated schematically in Figure 4-1. These tests were performed at a

temperature of 20 ± 2ºC and under a relative humidity of $55 \pm 5\%$. The samples for the wear tests were machined into plates having dimensions of $45 \times 8 \times 2.5$ mm^3 and each plate was mechanically ground to 4000-grit SiC paper and then washed in acetone in an ultrasonic bath for 15 minutes. In this condition prior to testing, the average surface roughness was about 0.7 μm. A flat-on-flat contact was chosen to maintain the contact pressure at a low level using a contact area between the two surfaces of about 90 mm^2. Two loads of 5 N and 23 N were used in this study and the apparent contact stresses were estimated as 5.6×10^{-2} and 2.6×10^{-1} MPa, respectively. The counter surface used in these tests was phosphor bronze with a hardness of 200 Hv. During testing, the stroke length of the oscillating motion was ~8.9 mm and the reciprocating frequency was 1 Hz which gave an average sliding velocity of 17.9 ± 0.1 mm s^{-1}.

Before and after the wear tests, the Vickers microhardness was measured with a load of 100 g and a dwell time of 15 s. Grain sizes were recorded after ECAP using electron back-scatter diffraction (EBSD). The microstructures of the worn surfaces were analysed using SEM-EDS. The topology of the surface roughness was measured using 3-D surface profile-meter produced by TAICAAN.

4.2 Results

Figure 4-2 shows the microstructure of Al-1050 measured by EBSD performed by a related study [223]. In the as-received condition, the grain size of the alloy was ~44 μm. After ECAP gave average grain sizes of ~15, ~11, ~4.9 and ~1.3 μm after 1, 2, 4 and 8 passes, respectively, where the grain size after 8 passes is similar to grain sizes reported in earlier investigations using high-purity [26, 32, 224, 225] and commercial purity [226] aluminium.

Figure 4-3 shows the variation of the microhardness with the number of passes of ECAP before the wear tests. As anticipated from earlier studies [19, 64], the hardness increases significantly after processing by ECAP. From 1 pass to 4 passes of ECAP processing, the hardness of Al-1050 increased with increasing of the strain. The microhardness of Al-1050 after 8 passes ECAP processing was very similar to that after 4 passes ECAP, which demonstrated that strain hardening of Al-1050 alloy

saturated at around strain of 4. Any more deformation straining beyond that cannot lead to more strengthening.
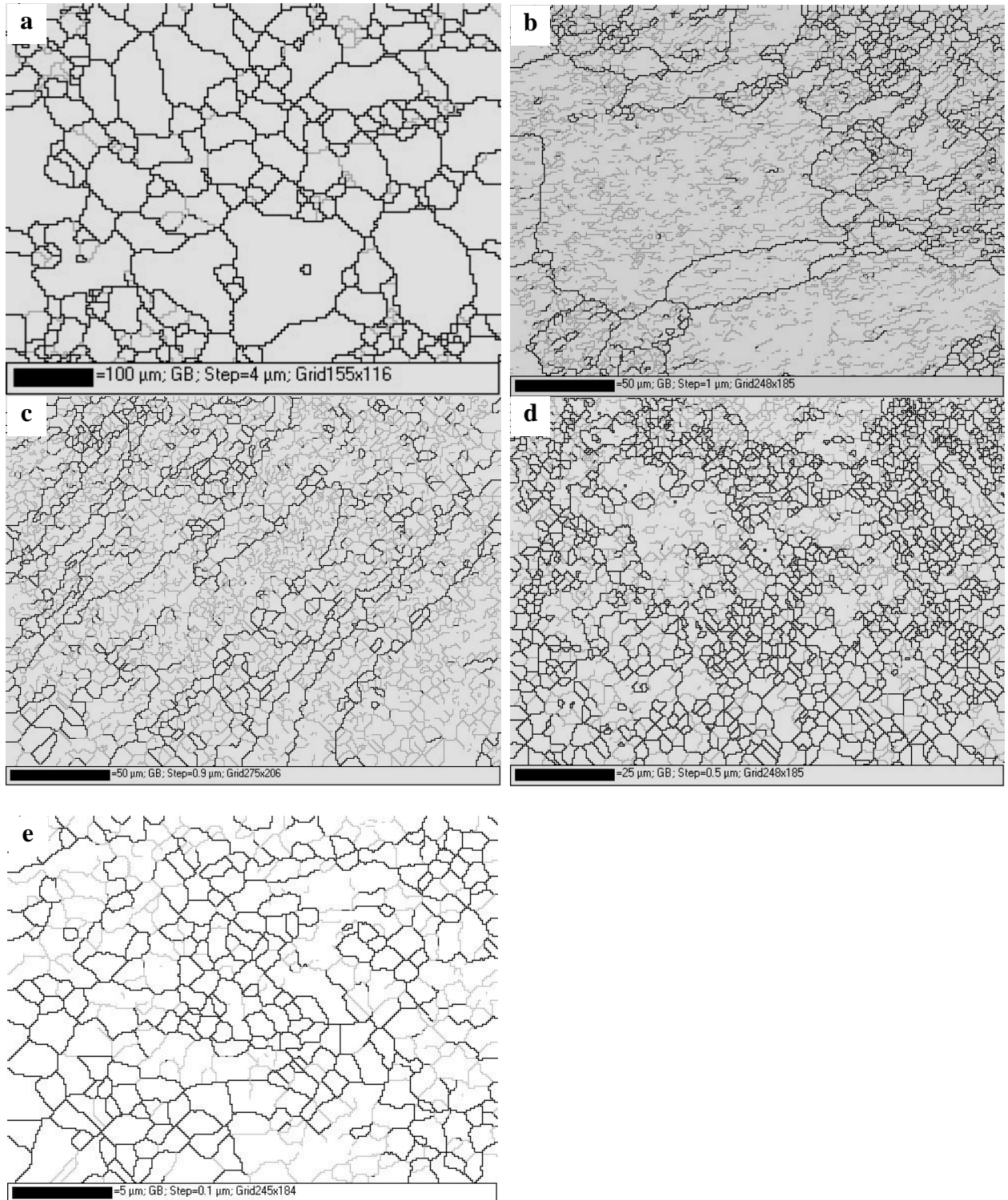
Figure 4-2 Microstructure of AA1050 alloys (a) in the as-received conditions and processed by ECAP for (b) 1, (c) 2, (d) 4 and (e) 8 passes [223].

The average values of the coefficients of friction during sliding testing are shown in Figure 4-4 for both the 5 N and 23 N testing conditions. For these experiments, the sampling rate of the friction transducer was 1 Hz and the test continued for 1500 s so that each point corresponds to an average value from 1500 datum points. It is apparent from Figure 4-4 that ECAP has essentially no influence on the measured coefficients of friction under the two loading conditions used in this study. Thus, under a load of 23 N the coefficients of friction varied from 0.62 to 0.66 whereas under a load of 5 N the coefficients of friction were slightly lower at 0.56 to 0.59.
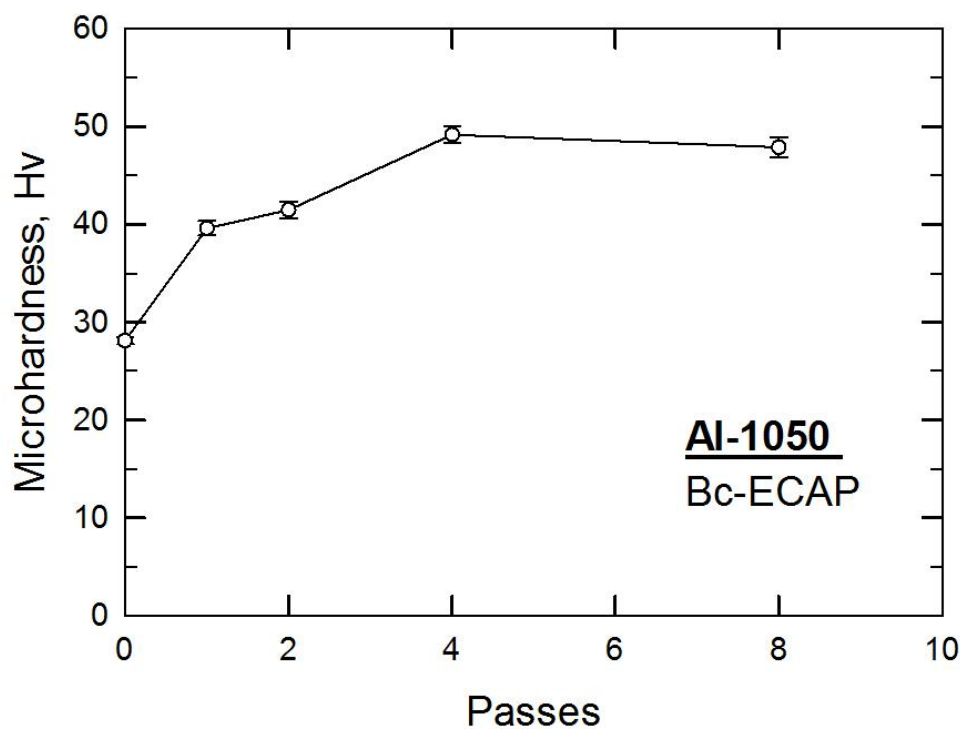
Figure 4-3 Microhardness versus number of passes after processing by ECAP.

The mass loss and wear rate of the samples after the wear test is shown in Figure 4-5 for the two different loading conditions. It has been shown theoretically that the mass loss may be estimated using the Archard abrasive equation [122] given by

$$V = K \frac{SL}{H}$$ (Eq.2-13)

Where V is the volume worn away during testing, S is the total sliding distance, L is the normal load, H is the hardness of the softer surface and K is the dimensionless wear coefficient specific to the sample under test. Since the samples processed by ECAP have a higher hardness than the as-received sample, as shown in Figure 4-3, it

is reasonable to anticipate from Eq. (2-13) that they will experience a smaller mass loss. Nevertheless, it is evident from Figure 4-5 that the samples processed by ECAP exhibited larger mass loss and, in addition, this mass loss increased with increasing numbers of passes for the samples tested under a load of 23 N. Because of the apparent different between the samples tested with loads of 23 N and 5 N, these samples will be examined separately.
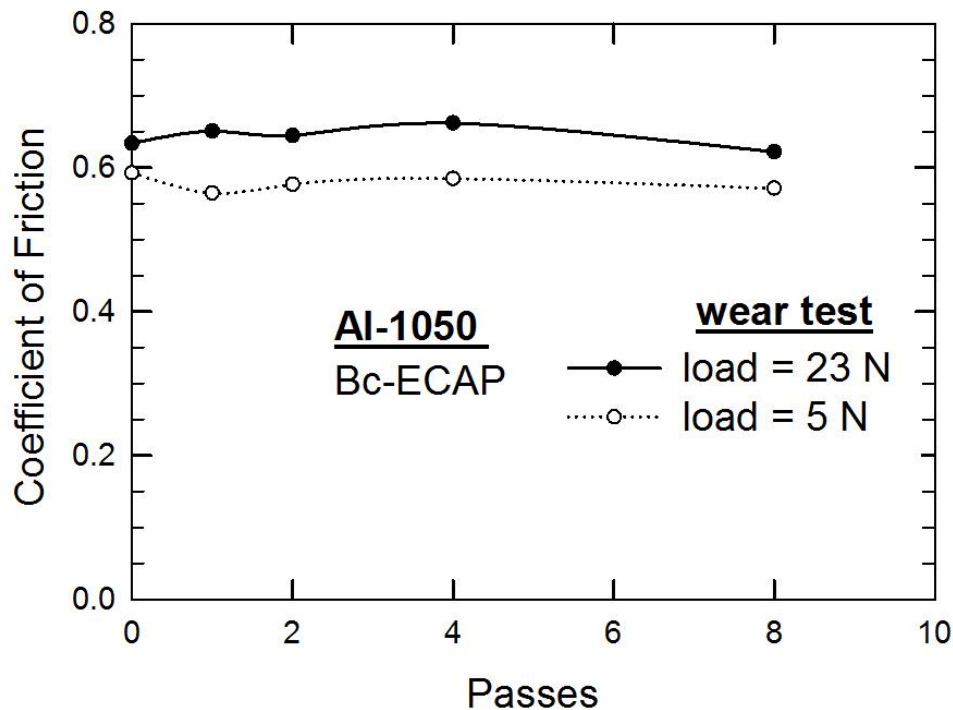
Figure 4-4 Coefficient of friction versus number of passes for the two loading conditions.

SEM study showed that all samples tested under a load of 23 N for 1500 s exhibited exceptionally severe wear with evidence for much white debris that became detached from the samples. The morphologies of the worn surfaces of all samples were reasonably similar and examples are shown in for Figure 4-6(a) the as-received condition and after ECAP through (b) 1 pass and (c) 8 passes. The appearance of the surfaces after ECAP is typical of adhesive wear and this has been widely reported for soft and ductile materials such as copper, aluminium and gold [227, 228]. Figure 4-7 shows the wear debris for (a) the as-received condition and (b) after ECAP through 8 passes. It is apparent from Figure 4-7 that the size of the debris is significantly smaller after processing by ECAP thereby confirming that particles are more easily detached from the surface during sliding wear of the ECAP processed material.
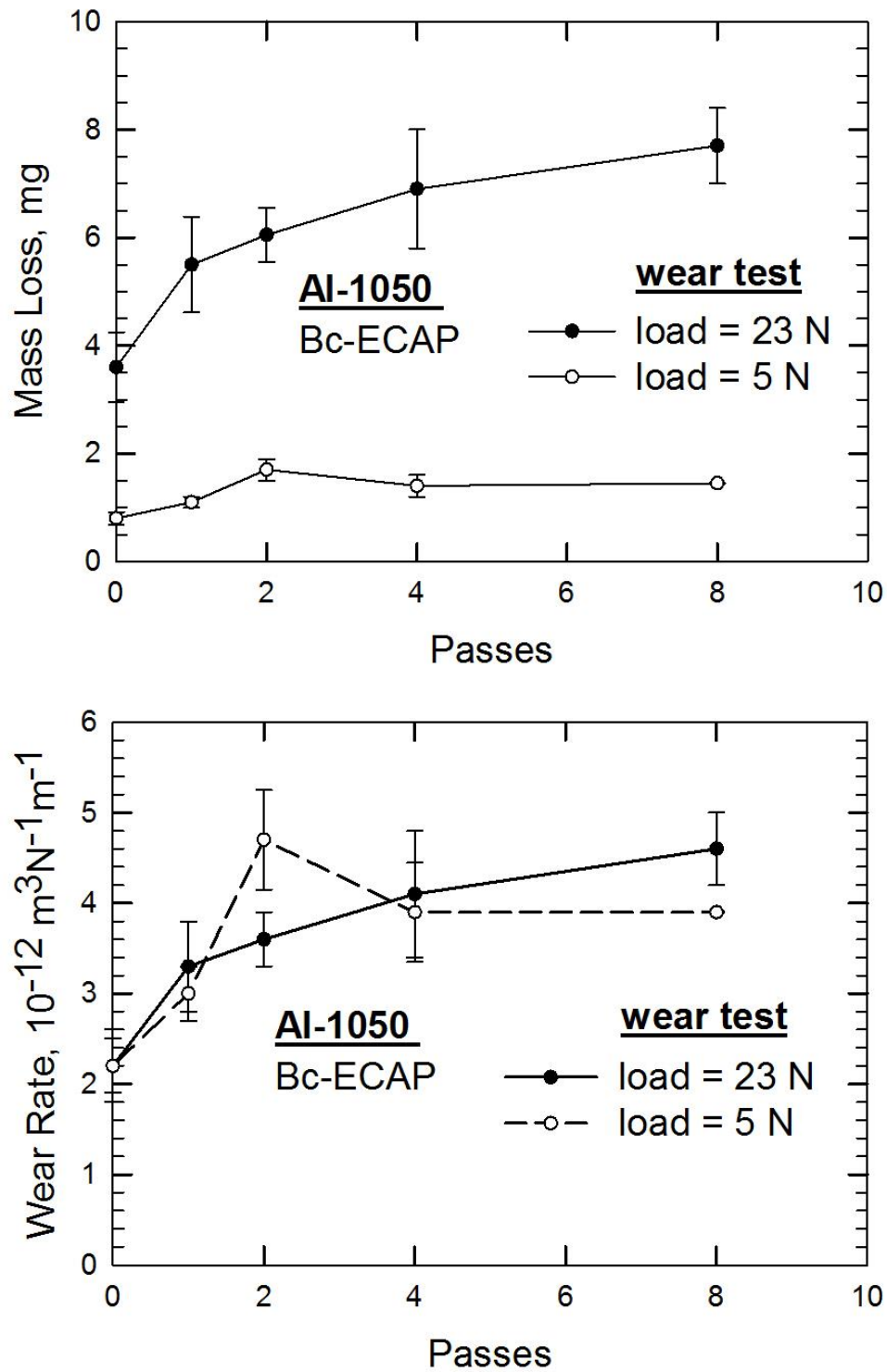
Figure 4-5 Mass loss (upper) and wear rate (lower) versus number of passes for the two loading conditions.
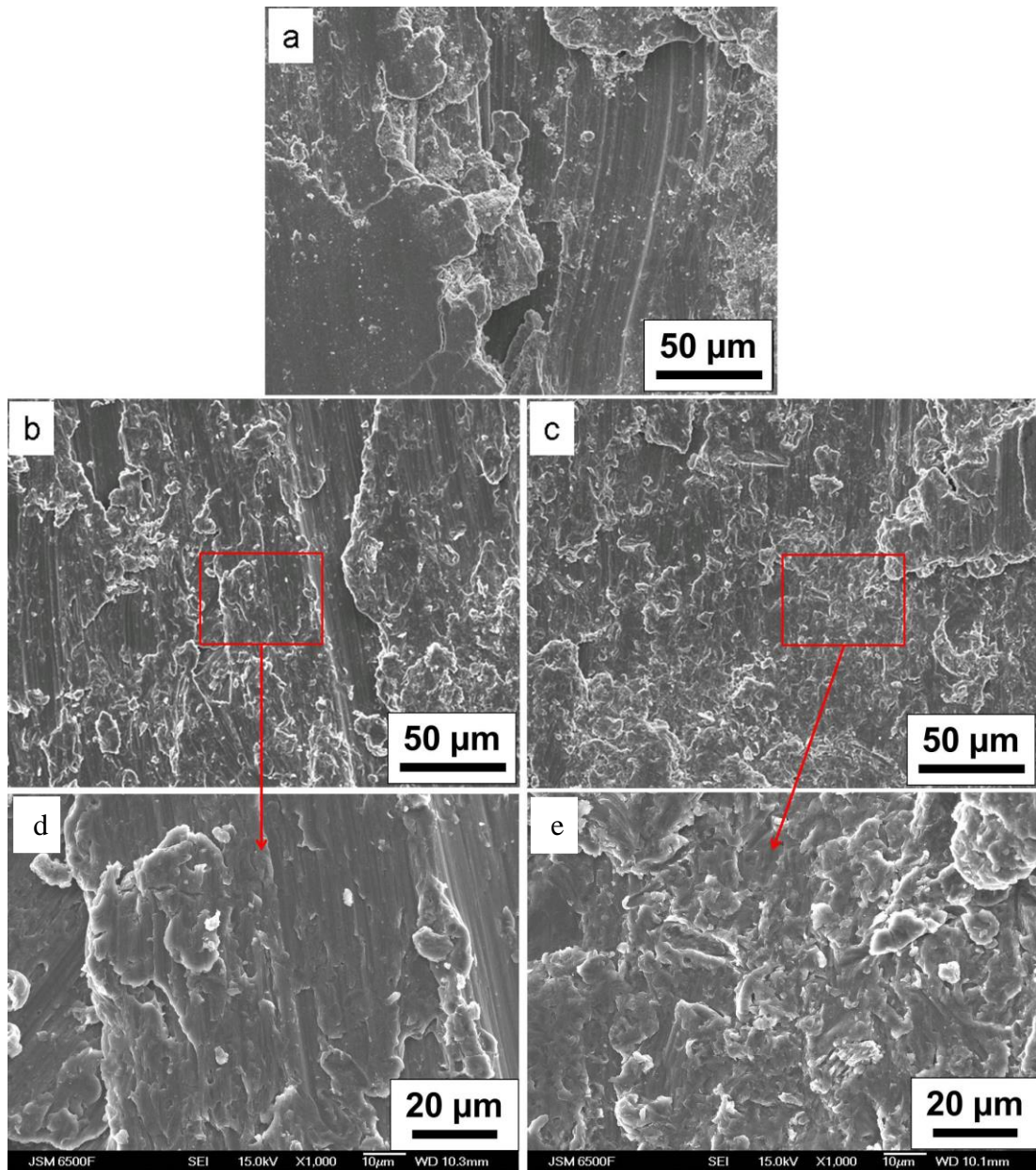
Figure 4-6 SEM micrographs of worn surfaces after wear tests under a load of 23 N: (a) as-received material, (b, d) after 1 pass of ECAP and (c, e) after 8 passes of ECAP.

During the sliding wear test under the lower load of 5 N, it was observed that the wear debris was a mixture of white flake-like particles and black powders. This is shown in Figure 4-8 where (a) and (b) are low and high magnification images, respectively: the lower portions of the figure show the EDS analyses of the small areas marked with rectangles in the upper images. It was noted that the white flake-like particles visible in Figure 4-8 (a) were observed from the beginning of each wear test whereas the black powder in Figure 4-8 (b) became visible at some point during the test. Similar results were also reported in an earlier investigation [229] and it was

proposed, in agreement with the current EDS analyses, that the white particles are monolithic aluminium detached from the sample whereas the black powder is an aluminium oxide phase having an amorphous structure.
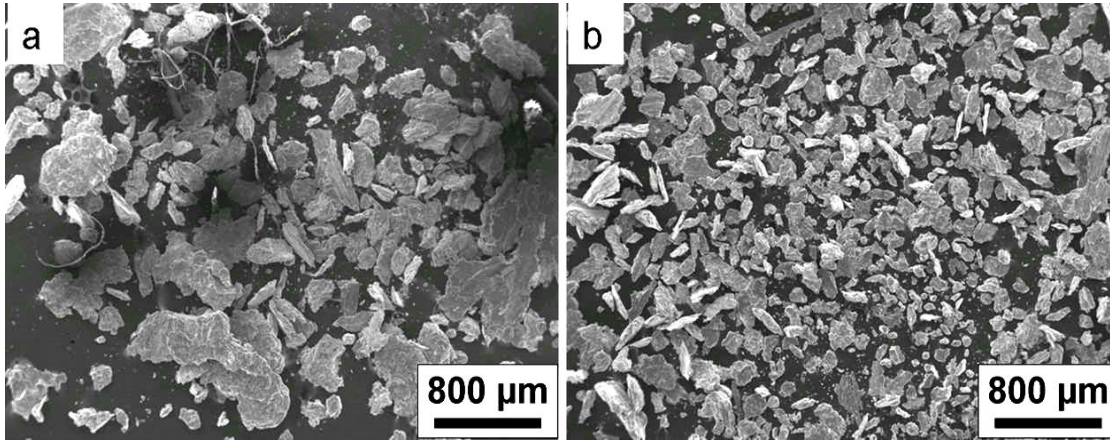
Figure 4-7 Wear debris of samples under a sliding load of 23 N: (a) for the as-received condition and (b) after 8 passes of ECAP.
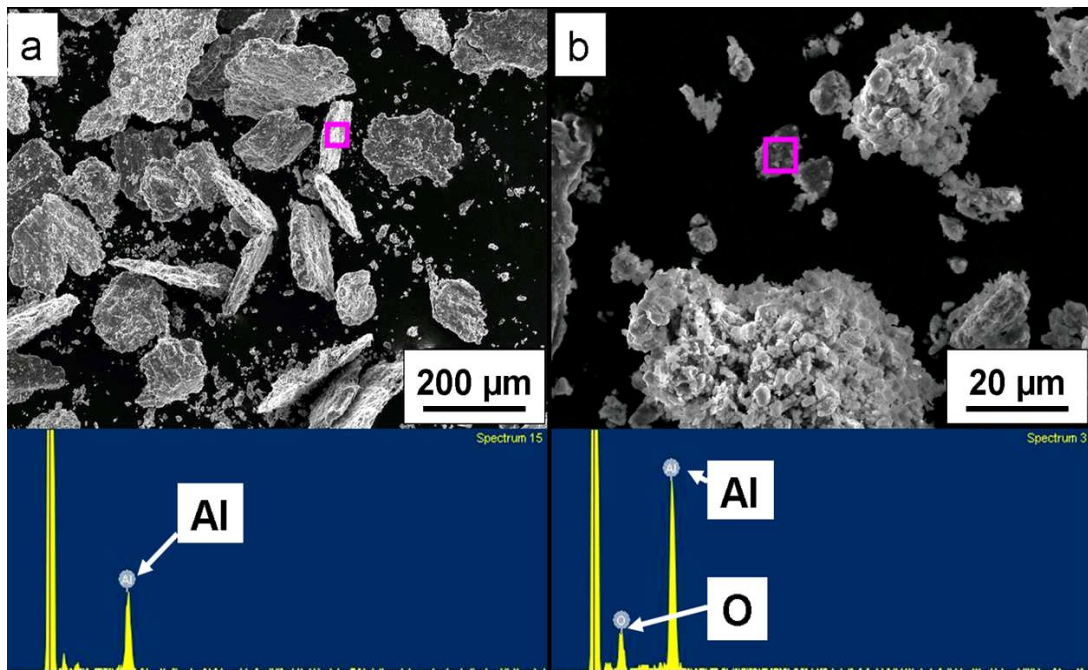
Figure 4-8 EDS analysis of wear debris from 8 passes ECAPed sample after wear test using a load of 5 N for (a) low and (b) high magnifications.

Material transfer was also evident with aluminium being transferred onto the pin surface and Figure 4-9 shows the counter surface and appropriate EDS analyses after 8 passes of ECAP. The image on the left shows a low magnification and the small area within the rectangle is shown at a higher magnification on the right. These observations show that the counter surface is partially covered by transferred

fragments and the EDS analyses confirms these transferred fragments are mixed components of aluminium and aluminium oxide. Many of the earlier studies used steel as the counter surface [229-232] and mechanically mixed layers (MML) were widely observed on the surfaces of aluminium samples when using an Al-steel wearing system. As Tandon [231] found, using XRD analyses of wear debris from an Al-steel wear system, that the MML from which the wear debris generated contained an iron-aluminium compound, as iron from the steel counter surface was apt to transfer and form iron-aluminium compound with the aluminium. In the present investigation, a phosphor bronze was used as the counter surface and this led to material transfer but not enough to the formation of mechanically mixed layers.
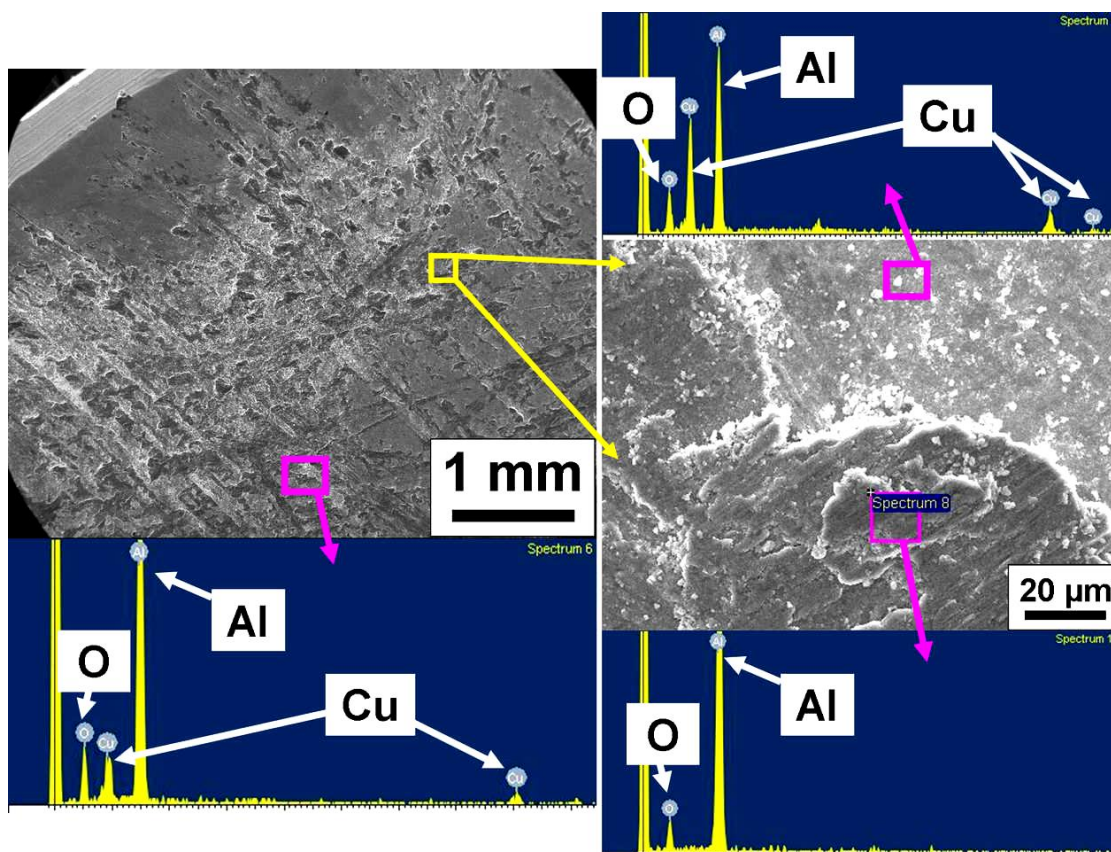
Figure 4-9 EDS analysis of the counter surface against 8 passes ECAPed sample after wear test using a load of 5 N.

Evidence for surface deformation was also visible on the worn surfaces of the samples after wear testing. Figure 4-10 shows an example using a load of 5 N after 8 passes of ECAP where the topological three-dimensional profile is shown at upper left, a portion of the worn surface is shown at lower right and two EDS analyses are

included for the small rectangles marked in the image. The three-dimensional profile shows that the worn surface is made up of grooves and some higher flats. It was found by EDS analysis that the grooves were close to pure aluminium and the higher flats contain aluminium oxide. It is evident from the color-coding in Figure 4-10 that the separation distance between the high flats and the grooves is typically of the order of several tens of microns, where this is similar to the thickness of the flake debris in Figure 4-8. This suggests that during the wear test the flakes are detached from the sample and leave pits which join at a later stage to form low-lying areas.
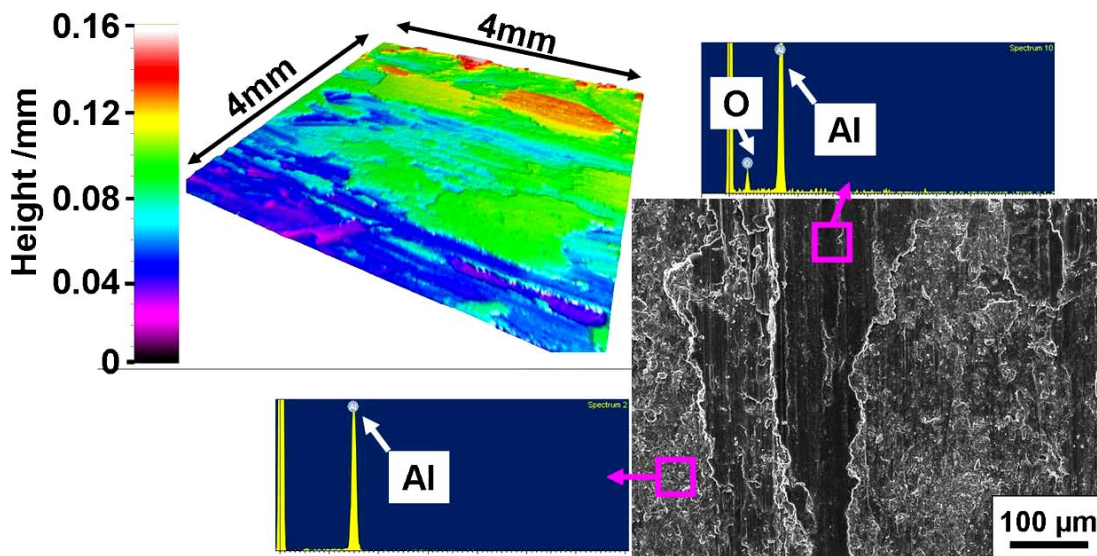
Figure 4-10 Three-dimensional analysis and EDS analysis of the worn surface of a 8 passes ECAP processed sample after wear test using a load of 5 N.

4.3 Discussion

Al and its alloy have unique properties such as low density, high thermal conductivity, high electric conductivity, good corrosion resistance and high strength to weight ratio [233]. Therefore, Al alloys have been extensively used in many areas from civic engineering to automobile, electric engineering and aircraft applications. SPD processing made Al and its alloys even more attractive as extensive studies showed that the strength of Al alloys were significantly improved after SPD processing [19, 64, 234].

The results of this study provide useful information on the wear characteristics of an Al-1050 alloy processed by ECAP to produce exceptional grain refinement.

Processing by ECAP increases the hardness of the material, and it leads to little or no change in the coefficients of friction when wear testing under two different loading conditions of 5 N and 23 N. There is a transfer of material to the counter surface during testing and there is also a very significant mass loss when using the higher load of 23 N. Studies on the debris, worn surfaces and wear rate all indicated that under these two load conditions, a severe platelet wear mode played a dominate role. With higher hardness, the ECAP processed materials had higher mass loss than the as received material, which appears to be inconsistent with the conventional Archard relationship given in Eq. 2-13.

The development of wear mechanism maps was the first attempt to delineate wear processes in a simple pictorial form [152] and to provide information that may be correlated with observed transitions between different wear processes [235]. The maps were developed using the following relationships for the normalized pressure at the sliding interface, $\widetilde{F}$, and the normalized velocity, $\widetilde{V}$, where the latter corresponds to the sliding velocity in wear divided by the velocity of heat flow [124] :

$$\widetilde{F} = \frac{L}{A_n H_0} \tag{Eq.2-26}$$

and

$$\widetilde{V} = \frac{v \times r_{cont}}{a_{therm}} \tag{Eq.2-27}$$

Where L is the normal force (N), A_n is the nominal contact area (m^2); H_o is the room temperature hardness (N m^{-2}), v is the sliding speed (m s^{-1}), r_{cont} is the radius of the nominal contact area and a_{therm} is the thermal diffusivity. Subsequently, this approach was used to develop a dry sliding map for aluminium and its alloys [155] and the result is shown in Figure 4-11where the normalized pressure is plotted logarithmically against the normalized velocity. The wear map was produced through an extensive literature survey and it is widely used as a guidance tool for predicting wear mechanisms. As in the wear mechanism map [155], the dashed lines delineate transitions between the different wear mechanisms and each separate wear mechanism is dominant within the designated area.

Calculations suggest the orders of magnitude values in the present investigation are $\tilde{F} \approx 10^{-4}$ since there is little difference in the hardness values for the different samples and $\tilde{V} \approx 10$. Therefore, inserting these values onto the wear mechanism map in Figure 4-11 leads to the lower oval designated contact (A) which suggests the occurrence of an oxidation-dominated wear for the two loading conditions used in this study. However, this is not consistent with the flake-like debris shown in Figure 4-6 and Figure 4-7 and the clear evidence for severe wear mechanism.

The wear mechanism was much more severe than expected, there are mainly two reasons. Firstly, in this test, the hardness of the pin material was higher than the disc material; this wear system often results in a more severe wear mode [236]. Secondly, During the initial time of sliding, the true contact area is initially smaller than the theoretical contact area due to the nature of the two surfaces [237]. Under the load of 5 N, the contact stress of the connecting areas will be higher than initially expected and this suggests the true contact stress is probably close to the upper oval in Figure 4-11. For these testing conditions, it is therefore reasonable to anticipate the occurrence of severe adhesion wear mechanism. Thus, during this initial period the surface of the softer material becomes significantly deformed and this generates extensive debris by adhesion such that the mass loss measured in Figure 4-5 is experienced primarily in this initial period.

As the test continues, black particles which contains high fraction of oxygen were produced, these particles generated spread over the sliding surface and may cause a decrease to the wear rate [228, 229, 238]. Until now, there is confliction on the formation procession of these fine black particles. The fine black particles might be produced by a complex mechanical alloying process [238], or they may be a hydroxide or similar high-oxygen content phase [239, 240]. As the total test duration used in this test was not quite long, the size and the amount of the small black debris are not comparable to the plate-like debris, so the total mass loss was still mostly caused by the loss of plate-like debris.

The dimensional wear coefficient, k, is widely used to compare wear rate in different classes of materials. Calculation suggests that, under the load of 23 N, the

dimensional wear coefficient of 4 passes ECAP processed sample is $\sim 4.1 \times 10^{-6}$ mm^2 N^{-1}; while under the load of 5 N, the dimensional wear coefficient of 4 passes ECAP processed sample is $\sim 3.8 \times 10^{-6}$ mm^2 N^{-1}; That means, although evidence of mild wear was observed under the load of 5 N, the wear was still dominated by severe wear mechanism, as it had the wear rate higher than 10^{-8} mm^2 N^{-1} [238].
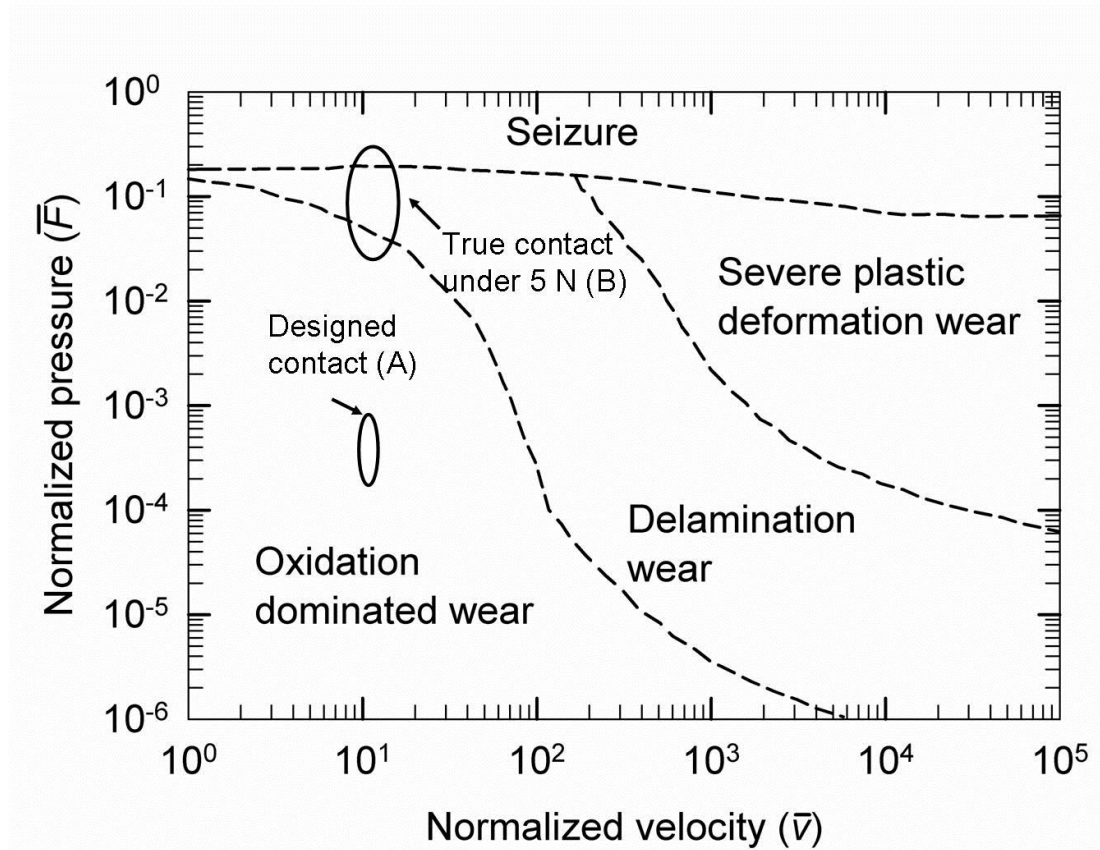
Figure 4-11 A wear mechanism map for aluminium and its alloys [155] showing the apparent designated area for the current wear tests at A and the corrected area at B when incorporating additional information concerning the wear process.

Finally, it is necessary to address the apparent disagreement with the Archard relationship given in Eq.2-13 since processing by ECAP leads to a higher hardness but also, as shown in Figure 4-5 for the samples tested under a load of 23 N, to an increase in the mass loss with increasing numbers of passes in ECAP. This decrease in the wear resistance after processing by ECAP is consistent with very recent studies of Al-1100 and Al-5052 alloys processed by ARB [196, 241], where the lower wear resistance was attributed to the lack of significant strain hardening in the alloys subjected to SPD processing. This conclusion is in agreement with the present results and it is further supported by a recent experimental observation, in which the strain hardening capacity of an aluminium alloy is exhausted after two passes of ECAP

[242]. This apparent discrepancy with the Archard equation is explained in part by the nature of the microstructure introduced by the ECAP process since processing by ECAP leads not only to a refined grain size but also to an increase in both the average grain boundary misorientation angle and the total fraction of high-angle boundaries with increasing numbers of ECAP passes [23, 224]. These microstructural changes are not incorporated into Eq. 2-13 but in practice they appear to account for the increased mass loss after larger numbers of ECAP passes.

4.4 Summary

An Al-1050 alloy was processed by ECAP leading to a refined microstructure and increased hardness. Samples processed by ECAP were subjected to wear testing under loads of 5 N and 23 N.

1.   ECAP refined the microstructure of Al-1050 gradually with increasing number of ECAP passes, and microhardness of Al-1050 was increased by ECAP processing. A saturation of hardness of Al-1050 reached at 4 passes of ECAP processing.

2.   The samples processed by ECAP have similar coefficients of friction to the unprocessed alloy at least for the two loading conditions used in this investigation but the ECAP processing leads to a decrease in the wear resistance and the mass loss increases with increasing numbers of ECAP passes.

3.   The results suggest that the wear tests under both loads were dominated by severe wear mechanism The decreasing wear resistance after ECAP is due, at least in part, to the loss of ductility caused by ECAP processing.

5. Reciprocating wear test of Al-1050 alloy processed by HPT

The present investigation was designed to study the wear behaviour of HPT-processed Al-1050 alloy sliding against SS316 stainless steel after processing by HPT. After HPT processing, the dry sliding wear behaviour of HPT-processed material was compared with the as-received material using TE77 wear tester, the same as used in Chapter 4. Following testing, the debris and worn surfaces were examined by SEM and EDS to identify the nature of the wear mechanisms.

5.1 Experimental procedures

The Al-1050 alloy was used in this study, the same as Chapter 4. HPT processing of the Al samples was performed under a pressure of 6 GPa for 2, 5, 7 revolutions.

Flat-on-flat dry sliding wear testing was conducted on both the as-received alloy and the HPT-processed alloy using TE77 high-frequency reciprocating test rig. Wear testing were performed at a temperature of 20 ± 2°C and under a relative humidity of 55 ± 5%. Before the wear test, each sample was mechanically ground to 4000-grit SiC paper and then washed in acetone in an ultrasonic bath for 15 minutes. Prior to wear testing, the average surface roughness was about 0.7 μm. As the HPT-processed samples were quite small, these disc samples with 10 mm diameter were stuck to a flat-ended pin and slid against a counter surface made of 316 stainless steel (~330 Hv) giving a contact area of about 78 mm^2. The edge of the pin surface was rounded. The pin was pressed and driven by an indenter during sliding where this design was used to inhibit edge cutting. During testing, the stroke length of the oscillating motion was ~8.9 mm and the reciprocating frequency was 1 Hz which gave an average sliding velocity of 17.9 ± 0.1 mm s^{-1}.

5.2 Results

The microhardness of Al-1050 processed via HPT was measured cross the diameter of each disc, the average hardness were plotted against the distance from the centre.
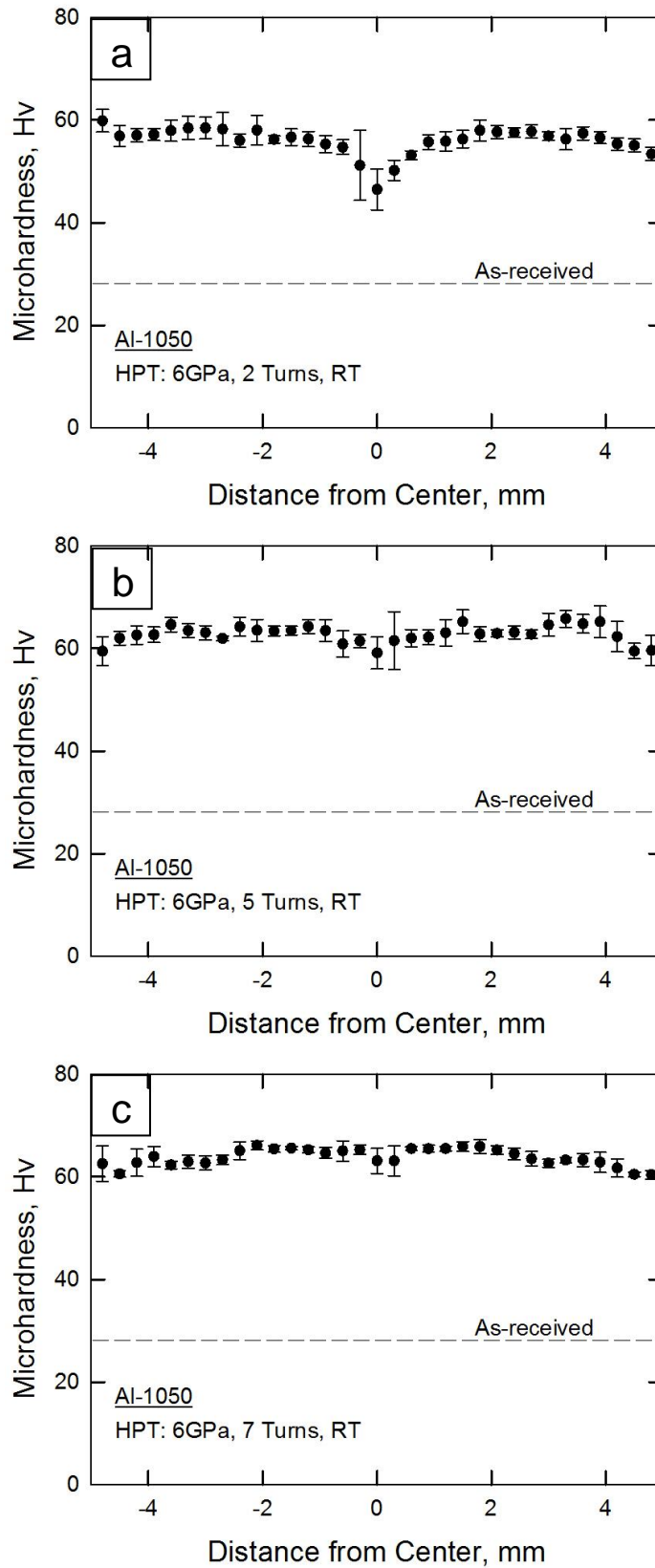
Figure 5-1 Variation of the average microhardness with distance from the centre after processing by HPT after (a) 2, (b) 5 and (c) 7 revolutions.
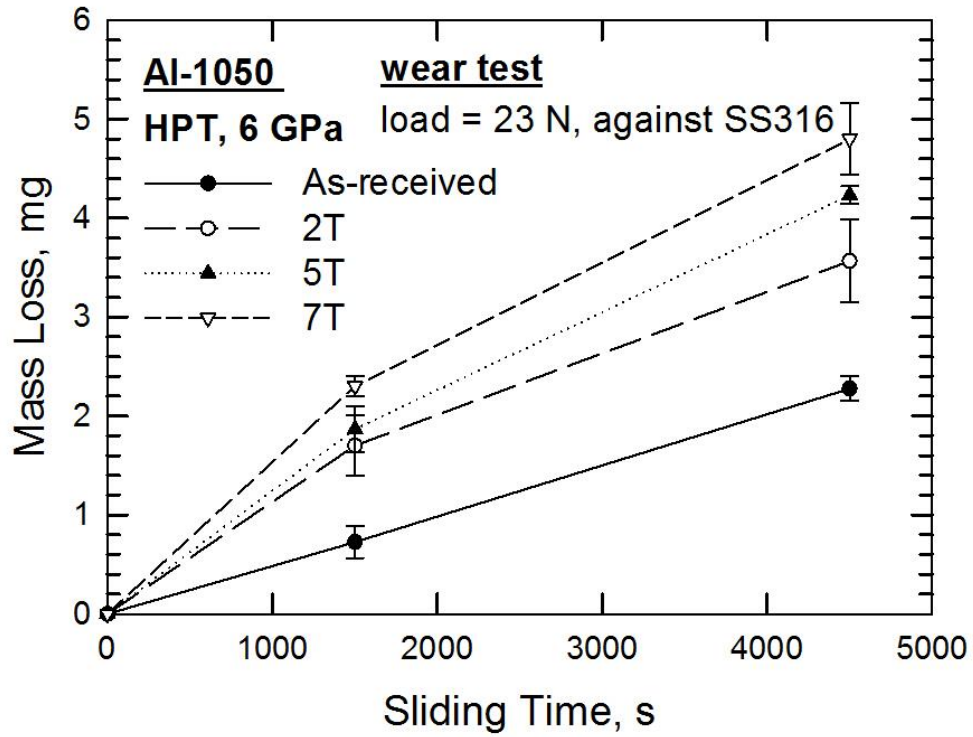
Figure 5-2 Mass loss of as-received and HPT-deformed samples versus siding time under load of 23 N.
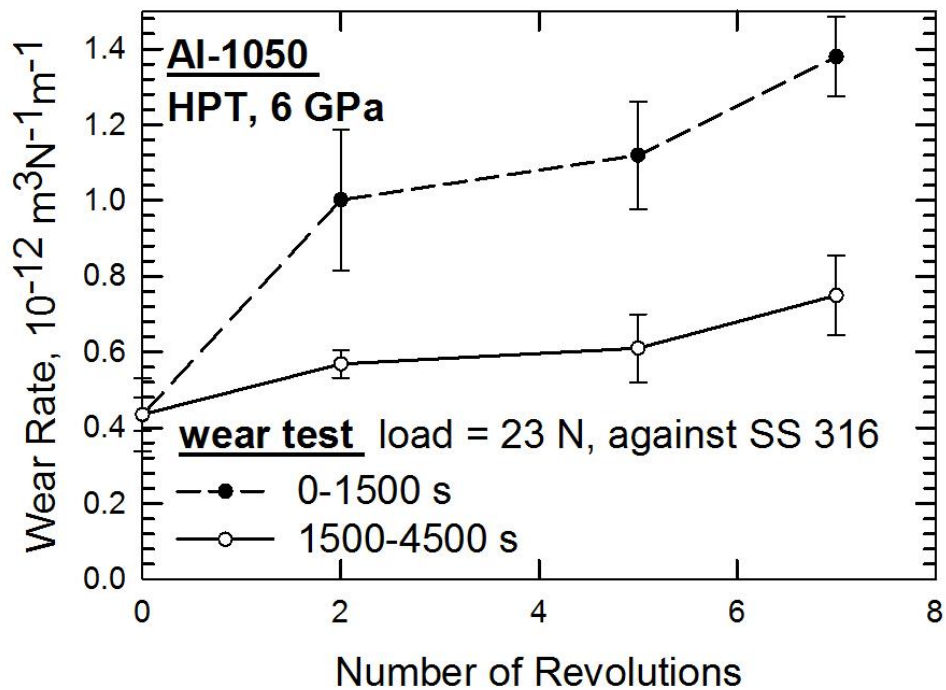
Figure 5-3 Wear rate of as-received and HPT-deformed samples versus HPT revolutions during different periods under 23 N.

As clearly shown in Figure 5-1, the microhardness of Al-1050 was improved significantly after HPT processing, from about 27 Hv to more than 60 Hv after 5 or 7 revolutions of HPT straining. Figure 5-1 also showed the evaluation of hardness homogeneity of Al-1050 though HPT processing. The Al-1050 achieved a reasonable homogeneous microhardness after 2 turns HPT processing, except the centre area which showed a much lower hardness that most of the sample, shown in Figure 5-1 (a). As reported earlier, a reasonably homogeneous hardness of aluminium can be obtained after 2 revolutions of HPT [190]. The hardness of Al-1050 was homogenous across the whole disc after 5 turns of HPT processing, as shown in Figure 5-1 (b).

Wear testing of the HPT processed samples were performed under a load of 23 N against SS316, the tests lasted 1500 s initially and were followed by a further 3000 s. In general, the mass loss of the HPT-deformed samples increased with the number of HPT revolutions. The mass loss and average wear rate of each sample versus sliding periods is demonstrated in Figure 5-2 and Figure 5-3. Similar to the ECAP-processed samples studied in Chapter 4, the HPT-processed samples had higher wear rate than the as-received sample, especially during the first 1500 s. During the following 3000 s, the wear rate of all samples decreased but the difference between each sample was negligible.

The wear surface of Al samples also showed evidence of two mechanisms. As shown in Figure 5-4, the wear surface of as-received Al-1050 (Figure 5-4(a)) and the HPT processed sample (Figure 5-4 (b)) are made up by two areas: the grey area and a dark area. Such wear surface was similar to that of Chapter 4. The grey area was formed when the plate debris detached form the surface, it was actually the pure aluminium exposed outside. The dark area was formed during the oxidation wear mechanism as the fine aluminium oxide was travelling on the wear surface and led to a polishing effect to this area.
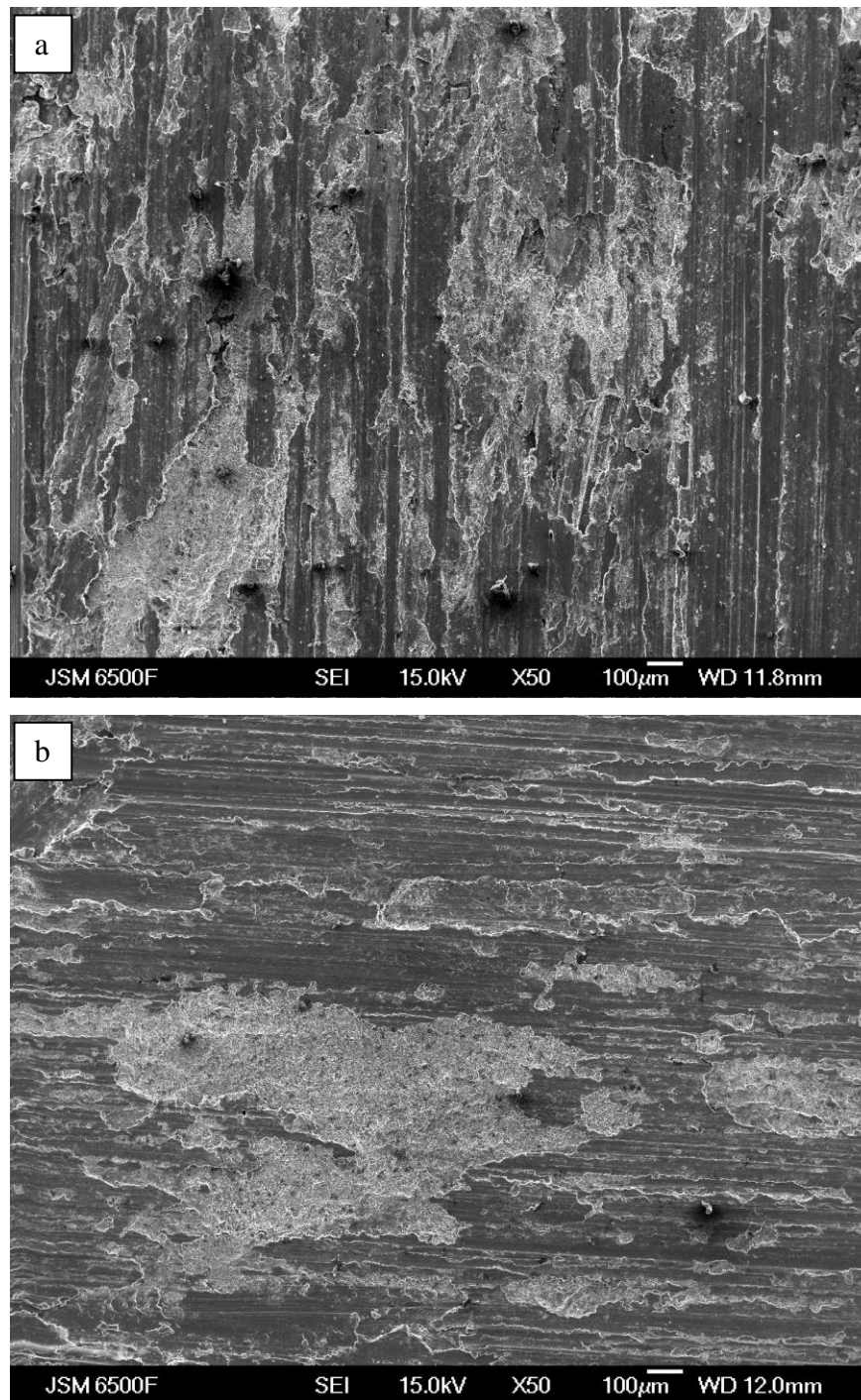
Figure 5-4 Wear surfaces of (a) as-received sample and (b) 5 revolutions HPT processed sample.

According to the debris study shown in Figure 5-5(a), during the first 1500 s the wear debris was a mixture of large plate-like debris and some finer particles. During the following 3000 s, only fine particles with sizes smaller than 10 µm were observed in Figure 5-5 (b). This means the wear procedure changed from a severe platelet mechanism to a mild complex oxidative wear mechanism. In Figure 5-5 (b),

99

some iron elements were detected in the wear debris, which were transferred from the steel counterpart during abrasive effects.
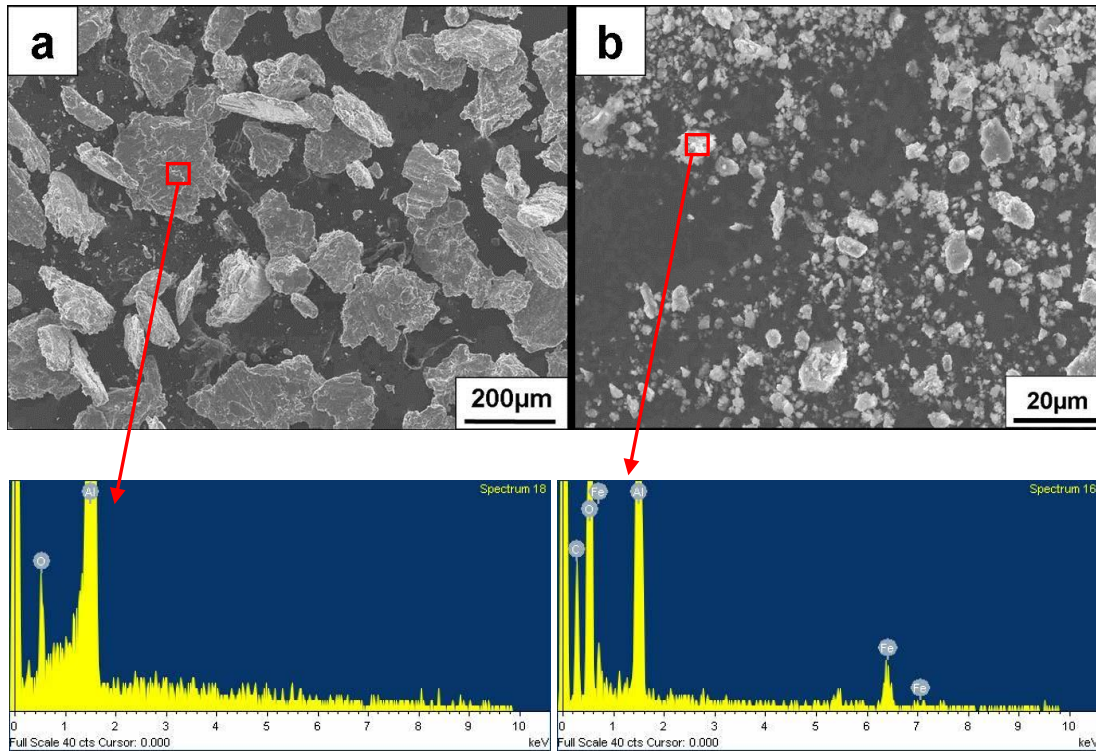
Figure 5-5 Wear debris of 5 revolutions HPT-deformed sample collected in different wear stages: (a) 0-1500 s, (b) 1500-4500 s.

Furthermore, records of the coefficient of friction also indicated a transformation of wear modes, as shown in Figure 5-6 to Figure 5-9. During testing, the coefficient of friction of all the samples became steady after a short unsteady period. It is worth pointing out that the as-received sample undertook an unsteady period of about 200 s (Figure 5-6) while all the HPT processed samples took a much longer period, for instance the 5 revolutions deformed sample undertook this period of about 750 s (Figure 5-8).
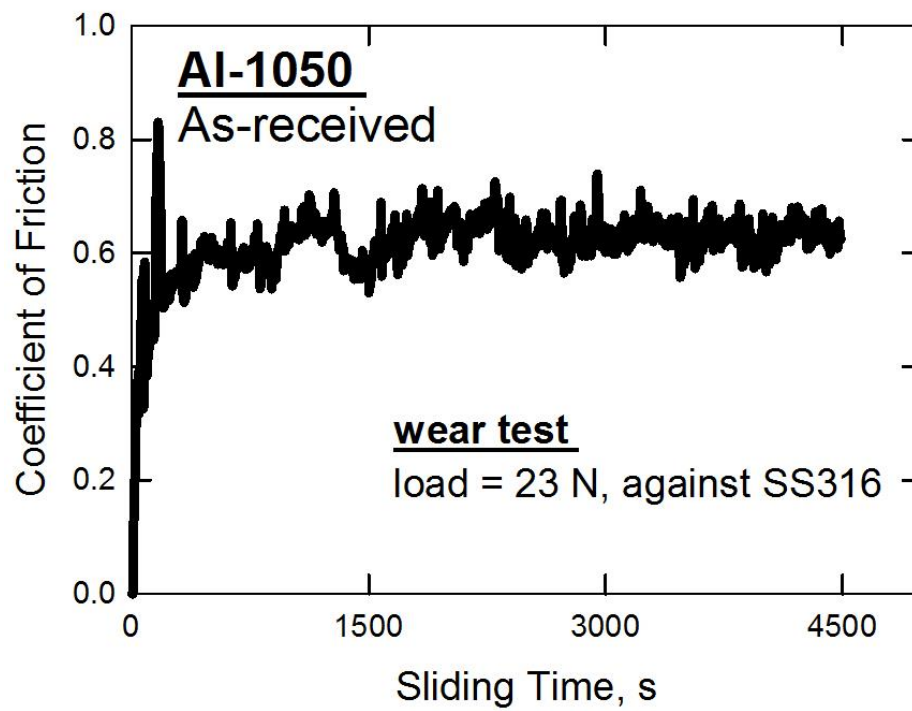
Figure 5-6 Coefficient of friction versus sliding time of as-received Al-1050.
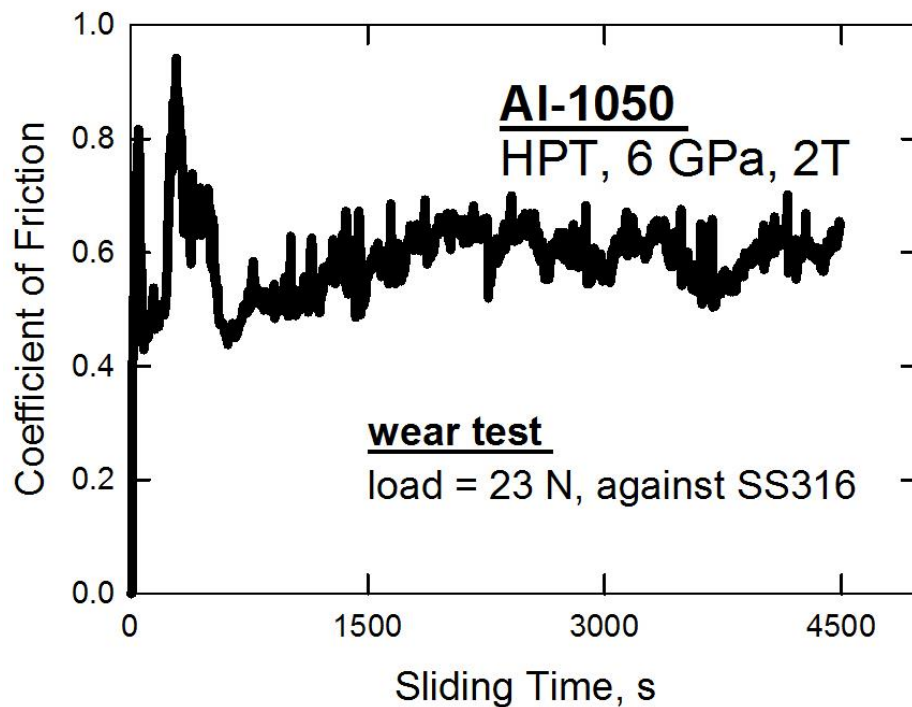
Figure 5-7 Coefficient of friction versus sliding time of Al-1050 after HPT for 2 turns.
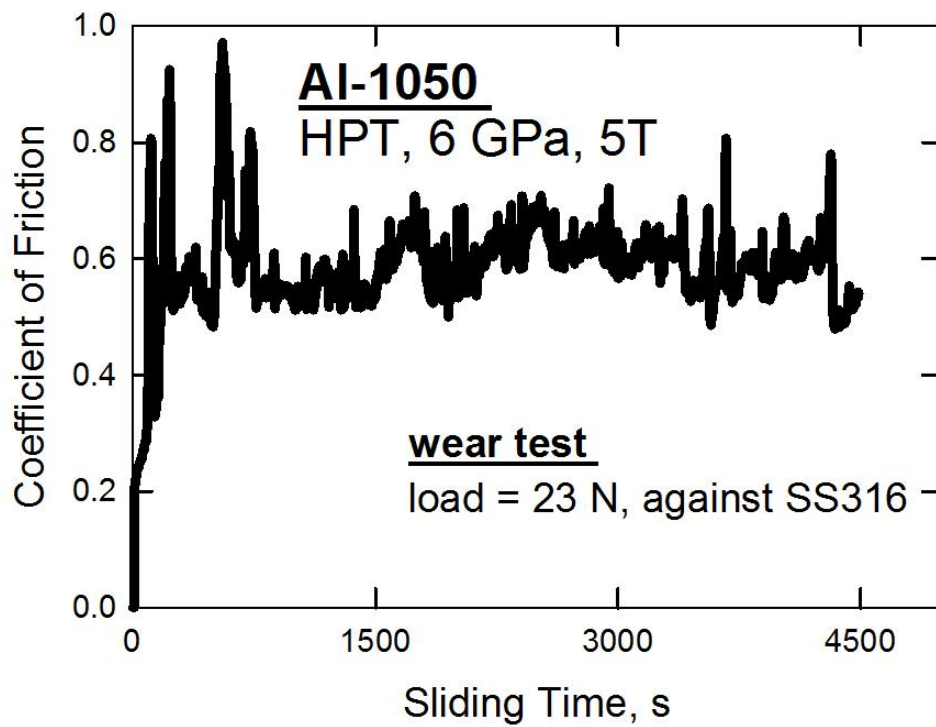
Figure 5-8 Coefficient of friction versus sliding time of Al-1050 after HPT for 5 turns.
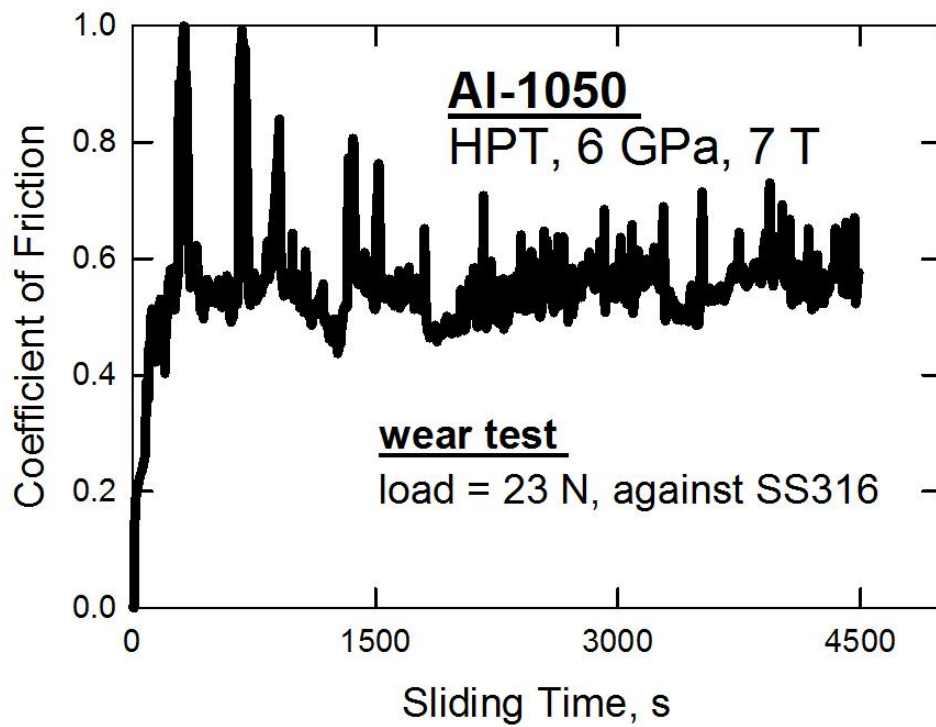
Figure 5-9 Coefficient of friction versus sliding time of Al-1050 after HPT for 7 turns.

5.3 Discussion

The results in Chapter 4 demonstrated that ECAP processing decreased wear resistance of Al-1050. Operating of severe wear mechanism and oxidation wear mechanism were observed. In the sliding tests of Chapter 4, bronze pins were sliding against Al-1050 plates. Although the contact pressure was designed to be very low, the wear showed very severe damages. According to previous wear studies of Al, using steel as the counter material promotes the operation of oxidation wear and leads to a slower wear damage [229, 239, 243]. Therefore in Chapter 5, the aluminium samples were made into pins sliding on the surface of steel. These designs were aimed to control the wear in a healthier oxidation wear mechanism with lower wear rete.

In addition, HPT processing was used to refine the microstructure of Al-1050, as it is widely reported that HPT processing is more effective in refining grains size of materials compared to ECAP. Furthermore, HPT processing was employed to get a more comprehensive understanding on the relationship of wear resistance and SPD processing.

Different materials were used as the counter parts in Chapter 4 and 5. Therefore, the wear rates of samples from Chapter 5 are not comparable with Chapter 4, as the wear testing was performed with many differences. Although the aluminium was processed using different SPD methods, and the wear testing was performed with different designs, the tests showed the same trend that SPD processing reduces the wear resistance of Al-1050.

Study in this chapter further confirms the transition from severe platelet wear to oxidation wear of Al-1050 which was observed in Chapter 4. As shown in Figure 5-5 (a), mixed debris was observed initially, and only fine debris was produced as the wear test carried on at the later stage, as shown in Figure 5-5 (b). Even during the oxidation wear region, the HPT-processed samples had slightly higher wear rate than the as-received Al, this might indicate a higher oxidation rate of HPT-processed Al and still need further investigation. As shown in Figure 5-6 to Figure 5-9, the COF

for all samples was unsteady during initial period of wear test which may corresponding to operation of severe platelet wear, afterwards wear was dominated by oxidation wear which had a steady COF. During the severe wear stage, COF was unsteady with some points having a very high COF value, which may be related to producing of large flake debris. The longer time of wear mode transition of HPT-processed sample is probably caused by the lack of work hardening capacity [186, 196].

5.4 Summary

An Al-1050 alloy was processed by HPT leading to an increased hardness. Samples processed by HPT were subjected to wear testing under loads of 5 N and 23 N.

1.   HPT processing improved hardness of Al-1050 to more than 60 Hv after 2 turns of processing. The hardness of Al-1050 became saturated across the disc after 5 turns of straining.

2.   The samples processed by HPT have similar coefficients of friction of 0.6 to the as-received alloy at least for the two loading conditions used in this investigation. HPT processing leads to a decrease in the wear resistance and to a mass loss that increases with increasing numbers of HPT turns.

3.   The transformation of wear mechanism from severe platelet wear to oxidative wear was observed for all the Al-1050 samples. UFG Al-1050 needed a longer duration for this transformation which led to larger amount of plate debris and higher wear loss.

6. Micro-scratch testing of pure titanium processed by HPT

This chapter investigates the micro-wear behaviour of commercial pure Ti processed by HPT and makes comparisons with as-received and annealed Ti. Firstly, the Ti samples were HPT processed under 3 GPa for up to 10 turns to achieve a homogeneous microstructure. The microstructure homogeneity was studied by testing microhardness of the Ti samples along the diameter of the disc. The tribological behaviour of Ti sample with different grain sizes was investigated by using micro-scratch testing and compared in a micro-contact scale.

6.1 Experimental procedures

A CP titanium alloy (Grade 2) was used in this investigation. Prior to micro-scratch testing, some of the materials were subjected to HPT processing. HPT processing was performed under a pressure of 3 GPa for 1, 5 and 10 revolutions. After HPT processing, some 10 turns HPT processed samples were annealed at a temperature of 500 °C for 10 minutes in order to study the effect of grain size on wear behaviour of Ti.

After HPT processing, all the samples including the as-received samples were prepared with 4000# SiC abrasive papers followed by polishing with 1 μm diamond paste which gave average roughness R_a of 15±5 nm for each sample. After cleaning with acetone, the samples were conducted to micro-scratch testing under a load of 100 mN and 200 mN for 1, 2, 5, 10, 50, 100, 200 turns. Scratch tests were performed at room temperature of 18 ± 2 °C and a relative humidity of 50 ± 5%. A diamond indenter with radius of 200 μm was used to create micro-scratch of 2 mm length on the disc surface. The testing area was located between 2 mm to 4 mm away from the centre of the discs. The indenter carried out a reciprocating movement on sample surface with a speed of 0.1 mm/s.

Specimens were tested in tension using an Instron testing facility at room temperature with an initial strain rate of 1.0×10^{-2} s^{-1}. The Vickers microhardness was measured using a test weight of 1000 g and a dwell time of 15 s. The microstructure of the samples was investigated by optical microscopy (OM) and TEM. The microstructures of the worn surfaces were analysed by SEM. The worn surface profiles were recorded using IFM.

6.2 Results

Figure 6-1 shows the microhardness measured along randomly selected diameter of Ti samples processed by HPT for 1, 5 and 10 turns. The lower dashed line in each figure indicates the average hardness of pure Ti at as-received state, which is about 183Hv. As shown in Figure 6-1 (a), the microhardness of Ti was very inhomogeneous after 1 turn of HPT processing. The hardness of the centre area was close to 200 Hv, which was much lower than the rest of the disc. After 5 turns of HPT processing, the hardness of the edge increased to around 300 Hv, while the centre hardness increased to 220 Hv, shown in Figure 6-1 (b). The microhardness appeared to be reasonably homogeneous cross the disc samples after 10 turns of torsion straining as shown in Figure 6-1 (c), which was also reported by other investigations performed on CP Ti [2, 244].

Microstructure of each sample was shown in Figure 6-2. The grain size of Ti at as-received stage was about 8.6 ± 0.6 µm (Figure 6-2 (a)). After HPT processing, large internal stresses were observed inside grains by showing extinction contours and the grain boundaries were not well defined. Both bright field image and dark field image were taken to estimate grain size (Figure 6-2 (c, d)), in which the average grain size of HPT-processed sample was around 130 nm, which is similar to previous reports [74, 97]. Some of the UFG samples were annealed at 500 ºC for 10 minutes after HPT processing. The grain boundaries became much better defined with some recrystallization in which some grains had diameter larger than 1 µm becoming visible (Figure 6-2 (b)). The average grain size of annealed sample was about 607 ± 54 nm. The microhardness of Ti increased from 183 Hv to about 305 Hv after HPT processing, and reduced to about 256 Hv after annealing due to the recrystalization that occurred during annealing.
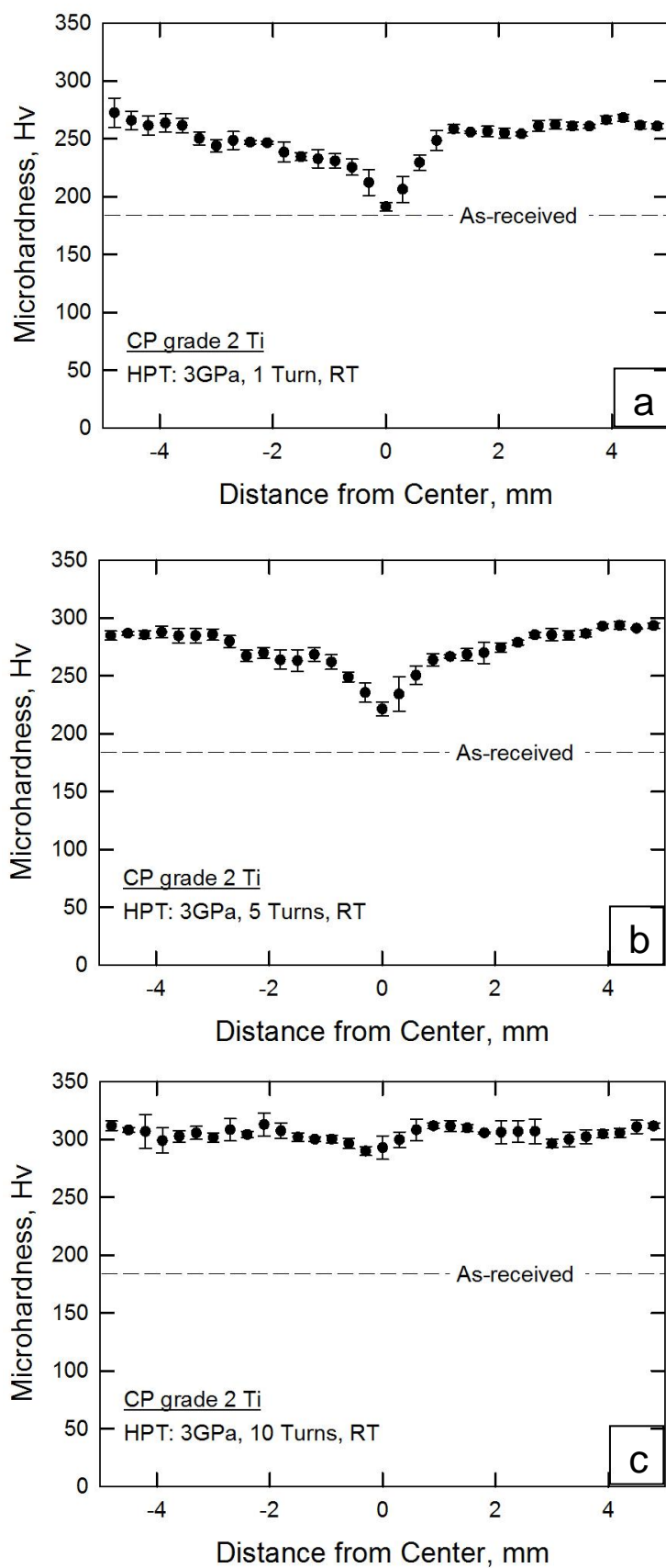
Figure 6-1 Variation of the average microhardness of Ti with distance from the centre after processing by HPT after (a) 1, (b) 5 and (c) 10 revolutions.
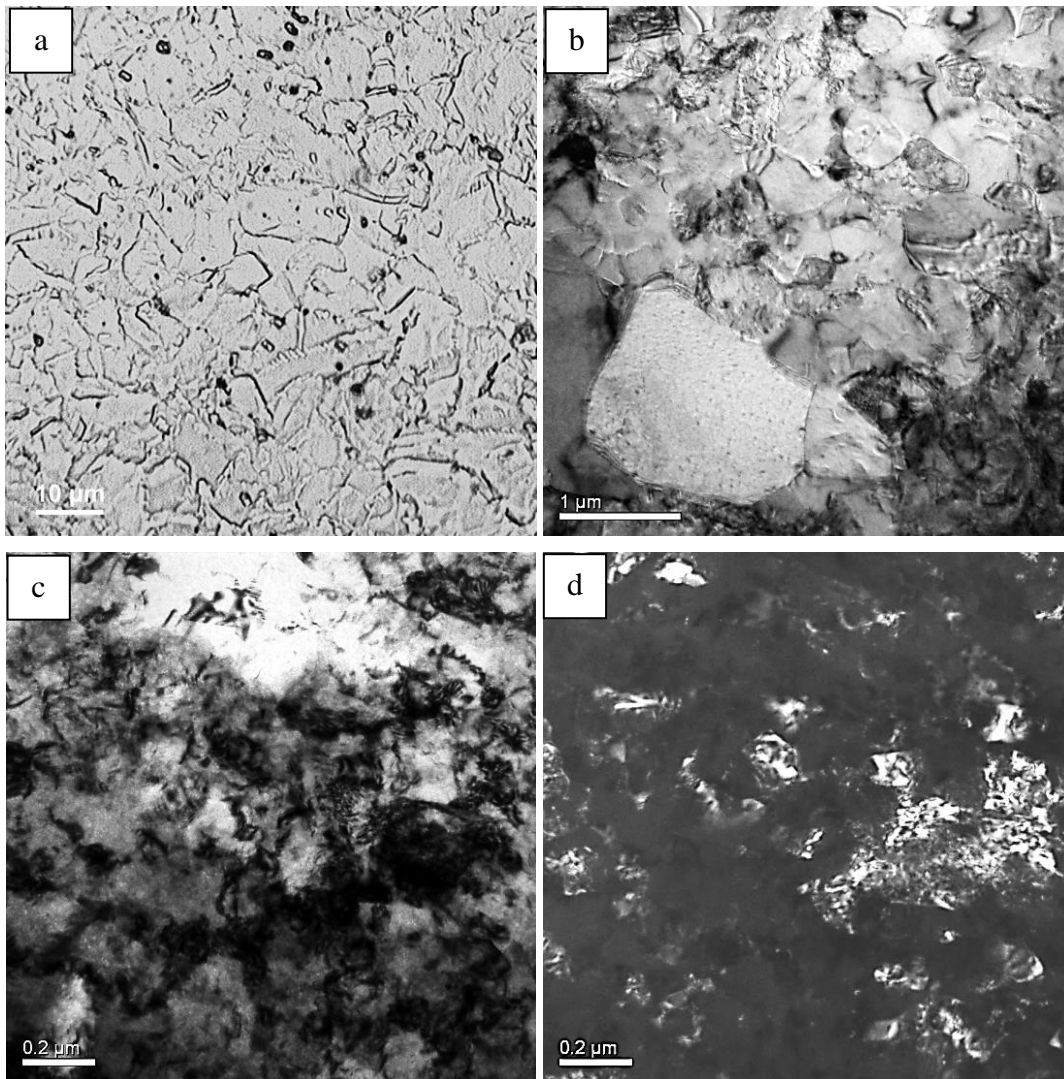
Figure 6-2 Microstructure of titanium: (a) as-received, (b) HPT-processed followed by annealing at 773K for 10 mins, (c) bright field TEM image of HPT-processed Ti, (d) dark field TEM image of HPT-processed Ti.

The tensile curves shown in Figure 6-3 demonstrate that the UTS of Ti increases from ~660 MPa in the as-received state to ~940 MPa after 10 revolutions of HPT but the elongation to failure decreases from ~40% to ~23%. This combination of high strength and reasonable ductility in Grade 2 CP Ti after HPT processing makes the UFG pure Ti compatible with the Ti-6Al-4V alloy where the UTS is ~980 MPa and the elongation to failure is ~14%. Details including grain sizes and mechanical properties of the Ti samples are listed in Table 6-1.
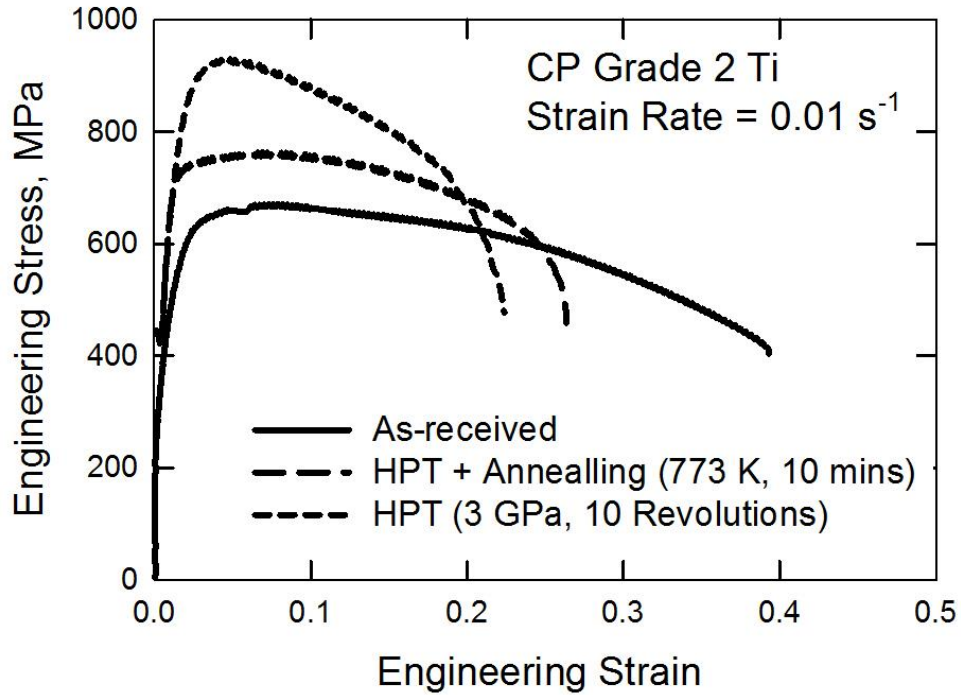
Figure 6-3 Tensile curves of different Ti substrates.

Table 6-1 Grain size and mechanical properties of Ti

	Grain size, μm	Microhardness, GPa	UTS, MPa	Elongation to failure, %
As-received	8.6 ± 0.6	1.83	660	40
HPT + annealing	0.61 ± 0.05	2.56	780	27
HPT 10 turns	0.13 ± 0.02	3.05	940	23
Ti-6Al-4V	N/A	3.09	980	14

The COF of each sample under load of 200 mN is shown in Figure 6-4. It is observed that the friction of samples was unsteady and independent with grain size. The average coefficient of friction of all the samples was about 0.6, as shown in Table 6-2, which indicates grain size had almost no effect on the coefficient of friction during micro-scratch testing. Generally, the HPT processed Ti and annealed Ti had slightly higher COF than the coarse-grained Ti, and the friction levels decreased slightly with sliding time while the COF of the coarse-grained Ti remained constant. After 200 turns of scratching under a load of 200 mN, all the samples had a similar COF.

Table 6-2 Average COF of each sample under 2 load conditions

	As-received	HPT processed + annealing	HPT 10 turns
Load = 100 mN	0.59±0.01	0.63±0.04	0.62±0.03
Load = 200 mN	0.54±0.01	0.55±0.03	0.60±0.03
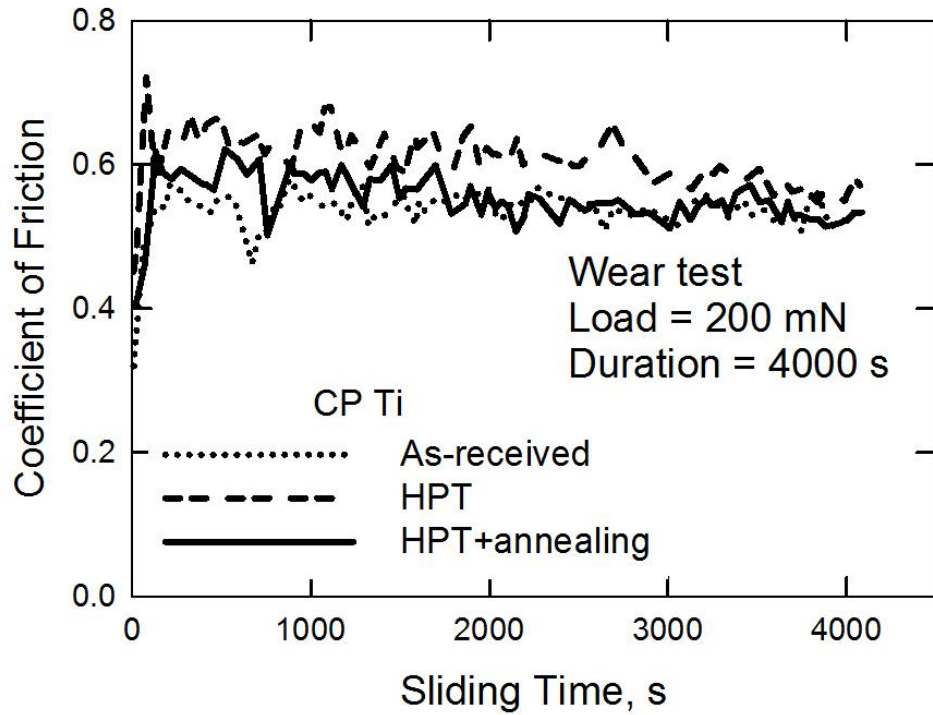
Figure 6-4 COF of each Ti sample during micro-scratch under load of 200 mN: (a)As-received sample; (b) HPT + annealing sample; (c) HPT-deformed.
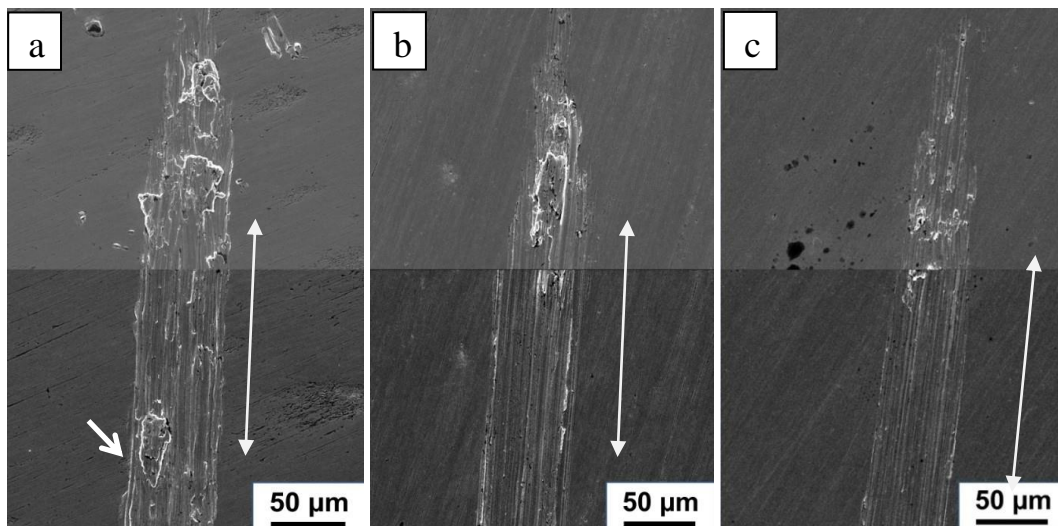
Figure 6-5 Worn scar of Ti samples after 50 turns scratch under load of 200 mN with white double arrows showing the sliding direction: (a) as-received sample; (b) HPT + annealing sample; (c) HPT-deformed sample.

The appearance of the worn surfaces for the as-received and HPT processed samples is shown in Figure 6-5, where the white double arrows indicate the sliding directions. Features on the surface were observed due to plastic deformation as materials were extruded to the end of the scratch scar from the middle; this wear mode is known as wedge formation or shear-tongue formation [134]. It is clear that shear tongues formed at the end of coarse-grained Ti as shown in Figure 6-5 (a), was much larger compared to the fine grained sample, shown in Figure 6-5 (c). Furthermore, large flake debris shown as the white arrow in Figure 6-5 (a) was observed in the wear scar of as-received sample which indicates the operating of adhesion.
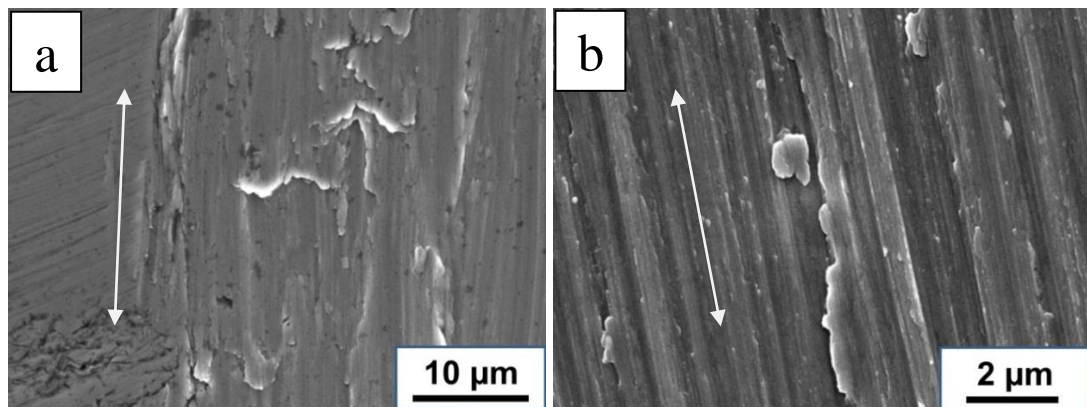
Figure 6-6 Surface appearance inside worn scar of Ti samples after 50 turns scratching under load of 200 mN: (a) as-received sample; (b) HPT-processed sample.

At higher magnification, the difference in the worn surface morphologies for the different samples can be seen. As shown in Figure 6-6(a), shear failure (fracture) was observed on the worn surface of the as-received Ti, therefore when the material near the interface was extruded by the indenter, the material undertook plastic deformation and fractured when its limit of ductility was reached. On the worn surface of HPT-processed sample, multiple grooves parallel to the sliding direction and small debris with diameter around 1 μm were observed in Figure 6-6 (b). The cross section of sub-surface damage has been studied using optical microscopy, and cannot show clear evidence of different deformation behaviour between the as-received and HPT-processed samples due to the shallow worn scar.

Figure 6-7 shows the topography of the wear scar. It is clear to see that the worn scar of as-received sample was very inhomogeneous, material was extruded from the scar and piled near the edge and formed ridges as shown in Figure 6-7 (a). On the other hand, the wear scar of the HPT-processed sample has a regular shape with depth

increasing from the edge to the middle of the scar as shown in Figure 6-7 (b). The difference between as-received sample and the HPT-processed samples was mostly caused by the different ductility of them. During the scratch testing, the surface of Ti sample was under a force of extrusion and compression. The as-received sample can be easily deformed by the indenter, so material was extruded and formed large chips, and those large chips piled up and formed the high surfaces, see Figure 6-7 (a). It is obvious in Figure 6-7 (a) that the edge of wear scar of as-received sample was higher than the normal surface, which means the ridges were formed at the edge of worn scar and this is another sign of plastic deformation during scratch test. For the HPT-processed sample, the indenter could not penetrate in to the sample as deep as for the as-received sample due to a higher strength of the UFG Ti. Furthermore, the HPT-processed sample had lower ductility, so the debris formed during scratch test was much smaller, and the worn scar showed characters of abrasive wear.
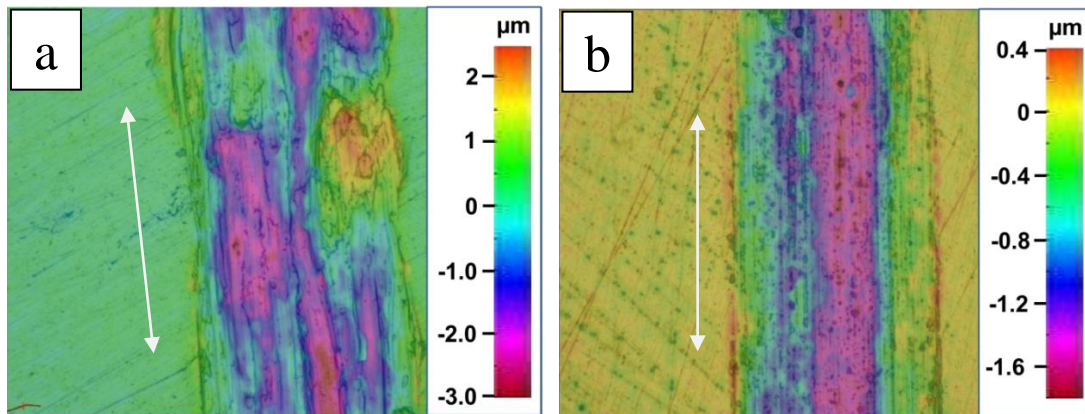
Figure 6-7 Worn scar of Ti samples after 50 turns scratch under load of 200 mN: As-received sample (b) HPT-processed sample.

Five lines scans taken perpendicular to the sliding direction were selected randomly from each wear scar, and their profiles were measured using IFM, shown in Figure 6-8. It is observed that the groove shape of the as-received sample was very different at different positions, and the groove of HPT-processed sample has much better homogenous shape. The profile of worn scar also showed signs of ploughing, especially for the as-received sample.
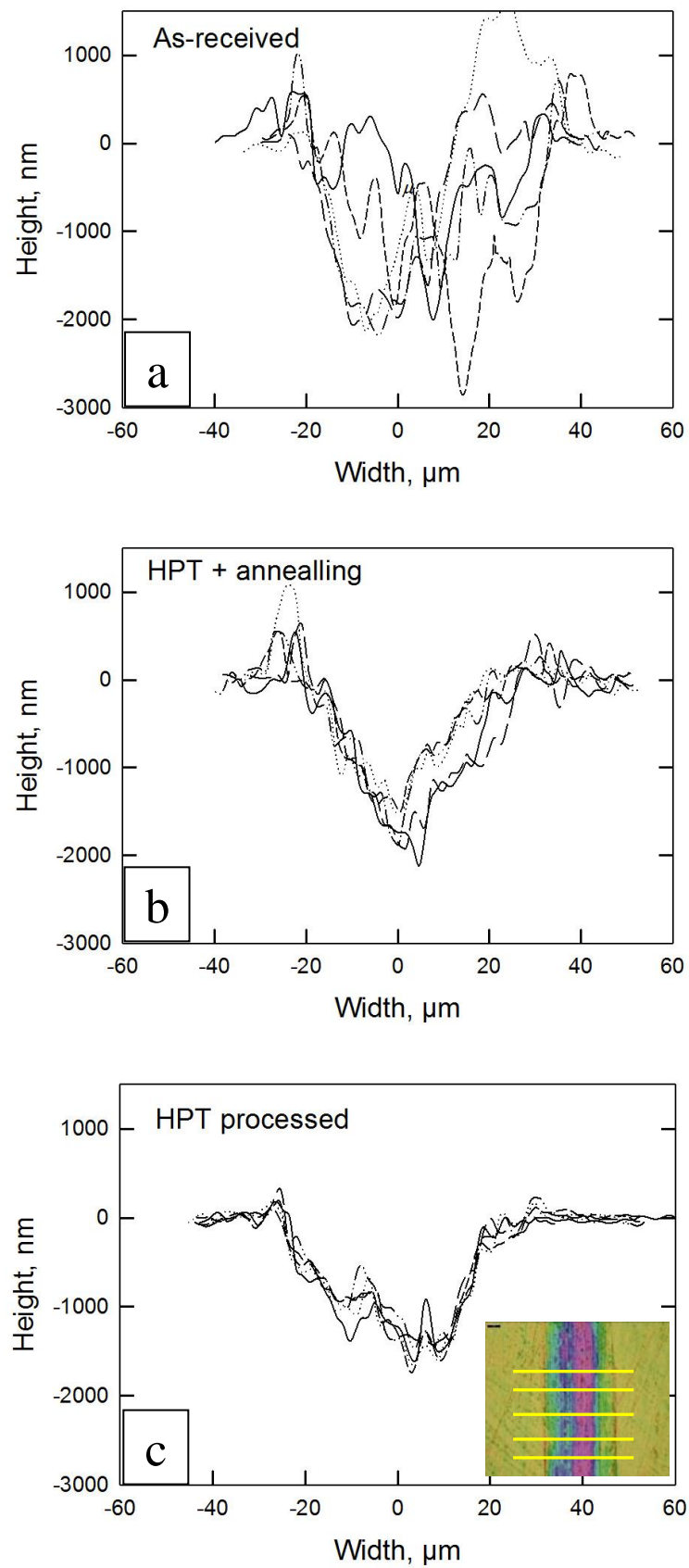
Figure 6-8 Worn scar profile of Ti samples after 50 turns scratch under 200 mN: (a) as-received sample; (b) HPT + annealing sample; (c) HPT-deformed sample.
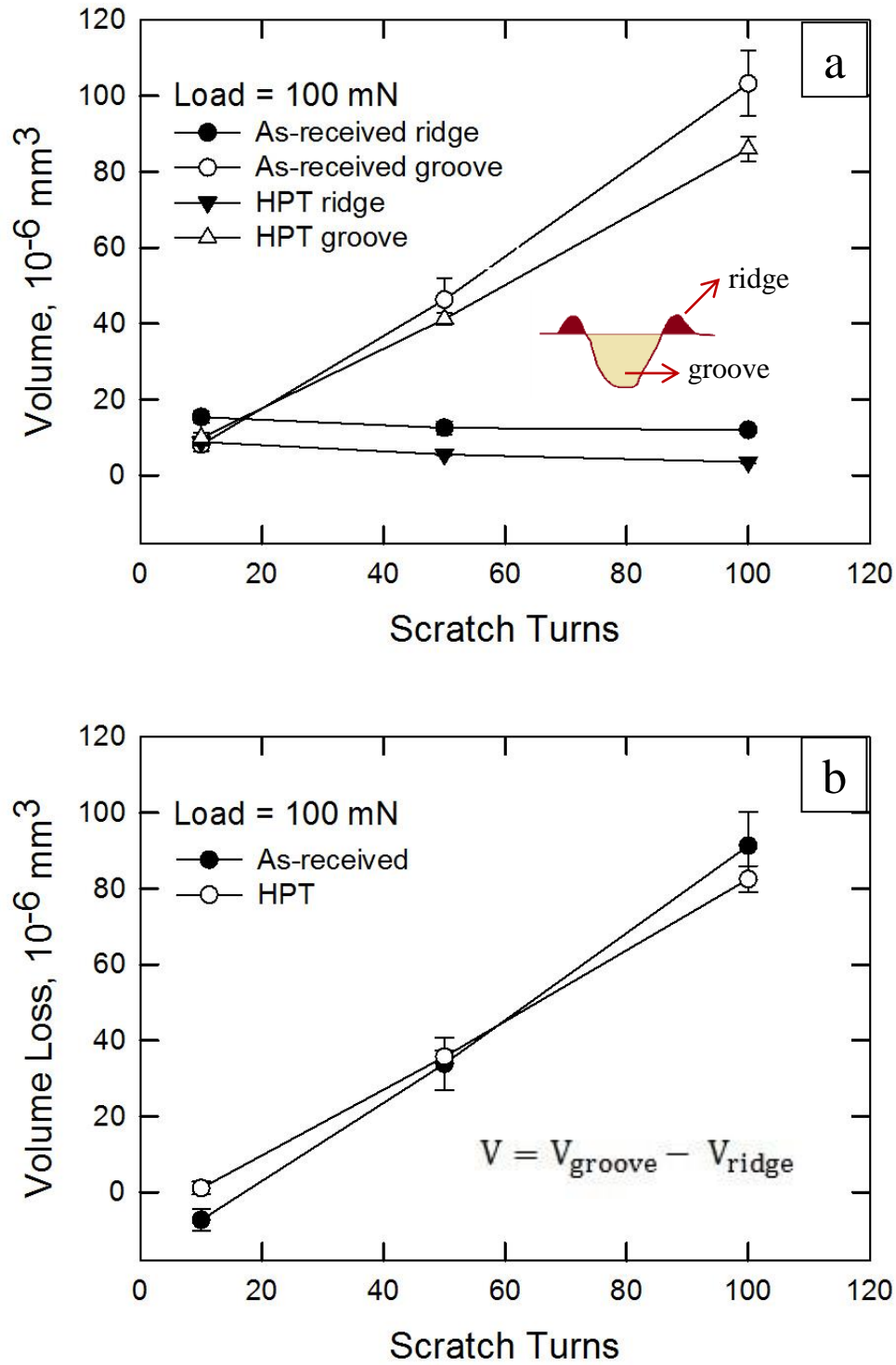
Figure 6-9 Volume loss of each sample versus number of scratch turns under load condition of 100 mN: (a) Volume of ridge (V_r) and groove (V_g); (b) Volume loss $V=V_g-V_r$
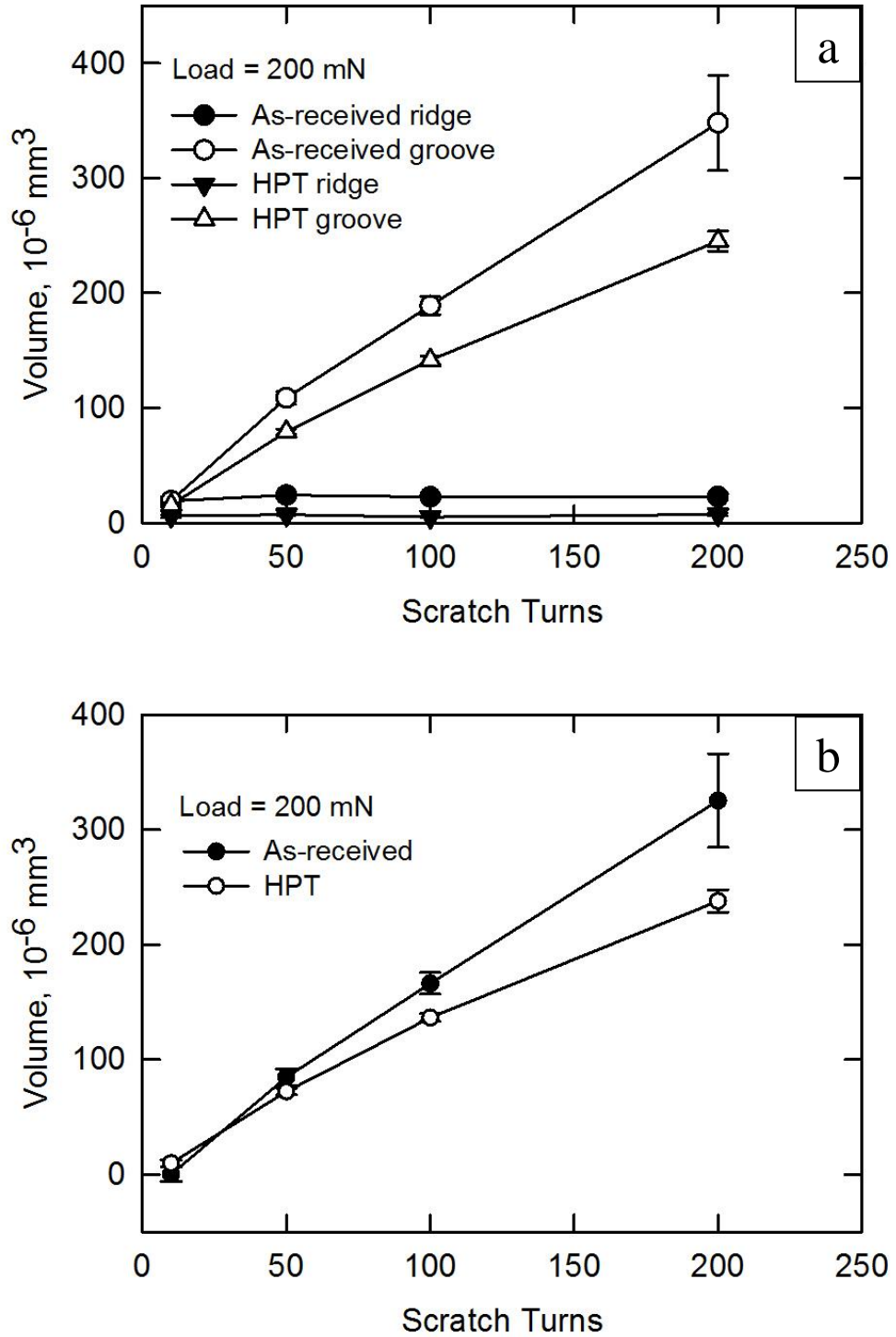
Figure 6-10 Volume loss of each sample versus number of scratch turns under load condition of 200 mN : (a) Volume of ridge (V_r) and groove (V_g); (b) Volume loss $V=V_g-V_r$.

Normally, each worn scar contains ridges and wear groove. Volume loss (V) can be defined by:

$$V = V_g - V_r \qquad\qquad\qquad\qquad\qquad\text{(Eq.6-1)}$$

Where V_g refers to the volume of worn groove below the original unworn surface, V_r refers to the volume of ridge formed above the mean surface. Volumes of these parts were measured and plotted against scratch numbers in Figure 6-9 and Figure 6-10. It was shown in these figures that the HPT-processed sample had a much smaller error scatter than as-received sample, as the ultra-fine grained sample had more homogeneous scar shape.

Based on the calculation from above Eq. (6-1), there is a minus volume loss for as-received sample under load of 100 mN when the scratch number is 10 as shown in Figure 6-9 (b), which is caused by the ploughing wear mechanism. For the coarse-grained sample, ploughing was dominated during the first several scratch turns. Therefore, the material was just extruded from the groove to the edges without falling out, so no volume loss occurred although grooves were formed. Large debris started to be detached from the sample after several scratches, which caused the volume loss of these samples started to increase. The as-received sample had deeper grooves and wider ridges, which caused a similar volume loss between as-received sample and HPT processed sample after 50 scratch turns. As shown in Figure 6-9 (a) and Figure 6-10 (a), the volume of ridge keeps constant after 10 scratch turns while the volume of groove keeps increasing with scratch turns. Therefore, when the scratching turns of testing was over 50, the trend became clearer that the HPT-processed sample had lower volume loss than CG Ti.

As clearly shown in the above results, the as-received Ti and SPD-processed Ti have different deformation behaviour during wear. The subsurface analysis for wear track was performed to investigate the plastic deformation of Ti during wear test. Initially, FIB cross section of the wear scar has been performed on the coarse-grained Ti, as shown in Figure 6-11 with white arrows showing the sliding direction. A fine grained layer with thickness of around 1.5 μm was observed under the wear scar, the grains at this region were observed having a flake shape. These results showed evidence of plastic deformation of the subsurface during wear. As the indenter was sliding on the

surface of Ti, plastic deformation of the material near up surface was dragged due to friction force. At this stage, only limited results were obtained due to limitation of accessing facilities. A more detailed study of this layer using FIB and EBSD together will provide more valuable information including grain orientation and angle of grain boundaries, which will be useful to investigate the deformation behaviour during wear of CG and UFG Ti.
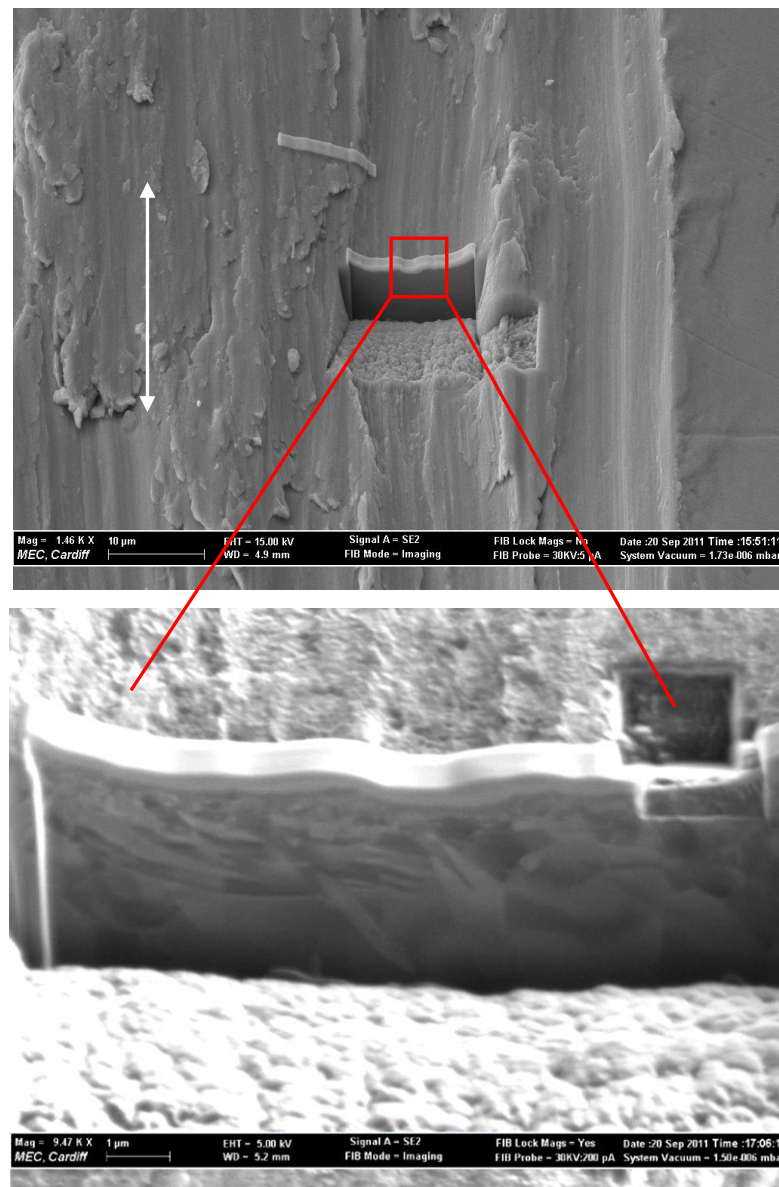
Figure 6-11 The FIB cross section and image of as-received Ti after 200 scratch turns under load of 200 mN.

6.3 Discussion

Ti and its alloys are attractive candidate materials for application from aerospace to sports and biomedical due to their high strength to weight ratio, excellent corrosion

resistance and good biocompatibility [81]. Ti alloys such as Ti-6Al-4V are most commonly used for biomedical applications, nevertheless, it is also noticeable that the alloy elements released from Ti alloys may cause long-term health problems [84, 86, 87]. Therefore, attempts have been made to produce UFG pure Ti with comparable high strength as Ti-6Al-4V and much better bioactivity [20, 104, 184, 193, 245]. Recent studies also reported the superior osteoblast cell compatibility of ultrafine-grain pure Ti substrates produced via SPD over coarse-grain pure Ti and Ti-6Al-4V substrates, which made UFG pure Ti even more attractive for biomedical applications [104, 105].

In this chapter, HPT processing was employed to refine grain size of CP Ti to around 130 nm, and the strength of the material was also improved significantly. The results from this investigation demonstrate that processing by HPT is effective in refining the microstructure of pure Ti and achieving a good combination of high strength and reasonable ductility. It worth pointing out that the hardness of HPT-processed CP Ti of this study (~305 Hv) is very close to the hardness of Ti-6Al-4V (~ 309 Hv), which indicates the possibility of using UFG Ti to replace Ti-6Al-4V for biomedical applications in the future.

The information at present available on the microstructures and mechanical properties of pure Ti processed using various SPD methods, including post-processing, are summarized in Table 6-3. From Grade 1 to Grade 4 Ti, the level of impurities increases with the grade number so that the strength of Grade 4 is generally the highest. From grade 1 to grade 4, impurities such as Fe, N and O in Ti alloy increase so that grade 4 Ti normally has the highest strength and lowest ductility. The data in Table 6-3 demonstrates the possibility of achieving various mechanical properties by combining different SPD methods with additional rolling and/or heat treatments. By comparison with ECAP, processing by HPT is especially effective in refining the grain size without a corresponding significant loss in ductility. This result may be due to the high hydrostatic pressure applied in HPT processing which serves to limit the nucleation and growth of micro-cracks [246].

Table 6-3 Grain size and mechanical properties of pure Ti processed by SPD

Ti Grades	Processing history	Grain size (nm)	UTS (MPa)	δ %	Ref
VT1-0	ECAP	300	810	15	[247]
Grade 1	ECAP	400	780	14	[95]
Grade 2	ECAP + thermo mechanical treatment (80%)	70	1150	11	[10]
Grade 2	ECAP	300	670	14	[248]
Grade 2	ECAP + rolling	140	905-937	7-27	[249]
Grade 2	ECAP(10) + CR (77%)		945	14.5	[250]
Grade 2	ECAP + extrusion		791	19.7	[251]
Grade 2	ECAP		750	7	[252]
Grade 2	ECAP	300	760	21	[253]
Grade 2	ECAP + CR (70%)	150	1080	32	[93]
Grade 3	ECAP + HPT (1.5 GPa)	200	730	25	[90]
Grade 3	ECAP	280	710	14	[20]
Grade 3	ECAP + CR (75%)	100	1150	8	[254]
Grade 3	HPT (5 GPa)	120	950	14	[255]
Grade 3	ECAP(8) + CR (73%) + Annealing (300 °C, 1 h)	~100	1037	12.5	[256]
Grade 4	HPT	~110	1600	5	[99]
Grade 4	ECAP + drawing	200-600	1280	10	[257]
Grade 4	ECAP	300	947	25	[253]
Grade 2	HPT (3 GPa)	130	940	23	This study

Re: CR = cold rolling, δ % = elongation to failure

In earlier studies of the processing of pure Ti by HPT, a pressure of 1.5 GPa gave grain refinement to ~200 nm [90] and a pressure of 5 GPa gave a grain size of ~ 120 nm with a transformation from a ductile α-phase with a hexagonal close-packed (HCP) structure to a hard and brittle ω-phase with a simple hexagonal structure [96]. In practice, the amount of the ω-phase increases with increasing strain so that the ductility of the material is reduced [96]. This contrasts with the present results using

a pressure of 3 GPa where the tensile results in Figure 6-3 showing that processing by HPT produces both a significantly improved strength and a reasonable ductility. It is worth pointing out that due to the limited size of Ti samples processed after HPT processing, the shape of tensile samples of is very different with the standard shape. The shape tensile sample may be a reason which leads to a higher ductility during tensile testing.
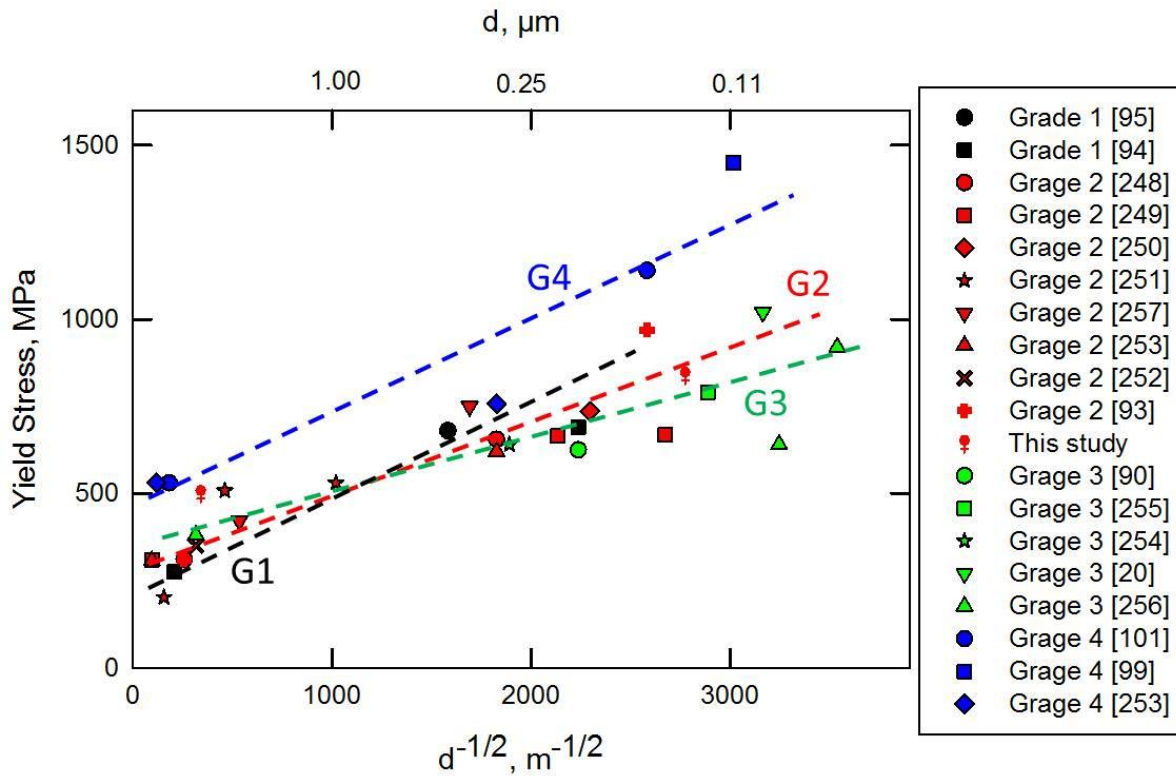
Figure 6-12 The yield strength of pure Ti before and after SPD processing.

Figure 6-12 demonstrates that SPD processing increases the yield strength of all four types of pure Ti and the yield strength and grain sizes fit well with the Hall-Petch relationship. Especially a grade 4 Ti processed by HPT at a pressure of 6 GPa gave a very high yield strength of 1450 MPa [99].

Recently, attentions have been paid to study the tribological behaviours of Ti processed via SPD [182, 184, 202, 213]. Initially, it was reported that UFG Ti had lower COF than coarse-grained Ti under various conditions [184], but this result was not consistent with a later study which revealed a similar COF around 0.6 for both CG Ti and UFG Ti [182]. This conflict might be caused by the different experimental setups used, as the indenter of friction tester used in Stolyarov's study [184] rotated

near the centre of Ti sample, while the indenter used in La's study [182] reciprocated on the surface of Ti samples. Nevertheless, all these studies showed the same trend of wear mechanism, that SPD processing inhibited adhesion and led to wear by micro-abrasion. Two recent studies reported a similar or slightly worse wear resistance of UFG Ti compared to CG Ti under very low contact pressures, and attributed this to the formation of oxide layer which masks the effect of microstructural change [202, 213]. Tribocorrosion tests in a phosphate buffer solution (PBS) demonstrated the better performance of UFG Ti processed by HPT compared to coarse-grained Ti under tribocorrosion conditions [193]. Furthermore, wear tests performed in liquid nitrogen environment showed that Ti with smallest grain size has the best wear resistance due to a higher strength and lower ductility at the extremely low temperature [258].

As already shown in previous studies, conflicting results due to different experimental setups used, and the large contact area developed during wear tests caused the wear process to be complex [182, 202]. All the previous studies compared the different wear behaviour between CG materials and UFG materials in a macro contact range, in which contact occurred at numerous asperities. Studies have indicated that micro-wear systems may behave in quite different ways from their larger counterparts [259, 260]. Therefore, the importance of investigating micro-wear behaviour of UFG materials has been recognized. In this study, micro scratching tests were employed for the first time ever to compare the wear behaviour of CG and UFG Ti, which not only simulate the work condition of micro components but also provide information to reveal the relationship between debris formation and material properties.

During sliding, wear debris are formed on the wear surface via work hardening, phase transitions and third body formation. The debris may also effects the whole wear mechanism [261, 262]. In this study, it was noticed that different properties of the samples lead to different debris formation mechanisms during scratching. The ductility and strength of materials affects both debris formation and the size of the debris that is formed. The occurrence of a phase transition is a possible explanation because there is evidence that the high pressures imposed in HPT processing may

produce phase transitions in pure Ti [96, 263] and a Ti alloy [264]. However, a further investigation is needed to explore this possibility.
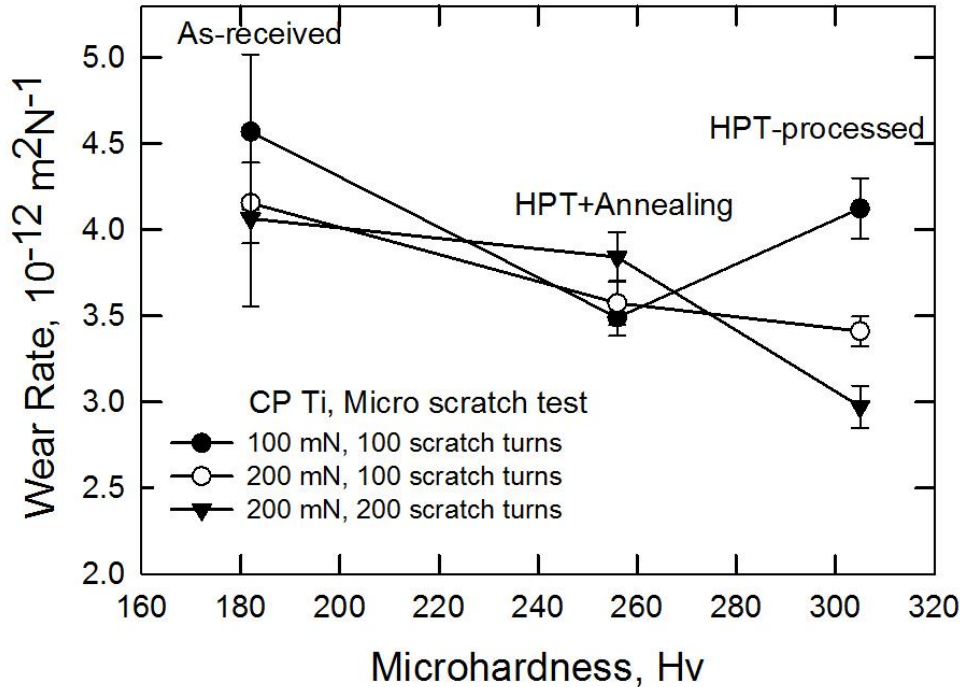
Figure 6-13 Specific wear rate versus microhardness of each Ti sample.

Previous studies using similar setups observed three wear modes: ploughing, wedge formation and cutting [134, 265]. The worn surface of as-received sample in this study showed clear characters of ploughing and wedge formation wear, while the HPT-processed sample undertook a milder abrasive wear. The wear mechanisms also affected the coefficient of friction. For the as-received Ti, the large debris formed by wedge formation was pushed out of the wear track as soon as it was formed, therefore, the effect of debris on COF was negligible. For the HPT-processed Ti and annealed Ti, tiny debris formed by abrasion wear was mostly trapped in the wear track, and the rolling of the debris might explain why the COF decreasing. In this study, under a load of 100 mN and 200 mN, the mean contact pressure P_m between two materials was predicted as 1.18 GPa and 1.49 GPa, respectively. The contact pressure is quite high, no evidence of oxidation wear was observed.

As shown in Figure 6-13, the wear rate of Ti decreases with increasing of microhardness, but not as much as expected according to Archard's equation.

Furthermore, a much smaller error scatter of wear rate was observed for the UFG Ti samples than the CG Ti, which indicates the more homogenous wear behaviour of UFG Ti compared to CG Ti.

6.4 Summary

High-pressure torsion was used to introduce significant grain refinement in CP Ti and micro-scratch tests were employed for the first time to examine the micro-tribological behaviour of samples having different grain sizes.

1.   The coefficient of friction of all samples was about 0.6 which shows the grain size of the material has little or no effect on the coefficient of friction during testing.

2.   Ploughing and wedge formation were the major wear modes for the coarse-grained samples whereas abrasive was the dominant wear mode for the ultrafine-grained samples.

3.   HPT-processed sample have slightly better wear resistance than CG Ti, however, this wear resistance of UFG Ti needs further improvement for wear applications.

7. Tribological behaviour and adhesion of TiN coating on Ti substrates processed by HPT

As shown in last chapter, HPT processing significantly improved the strength of pure Ti. However, the wear resistance of UFG Ti was still relatively low. In this chapter, TiN coating was deposited on both CG and UFG Ti substrates, their wear resistance and load bearing capacity on different Ti substrates were investigated.

7.1 Experimental procedures

The experiments were conducted on Grade 2 CP titanium. TiN coatings were deposited on the Ti substrates both before and after HPT using PVD in a magnetron sputter ion plating system. It is important to note that any application of a coating to UFG Ti requires a temperature under 350ºC because of the occurrence of recrystallization at higher temperatures [74]. The deposition processes were performed at a temperature below 150ºC to avoid recrystallization of the Ti substrates. Following deposition, the coating had a thickness of ~2.5 µm.

Rockwell indentation and scratch tests were performed to evaluate the adhesion of TiN coating on Ti substrates. After scratch testing, the surface profiles of the TiN coatings at the critical load were measured using an IFM operating in line scanning mode.

Wear tests were performed on micro-wear tester. The dry sliding tests were conducted under a constant load of 200 mN with a sliding speed of 200 µm s^{-1}. A diamond sphere tip with a radius of 20 µm travelled repeatedly on the coating surface for up to 1400 turns. The initial mean contact stress, P_{mean}, was estimated as ~11.2 GPa but this contact stress dropped dramatically when the probe penetrated into the coating. The surface profiles were recorded after wear testing using the ultimate focus optical microscope. Finally, the failure modes and wear mechanisms of the TiN coatings on the Ti substrates were analysed using SEM and EDX.

7.2 Results

The surface morphology of a coating on the as-received Ti substrate is shown in Figure 7-1. After deposition, the TiN coating had an average roughness, R_a, of ~230 nm, which is identical to the initial Ti substrate. It is reasonable to assume the coatings on the CG and UFG Ti have the same thickness because all depositions were conducted together in the same PVD system. As shown in Figure 7-1, TiN coating follows the morphology of substrate, therefore, the surface roughness of TiN coating can be easily controlled via controlling the surface roughness of substrate.
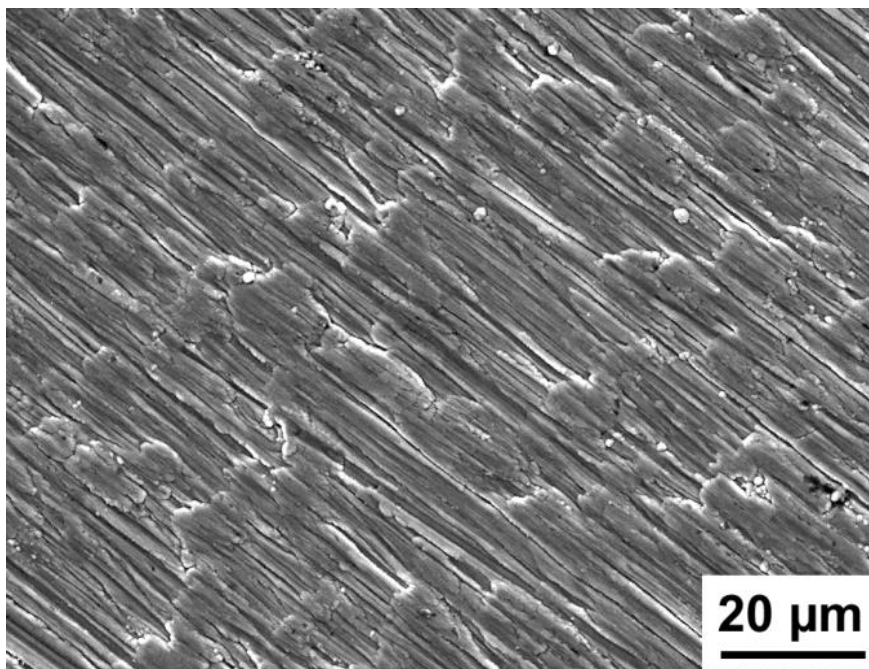
Figure 7-1 Unworn surface of a TiN coating on as-received Ti.

Optical images of the Rockwell indentations are shown in Figure 7-2, where Figure 7-2 (a) and (b) showed the indentations of TiN on CG Ti and UFG Ti, respectively. The load of 200 N caused deformation of the coating and the substrates. Circumferential cracking of the TiN coating was observed outside the indentation area on both samples which may be related to the elastic-plastic boundary of the substrates. The UFG Ti substrate had a higher strength and this improved strength gave a better support to the thin coating, thus the coating on UFG Ti had a much smaller indentation and less cracking. Delamination of the coating was not observed on either sample which demonstrates the good adhesion between the TiN coating and Ti substrates. The coating on both substrates had an adhesion level of HF2 which is readily acceptable for bio-applications [215].
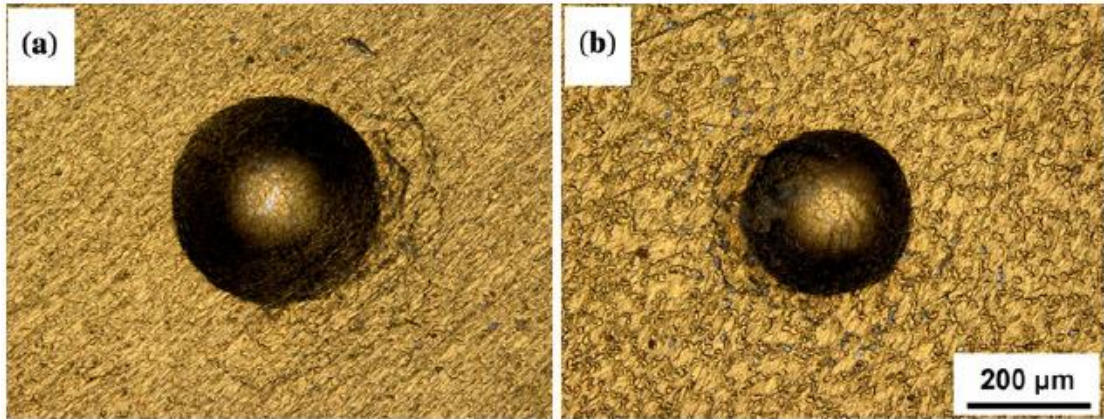
Figure 7-2 Rockwell C indentation of TiN on (a) CG Ti and (b) UFG Ti.
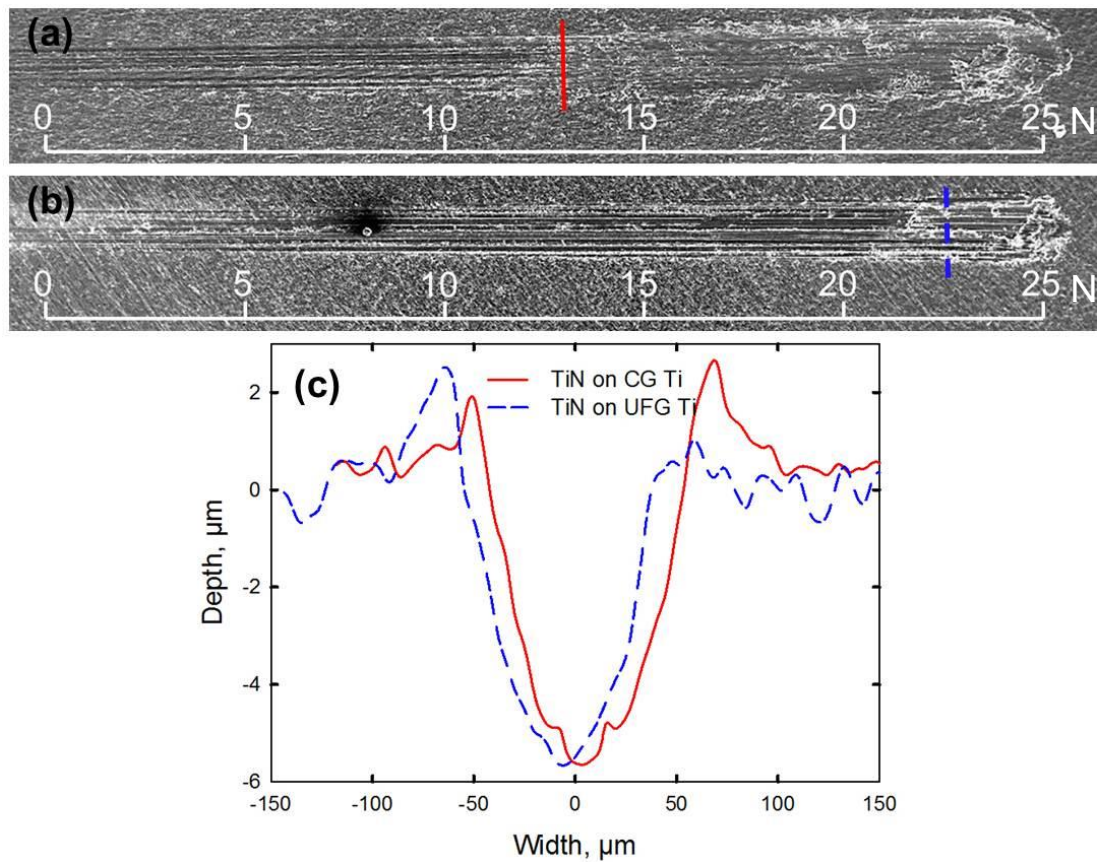
Figure 7-3 SEM image of scratched TiN on (a) CG and (b) UFG Ti substrates, with coloured lines showing the position of *Lc3* load, and (c) the cross section profile of each sample at the critical load.

The load L_{c3} was defined as the load under which the coating was totally removed from the substrate [216]. As shown in Figure 7-3, SEM micrographs after scratch testing indicate that L_{c3} of the TiN coating on CG Ti is 12.7 ± 0.2 N whereas L_{c3} for the TiN coating on UFG Ti is 22.5 ± 0.3 N. The initial cracking load of the coating is related to a sudden peak in the AE signal, as cracking of the coating produces strain

energy which is captured by the AE detector. As shown in Figure 7-4, the first cracking of the TiN coating on CG Ti occurs at ~2.5 N while for the TiN coating on UFG Ti a first crack appears at ~5.5 N. In earlier scratch studies, a 2 μm TiN coating gave values for L_{c3} of ~25 N and ~16 N on hot working steel and stainless steel, respectively [266, 267] and a 2 μm TiN coating on a Ti substrate gave a value for L_{c3} of ~36 N [217]. The values for L_{c3} of the TiN coating may vary between different studies because of differences in the interlayer and coating processes.

Using Alicona microscopy after scratch testing, the surface heights of the points along the lines marked in Figure 7-3 (a) and (b), representing the cross-sectional profiles of the samples, are recorded in Figure 7-3 (c). It is apparent that the samples have very similar widths and depths when the TiN delaminates from the substrates at the L_{c3} load. The TiN coating delaminated from the substrate when it reached a tensile limit regardless of the substrate and the indenter then penetrates into the material. In practice, the TiN coating on UFG Ti recorded a higher L_{c3} load due to the higher hardness of the ultrafine-grained material. These results demonstrate that a TiN coating with a UFG Ti substrate exhibit a better load-bearing capacity because the hard substrate prevents the indenter from penetrating into the coating.

Micro-wear testing was employed to examine the wear resistance of the TiN coatings. During the wear testing, a diamond probe with a radius of 20 μm was brought along the surfaces of the TiN coatings in a reciprocating manner. The COF of all samples showed a steady value of ~ 0.2 during these tests, as illustrated in Figure 7-5. These results confirm that the presence of a TiN coating successfully reduces the COF because earlier experiments gave a relatively high COF of ~ 0.6 for the uncoated Ti. Previous wear studies on TiN coatings reported COF values in the range from 0.2 to 1.0 where these values are highly influenced by the counter body and test conditions [266-268]. A similar COF for a TiN coating was also reported in earlier studies using a similar procedure and contact geometry [217, 269].
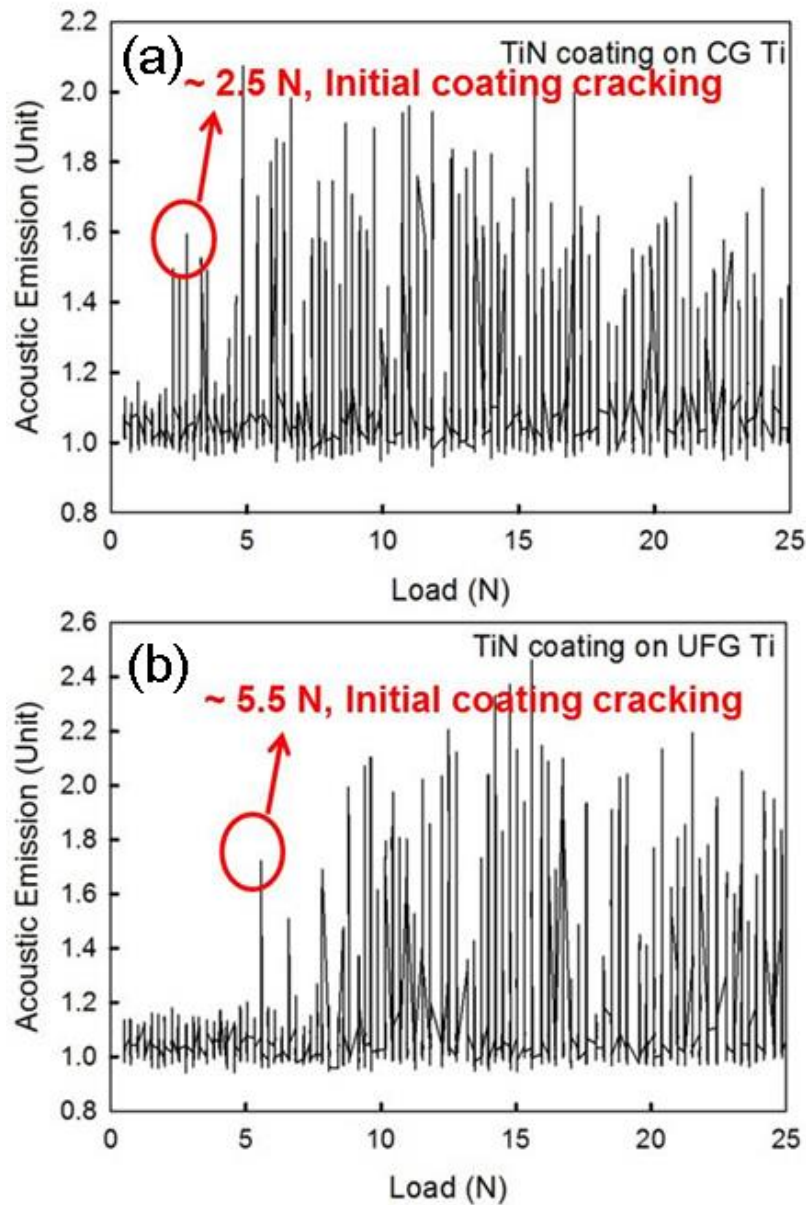
Figure 7-4 AE signals of TiN on (a) CG and (b) UFG Ti substrates.

Figure 7-6 shows the wear surface morphologies and cross-sections after 100, 300, 800 and 1400 wear repeats for (a) CG and (b) UFG Ti together with (c) the wear scar profiles. It is apparent that the strength of the substrate has an important effect on the wear of coatings such that the HPT-processed Ti gives better support to the applied coating. Thus, the wear track of a TiN coating on UFG Ti is always shallower and narrower than the same coating on CG Ti. Also, substantial deformation of the coating is noted, especially in the coating on the as-received Ti. It can be seen that ridges are formed more obviously at the edges of the wear scars for the coated CG Ti. There was no brittle failure of the coatings, by spalling or delamination, thereby

confirming a good bonding between the TiN coating and the Ti substrate and also the excellent ductility of the TiN coatings.
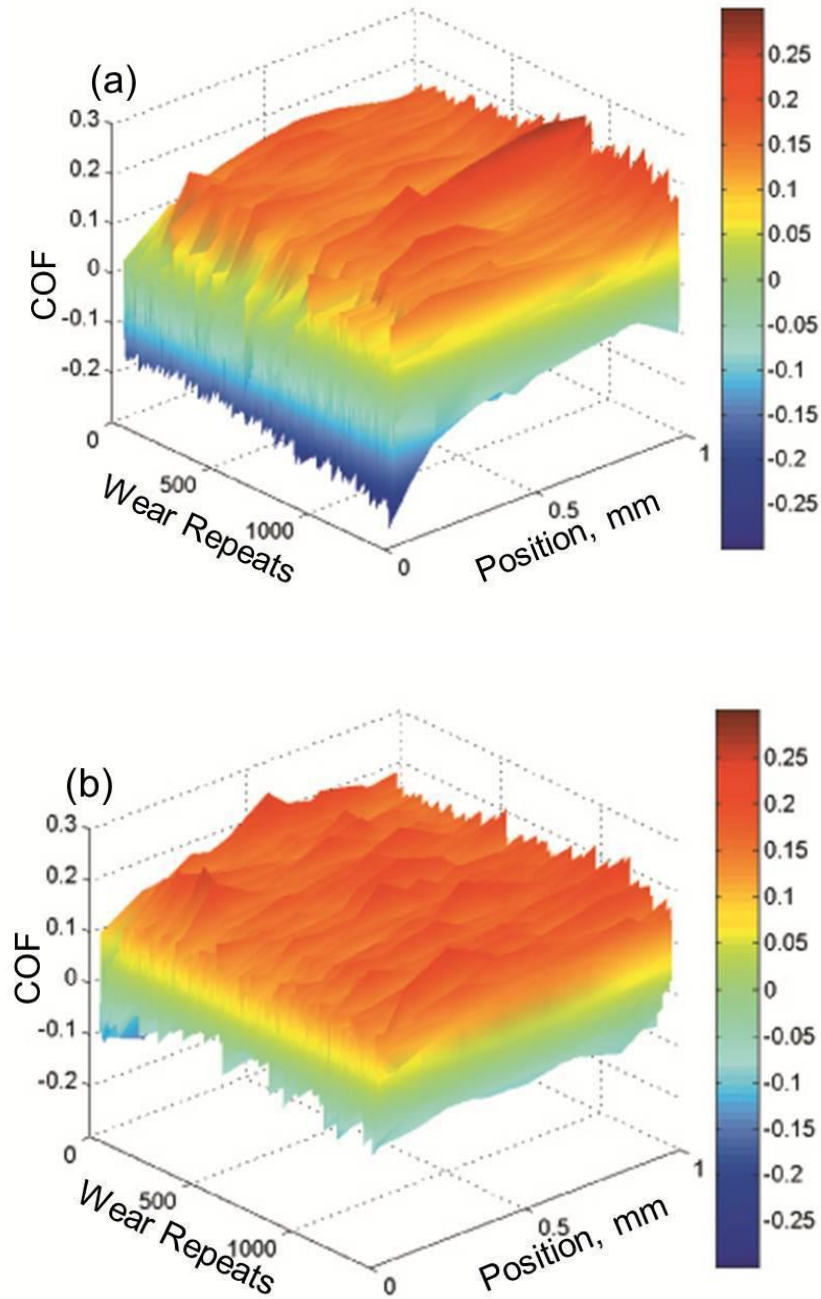
Figure 7-5 The COF of TiN coatings on (a) CG and (b) UFG Ti during micro-wear testing.

Figure 7-7 compares the surface morphologies and chemical elements of the TiN coatings on (a) the as-received CG Ti and (b) the UFG Ti after 1400 repeats. Larger volumes of the Ti element were detected by EDX compared to the N element at the

bottom of the wear track of the coated as-received sample compared with the HPT sample. This shows the TiN coating on the as-received sample is partly worn through by the indenter whereas 1400 repeats of the wear test penetrated only ~1000 nm into the coated UFG Ti sample.
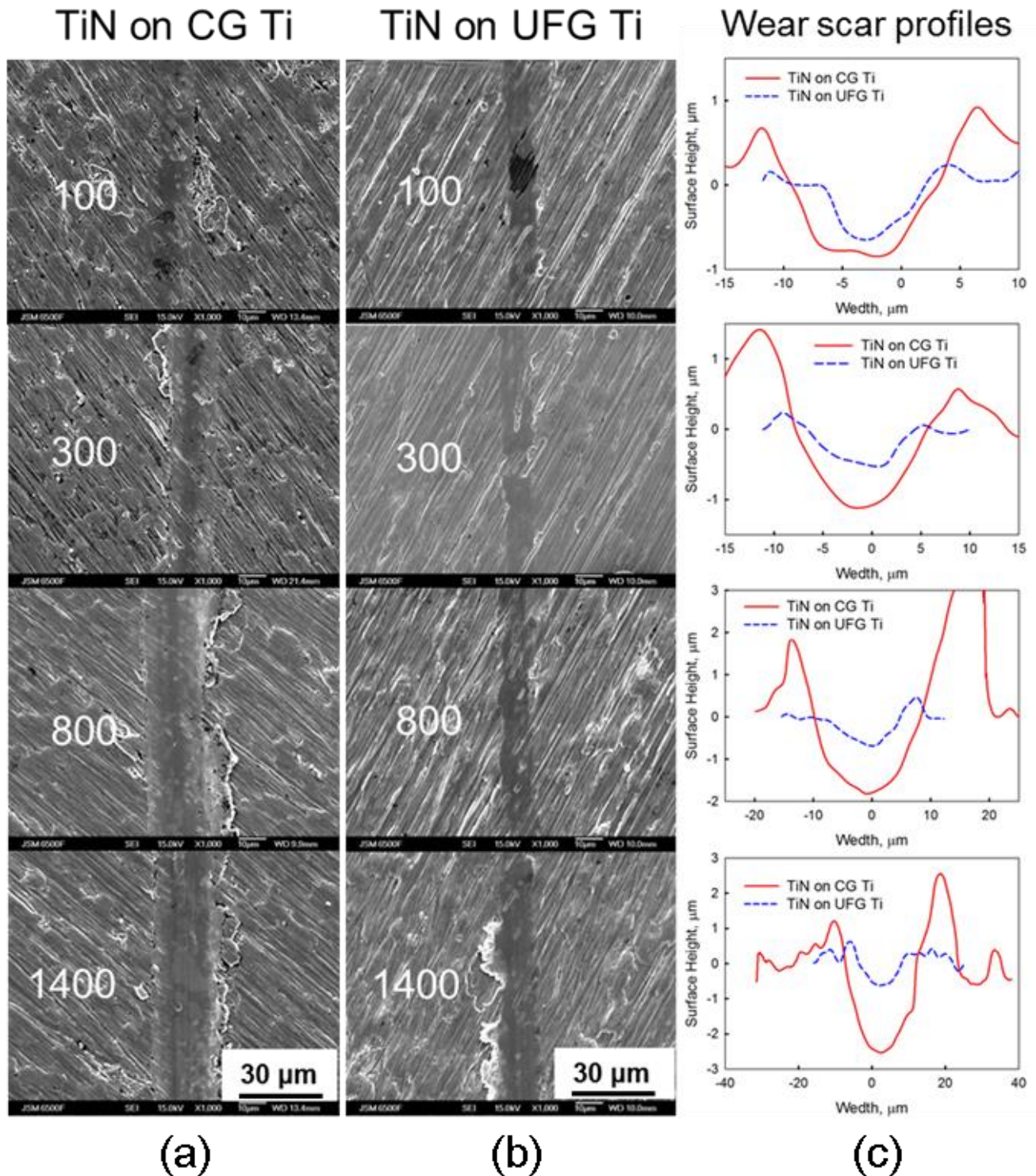
Figure 7-6 Wear surfaces of TiN on (a) CG and (b) UFG Ti samples after different numbers of scratching turns from 100 to 1400 and (c) the relevant wear scar profiles.
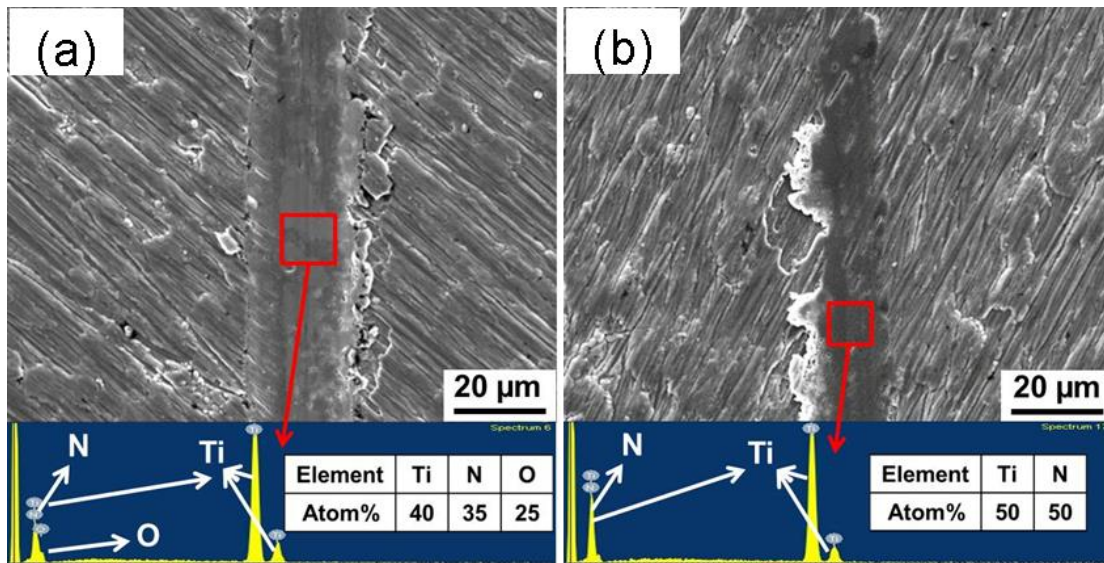
Figure 7-7 Wear surfaces of TiN coating on (a) CG Ti and (b) UFG Ti after 1400 repeats of micro-wear test.
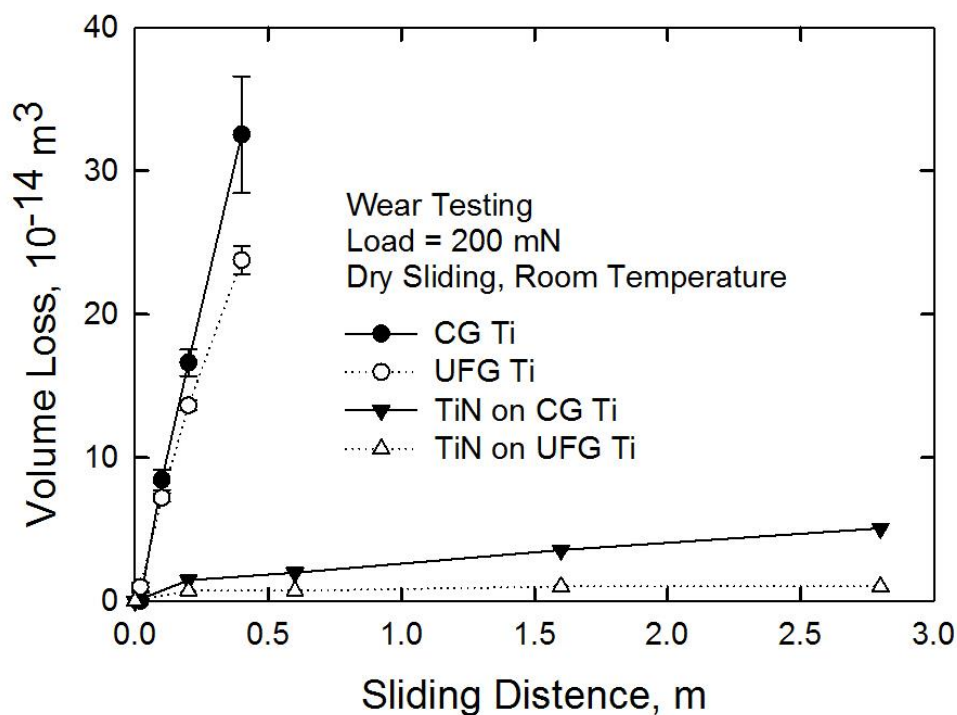
Figure 7-8 Volume loss of samples versus sliding distance during wear test.

The wear volume loss of materials during wear testing is shown in Figure 7-8. It can be seen that the Ti substrates without TiN coating have a very rapidly increasing volume loss during the wear test, and the volume loss of UFG Ti is slightly lower compared to CG Ti. The TiN coated Ti samples have a much lower wear loss even after a longer wear distance. It is estimated from the cross-sections that the wear rates

132

of TiN on as-received Ti is ~9.1×10^{-14} m^3 N^{-1} m^{-1} whereas on UFG Ti the wear rate is much lower at ~$(1.8 \pm 0.3) \times 10^{-14}$ m^3 N^{-1} m^{-1}. It is difficult to compare these wear rates with earlier studies, where there are reports for TiN coatings of wear rates between 7×10^{-15} and 5×10^{-14} m^3 N^{-1} m^{-1}, because these wear test results are highly influenced by testing conditions including the manner of the contact, the counter body, the sliding speed and the load [270-272]. Nevertheless, both TiN-coated Ti substrates show wear rates that are two orders of magnitude lower than the uncoated Ti which was studied earlier using the same wear tester and similar wear conditions described in Chapter 6.

Based on these results, it is reasonable to conclude that, with sufficient strength, good biocompatibility, an absence of the release of toxic elements and a very good abrasion resistance, the TiN-coated UFG Ti makes an excellent candidate material for future total joint replacements.

7.3 Discussion

During the service of total joint replacements, there are inevitable sliding contacts between the femoral cup and the tibial or acetabular head during motion of the human body. These contacts generate wear debris and they produce a dimensional loss for the bio-implants that may cause health problems for the patient [109]. As shown in Chapter 6, the sliding resistance of both CG and UFG Ti was poor. However, the deposition of a TiN coating on the Ti substrate provides a direct protection against wear. During scratch testing in the present experiments, the TiN coatings were well adhered to the substrates with no visible evidence for spalling or delamination.

The high strength of coatings are favourable to maintain the low surface roughness during sliding motion, which also lead to less wear loss the polyethylene counterpart [163, 273].

The results of the micro-wear tests show good deformation behaviour on both substrates. No significant cracking or delamination was observed even when the TiN coating on the CG Ti was worn through after 1400 repeats of sliding. By contrast,

there is a report of extensive TiN coating cracking inside the wear track during scratch testing using a 4 μm thick coating on a steel substrate [274]. Thus, the present results confirm the excellent characteristics for TiN coatings on Ti substrates.

The higher strength of UFG Ti by comparison with CG Ti also produces a better wear resistance to the TiN coating under the high contact pressure of the wear test. Typically, the contact pressure for human joints is in the range of ~0.5 - 20 MPa. For these conditions, the main contact stress lies within the TiN coating and the effect of the substrate on the wear resistance of the TiN coating is negligible. Thus, the higher strength of the UFG substrates provides the bio-implant with both good strength and an improved fatigue life.

In practice, the real contact conditions for bio-implants are not well defined and there may be higher wear rates and more severe wear mechanisms in some patients. For example, in some post-clinical studies there were reports of large wear debris, with a size of ~3 - 5 μm, in ceramic-on-ceramic bearing contacts associated with the wear regions formed on the implant heads [275, 276]. These large wear particles originate from very severe contacts of the implant, such as the presence of a micro-separation between the femoral head/neck and the cup rim [277]. As examined in the wear test of this study which employed a high contact stress, the TiN coating on UFG Ti exhibits very good wear resistance under extreme contact conditions because the high strength of UFG Ti inhibits deformation of the coating.

Since most of the abrasion and tribo-corrosion of bio-implants occur at the interface between the head and the cup, it is feasible to fabricate the bio-implant from UFG pure Ti processed by SPD and then apply a hard thin coating to protect the head of the implant. There are several possible reasons for the advantage of a coating but primarily it must be associated with the fundamental properties of the coating such as the thickness and the nature of the interlayer. The interlayer between the coating and the substrate can improve chemical bonding and provide a buffer layer that effectively reduces the stress gradient between the coating and substrate [278]. Although the roughness of the substrate is probably also important, it is not significant in the present study because all substrates had the same polishing history

before coating and the coatings were deposited at the same time on different substrates so that their properties are nominally the same. According to other reports [278], a TiN coating with a thickness of ~2-3 μm corresponds to an optimum scratch resistance, and it contrasts with thicknesses of ~1.5 μm which is too thin so that the coating is worn quickly or ~5 μm where delamination occurs easily [279]. As shown in Figure 7-3 (a) and (b), the TiN coating is detached abruptly from the Ti substrate when the diamond probe penetrates the TiN coating under L_{c3} load. Under these conditions, the scratch performance of the TiN coating is dictated not only by its own properties but also by the plastic deformation of the substrate. As depicted schematically in Figure 7-9, the coating is subjected to a tensile stress as the substrate is deformed by the indenter and it becomes detached from the Ti substrate when it reaches the tensile limit.
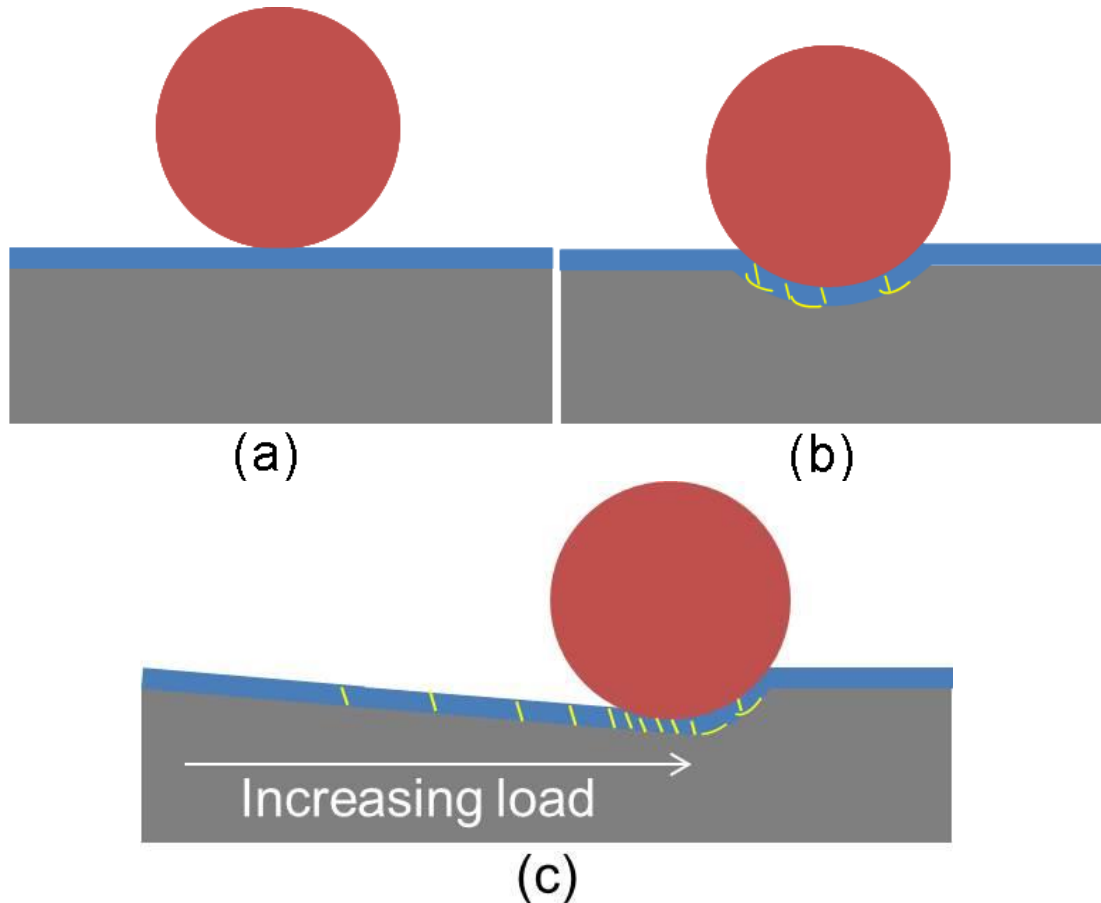
Figure 7-9 Schematic illustration of TiN coating failure during a scratch test: (a) cross section view of the initial state, (b) cross section view of the failure at $Lc3$ and (c) side view of the failure of coating at $Lc3$.

7.4 Summary

In this chapter, A TiN coating, with a thickness of ~2.5 μm, was deposited on unprocessed Ti and on Ti after processing by HPT. The wear resistance and adhesion of TiN on different substrates were studied.

1.   The wear resistance of Ti was improved by two orders using TiN coating compared with uncoated Ti.

2.   The TiN coating on UFG Ti had much higher critical load compared to the same coating on CG Ti, this property was related to the higher strength of the UFG Ti substrate.

3.   The results show that a TiN coating on ultrafine-grained Ti has an excellent potential for use in bio-implant applications. Advantages of this system include high strength, reasonable ductility, excellent abrasion resistance and a non-toxic ion release.

8. Adhesion of DLC-Zr coated Ti substrates processed by HPT

Doping with metallic elements, such as Cr [273, 280], Ti [281] and W [282], is reported that may also improve the adhesion and wear resistance. Recently, zirconium was used as a dopant metal to provide low-toxicity, good tribological behaviour and high corrosion resistance [283, 284].

The present investigation was initiated to explore the effect of substrate microstructure on the adhesion behaviour and scratch resistance of DLC-7Zr, DLC:H-7Zr and DLC-9Zr coatings deposited on grade 2 pure titanium substrates both with and without high-pressure torsion processing and, in addition, to make a direct comparison with deposition on a Ti-6Al-4V substrate.

8.1 Experimental procedures

The experiments were conducted using grade 2 pure titanium and the Ti-6Al-4V alloy with extra low interstitials. Initially, some of the grade 2 Ti samples were subjected to high-pressure torsion processing.

The DLC coatings were deposited using dc dual magnetron sputtering in an Ar atmosphere and Ar+CH$_4$ to produce non-hydrogenated and hydrogenated coatings, respectively. A TiN/TiCN interlayer with thickness of 450 nm was deposited in order to improve adhesion. The thickness of the functional coating was approximately 1 μm so that the total film thickness was of the order of ~1.4 μm.

The coating adhesion to the Ti substrates was evaluated using Rockwell C indentation and scratch testing where these are standard techniques commonly used to quantify the interfacial strength of coating-substrate systems. The cross-section profiles of the DLC coatings at the critical load were measured using an ultimate focus optical microscope operating in the line scanning mode.

8.2 Results

The chemical composition was determined by electron probe microanalysis applying a 10 keV voltage. The coating hardness was measured by depth-sensing indentation using a Berkovich indenter and a load of 5 mN. A series of 32 indentations from two distinct areas was carried out in order to critically evaluate the hardness of the coatings. In addition, the reduced Young modulus was derived from the indentation measurements using the standard method [285]. The Young modulus was calculated using the following parameters: $E_i = 1140$ GPa and $\nu_i = 0.07$ for the diamond indenter and $\nu = 0.3$ for the coating [285].

Table 8-1 shows the zirconium content, the hardness and the values of the Young modulus of the deposited coatings. It should be noted that the low indentation depth for the indenter (approximately 10% of the coating thickness) made it difficult to ascertain the effect from the substrate material when obtaining these mechanical properties. Details of the coating structure were studied by X-Ray diffraction, Raman spectroscopy and X-Ray photoelectron spectroscopy and these results were reported elsewhere [286]. All of the coatings investigated in this study (with Zr contents of 7-9 at.%) exhibited a nanocomposite structure with very small ZrC nanograins (up to ~2 nm) embedded within an amorphous carbon matrix.

Table 8-1 Summary of coatings chemical composition and mechanical properties.

System	Zr content (at.%)	Hardness (GPa)	E(GPa)
DLC_7Zr	7±1	11±2	120±3
DLC:H_7Zr	8±1	13±1	117±4
DLC_9Zr	10±1	12±2	131±3

3.3 Adhesion performance of the DLC coatings

Table 8-2 summaries the adhesion results of DLC coating on all three substrates. The Rockwell C indentation tests showed HF3 and HF4 for all samples with only minor delamination and micro-cracking observed around the indentation marks, thereby demonstrating an acceptable adhesion for all tested coatings. The scratch test results

showed that the DLC coatings with UFG Ti and Ti-6Al-4V substrates had similar critical loads and these loads were much higher than with the coarse-grained Ti as substrates. Thus, the UFG Ti and Ti-6Al-4V substrates provided better support with their higher hardness and this produced a higher critical load of the DLC coating. These results demonstrate again the important role of substrates for the adhesion of thin DLC coatings.

	CG Grade2 Ti	UFG Grade2 Ti	Ti-6Al-4V
DLC-7Zr			
DLC:H-7Zr			
DLC-9Zr			

Figure 8-1 Rockwell indentation of DLC on different Ti substrates.

Optical images of the Rockwell indentations are shown in Figure 8-1. It can be seen that the load of 200 N led to radial plastic deformation of the coating which caused circumferential cracking of the film outside the indentation area. Through-thickness cracks were observed on all coatings which may be related to the elastic-plastic boundary of the substrates. The indentation marks had a diameter of ~380 μm on the DLC/coarse-grained Ti samples which would cause more deformation at the edge and more delamination compared to the DLC/ultrafine-grained Ti and DLC/Ti-6Al-4V samples. This effect was mainly caused by the different hardness of the Ti

substrates. Furthermore, the doping of H content led to a decrease of the adhesion strength because all the indents of the DLC:H-7Zr coating showed a higher delamination than DLC-7Zr. It is obvious that the DLC-9Zr coatings with higher Zr content presented the best adhesion behaviour with only small cracks and minor coating delamination. Therefore, it may be possible to further enhance the coating adhesion by increasing the zirconium content. A more comprehensive study of the adhesion of DLC coatings with different Zr content is given elsewhere [286].

Table 8-2 Summary of adhesion testing results

| Substrate | Coating | Rockwell C | | Scratch | | | |
		Ø (µm)	adhesion	Lc1 (N)	Lc2 (N)	Lc3 (N)	Track width at Lc3 (µm)
CG Ti	DLC_7Zr	375	HF3	7±2	8±1	13±2	149.7
	DLC:H_7Zr	391	HF4	5±1	7±2	13±1	130.1
	DLC_9Zr	384	HF4	7±1	9±1	15±1	130.7
UFG Ti	DLC_7Zr	282	HF3	8±1	12±1	22±2	113.3
	DLC:H_7Zr	286	HF3	7±2	10±1	20±1	120.9
	DLC_9Zr	287	HF3	10±2	14±1	24±1	123.8
Ti-6Al-4V	DLC_7Zr	277	HF3	9±2	11±1	23±2	139.7
	DLC:H_7Zr	274	HF4	5±1	10±2	19±2	132.1
	DLC_9Zr	282	HF3	11±2	15±1	25±2	126.2

The scratch test results matched well with observation from the Rockwell indentations. Figure 8-2 shows the scratch tracks of the DLC-7Zr coating on the Ti substrates with increasing loads from 2 to 50 N. Generally, the plastic deformation of the Ti substrates was the main cause for the coating failure. As the diamond stylus was sliding with increasing normal load on the coating surface, the coating followed the deformation of the Ti substrate. The tensile stress both inside the coating and at the interface led to cracking and delamination of the coatings. As shown in Figure

8-2 (a), the DLC-7Zr coating on coarse-grained Ti failed at an early stage during the scratch test and the indenter caused extensive deformation of the substrate. On the other hand, the DLC-7Zr coatings deposited on ultrafine-grained Ti and Ti-6Al-4V failed at a higher load and the adhesion of the films deposited on both substrates was almost identical (Figure 8-2 (b) and (c)).
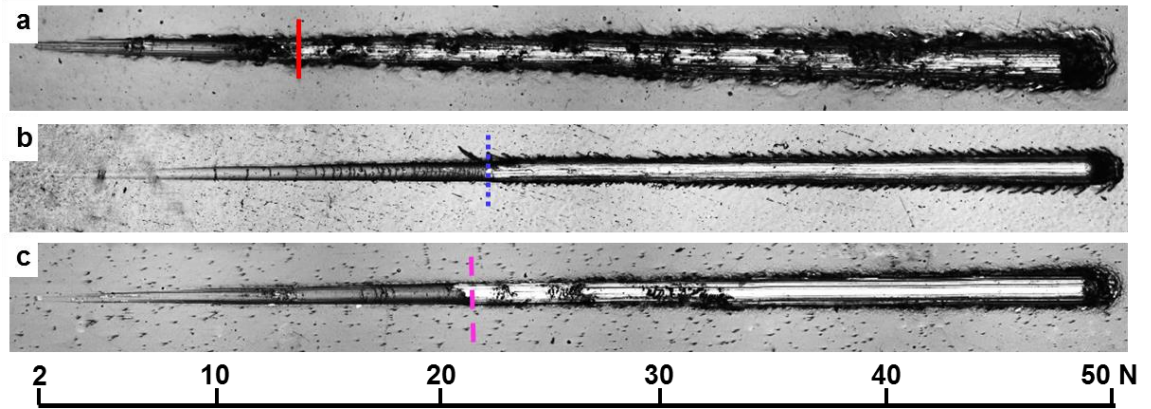
Figure 8-2 Scratch tracks of DLC-7Zr coatings on (a) coarse-grained Ti, (b) ultrafine-grained Ti, (c) Ti-6Al-4V substrates. With coloured lines showing the position of *Lc3* load.
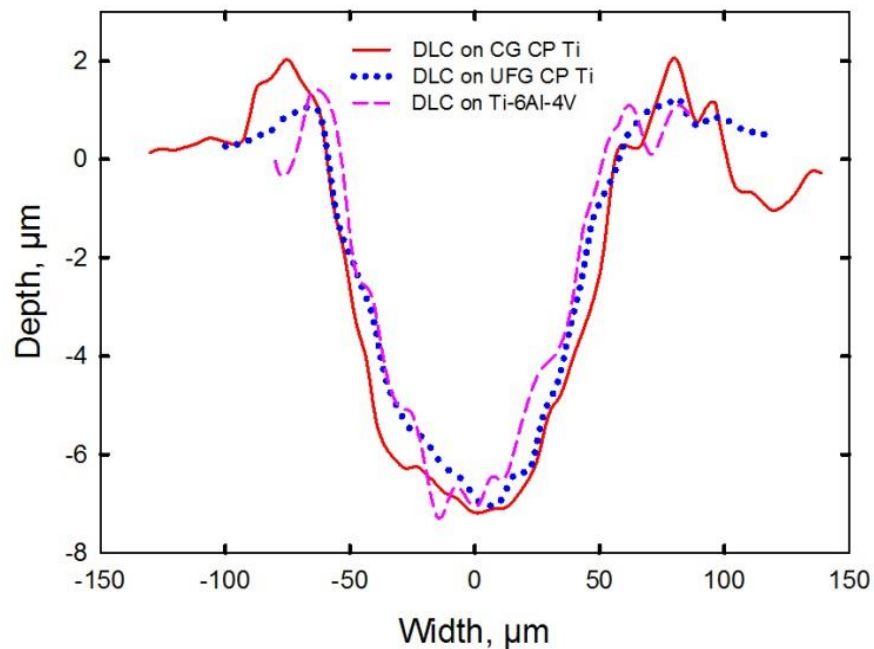
Figure 8-3 Cross-section of the scratch tracks at *Lc3* load indicated in Figure 8-2.

The cross-section of the scratch tracks where the substrate was revealed in the scratch track (see the short vertical lines in Figure 8-2 (a), (b) and (c)) was measured

using an ultimate focus optical microscope. Although the coating was deposited onto different substrates, these measurements showed that it always failed when the scratch track was approximately 7 μm deep and 130 μm wide as illustrated in Figure 8-3.

8.3 Discussion

In this study, DLC coatings were successfully deposited on the different Ti substrates and their scratch behaviour was studied. In terms of future bio-medical applications, the results provide a clear demonstration that it is possible to replace the conventional Ti-6Al-4V alloy with ultrafine-grained pure Ti having preferable mechanical properties which may be achieved through high-pressure torsion processing.

Various coating technologies are now available to provide wear resistance for bio-implants. Technologies such as MAO and internal oxidation (IO) have been used extensively to process Ti-6Al-4V and other bio-metals but these methods often involve a high processing temperature which may lead to recrystallization of ultrafine-grained structures [160, 204]. When ultrafine-grained materials are chosen as the substrates, the post processing temperature must not exceed the recrystallization temperature in order to restrict any grain growth of the ultrafine-grained structures. Moreover, the oxidation layers produced through these methods are often very rough and this will entail additional polishing before their use in implants. Thus, PVD methods are regarded as one of the best choices for surface modifying ultrafine-grained materials.

Despite the excellent tribological properties of DLC coatings, delamination of the coatings was a major problem which appeared to limit their application as articulating joints [172]. It is reasonable to anticipate that, once removed from the substrate, these DLC coating particles would act as a third body causing severe damage to the substrate or even severe reactions with the tissue. Therefore, a good adhesion between the thin coating and the substrate is essential for the coating/substrate system. The interposition of a gradient layer (Ti/TiN/TiCN) improves the interface shear strength and the load bearing capacity of the coating

[287]. It was observed in this study that, when using ultrafine-grained Ti as the substrate, the load bearing capacity of DLC coatings was improved extensively compared to those with coarse-grained Ti as substrates. A similar trend was observed also on TiN thin coatings on different Ti substrates studied in Chapter 7. The TiN on ultrafine-grained Ti also had a higher critical failure load as it prevented the thin coating from undergoing deformation. Figure 8-4 shows the critical load of the DLC coatings and TiN coating on Ti substrates plotted against the hardness of the substrate. The trend is clear because a harder substrate after high-pressure torsion leads to a higher critical load for the coatings. Therefore, on one hand it is very important to explore better coating parameters such as new interlayer designs and coating compositions in order to achieve a good performance of the coatings. On the other hand, it is also very important to enhance the properties of substrates through surface hardening or grain refinement (i.e. increase H/E ratio) and give a better support to the thin coatings.
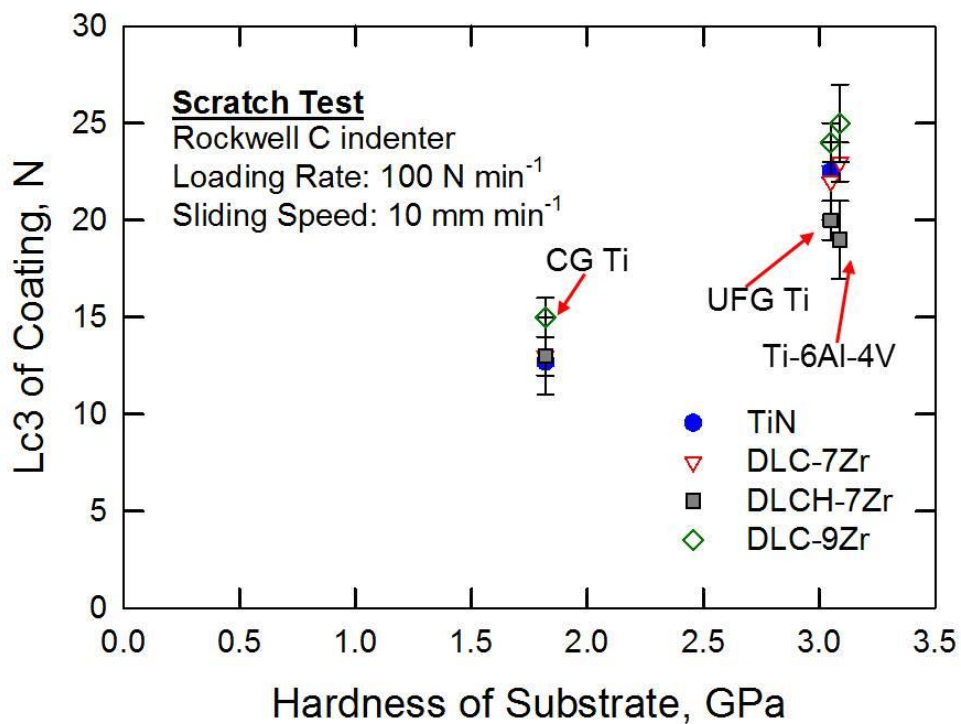
Figure 8-4 Critical load of coatings versus the hardness of substrates measured by scratch test.

The results from this research showed that the DLC coating failures occurred at the same depth and width of penetration for all three substrates, as is clearly observed in Figure 8-3. As the UFG Ti and Ti-6Al-4V had very similar hardness, therefore, the

data points were very close to each other. As shown in Figure 8-3, the critical load of all coating increased with increasing hardness of the substrates. Similar trend was also observed on various TiN coated substrates including stainless steel, high speed steel and WC [288]. An explanation was given by assuming the TiN coating adjusted to the elastic–plastic deformation of the substrates, therefore the coating underwent a cohesive–adhesive failure that leads to film delamination. A critical indentation width of 60 μm was observed in that study, where the coating failed as long as it was bended to this width regardless to the substrate material.

In this study, with good wear resistance and an extremely low coefficient of friction which benefits from the DLC coatings, the DLC/ultrafine-grained Ti system appears to be an exceptionally strong candidate material for future bio-implant applications.

8.4 Summary

The adhesion behaviour and scratch resistance of three diamond-like carbon coatings deposited on grade 2 pure Ti substrates before and after high-pressure torsion processing were investigated and a comparison was made with a Ti-6Al-4Vsubstrate. The following conclusions are reached:

1.   DLC coatings with a gradient TiN/TiCN interlayer show good adhesion on Ti substrates.

2.   Hydrogen-free DLC-Zr coatings have better adhesion than hydrogen-doped DLC-Zr coatings, and increase of the percentage of Zr increases the adhesion.

3.   The effect of substrate on the performance of the DLC coating under high load was highlighted, showing that coatings with ultrafine-grained pure Ti and Ti-6Al-4V substrates have similar scratch and indentation behaviour. Both are significantly better than the results obtained with coarse-grained Ti substrates.

9. General discussion

9.1 Strength modelling of Al-1050 and Ti

In general, the mechanisms of hardening in alloys after SPD processing include grain boundary strengthening, solid solution strengthening, precipitates strengthening, deformation twinning strengthening and dislocation strengthening. Critical resolved shear stress (CRSS), τ, is used to describe the degree of strengthening. The macroscopic yield strength of a polycrystalline material can be calculated as [289]:

$$\sigma_y = \Delta\sigma_{gb} + M\tau \qquad \text{(Eq.9-1)}$$

Where σ_y is the yield strength of material after SPD processing, $\Delta\sigma_{gb}$ is grain boundary strengthening, M is Taylor factor. For alloys which contain all the above strengthening mechanisms, CRSS increment is approximated as [289]:

$$\sigma_y = \Delta\sigma_{gb} + M(\tau_0 + \Delta\tau_{ss} + \Delta\tau_{prec} + \Delta\tau_d) \qquad \text{(Eq.9-2)}$$

Where τ_0 is the intrinsic stress, $\Delta\tau_{ss}$ is the solid solution strengthening, $\Delta\tau_{prec}$ is the precipitate strengthening, $\Delta\tau_d$ is the dislocation strengthening. While in current study, the Al-1050 and pure Ti are commercial pure materials which contain nearly no alloying elements, thus the grain boundary strengthening and dislocation strengthening act as the main strengthening mechanisms. Therefore, the above equation can be simplified as:

$$\sigma_y = M\tau_0 + \Delta\sigma_{gb} + M\Delta\tau_d = \sigma_0 + \Delta\sigma_{gb} + M\Delta\tau_d \qquad \text{(Eq.9-3)}$$

The dependence of yield stress on grain size strengthening in metals is well established by the following relationship [290]:

$$\sigma_y = \sigma_0 + a_2 Gb \frac{1}{d_{GS}} \qquad \text{(Eq.9- 4)}$$

where d_{GS} is the grain size, G is the shear modulus, b is Burgers vector, and the constant a_2 is assumed to be 2 [290].

The dislocation strengthening is expressed as [291]:

$$\Delta\tau_d = a_1 Gb \sqrt{\rho_{ig}} \qquad \text{(Eq.9-5)}$$

Where a_1 is a constant which is often taken as 0.3, ρ_{ig} is the volume average dislocation density stored inside grains. For ECAP processing, it is believed all the dislocations are statistically stored dislocations (SSD). While for HPT processing, as the deformation amount introduced by straining is increasing from the centre to the edge, geometrically necessary dislocations (GND) are formed to accompany the strain gradient effect [292, 293].

Plastic deformation of metals often takes place via dislocation generation and moving, moving dislocations maybe blocked by another dislocation, particle or grain boundaries, and these dislocation maybe stored inside grains. Kocks, Mecking and Estrin proposed a model to quantify the competition of storage and annihilation of dislocations [294-296]:

$$\frac{d\rho_{SSD}}{d\varepsilon} = k_1 \rho_{SSD}^{-0.5} - k_2 \rho_{SSD} \tag{Eq.9-6}$$

Where ε is strain, ρ_{SSD} is density of SSD in side grains, k_1 and k_2 are constants.

In Eq. 9-6, the term $k_1 \rho_{SSD}^{-0.5}$ stands for generation of dislocations due to straining, and is related with athermal storage of dislocations after travelling for a distance proportional to $\rho_{SSD}^{-0.5}$. k_1 was further evaluated as $2\theta_2 / Ga_1 b$, where θ_2 is the slope of the tensile curve of the material in athermal hardening stage [295]. The mean free path for dislocation moving, l, is proportional to $\rho_{SSD}^{-0.5}$ for large grains. While for a severely deformed material, the mean free path is assumed to be a constant which is determined by non-shear particles, impenetrable obstacles or cell walls. The Eq. 9-6 is further rewritten as following by introducing mean free path [296]:

$$\frac{d\rho_{SSD}}{d\varepsilon} = (bl)^{-1} - k_2 \rho_{SSD} \tag{Eq.9-7}$$

Thus the ρ_{SSD} can be obtained as:

$$\rho_{SSD} = (blk_2)^{-1} - \left((blk_2)^{-1} - \rho_0\right)e^{-k_2\varepsilon} \tag{Eq.9-8}$$

Where ρ_0 is the initial dislocation density.

Assuming the dislocation generation rate is constant all through the straining process and to calculate the first term of Eq. 9-7, the total amount of statistically stored dislocation generated via straining, ρ_g, is expressed as [296]:

$$\rho_g = (bl)^{-1}\varepsilon \qquad\qquad (Eq.9\text{-}9)$$

The dislocations formed by straining might stay inside grains as the statistically stored dislocations; form a grain boundary or join into an existing grain boundary; or disappear due to thermal active annihilation. While in cold severe plastic deformation processing, like both ECAP and HPT in this study were conducted under room temperature, the thermal active annihilation of dislocation was assumed to be very small to effect the grain refinement. Moreover, assume that the shape of grains have a Poission-Voronoi distribution, $d = 2.91/S_{GB}$, where S_{GB} is the area of grain boundaries per unit volume. Therefore, a model was proposed recently to predict the grain size of Al alloys after cold working, as following [35]:

$$d_r = \frac{2.91}{S_{GB}} = 2.91 \times 1.5 \times \frac{\bar{\theta}}{b\rho_{GB}} \qquad\qquad (Eq.9\text{-}10)$$

Where $\bar{\theta}$ is the average misorientation angle after straining, d_r is defined as the grain refinement of metal via straining, thus the grain size after straining can be expressed as [223]:

$$\frac{1}{d}_{GS} = \frac{1}{d_o} + \frac{1}{d_r} \qquad\qquad (Eq.9\text{-}11)$$

where d_0 is the original grain size. Therefore, Eq.9-11 could be used to predict the grain size of alloys after straining. The yield strength of alloys can be obtained by Eq.9-3 together with Eq.9-4, Eq.9-5 and Eq.9-11. The microhardness of materials can be approximated by Hv=3.3σ_y.

9.1.1 Strength of Al-1050 after ECAP processing

Figure 9-1 shows the comparison between measured grain size of Al-1050 processed by ECAP and the grain size predicted by Eq.9-11. It can be seen that the grain size of Al-1050 predicted by Eq.9-11 fits well with experiment results after a large strain. However, under a lower strain, the predicted grain size is always smaller than the real grain size.
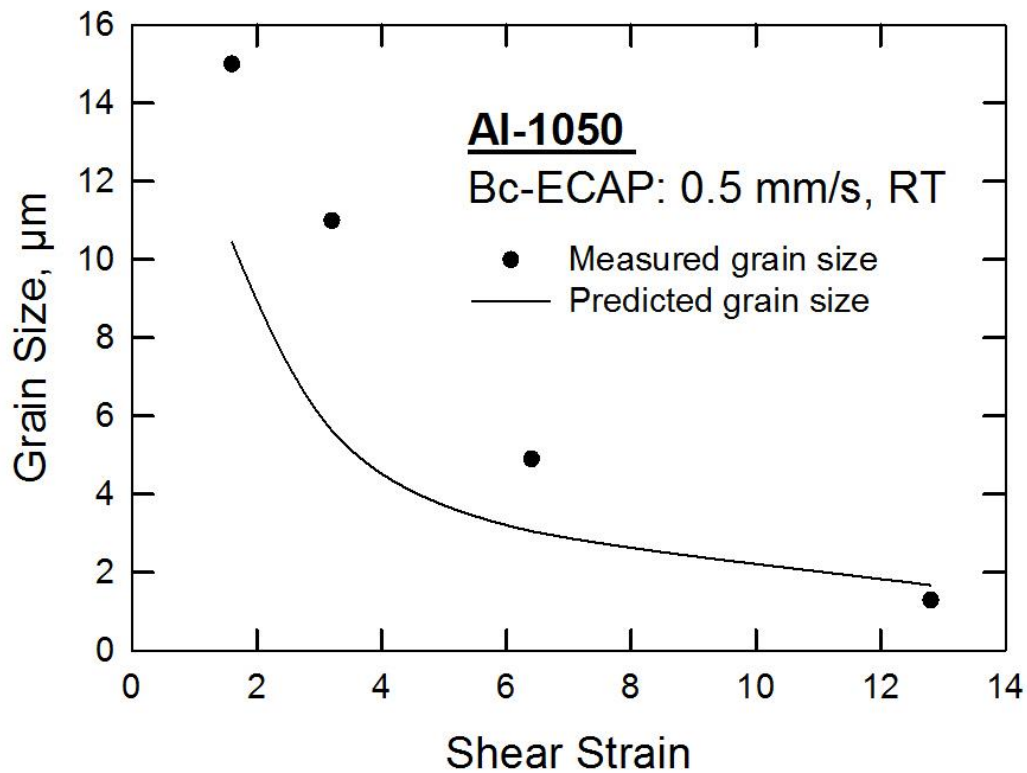
Figure 9-1 The measured and predicted grain size of Al-1050 processed by ECAP.
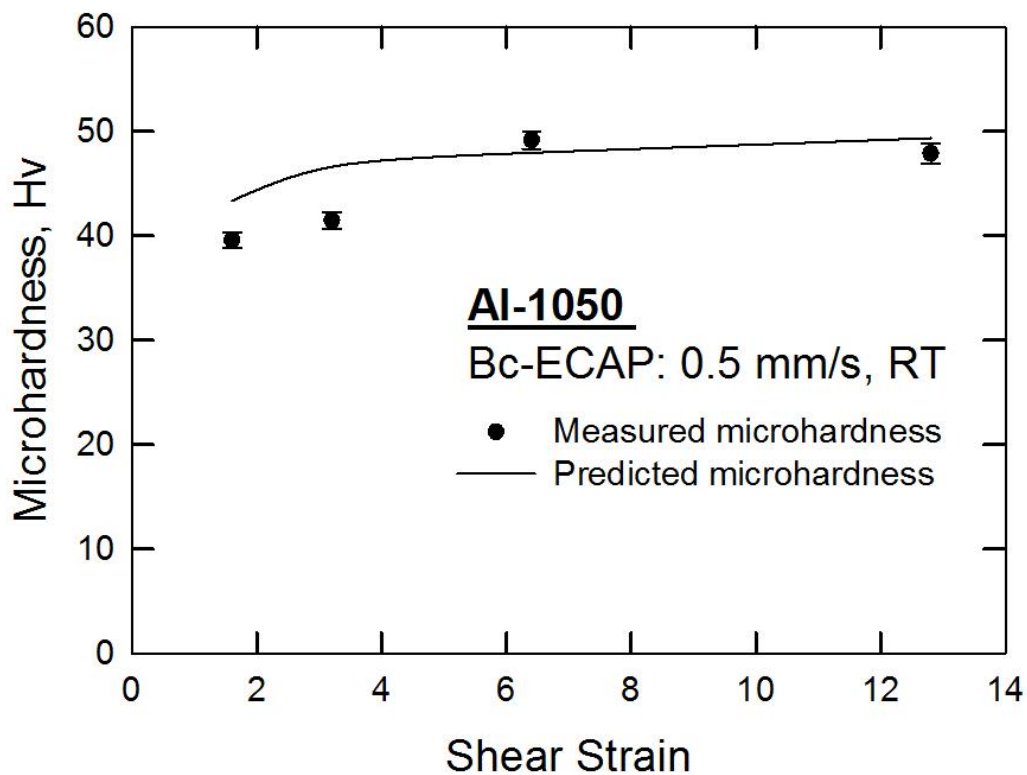
Figure 9-2 The measured and predicted microhardness of Al-1050 processed by ECAP.

The most possible reason for this different is that in the model, the average misorientation angle of grains was employed to predict the grain size. While for Al-1050 being deformed for a low strain, low angle grain boundaries took up a very large fraction of the grain boundaries. These low angle grain boundaries were shown as grey lines in the EBSD data which can be easily neglected when counting for grain sizes using mean intercept length method, see Figure 4-2 (b) and (c). After a large straining, high angle grain boundaries became as dominating, these grain boundaries were shown as black lines in the EBSD data and can be easily recognized when measuring grain size.

Figure 9-2 compares the measured microhardness with predicted microhardness obtained by Eq 9-3 and Eq 9-11. A very good correlation between the prediction and experiment results is shown in Figure 9-2, especially after large shear strain.

9.1.2 Strength of Al-1050 after HPT processing

During processing with HPT, the shear strain and equivalent strain imposed on the disc is expressed by Eq.2-3 and Eq.2-5, respectively. Differently from the case of ECAP processed Al-1050, geometrically necessary dislocations (GND) are also stored in grains which will provide additional dislocation strengthening effect to the material, as expressed by [292, 293]:

$$\rho_{ig} = \rho_{SSD} + \rho_{GND} \tag{Eq.9-12}$$

Where ρ_{ig} is the total density of dislocations stored inside grains, ρ_{GND} is density of GND. By inputting Eq.9-12 into Eq.9-5, the microhardness of Al-1050 after HPT processing can be predicted by Eq.9-3. As shown in Figure 9-3, microhardness of Al increased with imposed strain and reached to a saturation level after certain amount of straining. It is obvious that the saturation hardness of Al-1050 processed by HPT is around 64 Hv, which is much higher than 49 Hv of Al-1050 processed by ECAP. This different is mainly caused by strengthening of geometrically necessary dislocations stored in HPT processed samples, which is absent in ECAP processed Al-1050.
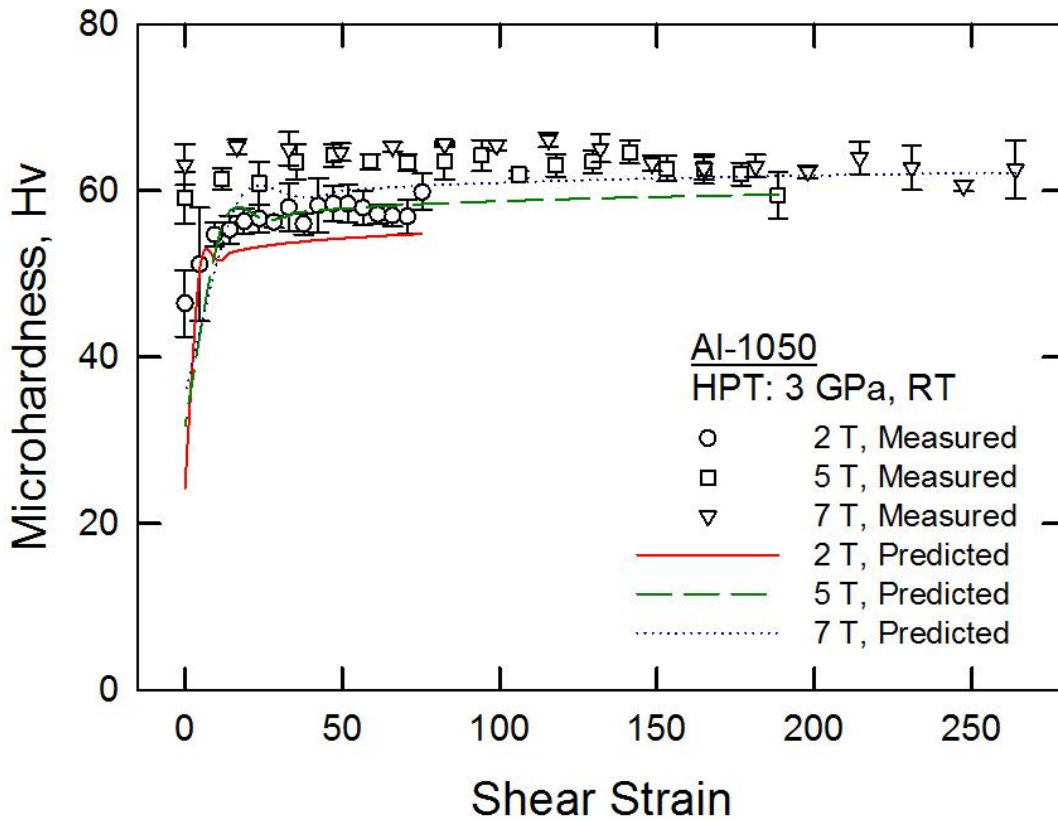
Figure 9-3 The measured and predicted microhardness versus the shear strain for Al-1050 discs processed by HPT through different numbers of turns.

In addition, Figure 9-3 shows that the hardening of Al-1050 via HPT processing saturates at around shear strain of 4, which is also clearly predicted by the strengthening model. However, the model fails to predict the microhardness of Al-1050 at very low strain, especially for the data collected in the centre of disc samples where the shear strain is believed to be 0. This might be caused by several reasons: Firstly, the deformation of materials is introduced by rotating of the two anvils, while in practice it is very possible the two anvils of the HPT facility have some misalignment with each other. This misalignment between two anvils introduces extra deformation to the disc sample especially in the centre area, which is not considered in the modelling. Secondly, the HPT processing of this study was conducted in a quasi-constrained facility. There is some restricted outflow of material around the periphery of the disc during the processing operation [297]. This outflow of material causes extra compression deformation along the axis direction, which is not included in the model. It was shown in an earlier study on an Al-6061alloy that the high pressure leads to very significant increase to the

microhardness value even in the absence of any torsional straining [298]. The outflow of material might also count for the difference of hardness between modelling and measurement in the large strain region.

9.1.3 Strength of pure Ti after HPT processing

Similar to Al-1050, the microhardness of pure Ti after HPT processing can also be predicted by Eq.9-3. For pure Ti, the σ_0 is taken as 238.3 MPa [299]. As shown in Figure 9-4, microhardness of pure Ti increased with imposed strain and reached to a saturation level after certain shear strain of around 10. The microhardness of the centre area of each sample was higher than prediction from modelling, similar to Al-1050 samples processed by HPT. There is a good correlation between experiments and model prediction, especially after large strain.
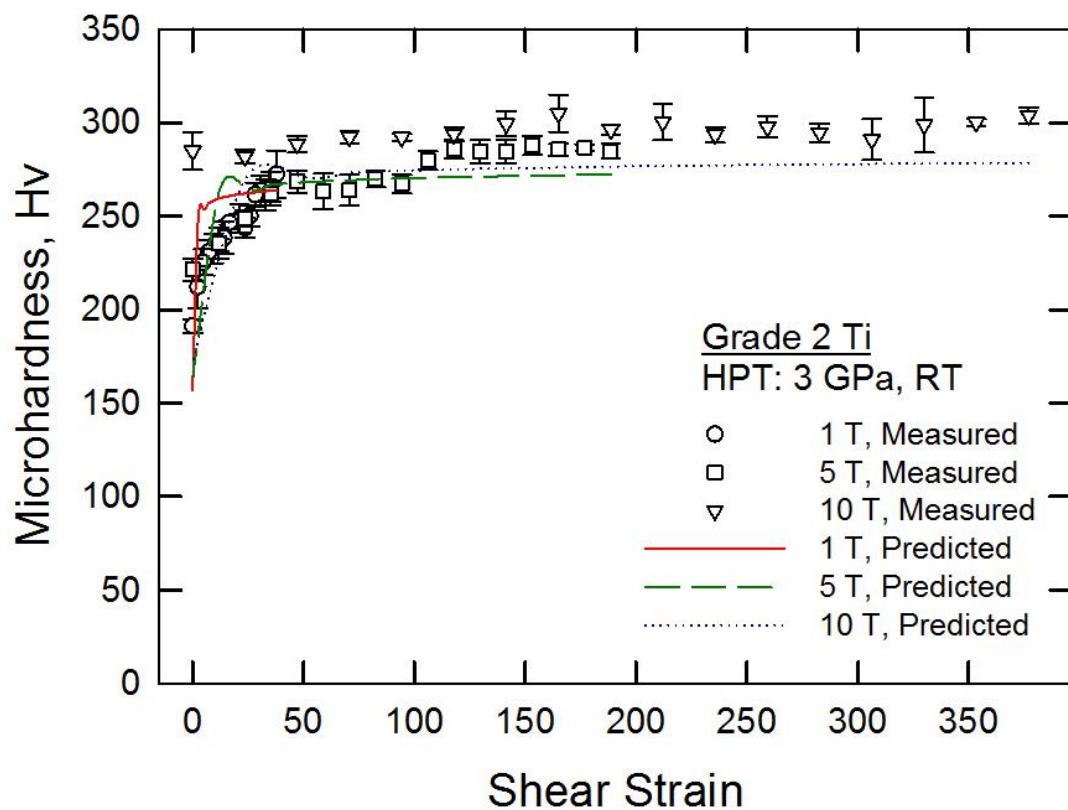
Figure 9-4 The measured and predicted microhardness versus the shear strain for pure Ti discs processed by HPT through different numbers of turns.

9.2 Effect of SPD processing on wear behaviour of Al and Ti

In Chapter 4, 5 and 6, the effect of SPD processing on wear resistance of Al and Ti were studied. SPD processing showed no effect on COF of Al or Ti, this is probably due to no change in crystal structure before and after SPD processing. From the researches of previous studies about Al and Ti [184], only one paper reported that SPD processing decreased the COF of Ti, and all others showed that SPD had no effect on COF of materials [186, 196-198].
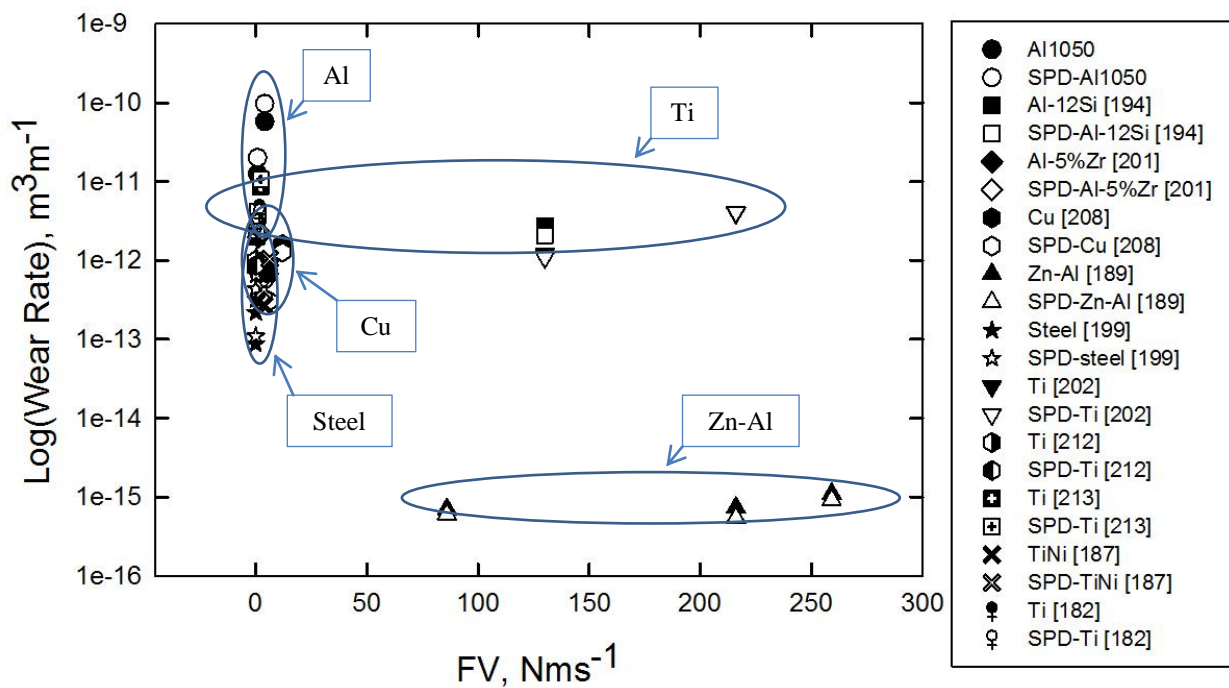
Figure 9-5 The map on log (wear rate) against F × V (pressure × sliding velocity) from the available literatures.

The results in Chapter 4 and 5 showed that SPD processing reduces the wear resistance of Al due to operation of adhesion wear and oxidation wear. However, results on Ti in Chapter 6 showed the positive effect of SPD on wear resistance of Ti, as the SPD processing successfully inhibits more plastic deformation during wear, and the strengthening introduced by SPD brought better wear resistance to Ti during abrasion wear. Although the wear test results in this study showed conflict evidence to each other for different alloys, they are consistent with the results of the same material from literature. The studies showed that SPD reduced wear resistance of Al [186, 196-198, 299]. In addition, studies demonstrated that SPD increased the wear resistance of Ti when oxidation wear was absent [182, 193].

Figure 9-5 plots the map of wear rate versus F×V (load × sliding velocity) from the available literatures and results obtained by this project. The F×V factor refers to the energy input per second introduced during the sliding test. It can be seen from Figure 9-5 that the wear rate of materials (Al, Cu) which have higher thermal conductivity are seem more sensitive with F×V than materials (Ti, Zn-Al) which have lower thermal conductivity. However, it is still hard to see the effect of SPD on wear resistance from this map, which probably because that SPD processing is only one among factors which influence the wear resistance of materials. Similarly, Figure 9-6 plots the map of wear rate versus microhardness of materials, all the black symbols refer to as-received materials and the white symbols refer to their SPD-processed state. As SPD processing normally improves the microhardness the materials, so the red lines with a negative slop in Figure 9-6 indicate that SPD reduces the wear resistance of material, while the red lines with positive slop mean wear resistance is enhanced by SPD processing.
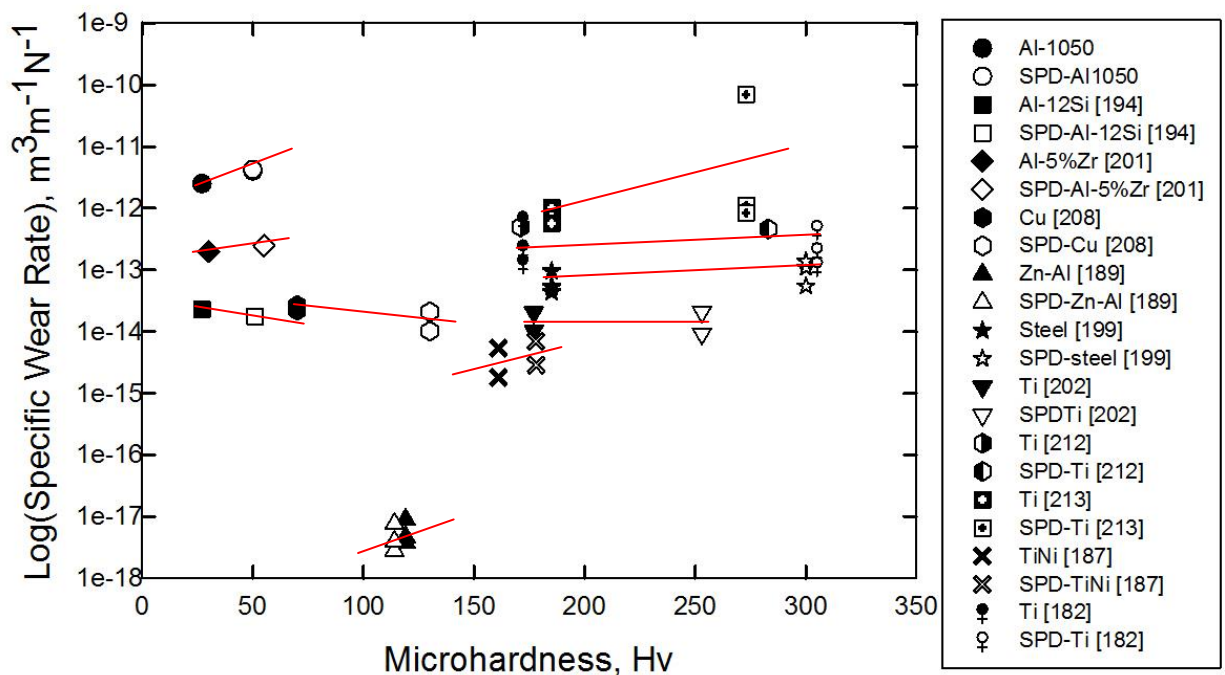
Figure 9-6 The map on log (wear rate) versus microhardness of materials.

In general, SPD processing has double-sides effect on wear resistance of materials. The main influence factors on improvement or reduction of wear resistance of SPD-processed materials from literature have been summarized in Table 9-1. Apparently,

as a result of SPD processing with smaller grain size, refined microstructure, higher hardness and higher strength, it will expect that all of them should benefit to improve wear resistance. On the other hand, other factors, which are also directly related to SPD, such as decreased ductility, reduced strain hardening capability, increased oxidation rate, unstable grain boundaries and so on, will expect to reduce wear resistance of SPD-processed materials. Among them, the lower ductility and reduced strain hardening capability are more likely the main causes in reducing wear resistance of SPD- processed alloys. Of course, many tribological factors, such as tribolayer, debris entrapment and counter surface et al. all play very important roles. Therefore, it is necessary for further studies on this topic to clarify the main wear mechanism operated during wear test.

Table 9-1 Influence factors on wear resistance of SPD-processed materials

Improve wear resistance	Reduce wear resistance
Smaller grain size	Decreased ductility
Refined microstructure	Low strain hardening capability
Higher hardness	Higher oxidation rate
Higher strength	Non-equilibrium and unstable grain boundary
	Strain-induced grain coalescence
	Strain incompatibility between surface and a deeper region

It is still possible to achieve a better wear resistance via SPD processing. However, this improvement may be not significant. As shown in previous results and literatures, although in some cases SPD processing improved the wear resistance of materials, that improvement was not remarkable as strength enhancement achieved by SPD. Therefore, a combination of SPD processing and surface coating may be more effective on improving the wear resistance of SPD materials.

9.3 Modellig the effect of substrate on load bearing capacity of thin coatings

9.3.1 A model based on volume law of mixtures

The effect of substrate on mechanical properties of thin coatings has drawn considerable attentions these years. In one study, TiN coatings were deposited on different materials. The scratch tests showed evidence of brittle failure of TiN

coating due to plastic deformation of the substrate. Cracking of TiN coatings was observed, especially on the soft copper substrate [274]. In another report, TiN coating with thickness of 0.5 μm was deposited on several different steel substrates [300]. Nanoscratch tests showed that the property of substrate also played an important role on the wear resistance of coated samples. The GT35 steel which had the highest H/E ratio was the best substrate among all the steel substrates by supplying the highest load bearing capacity to the coating.

As observed in Chapter 7 and 8, the PVD coatings on UFG Ti has a higher critical failure load due to the higher hardness of the substrate which prevents the thin coating from being deformed to the critical level. By simplifying the coating-substrate system as a two-layer composite, the overall hardness of the coating-substrate system may be represented by the following relationship according to Burnett-Rickerby model which is based on volume law of mixtures [47-50]:

$$H_{C,S} = \frac{V_C}{V_{total}} H_C + \frac{\chi^3 V_S}{V_{total}} H_S$$

(Eq.9-13)

where $H_{C,S}$ is the apparent hardness of the coating-substrate system, H_S is the hardness of the substrate, H_C is the hardness of the coating, χ is a factor by which the plastic zone changes, and the V_C, V_S and V_{total} are the deformation volume of the coating, substrate and total deformation volume, respectively. The volume of deformation zones are expressed by following equations:

$$V_C \approx \pi R_C^2 t$$

(Eq.9-14)

$$V_S \approx \frac{2}{3} \pi R_S^3$$

(Eq.9-15)

Where R_C and R_S are the radius of deformation zone of coating and substrate. The factor was determined via fitting experimental results by Burnett and Rickerby [48], and addressed as:

$$\chi = \left(\frac{E_C H_S}{E_S H_C} \right)^{1/2}$$

(Eq.9-16)

Where E_C is the Young's Modulus of the coating, and E_S is the Young's Modulus of the substrate. R_C and R_s can be obtained via equation :

$$R = r_{GEO} \left(\frac{E}{H} \right)^{1/2}$$

(Eq.9-17)

Where r_{GEO} is the geometrical length of the indentation volume.

As shown in Figure 8-3 that the indentation depth of all the samples was only around 7 μm, and this depth was obtained after the diamond indenter was removed. In this case, the measured indentation depth was underestimated due to the elastic recovery of materials. Therefore, it is more accurate to recalculate the indentation depth using measured indentation width considering the sphere shape of the indenter, according to the equation:

$$r_{GEO} = \left[\pi \beta^2 \left(R_{ind} - \frac{\beta}{3} \right) \right]^{1/3} \qquad \text{(Eq.9-18)}$$

$$\beta = R_{ind} - \sqrt{R_{ind}^2 - \frac{W^2}{4}} \qquad \text{(Eq.9-19)}$$

Where R_{ind} is the radius of diamond indenter, W is the track width at the critical load point, β is the indentation depth. Therefore, the overall hardness of this coating-substrate is achieved by rewriting equations (9-13 to 9-19):

$$H_{C,S} = \frac{E_C t + \frac{2}{3} r_{GEO} H_S \left(\frac{E_C}{H_C} \right)^{3/2}}{\frac{E_C}{H_C} t + \frac{2}{3} r_{GEO} \left(\frac{E_C}{H_C} \right)^{3/2}} \qquad \text{(Eq.9-20)}$$

During hardness testing, $H_{C,S}$ may be expressed by

$$H_{C,S} = \frac{L}{A_n} \qquad \text{(Eq.9-21)}$$

where L is the load and A_n is the contact area between the indenter and the test surface.

During the scratch testing, the indenter was travelling with an increasing normal load, it was always the front half of the spherical cap was supposed by the coating-substrate system. The present study used a spherical indenter so that the contact area is the front half of the spherical cap defined by

$$A_n = \pi R_{ind} \beta \qquad \text{(Eq.9-22)}$$

Therefore, the critical load, L_{C3}, is expressed as:

156

$$L_{C3} = H_{C,S} \pi R_{ind} (R_{ind} - \sqrt{R_{ind}^2 - \frac{W^2}{4}})$$
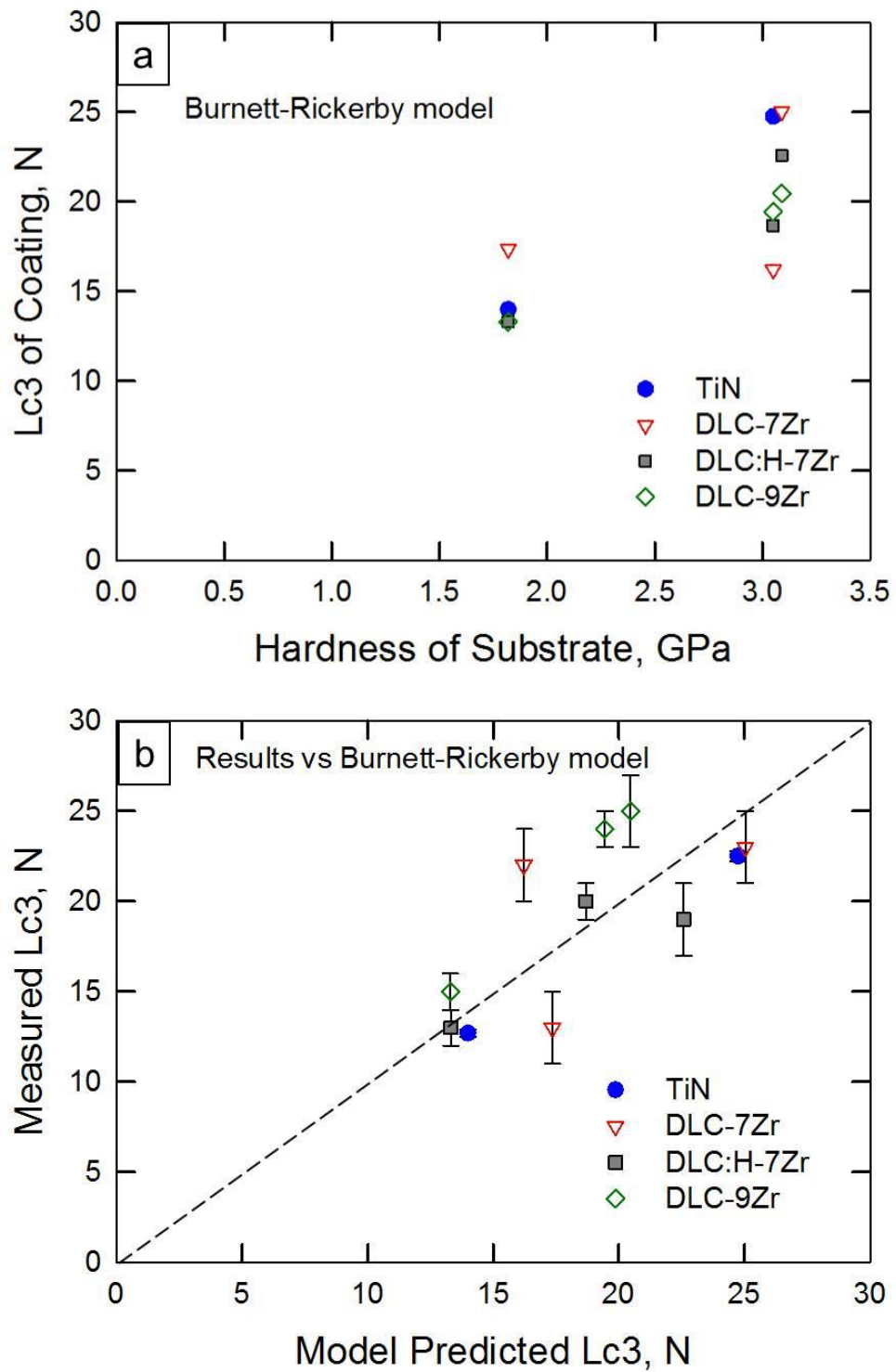
Figure 9-7 (a) Critical load of coatings versus the hardness of substrates calculated by B-R model and (b) experimental results versus calculation from B-R model.

Thus, the Eq.9-20 and Eq.9-23 clearly emphasise the effect of substrate strength on the scratch behaviour of thin coatings. Assuming that the hardness of the same coating on all substrates are the same and the coating failure occurs at the same depth of penetration, Eq.9-23 predicts that the critical load L_{c3} increases with increasing substrate hardness, H_S. It further explains that the DLC coatings, with thicknesses around 1 μm, often exhibit high critical loads with hard materials as substrates, such as more than 100 N on Si or glass [51].

As the track width of each sample is listed in Table 8-2, they can be applied to Eq.9-20 and Eq.9-23. The comparison between experimental results and Burnett-Rickerby model is plotted in Figure 9-7, it is shown that the prediction obtained by model fits well with our experiment results in Chapter 7 and 8. It worth noting that as the interlayers had a varying compositions and properties and they were much thinner than the coatings, thus this analysis simply neglected the properties of the interlayers although in practice the interlayer is important in improving the bonding. This might lead to the underestimating of the model. For the cases where the interlayer is very thick compared with the coatings, or the interlayer contributes very significant to the overall hardness of the coating, this model needs modifying for better accuracy. Moreover, errors might also be introduced due to the ridges formed at the edge of scratch tracks which made it difficult to measure the track width.

9.3.2 Applying this model for a wider range cases

In order to test the accuracy of the above modified Burnett-Rickerby model, scratch test data of a range of thin coatings on many different kinds of substrates was collected from literatures. These coatings were produced mostly by PVD and CVD methods, and all of them had a relatively thin thickness lower than 6 μm. The substrates vary from stainless steel, tool steel to WC. The details of coating and substrates were listed in Table 9-2, the information was than input to the Burnett-Rickerby model.

Figure 9-8 plots the track width at the critical of several coating on different substrates. It clearly shows that for a certain coating, there is a critical failure track width during scratch testing. For instance, about 100 μm for CrN processed by arc-

evaporate and 60 μm for TiN obtained via PACVD. This critical width is related to various reasons from coating ductility, internal stress, and interlayer properties, but regardless to the substrate property. This was also observed in our study on TiN and DLC coatings, as shown in Chapter 7 and 8.

Table 9-2 Summary of the details of scratch testing from literature

Coating					Substrate		Scratch			REF
Film	Method	H_C, GPa	E_C, GPa	t, μm	Metal	H_S, GPa	W, μm	Lc3, Exp	Lc3, Model	
CrN	Arc-evaporate	20	375	2.8	SCAM	2.7	98.8	21	12.7	[301]
CrN	Arc-evaporate	20	375	2.8	SUS420J	5.3	99.6	36	22.8	[301]
CrN	Arc-evaporate	20	375	2.8	SKD61	5.7	100.4	39	24.7	[301]
CrN	Arc-evaporate	20	375	2.8	SKH51	7.6	98.0	46	30.7	[301]
$CrN_{0.6}$	PVD	28.8*	240	4.1	M2	7.6	57	16.2*	13.4	[302]
$CrN_{0.6}$	PVD	28.8*	240	4.1	HWTS	5.3	54	8*	9.9	[302]
CrN	PVD	54*	240	3.3	M2	7.6	108	64.5*	50.1	[302]
CrN	PVD	54*	240	3.3	HWTS	5.3	101	33.8*	36.1	[302]
CrN	PVD	66*	240	3.5	M2	7.6	91	41.6*	43.6	[302]
CrN	PVD	66*	240	3.5	HWTS	5.3	98	31.1*	40.8	[302]
TiN	Arc-evaporate	26	550	4	SS304	3	111.3*	18*	19.1	[303]
TiN	Arc-evaporate	26	550	4	M2	8	96.4*	45*	32.6	[303]
TiN	Arc-evaporate	26	550	4	WC (a)	15	98.0*	82*	59.3	[303]
TiN	Arc-evaporate	26	550	4	WC (b)	18	97.2*	95*	69.2	[303]
TiN	Arc-evaporate	26	550	2.2	SCAM	2.7	105.6	20	14. 4	[301]
TiN	Arc-evaporate	26	550	2.2	SUS420J	5.3	105.6	35	25.7	[301]
TiN	Arc-evaporate	26	550	2.2	SKD61	5.7	106.4	38	27.8	[301]
TiN	Arc-evaporate	26	550	2.2	SKH51	7.6	104.2	48	34.8	[301]
TiN	PVD	18	600*	2.4	D9	2	114.5*	15.5	11.9	[304]
TiN	PVD	22*	251*	2	Ti-4Al-4Mo-2Sn	3.6*	150*	36	35.9	[217]
TiN	PVD	22*	251*	2	ASP23	7.5*	150*	75	71.1	[217]
TiN	PACVD	19	600	4	SS316	2.18	55*	9	4.1	[305]
TiN	PACVD	19	600	4	M2	8.27	56*	17.5	11.2	[305]
TiN	PACVD	19	600	4	WC	18.6	61*	32	27.4	[305]
TiN	PAPVD	19	600	2	SS316	2.18	101*	14*	10.1	[305, 306]

TiN	PAPVD	19	600	2	M2	8.27	96*	40*	31.1	[305, 306]
TiN	PAPVD	19	600	2	WC	18.6	100*	83*	74.2	[305, 306]
TiN	PAPVD	19	600	4	SS316	2.18	110*	16*	13.1	[305, 306]
TiN	PAPVD	19	600	4	M2	8.27	90*	45*	28.0	[305, 306]
TiN	PAPVD	19	600	4	WC	18.6	100*	93*	74.3	[305, 306]
TiN	PAPVD	19	600	6	SS316	2.18	100*	22*	12.2	[305, 306]
TiN	PAPVD	19	600	6	M2	8.27	111*	48*	43.2	[305, 306]
TiN	PAPVD	19	600	6	WC	18.6	100*	94*	74.3	[305, 306]

Note: *data not indicated in text, was obtained in the figures.
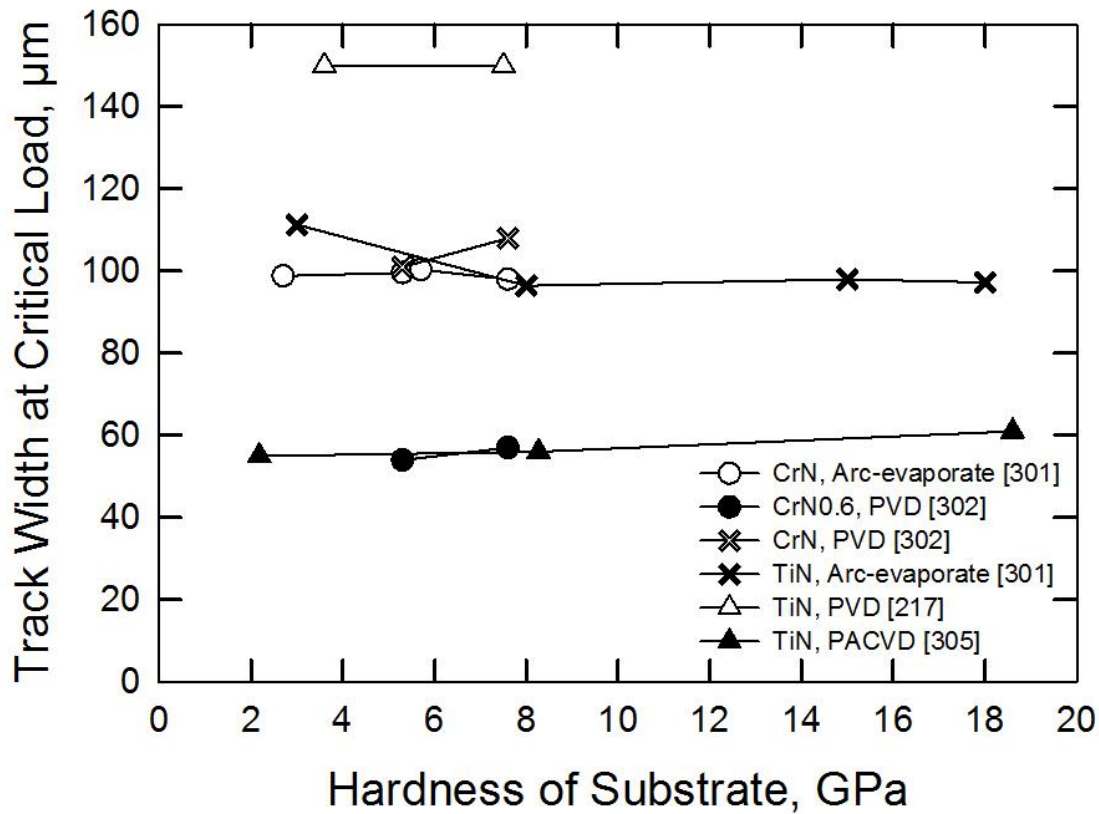
Figure 9-8 Scratch channel width at the critical load for various thin films on different substrates.

Figure 9-9 compares the critical load of each coating obtained from scratching test and the modelling. The dash line in Figure 9-9 stands for a perfect match between experimental results and model prediction. As shown in Figure 9-9, there are large errors for some cases which might be caused by the properties of interlayers or

introduced during the data collection stage. In general, there is a good correlation between experimental results and model prediction for most of the data points.

The model is based on physical understanding the plastic deformation behaviour of coatings during scratch test, and it does not contain any paramters obtained via fitting procedure. This model only requires the basic information of coating and substrate, including hardness, Young's modulus and thickness of the coating, the hardness of the substrate and a critical width of the coating on any substrate. It predicts the critical failure load of thin hard coatings with reasonable accuracy, which can be very useful tool for coating suppliers to predict critical failure load of their coating on a wide range substrates.
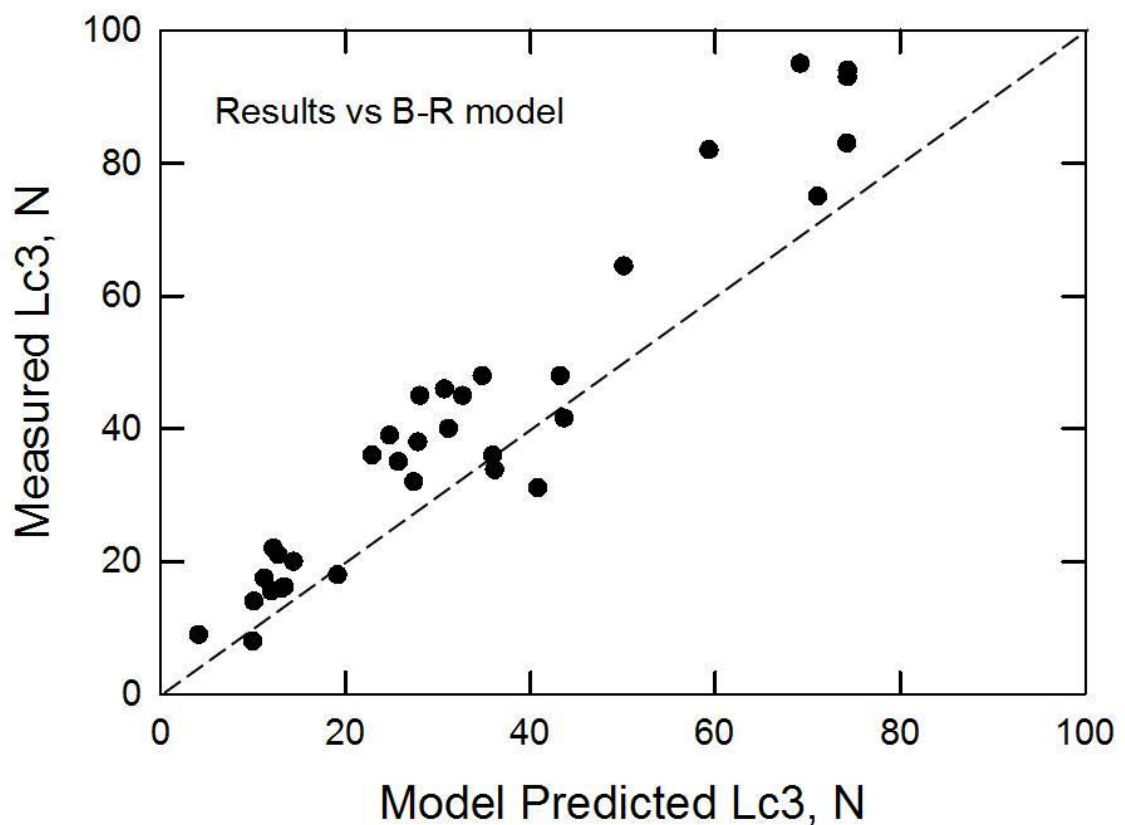
Figure 9-9 Comparison between experimental results and model prediction.

9.4 An improved bio-implant design

As addressed in section 2.1.7, materials for bio-implant applications are required to possess various properties. Up to date, many materials including steel, ceramic, alloys and even polymers were proposed for this application. However, none of them

could fulfill all the requirements. In this study, we propose an improved design for total hip replacements: to fabricate the main body (stem) of bio-implant from UFG pure Ti processed by SPD, and then apply a hard thin coating to protect the formal head of the implant, as demonstrated in Figure 9-10. The properties of this new design are compared with stainless steel, Co-Cr alloy and Ti alloy according to the requirement of bio-metals, as shown in Table 9-3. Firstly, a good corrosion resistance is required to prevent surface damage of the implants in the body fluid, which results in the release of metal ions by the implants into the body. All these candidates have very good corrosion resistance to act as a bio-metal. Ti alloys and pure Ti have superior corrosion resistance which is attributed to the dense oxidation layer formed on the top surface, and this TiO2 layer prevents a further reaction between the metal and the fluids. It is reported that UFG Ti processed via SPD methods have even better corrosion than CG Ti, due to the higher density of grain boundaries and dislocations which improves the passivation of Ti [100]. Secondly, good mechanical properties including high strength and fatigue life are of prime importance for bio-implant use. The materials should be strong enough to withstand the body weight of patients. The fatigue strength of the material determines the long-term success of the implant subjected to cyclic loading. As shown in Table 9-3, the stainless steel, Co-Cr alloy and Ti-6Al-4V all have very high strength and fatigue strength. As clearly shown in Chapter 6, pure Ti in CG state have very low strength of around 660 MPa, and the strength can be improved to around 940 MPa after HPT processing. And a recent study also reported enhanced fatigue strength of UFG pure Ti of 590 MPa after 10^7 cycles loading [101]. Besides, the current implant materials which have higher Young's Modulus Young's Modulus than the bone (~30 GPa), the stress shield effect prevents the needed stress being transferred to adjacent bone, results in bone weakening around the implant and leads to implant loosening. UFG pure Ti has the lowest Young's Modulus of 103 GPa among all these alloys. Thirdly, the wear resistance is very important for the long term service ability, the wear debris is regarded as the main reason for harmful ion release and body tissue reactions. As shown in Chapter 6, both the CG and UFG pure Ti has very poor wear resistance. However, the wear resistance of Ti could be improved by several orders via employing surface coating technologies such as TiN and DLC coating, as shown in Chapter 7. Fourthly, the major advantage of using UFG Ti as the implant metal is

that pure Ti does not contain any harmful alloying elements, the disadvantage of which have been addressed in section 2.1.7.

To sum up, it is anticipated this design will provide the implant with high strength, good fatigue life, good corrosion resistance, together with good wear and tribo-corrosion resistance from the coating. Additional advantages include a lower Young's Modulus compared with ceramics, stainless steel and Ti-6Al-4V; and a non-toxic ion release. Thus, the UFG pure Ti processed by SPD and further protected by coatings shows very strong potential as bio-implant material. A design of this type can be extended also to other coatings or to new materials, such as Ti-Zr, Ti-Nb, and Nb-Zr alloys, which may be employed for the main body of the implant. An advantage of these alloys is that their values for Young's modulus is close to that of human bones [214, 307-309], but the alloys will require additional strengthening using SPD methods.
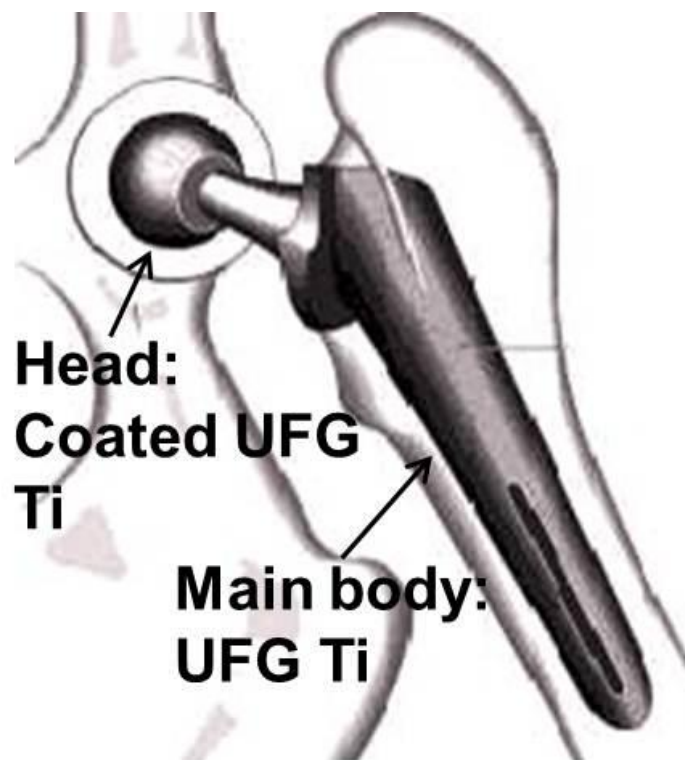
Figure 9-10 The proposed implant design.

The final concern of such a design is the cost. As compared to the cast metals such as steel and Co-Cr alloy, UFG pure Ti is more expensive and it requires SPD processing and coating, all these additional processing will involve further cost of the product. It is hard to estimate the prime cost of implant made by this new design. However, one

should note that for a total joint replacement surgery, the cost of material only takes less than one tenth of the total cost. Huge fraction of total cost due to the medical experiments and post-surgery health care is unavoidable for all the medical related products. Therefore, it is still worth consideration to employ modern technologies such as SPD processing and PVD coating to make the implant with better service ability and less possibility of early failure.

Table 9-3 Comparison on properties of several bio-metals

	SS316	CoCrMo	Ti-6Al-4V	UFG Ti +coating
Corrosion Resistant	Good	Good	Good	Good
Strength, MPa	950	1750	980	940
Fatigue, MPa (10^7Cycle)	440	400-500	500-600	590 [101]
Wear resistant	Poor	Good	Poor	Good
Bio-tolerant	Poor	Poor	Good	Good [104]
Young's Modulus, GPa	205	240	110	103
Toxic Release	Cr, Ni	Co, Cr	Al, V	No

Note: Grey shading indicates that the properties of the metal are not suitable for bio-implant use.

10.   Conclusions

This study has conducted several experimental works to compare the wear behaviour of SPD processed Al-1050 and CP Ti with their coarse-grained counterparts. Wear testing of Al-1050 were performed on a flat area contact, wear testing of Ti were conducted in a micro-contact range. After wear testing, the wear surfaces and debris were examined carefully to determine the dominating wear mechanism. The effect of UFG structure on the wear mechanisms and their transaction were discussed. In order to enhance the wear resistance of SPD materials, surface coatings were also considered to provide a protective layer. The adhesion performance of thin coatings on CG and UFG Ti substrates were compared using Rockwell indentation and scratch tests. The effect of substrate hardness on critical failure load of thin coatings was studied, and further explained using physical modelling. The main conclusions are as follows:

ECAP processing brings significant increase of hardness to Al-1050 via refining microstructure. Samples processed by ECAP were subjected to wear testing against copper alloy. The samples processed by ECAP have similar coefficients of friction to the unprocessed alloy at least for the two loading conditions used in this investigation. The ECAP processing leads to a decrease in the wear resistance and to a mass loss that increases with increasing numbers of ECAP passes. The wear results show excellent agreement with a wear mechanism map when it is recognized that the true contact stress of the connecting areas is significantly higher than expected. The map predicts, and the experiments confirm, the occurrence of a severe platelet wear mechanism. The results suggest that the wear tests are dominated by a severe wear mechanism and the decreasing wear resistance after ECAP is due to the characteristics of grain refinement in ECAP procedure and the inherent loss of strain hardening capacity.

HPT processing performed at a pressure of 6 GPa also leads to significant strength improvement of Al-1050. Wear testing using mild steel as counter material showed clear evidence of transition from severe platelet wear to oxidation wear of both as-received and HPT-processed Al-1050. All the samples have similar coefficient of

friction around 0.6. HPT-processed samples have higher mass loss, which indicates that HPT processing also decreases the wear resistance of Al-1050. HPT-processed samples take a longer period than as-received sample for wear mechanism changes from severe wear to oxidation wear. As Al-1050 is a commercial purity aluminium which has low wear resistance, even oxidation wear of Al-1050 has a very high wear rate in the magnification of 10^{-7} mm^{2}N^{-1}. Therefore Chapter 5, the wear mechanism which produces large debris is named as severe wear, while the wear mechanism which produces tiny debris and involves oxidation process is named as mild wear.

HPT processing of 3 GPa increases microhardness of pure Ti from 182 Hv at the as-received state to ~305 Hv after 10 revolutions of straining, and makes the Grade 2 Ti having comparable strength to Ti-6Al-4V. The micro-scratch tests were employed to examine the micro-tribological behaviour of Ti samples having different grain sizes. Coefficient of friction of all samples is about 0.6, which indicates that grain size of the material has no effect on the coefficient of friction during test. Ploughing and wedge formation were main wear modes for coarse-grained samples, and abrasive was the dominate wear mode for ultrafine-grained samples.

SPD increases the strength of materials, and decreases their ductility and work hardening capacity. Therefore, SPD processing shows a double-side effect on wear resistance of materials, which is highly depended on the main wear mechanism during sliding.

TiN coating and DLC coatings were deposited on CG and UFG Ti. The results indicated that the wear resistance of Ti was improved by two orders by coatings. Adhesion testing showed that the UFG Ti processed by SPD was better substrates compared to CG Ti, as UFG Ti provided the coating with better support with its improved strength. And these adhesion results were successfully explained with a composite hardness model. This model showed relatively good accuracy to predict the critical load of a wide range of thin coatings on different substrates. The combination of SPD processing and coating technologies leads to new design of bio-implants for total joint replacement application.

11.   Future work

The wear resistance of pure Al processed via both ECAP and HPT was compared with CG Al in Chapter 5 and 6, and the results showed the decreased wear resistance of UFG Al. However the strength improvement of Al via SPD processing was very significant. Currently, Al-Si alloy is the mostly widely used Al alloy in tribology contacts, such as valve lifters, piston cylinders and heads. The hard Si particles in Al-Si alloy benefit the wear resistance. Applying SPD processing to Al-Si will bring two main changes: Firstly, SPD processing will lead to grain refinement and strength improvement of the Al matrix, which has been extensively reported for other materials in the literature. Secondly, SPD processing will refine the brittle Si particles. It is still unknown whether the change of Si particle will bring a better wear resistance to the material. Therefore, it is very interesting to study the effect of SPD processing on wear resistance of Al-Si alloys.

In Chapter 6, micro-scratch testing of Ti with different grain sizes was investigated. Wear mechanism during the micro-scratch testing were investigated by studying the wear surface after wear test. In-situ SEM micro-scratch study will be more efficient in observing wear mechanisms and their transactions. As during the scratch testing described in Chapter 6, wear of Ti samples was dominated by plastic deformation behaviours which were not related to air environment. So in-situ wear study equipped within SEM under similar load conditions will clearly demonstrate the wear mechanisms.

The results of Chapter 7 and 8 were very promising, thus the concept of using coated UFG Ti as bio-implant metal will deserve further research. Firstly, all these previous experimental works were conducted under dry sliding conditions. Further experiments in body liquid environment and using joint simulators are necessary to monitor the work condition of bio-implant in a similar manner. Secondly, as clearly shown in section 9.4, the effect of substrate on the performance of coatings was dominating when the coating was very thin. This effect could be eliminated by depositing thick coatings. Therefore, thick coatings produced by oxidation or nitriding methods on UFG Ti are worth exploration for the possibility of bio-implant

applications. SPD processing introduces grain boundaries and dislocations to the metals, and these lattice defects may act as fast atomic diffusion channels, which can be used to accelerate the chemical reaction during oxidation or nitriding treatment. Meanwhile, the large numbers of high-angle grain boundaries and other non-equilibrium defects constitute high stored energy, this may also lead to a better chemical reactivity to the UFG alloys processed by SPD. Therefore, it is very possible oxidation or nitriding of UFG alloys can be performed at a much lower temperature compared to CG alloys. Moreover, it is possible that under the same temperature and duration of oxidation or nitriding, a thicker surface layer can be formed on top of UFG alloys compared to CG alloy.

In this study, pure Ti with UFG structure was investigated as a potential candidate as bio-implant metal. UFG pure Ti has all these properties suitable for this application except its Young's modulus of 103 GPa, which is very high compared to Young's modulus of bones. Recently, researchers are suggesting new Ti alloys such as Ti-13Nb-13Ta and Ti-29Nb-13Ta-4Zr for bio-implant use, these alloys have very low Young's Modulus close to the bone. Therefore, processing these new Ti alloys via SPD and relative coating could enhance their strength and wear resistance, which is very attractive for bio-implant applications.

In Chapter 9, a simple model was proposed based on law of mixtures. This model showed good prediction of critical load of thin coatings on various substrates. This model assumes that the hardness of both coating and substrate is homogeneous along the cross-section. In reality, there are many coatings with gradually changing chemical composition and hardness or deposited on substrates with changing hardness along the cross-section. Applying this model to such a case will require substantial calculation work. Computing software offers an alternative solution, it will be useful to build a finite element model on scratch of thin coatings based on the understanding in section 9.3. The finite element model will be able to predict the scratch critical load of many complex coatings in an effective manner.

References

[1]   Valiev RZ, Langdon TG. *Principles of equal-channel angular pressing as a processing tool for grain refinement*. Progress in Materials Science 2006;51:881.

[2]   Zhilyaev AP, Langdon TG. *Using high-pressure torsion for metal processing: Fundamentals and applications*. Progress in Materials Science 2008;53:893.

[3]   Saito Y, Tsuji N, Utsunomiya H, Sakai T, Hong RG. *Ultra-fine grained bulk aluminium produced by accumulative roll-bonding (ARB) process*. Scripta Materialia 1998;39:1221.

[4]   Tsuji N, Saito Y, Utsunomiya H, Tanigawa S. *Ultra-fine grained bulk steel produced by accumulative roll-bonding (ARB) process*. Scripta Materialia 1999;40:795.

[5]   Valiev RZ, Alexandrov IV, Zhu YT, Lowe TC. *Paradox of strength and ductility in metals processed by severe plastic deformation*. Journal of Materials Research 2002;17:5.

[6]   Furukawa M, Horita Z, Nemoto M, Langdon TG. *The use of severe plastic deformation for microstructural control*. Materials Science and Engineering A 2002;324:82.

[7]   Valiev R. *Nanostructuring of metals by severe plastic deformation for advanced properties*. Nature Materials 2004;3:511.

[8]   Valiev RZ, Estrin Y, Horita Z, Langdon TG, Zehetbauer MJ, Zhu YT. *Producing bulk ultrafine-grained materials by severe plastic deformation*. JOM 2006;58 (4):33.

[9]   Kim WJ, Sa YK. *Micro-extrusion of ECAP processed magnesium alloy for production of high strength magnesium micro-gears*. Scripta Materialia 2006;54:1391.

[10]   Latysh V, Krallics Gy, Alexandrov I, Fodor A. *Application of bulk nanostructured materials in medicine*. Current Applied Physics 2006;6:262.

[11]   Zhu YT, Lowe TC, Langdon TG. *Performance and applications of nanostructured materials produced by severe plastic deformation*. Scripta Materialia 2004;51:825.

[12]   Sanders PG, Fougere GE, Thompson LJ, Eastman JA, Weertman JR. *Improvements in the synthesis and compaction of nanocrystalline materials*. Nanostructured Materials 1997;8:243.

[13]   Eckert J, Holzer JC, Krill CE, Johnson WL. *Reversible grain size changes in ball-milled nanocrystalline Fe-Cu alloys*. Journal of Materials Research 1992;7:1980.

[14]   Valiev RZ, Ivanisenko YuV, Rauch EF, Baudelet B. *Structure and deformation behaviour of armco iron subjected to severe plastic deformation*. Acta Materialia 1996;44:4705.

[15] Valiev RZ, Korznikov AV, Mulyukov RR. *Structure and properties of ultrafine-grained materials produced by severe plastic deformation*. Materials Science and Engineering A 1993;168:141.

[16] Huang JY, Zhu YT, Jiang H, Lowe TC. *Microstructures and dislocation configurations in nanostructured Cu processed by repetitive corrugation and straightening*. Acta Materialia 2001;49:1497.

[17] Shin DH, Park JJ, Kim YS, Park KT. *Constrained groove pressing and its application to grain refinement of aluminium*. Materials Science and Engineering A 2002;328:98.

[18] Segal VM, Reznikov VI, Drobyshevskiy AE, Kopylov VI. *Plastic working of metals by simple shear*. Russian Metallurgy 1981:99.

[19] Horita Z, Fujinami T, Nemoto M, Langdon TG. *Improvement of mechanical properties for Al alloys using equal-channel angular pressing*. Journal of Materials Processing Technology 2001;117:288.

[20] Stolyarov VV, Zhu YT, Alexandrov IV, Lowe TC, Valiev RZ. *Influence of ECAP routes on the microstructure and properties of pure Ti*. Materials Science and Engineering A 2001;299:59.

[21] Nakashima K, Horita Z, Nemoto M, Langdon TG. *Development of a multi-pass facility for equal-channel angular pressing to high total strains*. Materials Science and Engineering A 2000;281:82.

[22] Iwahashi Y, Wang J, Horita Z, Nemoto M, Langdon TG. *Principle of equal-channel angular pressing for the processing of ultra-fine grained materials*. Scripta Materialia 1996;35:143.

[23] Wang JT, Horita ZJ, Furukawa M, Nemoto M, Tsenev NK, Valiev RZ, Ma Y, Langdon TG. *An investigation of ductility and microstructural evoluation in an Al-3%Mg alloy with submicron grain-size*. Journal of Materials Research 1993;8:2810.

[24] Segal VM. *Materials processing by simple shear*. Materials Science and Engineering A 1995;197:157.

[25] Iwahashi Y, Horita Z, Nemoto M, Langdon TG. *An investigation of microstructural evolution during equal-channel angular pressing*. Acta Materialia 1997;45:4733.

[26] Iwahashi Y, Horita Z, Nemoto M, Langdon TG. *The process of grain refinement in equal-channel angular pressing*. Acta Materialia 1998;46:3317.

[27] Furukawa M, Iwahashi Y, Horita Z, Nemoto M, Langdon TG. *The shearing characteristics associated with equal-channel angular pressing*. Materials Science and Engineering A 1998;257:328.

[28] Oh-ishi K, Horita Z, Furukawa M, Nemoto M, Langdon TG. *Communications - Optimizing the rotation conditions for grain refinement in equal-channel angular pressing*. Metallurgical and Materials Transactions A 1998;29:2011.

[29] Lee S, Langdon TG. *Influence of equal-channel angular pressing on the superplastic properties of commercial aluminium alloys*. Superplasticity-Current Status and Future Potential 2000;601:359.

[30] Xu C, Furukawa M, Horita Z, Langdon TG. *The evolution of homogeneity and grain refinement during equal-channel angular pressing: A model for grain refinement in ECAP*. Materials Science and Engineering A 2005;398:66.

[31] Berbon PB, Furukawa M, Horita Z, Nemoto M, Langdon TG. *Influence of pressing speed on microstructural development in equal-channel angular pressing*. Metallurgical and Materials Transactions A 1999;30:1989.

[32] Terhune SD, Swisher DL, Oh-ishi K, Horita Z, Langdon TG, McNelley TR. *An investigation of microstructure and grain-boundary evolution during ECA pressing of pure aluminium*. Metallurgical and Materials Transactions A 2002;33:2173.

[33] Langdon TG. *The principles of grain refinement in equal-channel angular pressing*. Materials Science and Engineering A 2007;462:3.

[34] Furukawa M, Horita Z, Langdon TG. *Factors influencing the shearing patterns in equal-channel angular pressing*. Materials Science and Engineering A 2002;332:97.

[35] Starink MJ, Qiao XG, Zhang JW, Gao N. *Predicting grain refinement by cold severe plastic deformation in alloys using volume averaged dislocation generation*. Acta Materialia 2009;57:5796.

[36] Bridgman P. *On Torsion Combined with Compression*. Journal of Applied Physics 1943;14:273.

[37] Xu C, Horita Z, Langdon TG. *The evolution of homogeneity in an aluminium alloy processed using high-pressure torsion*. Acta Materialia 2008;56:5168.

[38] Zhilyaev AP, Nurislamova GV, Kim B-K, Baró MD, Szpunar JA, Langdon TG. *Experimental parameters influencing grain refinement and microstructural evolution during high-pressure torsion*. Acta Materialia 2003;51:753.

[39] Zhilyaev AP, McNelley TR, Langdon TG. *Evolution of microstructure and microtexture in fcc metals during high-pressure torsion*. Journal of Materials Science 2007;42:1517.

[40] Figueiredo RB, Langdon TG. *Using severe plastic deformation for the processing of advanced engineering materials*. Materials Transactions 2009;50:1613.

[41] Krystian M, Setman D, Mingler B, Krexner G, Zehetbauer MJ. *Formation of superabundant vacancies in nano-Pd-H generated by high-pressure torsion*. Scripta Materialia 2010;62:49.

[42] Zhang JW, Gao N, Starink MJ. *Al-Mg-Cu based alloys and pure Al processed by high pressure torsion: The influence of alloying additions on strengthening*. Materials Science and Engineering A 2010;527:3472.

[43] Wetscher F, Vorhauer A, Stock R, Pippan R. *Structural refinement of low alloyed steels during severe plastic deformation*. Materials Science and Engineering A 2004;387-389:809.

[44] Sakai G, Horita Z, Langdon TG. *Grain refinement and superplasticity in an aluminium alloy processed by high-pressure torsion*. Materials Science and Engineering A 2005;393:344.

[45] Xu C, Langdon TG. *The development of hardness homogeneity in aluminium and an aluminium alloy processed by ECAP*. Journal of Materials Science 2007;42:1542.

[46] Balogh L, Ungár T, Zhao Y, Zhu YT, Horita Z, Xu C, Langdon TG. *Influence of stacking-fault energy on microstructural characteristics of ultrafine-grain copper and copper-zinc alloys*. Acta Materialia 2008;56:809.

[47] Zhao YH, Horita Z, Langdon TG, Zhu YT. *Evolution of defect structures during cold rolling of ultrafine-grained Cu and Cu-Zn alloys: Influence of stacking fault energy*. Materials Science and Engineering A 2008;474:342.

[48] Zhilyaev AP, Kim B-K, Szpunar JA, Báro MD, Langdon TG. *The microstructural characteristics of ultratine-grained nickel*. Materials Science and Engineering A 2005;391:377.

[49] Zhilyaev AP, Oh-ishi K, Langdon TG, McNelley TR. *Microstructural evolution in commercial purity aluminium during high-pressure torsion*. Materials Science and Engineering A 2005;410:277.

[50] Serre P, Figueiredo RB, Gao N, Langdon TG. *Influence of strain rate on the characteristics of a magnesium alloy processed by high-pressure torsion*. Materials Science and Engineering A 2011;528:3601.

[51] Saito Y, Utsunomiya H, Suzuki H, Sakai T. *Improvement in the r-value of aluminium strip by a continuous shear deformation process*. Scripta Materialia 2000;42:1139.

[52] Utsunomiya H, Hatsuda K, Sakai T, Saito Y. *Continuous grain refinement of aluminium strip by conshearing*. Materials Science and Engineering A 2004;372:199.

[53] Zhu YT, Jiang HG, Huang JY, Lowe TC. *A new route to bulk nanostructured metals*. Metallurgical and Materials Transactions A 2001;32:1559.

[54] Huang JY, Zhu YT, Alexander DJ, Liao XZ, Lowe TC, Asaro RJ. *Development of repetitive corrugation and straightening*. Materials Science and Engineering A 2004;371:35.

[55] Varyukhin V, Beygelzimer Y, Synkov S, Orlov D. *Application of twist extrusion*. Materials Science Forum 2006; 503-504:335.

[56] Beygelzimer Y, Varyukhin V, Synkov S, Orlov D. *Useful properties of twist extrusion*. Materials Science and Engineering A 2009;503:14.

[57] Saito Y, Utsunomiya H, Tsuji N, Sakai T. *Novel ultra-high straining process for bulk materials - development of the accumulative roll-bonding (ARB) process*. Acta Materialia 1999;47:579.

[58] Orlov D, Beygelzimer Y, Synkov S, Varyukhin V, Tsuji N, Horita Z. *Plastic flow, structure and mechanical properties in pure Al deformed by twist extrusion*. Materials Science and Engineering A 2009;519:105.

[59] Semenova IP, Polyakov AV, Raab GI, Lowe TC, Valiev RZ. *Enhanced fatigue properties of ultrafine-grained Ti rods processed by ECAP-Conform*. Journal of Materials Science 2012;47:7777.

[60] Edalati K, Horita Z. *Processing sheets and wires by continuous high-pressure torsion*. Reviews on Advanced Materials Science 2012;31:5.

[61] Edalati K, Horita Z. *Continuous high-pressure torsion*. Journal of Materials Science 2010;45:4578.

[62] Wang JT, Li Z, Wang J, Langdon TG. *Principles of severe plastic deformation using tube high-pressure shearing*. Scripta Materialia 2012;67:810.

[63] Arzaghi M, Fundenberger JJ, Toth LS, Arruffat R, Faure L, Beausir B, Sauvage X. *Microstructure, texture and mechanical properties of aluminium processed by high-pressure tube twisting*. Acta Materialia 2012;60:4393.

[64] Horita Z, Fujinami T, Nemoto M, Langdon TG. *Equal-channel angular pressing of commercial aluminium alloys: Grain refinement, thermal stability and tensile properties*. Metallurgical and Materials Transactions A 2000;31:691.

[65] Wang YM, Chen MW, Zhou FH, Ma E. *High tensile ductility in a nanostructured metal*. Nature 2002;419:912.

[66] Wang YM, Ma E. *Three strategies to achieve uniform tensile deformation in a nanostructured metal*. Acta Materialia 2004;52:1699.

[67] Lu L, Shen YF, Chen XH, Qian LH, Lu K. *Ultrahigh strength and high electrical conductivity in copper*. Science 2004;304:422.

[68] Chen MW, Ma E, Hemker KJ, Sheng HW, Wang YM, Cheng XM. *Deformation twinning in nanocrystalline aluminium*. Science 2003;300:1275.

[69] Wu X, Tao N, Hong Y, Lu J, Lu K. *Gamma -> epsilon martensite transformation and twinning deformation in fcc cobalt during surface mechanical attrition treatment*. Scripta Materialia 2005;52:247.

[70] Ma E. *Eight routes to improve the tensile ductility of bulk nanostructured metals and alloys*. JOM 2006;58(4):49.

[71] Zhang X, Wang H, Scattergood RO, Narayan J, Koch CC, Sergueeva AV, Mukherjee AK. *Studies of deformation mechanisms in ultra-fine-grained and nanostructured Zn*. Acta Materialia 2002;50:4823.

[72] Park YS, Chung KH, Kim NJ, Lavernia EJ. *Microstructural investigation of nanocrystalline bulk Al-Mg alloy fabricated by cryomilling and extrusion*. Materials Science and Engineering A 2004;374:211.

[73] Horita Z, Ohashi K, Fujita T, Kaneko K, Langdon TG. *Achieving high strength and high ductility in precipitation-hardened alloys*. Advanced Materials 2005;17:1599.

[74] Valiev RZ, Sergueeva AV, Mukherjee AK. *The effect of annealing on tensile deformation behavior of nanostructured SPD titanium*. Scripta Materialia 2003;49:669.

[75] Langdon TG. *Grain boundary sliding revisited: Developments in sliding over four decades*. Journal of Materials Science 2006;41:597.

[76] Langdon TG. *Seventy-five years of superplasticity: historic developments and new opportunities*. Journal of Materials Science 2009;44:5998.

[77] Horita Z, Furukawa M, Nemoto M, Barnes AJ, Langdon TG. *Superplastic forming at high strain rates after severe plastic deformation*. Acta Materialia 2000;48:3633.

[78] Horita Z, Langdon TG. *Achieving exceptional superplasticity in a bulk aluminium alloy processed by high-pressure torsion*. Scripta Materialia 2008;58:1029.

[79] Kai M, Horita Z, Langdon TG. *Developing grain refinement and superplasticity in a magnesium alloy processed by high-pressure torsion*. Materials Science and Engineering A 2008;488:117.

[80] Figueiredo RB, Langdon TG. *Principles of grain refinement and superplastic flow in magnesium alloys processed by ECAP*. Materials Science and Engineering A 2009;501:105.

[81] Geetha M, Singh AK, Asokamani R, Gogia AK. *Ti based biomaterials, the ultimate choice for orthopaedic implants - A review*. Progress in Materials Science 2009;54:397.

[82] Leopold SS. *Numbers for breakfast: summary of hip arthroplasty outcomes from the national joint registry for England and wales 8th annual report (2011)*. The Journal of Bone and Joint Surgery-American volume 2011;93:1.

[83] Kurtz S, Ong K, Lau E, Mowat F, Halpern M. *Projections of primary and revision hip and knee arthroplasty in the United States from 2005 to 2030*. Journal of Bone and Joint Surgery-American Volume 2007;89A:780.

[84] Okazaki Y, Gotoh E. *Comparison of metal release from various metallic biomaterials in vitro*. Biomaterials 2005;26:11.

[85] Okazaki Y, Goth E. *Metal release from stainless steel, Co-Cr-Mo-Ni-Fe and Ni-Ti alloys in vascular implants*. Corrosion Science 2008;50:3429.

[86] Li Y, Wong C, Xiong J, Hodgson P, Wen C. *Cytotoxicity of Titanium and Titanium Alloying Elements*. Journal of Dental Research 2010;89:493.

[87] Makihira S, Mine Y, Nikawa H, Shuto T, Iwata S, Hosokawa R, Kamoi K, Okazaki S, Yamaguchi Y. *Titanium ion induces necrosis and sensitivity to lipopolysaccharide in gingival epithelial-like cells*. Toxicology in Vitro 2010;24:1905.

[88] Long M, Rack HJ. *Titanium alloys in total joint replacement - a materials science perspective*. Biomaterials 1998;19:1621.

[89] Elias CN, Lima JHC, Valiev R, Meyers MA. *Biomedical applications of titanium and its alloys*. JOM 2008(3);60:46.

[90] Stolyarov VV, Zhu YT, Lowe TC, Islamgaliev RK, Valiev RZ. *A two step SPD processing of ultrafine-grained titanium*. Nanostructured Materials 1999;11:947.

[91] Stolyarov VV, Zhu YT, Alexandrov IV, Lowe TC, Valiev RZ. Influence of ECAP routes on the microstructure and properties of pure Ti. Materials Science and Engineering A 2001; 299:59.

[92] Stolyarov VV, Zhu YT, Alexandrov IV, Lowe TC, Valiev RZ. *Grain refinement and properties of pure Ti processed by warm ECAP and cold rolling*. Materials Science and Engineering A 2003;343:43.

[93] Sordi VL, Ferrante M, Kawasaki M, Langdon TG. *Microstructure and tensile strength of grade 2 titanium processed by equal-channel angular pressing and by rolling*. Journal of Materials Science 2012;47:7870.

[94] Zhao X, Yang X, Liu X, Wang X, Langdon TG. *The processing of pure titanium through multiple passes of ECAP at room temperature*. Materials Science and Engineering A 2010;527:6335.

[95] Zhao X, Fu W, Yang X, Langdon TG. *Microstructure and properties of pure titanium processed by equal-channel angular pressing at room temperature*. Scripta Materialia 2008;59:542.

[96] Todaka Y, Sasaki J, Moto T, Umemoto M. *Bulk submicrocrystalline omega-Ti produced by high-pressure torsion straining*. Scripta Materialia 2008;59:615.

[97] Edalati K, Matsubara E, Horita Z. *Processing Pure Ti by High-Pressure Torsion in Wide Ranges of Pressures and Strain*. Metallurgical and Materials Transactions A 2009;40A:2079.

[98] Sabirov I, Valiev RZ, Semenova IP, Pippan R. *Effect of Equal Channel Angular Pressing on the Fracture Behaviour of Commercially Pure Titanium*. Metallurgical and Materials Transactions A 2010;41A:727.

[99] Islamgaliev RK, Kazyhanov VU, Shestakova LO, Sharafutdinov AV, Valiev RZ. *Microstructure and mechanical properties of titanium (Grade 4) processed by high-pressure torsion*. Materials Science and Engineering A 2008;493:190.

[100] Balyanov A, Kutnyakova J, Amirkhanova NA, Stolyarov VV, Valiev RZ, Liao XZ, Zhao YH, Jiang YB, Xu HF, Lowe TC, Zhu YT. *Corrosion resistance of ultra fine-grained Ti*. Scripta Materialia 2004;51:225.

[101] Semenova IP, Valiev RZ, Yakushina EB, Salimgareeva GH, Lowe TC. *Strength and fatigue properties enhancement in ultrafine-grained Ti produced by severe plastic deformation*. Journal of Materials Science 2008;43:7354.

[102] Semenova IP, Yakushina EB, Nurgaleeva VV, Valiev RZ. *Nanostructuring of Ti-alloys by SPD processing to achieve superior fatigue properties*. International Journal of Materials Research 2009;100:1691.

[103] Estrin Y, Vinogradov A. *Fatigue behaviour of light alloys with ultrafine grain structure produced by severe plastic deformation: An overview*. International Journal of Fatigue 2010;32:898.

[104] Faghihi S, Azari F, Zhilyaev AP, Szpunar JA, Vali H, Tabrizian M. *Cellular and molecular interactions between MC3T3-E1 pre-osteoblasts and nanostructured titanium produced by high-pressure torsion*. Biomaterials 2007;28:3887.

[105] Park JW, Kim YJ, Park CH, Lee DH, Ko YG, Jang JH, Lee CS. *Enhanced osteoblast response to an equal channel angular pressing-processed pure titanium substrate with microrough surface topography*. Acta Biomaterialia 2009;5:3272.

[106] Bindu S, Sanosh KP, Smetana K, Balakrishnan A, Kim TN. *An in vivo Evaluation of Ultra-fine Grained Titanium Implants*. Journal of Materials Science & Technology 2009;25:556.

[107] Valiev RZ, Semenova IP, Latysh VV, Rack H, Lowe TC, Petruzelka J, Dluhos L, Hrusak D, Sochova J. *Nanostructured titanium for biomedical applications*. Advanced Engineering Materials 2008;10:B15.

[108] Marino CEB, Mascaro LH. *EIS characterization of a Ti-dental implant in artificial saliva media: dissolution process of the oxide barrier*. Journal of Electroanalytical Chemistry 2004;568:115.

[109] Diomidis N, Mischler S, More NS, Roy M. *Tribo-electrochemical characterization of metallic biomaterials for total joint replacement*. Acta Biomaterialia 2012;8:852.

[110] Qiao XG, Gao N, Moktadir Z, Kraft M, Starink MJ. *Fabrication of MEMS components using ultrafine-grained aluminium alloys*. Journal of Micromechanics and Microengineering 2010;20:045029.

[111] Qiao XG, Bah MT, Zhang JW, Gao N, Moktadir Z, Kraft M, Starink MJ. *Microembossing of ultrafine grained Al: microstructural analysis and finite element modelling*. Journal of Micromechanics and Microengineering 2010;20:105002.

[112] Gell M. *Applying nanostructured materials to future gas-turbine engines*. JOM 1994(10);46:30.

[113] Kusadome Y, Ikeda K, Nakamori Y, Orimo S, Horita Z. *Hydrogen storage capability of MgNi2 processed by high pressure torsion*. Scripta Materialia 2007;57:751.

[114] Jost HP. *Tribology-origin and future*. Wear 1990;136:1.

[115] Jost HP. *Tribology: how a word was coined 40 years ago*. Proceedings of the Institution of Mechanical Engineers Part J-Journal of Engineering Tribology 2009;223:240.

[116] Williams JA. *Engineering Tribology*. Oxford University Press, 1994.

[117] Dwyer-Joyce RS. *Tribological Design Data*. London: The Tribology Group of The Institution of Mechanical Engineers, 1997.

[118] Bhushan B. *Introduction to tribology*. New York: John Wiley & Sons, 2002.

[119] Bowden FP, Tabor D. *The friction and lubrication of solids*. Oxford: Clarendon Press, 1964.

[120] Meng HC, Ludema KC. *Wear models and predictive equations-their form and content*. Wear 1995;181-183:443.

[121] Williams JA. *Wear modelling: analytical, computational and mapping: a continuum mechanics approach*. Wear 1999;225-229:1.

[122] Archard JF. *Contact and rubbing of flat surfaces*. Journal of Applied Physics 1953;24:981.

[123] Kato K. *Classification of wear mechanisms/models*. Proceedings of the Institution of Mechanical Engineers Part J-Journal of Engineering Tribology 2002;216:349.

[124] Ashby MF, Lim SC. *Wear-mechanism maps*. Scripta Materialia 1990;24:805.

[125] Rigney DA. *Comments on the sliding of wear of metals*. Tribology International 1997;30:361.

[126] Gohar R, Rahnejat H. *Fundamentals of tribology*. London: Imperial College Press, 2008.

[127] Khruschov MM. *Principles of abrasive wear*. Wear 1974;28:69.

[128] Kato K. *Abrasive wear of metals*. Tribology International 1997;30:333.

[129] Challen JM, Oxley PLB. *Explanation of the different regimes of friction and wear using asperity deformation models*. Wear 1979;53:229.

[130] Challen JM, Oxley PLB. *Slip-line fields for explaining the mechanics of polishing and related processes*. International Journal of Mechanical Sciences 1984;26:403.

[131] Kayaba T, Hokkirigawa K, Kato K. *Analysis of the abrasive wear mechanism by successive observations of wear processes in a scanning electron-microscope tribosystem*. Wear 1986;110:419.

[132] Kitsunai H, Kato K, Hokkirigawa K, Inoue H. *The transitions between microscopic wear modes during repeated sliding friction observed by a scanning electron-microscope tribosystem*. Wear 1990;135:237.

[133] Kitsunai H, Hokkirigawa K, Tsumaki N, Kato K. *Transitions of microscopic wear mechanism for Cr2O3 ceramic coatings during repeated sliding observed in a scanning electron-microscope tribosystem*. Wear 1991;151:279.

[134] Kato K. *Micromechanisms of wear - wear modes*. Wear 1992;153:277.

[135] Quinn TFJ. *Oxidational wear modeling: part 1*. Wear 1992;153:179.

[136] Quinn TFJ. *Oxidational wear modeling: part 2*. Wear 1994;175:199.

[137] Quinn TFJ. *Oxidational wear modeling: part 3*. Wear 1998;216:262.

[138] Mischler S, Debaud S, Landolt D. *Wear-accelerated corrosion of passive metals in tribocorrosion systems*. Journal of the Electrochemical Society 1998;145:750.

[139] Landolt D, Mischler S, Stemp M. *Electrochemical methods in tribocorrosion: a critical appraisal*. Electrochimica Acta 2001;46:3913.

[140] Ismail MNF, Harvey TJ, Wharton JA, Wood RJK, Humphreys A. *Surface potential effects on friction and abrasion of sliding contacts lubricated by aqueous solutions*. Wear 2009;267:1978.

[141] Elleuch K, Fouvry S. *Wear analysis of A357 aluminium alloy under fretting*. Wear 2002;253:662.

[142] Szolwinski MP, Farris TN. *Mechanics of fretting fatigue crack formation*. Wear 1996;198:93.

[143] Berthier Y, Vincent L, Godet M. *Fretting fatigue and fretting wear*. Tribology International 1989;22:235.

[144] Philipp A, Lauterborn W. *Cavitation erosion by single laser-produced bubbles*. Journal of Fluid Mechanics 1998;361:75.

[145] Wood RJK. *The sand erosion performance of coatings*. Materials & Design 1999;20:179.

[146] Ramesh CS, Keshavamurthy R, Channabasappa BH, Pramod S. *Influence of heat treatment on slurry erosive wear resistance of Al6061 alloy*. Materials & Design 2009;30:3713.

[147] Clark HM, Hartwich RB. *A re-examination of the 'particle size effect' in slurry erosion*. Wear 2001;248:147.

[148] Fang CK, Chuang TH. *The effect of humidity on the erosive wear of 6063 Al alloy*. Wear 1999;236:144.

[149] Mann BS, Arya V. *An experimental study to corelate water jet impingement erosion resistance and properties of metallic materials and coatings*. Wear 2002;253:650.

[150] Steller J. *International Cavitation Erosion Test and quantitative assessment of material resistance to cavitation*. Wear 1999;233-235:51.

[151] Jahanmir S. *The relationship of tangential stress to wear particle formation mechanisms*. Wear 1985;103:233.

[152] Lim SC, Ashby MF. *Wear-mechanism maps*. Acta Materialia 1987;35:1.

[153] Lim SC. *Recent developments in wear-mechanism maps*. Tribology International 1998;31:87.

[154] Lim SC. *The relevance of wear-mechanism maps to mild-oxidational wear*. Tribology International 2002;35:717.

[155] Liu Y, Asthana R, Rohatgi P. *A map for wear mechanisms in aluminium-alloys*. Journal of Materials Science 1991;26:99.

[156] Chen H, Alpas AT. *Sliding wear map for the magnesium alloy Mg-9Al-0.9 Zn (AZ91)*. Wear 2000;246:106.

[157] Childs THC. *The mapping of metallic sliding wear*. Proceedings of the Institution of Mechanical Engineers Part C 1988;202:379.

[158] Bolelli G, Cannillo V, Lusvarghi L, Manfredini T. *Wear behaviour of thermally sprayed ceramic oxide coatings*. Wear 2006;261:1298.

[159] Rama Krishna L, Somaraju KRC, Sundararajan G. *The tribological performance of ultra-hard ceramic composite coatings obtained through microarc oxidation*. Surface & Coatings Technology 2003;163-164:484.

[160] Wheeler JM, Collier CA, Paillard JM, Curran JA. *Evaluation of micromechanical behaviour of plasma electrolytic oxidation (PEO) coatings on Ti-6Al-4V*. Surface & Coatings Technology 2010;204:3399.

[161] Choy KL. *Chemical vapour deposition of coatings*. Progress in Materials Science 2003;48:57.

[162] Rie K-T, Gebauer A, Wöhle J. *Plasma assisted CVD for low temperature coatings to improve the wear and corrosion resistance*. Surface & Coatings Technology 1996;86-87:498.

[163] Byeli AV, Kukareko VA, Kononov AG. *Titanium and zirconium based alloys modified by intensive plastic deformation and nitrogen ion implantation for*

biocompatible implants. Journal of the Mechanical Behaviour of Biomedical Materials 2012;6:89.

[164] Alsaran A, Purcek G, Hacisalihoglu I, Vangolu Y, Bayrak Ö, Karaman I, Celik A. *Hydroxyapatite production on ultrafine-grained pure titanium by micro-arc oxidation and hydrothermal treatment*. Surface & Coatings Technology 2011;205:S537.

[165] PalDey S, Deevi SC. *Single layer and multilayer wear resistant coatings of (Ti,Al)N: a review*. Materials Science and Engineering A 2003;342:58.

[166] Hoche H, Schmidt J, Gross S, Trossmann T, Berger C. *PVD coating and substrate pretreatment concepts for corrosion and wear protection of magnesium alloys*. Surface & Coatings Technology 2011;205:S145.

[167] Heinke W, Leyland A, Matthews A, Berg G, Friedrich C, Broszeit E. *Evaluation of PVD nitride coatings, using impact, scratch and Rockwell-C adhesion tests*. Thin Solid Films 1995;270:431.

[168] Starosvetsky D, Gotman I. *Corrosion behavior of titanium nitride coated Ni-Ti shape memory surgical alloy*. Biomaterials 2001;22:1853.

[169] Piscanec S, Ciacchi LC, Vesselli E, Comelli G, Sbaizero O, Meriani S, De Vita A. *Bioactivity of TiN-coated titanium implants*. Acta Materialia 2004;52:1237.

[170] Balla VK, Bhat A, Bose S, Bandyopadhyay A. *Laser processed TiN reinforced Ti6Al4V composite coatings*. Journal of the Mechanical Behaviour of Biomedical Materials 2012;6:9.

[171] Tiainen VM. *Amorphous carbon as a bio-mechanical coating - mechanical properties and biological applications*. Diamond & Related Materials 2001;10:153.

[172] Joyce TJ. *Examination of failed ex vivo metal-on-metal metatarsophalangeal prosthesis and comparison with theoretically determined lubrication regimes*. Wear 2007;263:1050.

[173] Falub CV, Müeller U, Thorwarth G, Parlinska-Wojtan M, Voisard C, Hauert R. *In vitro studies of the adhesion of diamond-like carbon thin films on CoCrMo biomedical implant alloy*. Acta Materialia 2011;59:4678.

[174] Hauert R, Thorwarth G, Müeller U, Stiefel M, Falub CV, Thorwarth K, Joyce TJ. *Analysis of the in-vivo failure of the adhesive interlayer for a DLC coated articulating metatarsophalangeal joint*. Diamond & Related Materials 2012;25:34.

[175] Abd EI Aal MI, EI Mahallawy N, Shehata FA, Abd El Hameed M, Yoon EY, Kim HS. *Wear properties of ECAP-processed ultrafine grained Al-Cu alloys*. Materials Science and Engineering A 2010;527:3726.

[176] Zhang ZG, Hosoda S, Kim I-S, Watanabe Y. *Grain refining performance for Al and Al-Si alloy casts by addition of equal-channel angular pressed Al-5 mass% Ti alloy*. Materials Science and Engineering A 2006;425:55.

[177] Moshkovich A, Perfilyev V, Lapsker I, Gorni D, Rapoport L. *The effect of grain size on stribeck curve and microstructure of copper under friction in the steady friction state*. Tribology Letters 2011;42:89.

[178] Gao LL, Cheng XH. *Effect of ECAE on microstructure and tribological properties of Cu-10%Al-4%Fe alloy*. Tribology Letters 2007;27:221.

[179] Gao LL, Cheng XH. *Microstructure and dry sliding wear behaviour of Cu-10%Al-4Fe alloy produced by equal channel angular extrusion*. Wear 2008;265:986.

[180] Gao LL, Cheng XH. *Microstructure, phase transformation and wear behaviour of Cu-10%Al-4Fe alloy processed by ECAE*. Materials Science and Engineering A 2008;473:259.

[181] Bera S, Zúberová Z, Hellmig RJ, Estrin Y, Manna I. *Synthesis of copper alloys with extended solid solubility and nano Al(2)O(3) dispersion by mechanical alloying and equal channel angular pressing*. Philosophical Magazine 2010;90:1465.

[182] La P, Ma J, Zhu YT, Yang J, Liu W, Xue Q, Valiev RZ. *Dry-sliding tribological properties of ultrafine-grained Ti prepared by severe plastic deformation*. Acta Materialia 2005;53:5167.

[183] Wen M, Wen C, Hodgson PD, Li YC. *Tribological behaviour of pure Ti with a nanocrystalline surface layer under different loads*. Tribology Letters 2012;45:59.

[184] Stolyarov VV, Shuster LSh, Migranov MSh, Valiev RZ, Zhu YT. *Reduction of friction coefficient of ultrafine-grained CP titanium*. Materials Science and Engineering A 2004;371:313.

[185] Semenov VI, Jeng Y-R, Huang S-J, Dao Y-Zh, Hwang S-J, Shuster L-Sh, Chertovskikh S-V, Lin P-Ch. *Tribological properties of the AZ91D magnesium alloy hardened with silicon carbide and by severe plastic deformation*. Journal of Friction and Wear 2009;30:194.

[186] Kim YS, Ha JS, Kim WJ. *Dry sliding wear characteristics of severely deformed 6061 aluminium and AZ61 magnesium alloys*. Materials Science Forum 2 2004;449-454:597.

[187] Cheng X, Li Z, Xiang G. *Dry sliding wear behaviour of TiNi alloy processed by equal channel angular extrusion*. Materials & Design 2007;28:2218.

[188] Korshunov LG, Pushin VG, Chernenko NL, Makarov VV. *Structural transformations, strengthening, and wear resistance of titanium nickelide upon abrasive and adhesive wear*. Physics of Metals and Metallography 2010;110:91.

[189] Purcek G, Saray O, Kucukomeroglu T, Haouaoui M, Karaman I. *Effect of equal-channel angular extrusion on the mechanical and tribological properties of as-cast Zn-40Al-2Cu-2Si alloy*. Materials Science and Engineering A 2010;527:3480.

[190] Xu C, Horita Z, Langdon TG. *The evolution of homogeneity in processing by high-pressure torsion*. Acta Materialia 2007;55:203.

[191] Ikeda K, Takata N, Yamada K, Yoshida F, Nakashima H, Tsuji N. *Grain boundary structure in ARB processed copper*. Materials Science Forum 2006;503-504:925.

[192] Takata N, Yamada K, Ikeda K, Yoshida F, Nakashima H, Tsuji N. *Annealing behaviour and recrystallized texture in ARB processed copper*. Materials Science Forum 2006;503-504:919.

[193] Faghihi S, Li D, Szpunar JA. *Tribocorrosion behaviour of nanostructured titanium substrates processed by high-pressure torsion*. Nanotechnology 2010;21:485703.

[194] Kucukomeroglu T. *Effect of equal-channel angular extrusion on mechanical and wear properties of eutectic Al-12Si alloy*. Materials & Design 2010;31:782.

[195] Nickel D, Alisch G, Podlesak H, Hockauf M, Fritsche G, Lampke T. *Microstructure, corrosion and wear behaviour of UFG-powder-metallurgical Al-Cu alloys, Al-Cu/Al(2)O(3)(p) and Al-Cu/SiC(p) composites*. Reviews on Advanced Materials Science 2010;25:261.

[196] Kim YS, Yu HS, Shin DH. *Low sliding-wear resistance of ultrafine-grained Al alloys and steel having undergone severe plastic deformation*. International Journal of Materials Research 2009;100:871.

[197] Eizadjou M, Manesh HD, Janghorban K. *Microstructure and mechanical properties of ultra-fine grains (UFGs) aluminium strips produced by ARB process*. Journal of Alloys and Compounds 2009;474:406.

[198] Talachi AK, Eizadjou M, Manesh HD, Janghorban K. *Wear characteristics of severely deformed aluminium sheets by accumulative roll bonding (ARB) process*. Materials Characterization 2011;62:12.

[199] Kim YS, Lee TO, Shin DH. *Microstructural evolution and mechanical properties of ultrafine grained commercially pure 1100 aluminium alloy processed by accumulative roll-bonding (ARB)*. Materials Science Forum 2004;449-454:625.

[200] Sato H, El-hadad S, Sitdikov O, Watanabe Y. *Effects of processing routes on wear property of Al-Al3Ti alloys severely deformed by ECAP*. Materials Science Forum 2008;584-586:971.

[201] El-Hadad S, Sato H, Watanabe Y. *Anisotropic mechanical properties of equal channel angular pressed Al-5% Zr alloy containing platelet particles*. Materials Science and Engineering A 2010;527:4674.

[202] Purcek G, Saray O, Kul O, Karaman I, Yapici GG, Haouaoui M, Maier HJ. *Mechanical and wear properties of ultrafine-grained pure Ti produced by multi-pass equal-channel angular extrusion*. Materials Science and Engineering A 2009;517:97.

[203] Karaman I, Haouaoui M, Maier HJ. *Nanoparticle consolidation using equal channel angular extrusion at room temperature*. Journal of Materials Science 2007;42:1561.

[204] Purcek G, Saray O, Rubitschek F, Niendorf T, Maier HJ, Karaman I. *Effect of internal oxidation on wear behavior of ultrafine-grained Nb-Zr*. Acta Materialia 2011;59:7683.

[205] Kim YS, Ha JS, Shin DH. *Sliding wear characteristics of ultrafine-grained non-strain-hardening aluminium-magnesium alloys*. Material Science Forum 2005;475-479:401.

[206] Eizadjou M, Talachi AK, Manesh HD, Janghorban K. *Sliding wear behavior of Severely deformed 6061 aluminium alloy by accumulative roll bonding (ARB) process*. Material Science Forum 2011;667-669:1107.

[207] Ba DM, Ma SN, Meng FJ, Li CQ. *Friction and wear behaviors of nanocrystalline surface layer of chrome-silicon alloy steel*. Surface & Coatings Technology 2007;202:254.

[208] Zhang YS, Han Z, Wang K, Lu K. *Friction and wear behaviors of nanocrystalline surface layer of pure copper*. Wear 2006;260:942.

[209] Korshunov LG, Noskova NI, Korznikov AV, Chernenko NL, Vil'danova NF. *Effect of severe plastic deformation on the microstructure and tribological properties of a babbit B83*. Physics of Metals and Metallography 2009;108:519.

[210] Kato H, Todaka Y, Umemoto M, Morisako K, Hashimoto M, Haga M. *Dry sliding wear properties of sub-microcrystalline ultra-low carbon steel produced by high-pressure torsion straining*. Materials Transactions 2012;53:128.

[211] Wang ZB, Tao NR, Li S, Wang W, Liu G, Lu J, Lu K. *Effect of surface nanocrystallization on friction and wear properties in low carbon steel*. Materials Science and Engineering A 2003;352:144.

[212] Alsaran A, Purcek G, Hacisalihoglu I, Vangolu Y, Bayrak Ö, Celik A. *Hydroxyapatite production on ultrafine-grained pure titanium by micro-arc oxidation and hydrothermal treatment*. Surface & Coatings Technology 2011;205:S537.

[213] Garbacz H, Gradzka-Dahlke M, Kurzydłowski KJ. *The tribological properties of nano-titanium obtained by hydrostatic extrusion*. Wear 2007;263:572.

[214] Suresh KS, Geetha M, Richard C, Landoulsi J, Ramasawmy H, Suwas S, Asokamani R. *Effect of equal channel angular extrusion on wear and corrosion behavior of the orthopedic Ti-13Nb-13Zr alloy in simulated body fluid*. Materials Science and Engineering C 2012;32:763.

[215] Vidakis N, Antoniadis A, Bilalis N. *The VDI 3198 indentation test evaluation of a reliable qualitative control for layered compounds*. Journal of Materials Processing Technology 2003;143-144:481.

[216] Bull SJ. *Failure mode maps in the thin film scratch adhesion test*. Tribology International 1997;30:491.

[217] Stallard J, Poulat S, Teer DG. *The study of the adhesion of a TiN coating on steel and titanium alloy substrates using a multi-mode scratch tester*. Tribology International 2006;39:159.

[218] Kato K. *Microwear mechanisms of coatings*. Surface & Coatings Technology 1995;77:469.

[219] Gee MG, Gee AD. *A cost effective test system for micro-tribology experiments*. Wear 2007;263:1484.

[220] Winkless L, Martinot E, Gee MG, Cuenat A. *Microtribology friction measurements on microtextured silicon*. Tribology: Materials, Surfaces & Interfaces 2009:165.

[221] Gee MG. *Model scratch corrosion studies for WC/Co hardmetals*. Wear 2010;268:1170.

[222] Gee MG, Nunn JW, Muniz-Piniella A. *Micro-tribology experiments on engineering coatings*. Wear 2011;271:2673.

[223] Qiao XG, Gao N, Starink MJ. *A model of grain refinement and strengthening of Al alloys due to cold severe plastic deformation*. Philosophical Magazine 2012;92:446.

[224] Kawasaki M, Horita Z, Langdon TG. *Microstructural evolution in high purity aluminium processed by ECAP*. Materials Science and Engineering A 2009;524:143.

[225] Nakashima K, Horita Z, Nemoto M, Langdon TG. *Influence of channel angle on the development of ultrafine grains in equal-channel angular pressing*. Acta Materialia 1998;46:1589.

[226] Salem AA, Langdon TG, McNelley TR, Kalidindi SR, Semiatin SL. *Strain-path effects on the evolution of microstructure and texture during the severe-plastic deformation of aluminium*. Metallurgical and Materials Transactions A 2006;37A:2879.

[227] Kuo SM, Rigney DA. *Sliding behaviour of aluminium*. Materials Science and Engineering A 1992;157:131.

[228] Rigney DA. *Transfer, mixing and associated chemical and mechanical processes during the sliding of ductile materials*. Wear 2000;245:1.

[229] Zhang J, Alpas AT. *Transition between mild and severe wear in aluminium alloys*. Acta Materialia 1997;45:513.

[230] Pramila BN, Biswas SK. *Effect of magnesium addition and heat-treatment on mild wear of hypoeutectic aluminium-silicon alloys*. Acta Materialia 1991;39:833.

[231] Tandon KN, Li XY. *Wear debris characterization of Al-Si alloys sliding against steel under dry wear conditions*. Scripta Materialia 1997;38:7.

[232] Li XY, Tandon KN. *Microstructural characterization of mechanically mixed layer and wear debris in sliding wear of an Al alloy and an Al based composite*. Wear 2000;245:148.

[233] Nethercot DA. *Structural use of aluminium in the construction industry*. Materials Science Forum 2002;396-404:15.

[234] Wang J, Iwahashi Y, Horita Z, Furukawa M, Nemoto M, Valiev RZ, Langdon TG. *An investigation of microstructural stability in an Al-Mg alloy with submicrometer grain size*. Acta Materialia 1996;44:2973.

[235] Lim SC, Ashby MF, Brunton JH. *Wear-rate transitions and their relationship to wear mechanisms*. Acta Materialia 1987;35:1343.

[236] Rigney DA. *The roles of hardness in the sliding behaviour of materials*. Wear 1994;175:63.

[237] Blau PJ. *Interrelationships of the friction and wear break-in behaviour of metals in sliding contact*. Wear 1981;71:29.

[238] Hiratsuka K, Muramoto K. *Role of wear particles in severe-mild wear transition*. Wear 2005;259:467.

[239] Kim HJ, Karthikeyan S, Rigney D. *The structure and composition of aluminium wear debris generated by unlubricated sliding in different environments*. Wear 2007;263:849.

[240] Kim HJ, Windl W, Rigney D. *Structure and chemical analysis of aluminium wear debris: Experiments and ab initio simulations*. Acta Materialia 2007;55:6489.

[241] Kim YS, Yu HS, Shin DH. *Tribological characteristics of coarse and ultra-fine grained ferrite-martensite dual phase steel fabricated by equal channel angular pressing*. Solid State Phenomena 2007;124-126:1389.

[242] Cetlin PR, Aguilar MTP, Figueiredo RB, Langdon TG. *Avoiding cracks and inhomogeneities in billets processed by ECAP*. Journal of Materials Science 2010;45:4561.

[243] Liew WYH. *Effect of relative humidity on the unlubricated wear of metals*. Wear 2006;260:720.

[244] Edalati K, Horita Z, Yagi S, Matsubara E. *Allotropic phase transformation of pure zirconium by high-pressure torsion*. Materials Science and Engineering A 2009;523:277.

[245] Garbacz H, Kurzydlowski KJ. *Properties of nanotitanium for potential medical applications*. Macromolecular Symposia 2007;253:128.

[246] Lapovok RY. *The role of back-pressure in equal channel angular extrusion*. Journal of Materials Science 2005;40:341.

[247] Vinogradov AY, Stolyarov VV, Hashimoto S, Valiev RZ. *Cyclic behavior of ultrafine-grain titanium produced by severe plastic deformation*. Materials Science and Engineering A 2001;318:163.

[248] Ko YG, Shin DH, Park K-T, Lee CS. *An analysis of the strain hardening behaviour of ultra-fine grain pure titanium*. Scripta Materialia 2006;54:1785.

[249] Yapici GG, Karaman I, Maier HJ. *Mechanical flow anisotropy in severely deformed pure titanium*. Materials Science and Engineering A 2006;434:294.

[250] Stolyarov VV, Zeipper L, Mingler B, Zehetbauer M. *Influence of post-deformation on CP-Ti processed by equal channel angular pressing*. Materials Science and Engineering A 2008;476:98.

[251] Kang D-H, Kim T-W. *Mechanical behaviour and microstructural evolution of commercially pure titanium in enhanced multi-pass equal channel angular pressing and cold extrusion*. Materials & Design 2010;31:S54.

[252] Zhang Y, Figueiredo RB, Alhajeri SN, Wang JT, Gao N, Langdon TG. *Structure and mechanical properties of commercial purity titanium processed by ECAP at room temperature*. Materials Science and Engineering A 2011;528:7708.

[253] Purcek G, Yapici GG, Karaman I, Maier HJ. *Effect of commercial purity levels on the mechanical properties of ultrafine-grained titanium*. Materials Science and Engineering A 2011;528:2303.

[254] Stolyarov VV, Zhu YT, Lowe TC, Valiev RZ. *Microstructure and properties of pure Ti processed by ECAP and cold extrusion*. Materials Science and Engineering A 2001;303:82.

[255] Sergueeva AV, Stolyarov VV, Valiev RZ, Mukherjee AK. *Advanced mechanical properties of pure titanium with ultrafine grained structure*. Scripta Materialia 2001;45:747.

[256] Stolyarov VV, Zhu YT, Alexandrov IV, Lowe TC, Valiev RZ. *Grain refinement and properties of pure Ti processed by warm ECAP and cold rolling*. Materials Science and Engineering A 2003;343:43.

[257] Sabirov I, Perez-Prado MT, Molina-Aldareguia JM, Semenova IP, Salimgareeva GKh, Valiev RZ. *Anisotropy of mechanical properties in high-strength ultra-fine-grained pure Ti processed via a complex severe plastic deformation route*. Scripta Materialia 2011;64:69.

[258] Jain A, Basu B, Manoj Kumar BV, Harshavardhan, Sarkar J. *Grain size-wear rate relationship for titanium in liquid nitrogen environment*. Acta Materialia 2010;58:2313.

[259] Bhushan B, Israelachvili JN, Landman U. *Nanotribology - friction, wear and lubrication at the atomic-scale*. Nature 1995;374:607.

[260] Williams JA, Le HR. *Tribology and MEMS*. Journal of Physics D 2006;39:R201.

[261] Sasada T, Oike M, Emori N. *The effect of abrasive grain-size on the transition between abrasive and adhesive wear*. Wear 1984;97:291.

[262] Rigney DA. *Sliding wear of metals*. Annual Review of Materials Science 1988;18:141.

[263] Umemoto M, Todaka Y, Sasaki J, Shuro I. *Strain gradient hardening and pressure induced phase transformation of metals by HPT*. Materials Science Forum 2008;584-586:493.

[264] Wang YB, Zhao YH, Lian Q, Liao XZ, Valiev RZ, Ringer SP, Zhu YT, Lavernia EJ. *Grain size and reversible beta-to-omega phase transformation in a Ti alloy*. Scripta Materialia 2010;63:613.

[265] Hokkirigawa K, Kato K, Li ZZ. *The effect of hardness on the transition of the abrasive wear mechanism of steels*. Wear 1988;123:241.

[266] Dobrzanski LA, Polok M, Adamiak M. *Structure and properties of wear resistance PVD coatings deposited onto X37CrMoV5-1 type hot work steel*. Journal of Materials Processing Technology 2005;164-165:843.

[267] Guruvenket S, Li D, Klemberg-Sapieha JE, Martinu L, Szpunar J. *Mechanical and tribological properties of duplex treated TiN, nc-TiN/a-SiNx and nc-TiCN/a-SiCN coatings deposited on 410 low alloy stainless steel*. Surface & Coatings Technology 2009;203:2905.

[268] Yilbas BS, Shuja SZ. *Laser treatment and PVD TiN coating of Ti-6Al-4V alloy*. Surface & Coatings Technology 2000;130:152.

[269] Jeong S-H, Shin Y-H, Kim H-J, Song S-J, Lee Y-Z. *A study on scuffing and transition of friction and wear of TiN films using ultrasonic backward radiation*. Wear 2007;263:1386.

[270] Takadoum J, Bennani HH, Allouard M. *Friction and wear characteristics of TiN, TiCN acid diamond-like carbon films*. Surface & Coatings Technology 1997;88:232.

[271] Yang Q, Zhao LR. *Dry sliding wear of magnetron sputtered TiN/CrN superlattice coatings*. Surface & Coatings Technology 2003;173:58.

[272] Öztürk A, Ezirmik KV, Kazmanli K, Ürgen M, Eryilmaz OL, Erdemir A. *Comparative tribological behaviors of TiN-, CrN- and MoN-Cu nanocomposite coatings*. Tribology International 2008;41:49.

[273] Dong H, Shi W, Bell T. *Potential of improving tribological performance of UHMWPE by engineering the Ti6Al4V counterfaces*. Wear 1999;225:146.

[274] Hainsworth SV, Soh WC. *The effect of the substrate on the mechanical properties of TiN coatings*. Surface & Coatings Technology 2003;163-164:515.

[275] Nevelos JE, Ingham E, Doyle C, Fisher J, Nevelos AB. A*nalysis of retrieved alumina ceramic components from Mittelmeier total hip prostheses*. Biomaterials 1999;20:1833.

[276] Hatton A, Nevelos JE, Matthews JB, Fisher J, Ingham E. *Effects of clinically relevant alumina ceramic wear particles on TNF-alpha production by human peripheral blood mononuclear phagocytes*. Biomaterials 2003;24:1193.

[277] Hatton A, Nevelos JE, Nevelos AA, Banks RE, Fisher J, Ingham E. *Alumina-alumina artificial hip joints. Part I: a histological analysis and characterisation of wear debris by laser capture microdissection of tissues retrieved at revision*. Biomaterials 2002;23:3429.

[278] Voevodin AA, Rebholz C, Matthews A. *Comparative tribology studies of hard ceramic and composite metal-DLC coatings in sliding friction conditions*. Tribology Transactions 1995;38:829.

[279] Takadoum J, Bennani HH. *Influence of substrate roughness and coating thickness on adhesion, friction and wear TiN films*. Surface & Coatings Technology 1997;96:272.

[280] Pardo A, Gómez-Aleixandre C, Orwa JO, Cimmino A, Prawer S. *Modification of characteristics of diamond-like carbon thin films by low chromium content addition*. Diamond & Related Materials 2012;26:39.

[281] Zhao F, Li H, Ji L, Wang Y, Zhou H, Chen J. *Ti-DLC films with superior friction performance*. Diamond & Related Materials 2010;19:342.

[282] Czyzniewski A. *Optimising deposition parameters of W-DLC coatings for tool materials of high speed steel and cemented carbide*. Vacuum 2012;86:2140.

[283] Lee DBN, Roberts M, Bluchel CG, Odell RA. *Zirconium: biomedical and nephrological applications*. Asaio Journal 2010;56:550.

[284] Kumar P, Dilli Badu P, Mohan L, Anandan C, Grips VKW. *Wear and corrosion resistance of Zr doped DLC on Ti-13Zr-13Nb biomedical alloy*. Journal of Materials Engineering and Performance 2012;22:283.

[285] Oliver WC, Pharr GM. *An improved technique for determining hardness and elastic-modulus using load and displacement sensing indentation experiments*. Journal of Materials Research 1992;7:1564.

[286] Escudeiro A, Polcar T, Cavaleiro A. *a-C(:H) doped with Zr coatings deposited on biomedical Ti-based substrates: tribological properties*. Thin Solid Films 2012:In Press.

[287] Chen J, Bell GA, Beake BD, Dong H. *Low temperature nano-tribological study on a functionally graded tribological coating using nanoscratch tests*. Tribology Letters 2011;43:351.

[288] Ichimura H, Rodrigo A. *The correlation of scratch adhesion with composite hardness for TiN coatings*. Surface & Coatings Technology 2000;126:152.

[289] Wang SC, Lefebvre F, Yan JL, Sinclair I, Starink MJ. *VPPA welds of Al-2024 alloys: Analysis and modelling of local microstructure and strength*. Materials Science and Engineering A 2006;431:123.

[290] Nes E, Pettersen T, Marthinsen K. *On the mechanisms of work hardening and flow-stress saturation*. Scripta Materialia 2000;43:55.

[291] Ashby MF. *Deformation of plastically non-homogeneous materials*. Philosophical Magazine 1970;21:399.

[292] Fleck NA, Hutchinson JW. *A reformulation of strain gradient plasticity*. Journal of the Mechanics and Physics of Solids 2001;49:2245.

[293] Fleck NA, Ashby MF, Hutchinson JW. *The role of geometrically necessary dislocations in giving material strengthening*. Scripta Materialia 2003;48:179.

[294] Kocks UF, Jonas JJ, Mecking H. *Development of strain-rate gradients*. Acta Materialia 1979;27:419.

[295] Mecking H, Kocks UF. *Kinetics of flow and strain-hardening*. Acta Materialia 1981;29:1865.

[296] Estrin Y, Mecking H. *A unified phenomenological description of work-hardening and creep based on one-parameter models*. Acta Materialia 1984;32:57.

[297] Figueiredo RB, Pereira PHR, Aguilar MTP, Cetlin PR, Langdon TG. *Using finite element modeling to examine the temperature distribution in quasi-constrained high-pressure torsion*. Acta Materialia 2012;60:3190.

[298] Xu C, Horita Z, Langdon TG. *Evaluating the influence of pressure and torsional strain on processing by high-pressure torsion*. Journal of Materials Science 2008;43:7286.

[299] Hyun CY, Kim HK. *The comparson of yield and fatigue strength dependence on grain size of pure Ti produced by severe plastic deformation*. Reviews on Advanced Materials Science 2011;28:69.

[300] Zhang TH, Huan Y. *Substrate effects on the micro/nanomechanical properties of TiN coatings*. Tribology Letters 2004;17:911.

[301] Ichimura H, Ishii Y. *Effects of indenter radius on the critical load in scratch testing*. Surface & Coatings Technology 2003;165:1.

[302] Kamminga J-D, van Essen P, Hoy R, Janssen GCAM. *Substrate dependence of the scratch resistance of CrNx coatings on steel*. Tribology Letters 2005;19:65.

[303] Ichimura H, Rodrigo A. *The correlation of scratch adhesion with composite hardness for TiN coatings*. Surface & Coatings Technology 2000;126:152.

[304] Kataria S, Kumar N, Dash S, Ramaseshan R, Tyagi AK. *Evolution of deformation and friction during multimode scratch test on TiN coated D9 steel*. Surface & Coatings Technology 2010;205:922.

[305] Rodrigo A, Ichimura H. *Analytical correlation of hardness and scratch adhesion for hard films*. Surface & Coatings Technology 2001;148:8.

[306] Rodrigo A, Perillo P, Ichimura H. *On the correlation of substrate microhardness with the critical load of scratch adherence for hard coatings*. Surface & Coatings Technology 2000;124:87.

[307] Zhao X, Niinomi M, Nakai M, Miyamoto G, Furuhara T. *Microstructures and mechanical properties of metastable Ti-30Zr-(Cr, Mo) alloys with changeable Young's modulus for spinal fixation applications*. Acta Biomaterialia 2011;7:3230.

[308] Kent D, Wang G, Yu Z, Ma X, Dargusch M. *Strength enhancement of a biomedical titanium alloy through a modified accumulative roll bonding technique*. Journal of the Mechanical Behaviour of Biomedical Materials 2011;4:405.

[309] Rubitschek F, Niendorf T, Karaman I, Maier HJ. *Corrosion fatigue behaviour of a biocompatible ultrafine-grained niobium alloy in simulated body fluid*. Journal of the Mechanical Behaviour of Biomedical Materials 2012;5:181.

Appendix: Several selected papers published during this PhD project

The following four papers are selected and their PDF versions are attached as the appendix:

1. **C.T. Wang**, N. Gao, R.J.K. Wood and T.G. Langdon (2011) *Wear behaviour of an aluminium alloy processed by equal-channel angular pressing*. Journal of Materials Science, 46, (1), 123-130.

2. **C.T. Wang**, N. Gao, M.G. Gee, R.J.K. Wood and T.G. Langdon (2012) *Effect of grain size on the micro-tribological behaviour of pure titanium processed by high-pressure torsion*. Wear, 280-281, 28-35.

3. **C.T. Wang**, N. Gao, M.G. Gee, R.J.K. Wood and T.G. Langdon (2013) *Processing of an ultrafine-grained titanium by high-pressure torsion: An evaluation of the wear properties with and without a TiN coating*. Journal of the Mechanical Behaviour of Biomedical Materials, 17, 166-175.

4. **C.T. Wang**, A. Escudeiro, T. Polcar, A. Cavaleiro, R.J.K. Wood, N. Gao and T.G. Langdon (2013) *Indentation and scratch testing of DLC-Zr coatings on ultrafine-grained titanium processed by high-pressure torsion*. Wear, in press.

Wear behavior of an aluminum alloy processed by equal-channel angular pressing

Chuan Ting Wang · Nong Gao · Robert J. K. Wood ·
Terence G. Langdon

Abstract Wear tests were conducted on an aluminum Al-1050 alloy after processing by equal-channel angular pressing (ECAP). The results show that the coefficient of friction remains unchanged after processing by ECAP, but there is a decrease in the wear resistance and a mass loss that increases with increasing numbers of ECAP passes. The results are consistent with a wear mechanism map and confirm the occurrence of a severe wear mechanism. The decreasing wear resistance after ECAP is attributed to the significant grain refinement introduced by ECAP and the lack of a strain hardening capability.

Introduction

Processing through the application of severe plastic deformation (SPD) has become important over the last decade for the production of metals having ultrafine grain sizes [1]. Several SPD techniques are now available and the most promising are equal-channel angular pressing (ECAP) [2], high-pressure torsion (HPT) [3], and accumulative roll bonding (ARB) [4, 5]. In general, the ultrafine-grained

C. T. Wang · R. J. K. Wood
National Centre for Advanced Tribology at Southampton,
School of Engineering Sciences, University of Southampton,
Southampton SO17 1BJ, UK

C. T. Wang · N. Gao · T. G. Langdon
Materials Research Group, School of Engineering Sciences,
University of Southampton, Southampton SO17 1BJ, UK

T. G. Langdon (✉)
Departments of Aerospace and Mechanical Engineering
and Materials Science, University of Southern California,
Los Angeles, CA 90089-1453, USA
e-mail: langdon@usc.edu

materials produced using these techniques exhibit superior mechanical properties including high strength [6], enhanced fatigue properties [7] and, if the grains are reasonably stable at elevated temperatures, excellent superplastic forming capabilities [8].

Most of the studies conducted to date have focused on the microstructural evolution during SPD processing [9, 10] or the subsequent mechanical properties of the metals attained using these processes [11, 12]. However, the novel and often extraordinary properties offered by SPD processing means that these materials have potential uses in many applications ranging from precision instruments [13] to MEMS devices [14, 15] and biomedical and dental implants [16, 17].

In order to make better use of materials processed by SPD, it is very important to study their wear resistance. In practice, the wear of a component leads to an increased clearance and to a loss of precision in moving structural parts and, conversely, a high wear resistance may yield a longer service life. Nevertheless, despite the clear importance of wear in industrial applications, there are only a limited number of reports to date describing the wear characteristics of metals processed by SPD. Table 1 summarizes the information currently available for a range of ultrafine-grained materials processed by ECAP, ARB, surface mechanical attrition treatment (SMAT) and hydrostatic extrusion (HE) [18–33]. It is apparent from inspection of Table 1 that there is no consistent effect of SPD processing on the wear properties of materials since in some experiments SPD leads to an increase in the wear resistance, in others there is no significant effect and in others the wear resistance decreases. In practice, it is important to note that the wear property is a system property that is influenced, or even significantly affected, by a range of factors including the load level, the sliding

Table 1 Wear properties of materials processed by SPD

Material	SPD method	Wear rig	Lubrication condition	Effect of SPD on friction coefficient	Effect of SPD on wear resistance	Reference
Al–Al$_3$Ti	ECAP	Block-on-disk	N/A	N/A	No effect	Sato et al. [18]
Al–2,3,5%Cu	ECAP	Pin-on-disk	Unlubricated	N/A	Increases	Abd El Aal et al. [19]
Al–12% Si	ECAP	Pin-on-disk	Unlubricated	N/A	Decreases	Kucukomeroglu [20]
Al-1100	ARB	Pin-on-disk	Unlubricated	N/A	Decreases	Kim et al. [21]
Al-5052	ARB	Pin-on-disk	Unlubricated	N/A	Decreases	Kim et al. [21]
Al-6061	ARB	Pin-on-disk	Unlubricated	N/A	Decreases	Kim et al. [22]
Cu–10%Al–4%Fe	ECAP	Ring-on-block	Unlubricated	Reduced	Increases	Gao and Cheng [23–25]
Mg AZ61 alloy	ECAP	Pin-on-disk	Unlubricated	N/A	No effect	Kim et al. [22]
Sn–11.5%Sb–5.5%Cu	ECAP	Pin-on-disk	Lubricated	Reduced	Increases	Korshunov et al. [26]
			Unlubricated	N/A	Decreases	
Low carbon steel	SMAT	Reciprocating sliding tester	Unlubricated	Reduced	Increases	Wang et al. [27]
Low carbon steel	ECAP	Pin-on-disk	Unlubricated	N/A	Decreases	Kim et al. [21]
Ti	ECAP		Unlubricated	Reduced	Increases	Stolyarov et al. [28]
Ti	ECAP	SRV oscillating tester	Unlubricated	No effect	Increases	La et al. [29]
Ti	HE	Pin-on-disk	Unlubricated	N/A	No effect	Garbacz et al. [30]
			Various conditions	N/A	Decreases	Garbacz et al. [30]
Ti	ECAP	Pin-on-disk	Unlubricated	N/A	No effect	Purcek et al. [31]
TiNi	ECAP	Ring-on-block	Unlubricated	N/A	Increases	Cheng et al. [32]
Zn–40%Al–2%Cu–2%Si	ECAP	Pin-on-disk	Unlubricated	Reduced	Increases	Purcek et al. [33]

velocity, the use of any lubricants, and the properties of the counter surface. The variability in results documented in Table 1 demonstrates that more information is needed, and especially systematic experiments are required, in order to reach definitive conclusions concerning the effect of SPD processing on the wear properties of different materials.

The present investigation was initiated to study the wear behavior of an Al-1050 alloy after processing by ECAP. This alloy was selected because it is single phase, it has a simple f.c.c. crystal structure, and extensive information is already available on the properties of aluminum-based alloys after processing by ECAP. The wear properties were investigated using a reciprocating dry sliding wear tester with the testing conducted without any lubrication. Following testing, the debris and worn surfaces were examined using various analytical procedures.

Experimental material and procedures

The investigation used a commercial Al-1050 aluminum alloy having a composition close to Al–0.25% Fe–0.15% Si (in wt%). The alloy was supplied as rods with diameters of 9.5 mm and these rods were cut into individual billets having lengths of ~65 mm. The billets were processed by

ECAP at room temperature for 1, 2, 4, and 8 passes, respectively, using a pressing speed of 0.5 mm s^{-1} and an ECAP die having an angle of 90° between the two channels and an outer arc of curvature of 20° at the point of intersection of the two channels. The principles of processing by ECAP were described in an earlier report [34] and it can be shown that these two angles lead to an imposed strain of ~1 on each passage through the die [35]. The billets were pressed using processing route Bc in which each billet is rotated in the same sense by 90° around the longitudinal axis between each pass through the die [36], where route Bc was selected because it leads most expeditiously to a reasonably homogeneous array of ultrafine grains separated by a high fraction of high-angle boundaries [37].

Dry sliding wear tests were conducted on both the as-received alloy and the alloy after processing by ECAP using a Phoenix TE77 high-frequency reciprocating test rig as illustrated schematically in Fig. 1. These tests were performed at a temperature of 20 ± 2 °C and under a relative humidity of 55 ± 5%. The samples for the wear tests were machined into plates having dimensions of 45 × 8 × 2.5 mm^3 and each plate was mechanically ground to 4000-grit SiC paper and then washed in acetone in an ultrasonic bath for 15 min. In this condition prior to testing, the average surface roughness was about 0.7 μm.
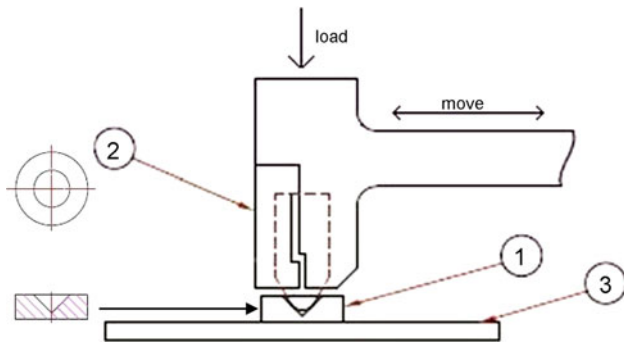
Fig. 1 Schematic illustration of the high-frequency reciprocating test rig used for the wear tests: *1* counter surface, *2* holder, *3* sample fixed in position

The counter surface used in these tests had a diameter of 12 mm which gave a contact area between the two surfaces of about 90 mm^2 and the counter pin was made of phosphor bronze with a hardness of 200 Hv. The edge of the counter surface was rounded and the counter surface pin was pressed and driven by an indenter during sliding. This design was used in order to inhibit edge cutting. Two loads of 5 and 23 N were used in this study and the apparent contact stresses were estimated as 5.6×10^{-2} and 2.6×10^{-1} MPa, respectively. During testing, the stroke length of the oscillating motion was ~ 8.9 mm and the reciprocating frequency was 1 Hz which gave an average sliding velocity of the order of 17.9 ± 0.1 mm s^{-1}.

Before and after the wear tests, the Vickers microhardness was measured using a Matsuzawa Seiki MHT-1 microhardness tester with a load of 100 g and using a dwell time of 15 s. The mass loss of each sample in the wear test was measured using a Mettler AE240 microbalance having an accuracy of 0.1 mg. Grain sizes were recorded after ECAP using electron back-scatter diffraction (EBSD). The microstructures of the worn surfaces were analyzed using scanning electron microscopy with energy dispersion spectroscopy (SEM–EDS) using a JEOL JSM 6500 instrument and energy dispersive X-ray spectrometry was conducted with an INCA EDX analyser. The topology of the surface roughness and three-dimensional surface profiles were recorded using a XYRIS 2000 TL/CL metrology system produced by TAICAAN.

Experimental results

Microstructure and hardness after processing

In the as-received condition, the grain size of the alloy was ~ 44 μm. Measurements by EBSD after ECAP gave average grain sizes of ~ 15, ~ 11, ~ 4.9, and ~ 1.3 μm after 1, 2, 4, and 8 passes, respectively, where the grain size
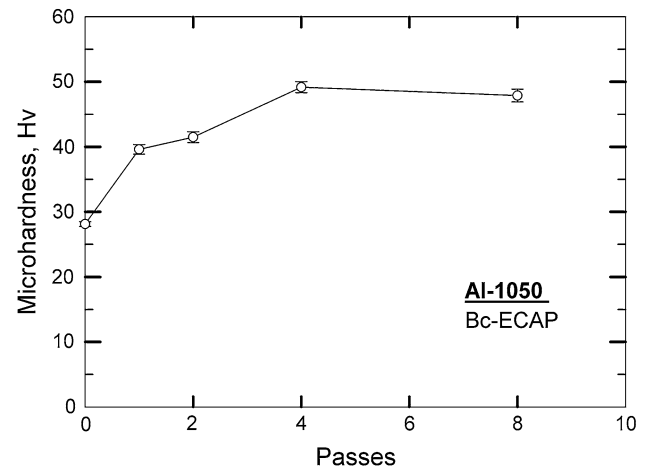
Fig. 2 Microhardness versus number of passes after processing by ECAP

after 8 passes is similar to grain sizes reported in earlier investigations using high-purity [9, 10, 38, 39] and commercial purity [40] aluminum. Figure 2 shows the variation of the microhardness with the number of passes of ECAP before the wear tests. As anticipated from earlier studies [6, 41], the hardness increases significantly after processing by ECAP.

Wear behavior of the as-received and ECAP processed samples using a dry sliding test

The average values of the coefficients of friction during sliding testing are shown in Fig. 3, for both the 5 and 23 N testing conditions. For these experiments, the sampling rate of the friction transducer was 1 Hz and the test continued for 1500 s so that each point corresponds to an average value from 1,500 datum points. It is readily apparent from Fig. 3 that ECAP has essentially no influence on the
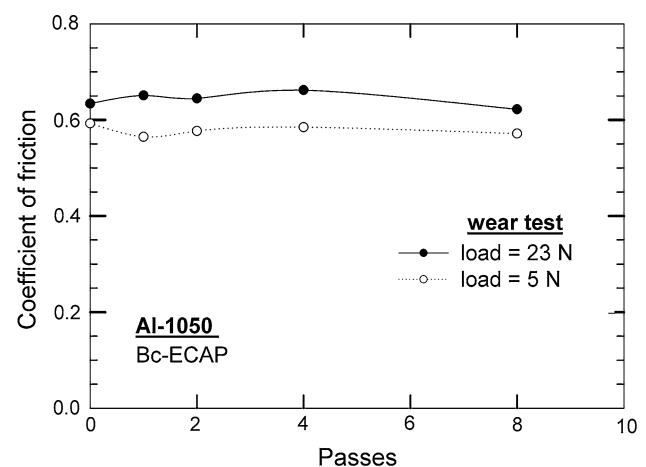
Fig. 3 Coefficient of friction versus number of passes for the two loading conditions
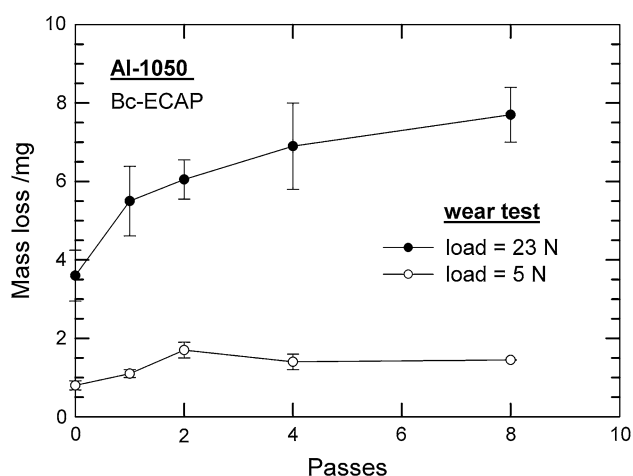
Fig. 4 Mass loss versus number of passes for the two loading conditions

measured coefficients of friction under the two loading conditions used in this study. Thus, under a load of 23 N the coefficients of friction varied from 0.62 to 0.66 whereas under a load of 5 N the coefficients of friction were slightly lower at 0.56–0.59.

The mass loss of the samples after the wear test is shown in Fig. 4, for the two different loading conditions. It has been shown theoretically that the mass loss may be estimated using the Archard equation [42] given by

$$V = K\frac{SL}{3H} \tag{1}$$

where V is the volume worn away during testing, S is the total sliding distance, L is the normal load, H is the hardness of the softer surface, and K is a dimensionless wear coefficient specific to the sample under test. Since the samples processed by ECAP have a higher hardness than the as-received sample, as shown in Fig. 2, it is reasonable to anticipate from Eq. 1 that they will experience a smaller mass loss. Nevertheless, it is evident from Fig. 4 that the samples processed by ECAP exhibit a larger mass loss and, in addition, this mass loss increases with increasing numbers of passes for the samples tested under a load of 23 N. Because of the apparent differences between the samples tested with loads of 23 and 5 N, these samples are examined separately in the following two sections.

Testing under a load of 23 N for 1500 s

All samples tested under a load of 23 N for 1500 s exhibited exceptionally severe wear with evidence for much white debris that became detached from the samples. An SEM study showed that the morphologies of the worn surfaces of all samples were reasonably similar and examples are shown in Fig. 5 for (a) the as-received condition and after ECAP through (b) 1 pass and (c) 8 passes.
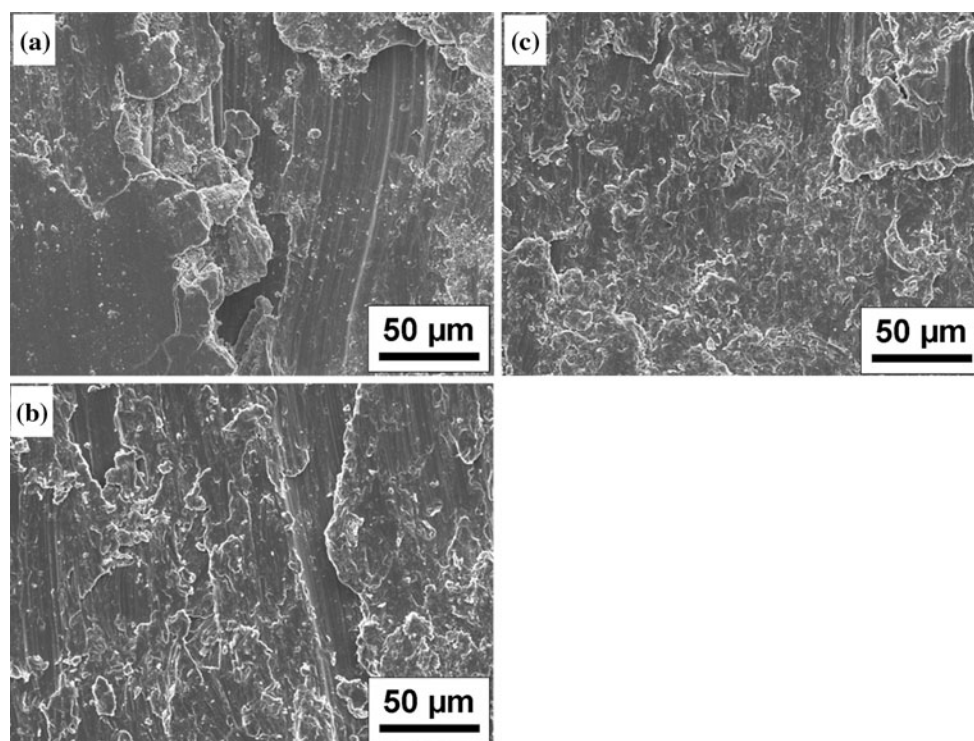
Fig. 5 SEM micrographs of worn surfaces after wear tests under a load of 23 N: **a** as-received material, **b** after 1 pass of ECAP, and **c** after 8 passes of ECAP
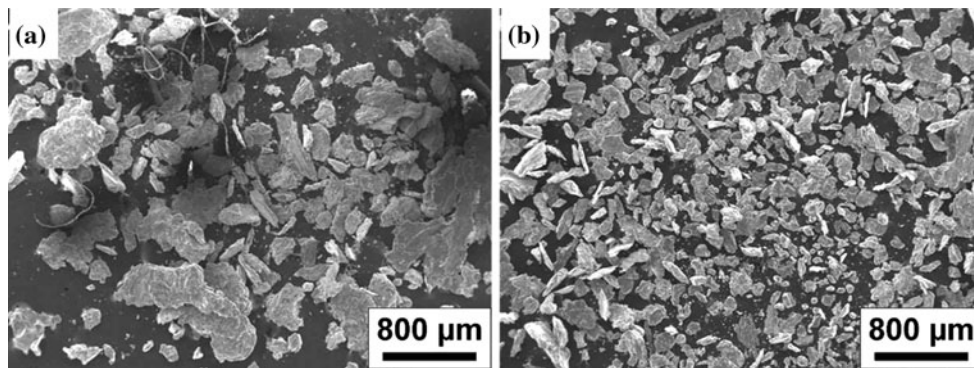
Fig. 6 Wear debris of samples under a sliding load of 23 N: **a** for the as-received condition and **b** after 8 passes of ECAP

The appearance of the worn surfaces of the samples is typical of adhesive wear and this has been widely reported for soft and ductile materials such as copper, aluminum, and gold [43, 44]. Figure 6 shows the wear debris for (a) the as-received condition and (b) after ECAP through 8 passes. Some of the debris in Fig. 6 has a higher appearance probably because of charging effects associated with the orientations of the debris on the SEM holder. It is readily apparent from Fig. 6 that the size of the debris is significantly smaller after processing by ECAP.

Testing under a load of 5 N for 1500 s

During the sliding wear test under the lower load of 5 N, it was observed that the wear debris was a mixture of white flake-like particles and black powder. This is shown in Fig. 7 where (a) and (b) are low and high magnification images, respectively: the lower portions of Fig. 7 show the EDS analyses of the small areas marked with rectangles in the upper images. It was noted that the white flake-like

particles visible in Fig. 7a were observed from the beginning of each wear test whereas the black powder in Fig. 7b became visible at some point during the test. Similar results were also reported in an earlier investigation [45] and it was proposed, in agreement with the current EDS analyses, that the white particles are monolithic aluminum detached from the sample.

Material transfer was also evident with aluminum transferred onto the pin surface. Figure 8 shows the counter surface and appropriate EDS analyses after 8 passes of ECAP: the image on the left is at a low magnification and the small area within the rectangle is given at a higher magnification on the right. These observations show that the counter surface is partially covered by transferred fragments and the EDS analyses confirm these transferred fragments are mixed components of aluminum and aluminum oxide. Many of the earlier studies used steel as the counter surface [45–48] and mechanically mixed layers (MML) were widely observed on the surfaces of aluminum samples when using an Al-steel wearing system. In the

Fig. 7 EDS analysis of wear debris from 8 passes of ECAP after wear test using a load of 5 N for **a** low and **b** high magnifications
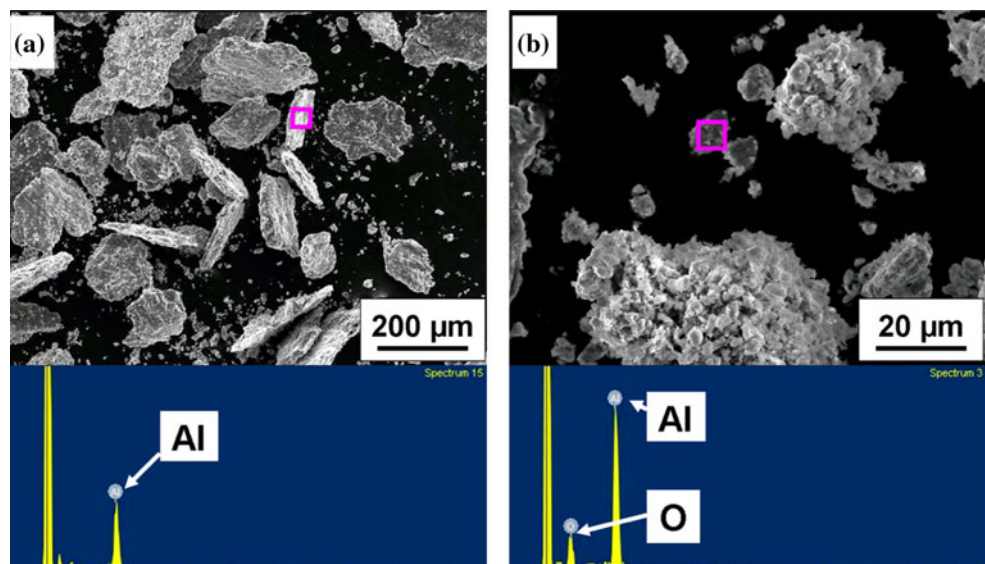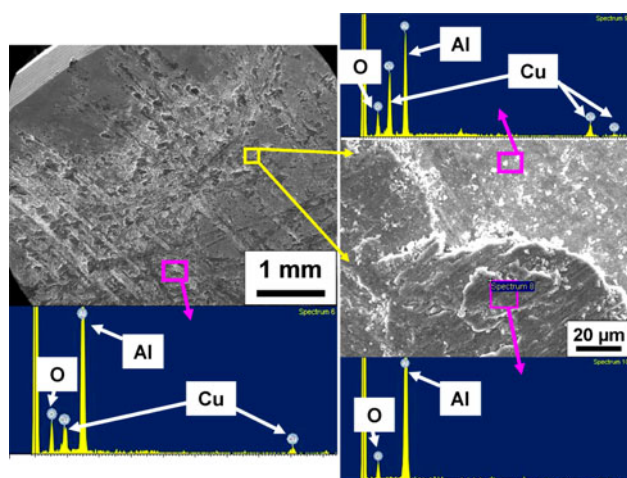
Fig. 8 EDS analysis of the counter surface against 8 passes of ECAP sample after wear test using a load of 5 N

present investigation, the use of a phosphor bronze as the counter surface led to material transfer but not to the formation of MML.

Evidence for surface deformation was also visible on the worn surfaces of the samples after wear testing. Figure 9 shows an example using a load of 5 N after 8 passes of ECAP where the topological three-dimensional profile is shown at upper left, a portion of the worn surface is shown at lower right and two EDS analyses are included for the small rectangles marked in the image. The three-dimensional profile shows that the worn surface is made up of low-lying areas and some higher flats. It was found by EDS analysis that these low-lying areas were close to pure aluminum and the higher flats contained a high fraction of oxygen. It is evident from the color-coding in Fig. 9 that the separation distance between the high flats and the low-lying areas is typically of the order of several tens of microns, where this is similar to the thickness of the flake debris in Fig. 7. This suggests that during the wear test the flakes are detached from the sample and leave pits which join at a later stage to from low-lying areas.
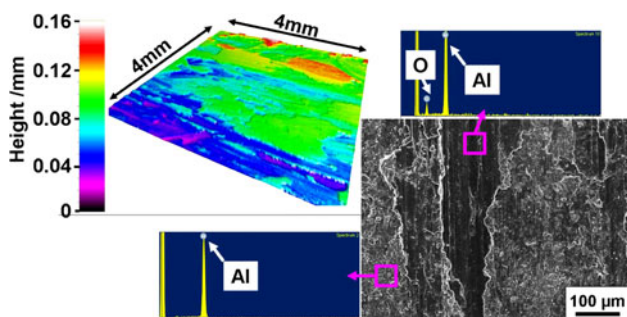
Fig. 9 Three-dimensional analysis and EDS analysis of the worn surface of an 8 pass ECAP sample after wear test using a load of 5 N

Discussion

The results of this investigation provide useful information on the wear characteristics of an Al-1050 alloy processed by ECAP to produce exceptional grain refinement. Processing by ECAP increases the hardness of the material, it leads to little or no change in the coefficients of friction when wear testing under two different loading conditions of 5 and 23 N, there is a transfer of material to the counter surface during testing and there is also a very significant mass loss when using the higher load of 23 N. Studies of the debris, worn surfaces, and wear rates all indicate that these two loading conditions produce a severe wear mechanism. However, the higher hardness introduced by ECAP leads to a higher mass loss than in the as-received material and this appears to be inconsistent with the conventional Archard relationship given in Eq. 1.

The development of wear mechanism maps was the first attempt to delineate the wear processes in a simple pictorial form [49] and to provide information that may be correlated with observed transitions between different wear processes [50]. The maps were developed using the following relationships for the normalized pressure at the sliding interface, $\bar{F}$, and the normalized velocity, $\bar{v}$, where the latter corresponds to the sliding velocity in wear divided by the velocity of heat flow [49]:

$$\bar{F} = \frac{F}{A_n H_o} \tag{2}$$

and

$$\bar{v} = \frac{v r_o}{a} \tag{3}$$

where F is the normal force (N), A_n is the nominal contact area (m^2); H_o is the room temperature hardness (N m^{-2}), v is the sliding speed (m s^{-1}), r_o is the radius of the nominal contact area, and a is the thermal diffusivity. Subsequently, this approach was used to develop a dry sliding map for aluminum and its alloys [51] and the result is shown in Fig. 10 where the normalized pressure is plotted logarithmically against the normalized velocity. The dashed lines delineate transitions between the different wear mechanisms and each separate wear mechanism is dominant within the designated area.

Calculations suggest the orders of magnitude values in the present investigation are $\bar{F} \approx 10^{-4}$ since there is little difference in the hardness values for the different samples and $\bar{v} \approx 10$. Therefore, inserting these values into the wear mechanism map in Fig. 10 leads to the lower oval designated contact (A), which suggests the occurrence of an oxidation-dominated wear for the two loading conditions used in this study. However, this is not consistent with the
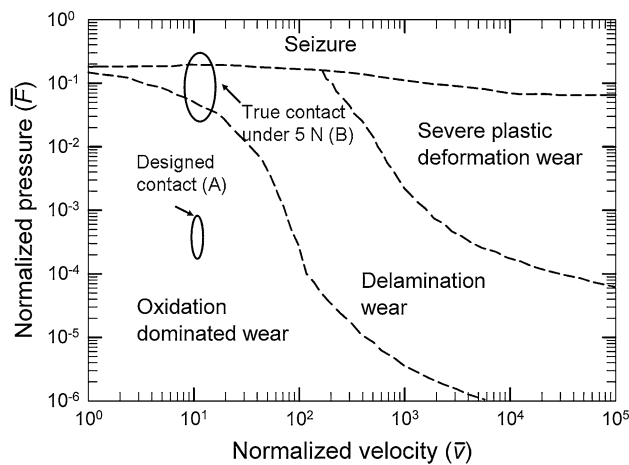
Fig. 10 A wear mechanism map for aluminum and its alloys [51] showing the apparent designated area for the current wear tests at A and the corrected area at B when incorporating additional information concerning the wear process

flake-like debris shown in Figs 6 and 7 and the clear evidence for a severe wear mechanism.

The dimensional wear coefficient, k, is widely used to compare wear rates in different classes of materials and it is defined by

$$k = \frac{V}{SL} \qquad (4)$$

Calculation suggests that under the load of 23 N the dimensional wear coefficient for the sample processed by ECAP through 4 passes is $\sim 4.1 \times 10^{-6}$ mm^2 N^{-1} while under the load of 5 N the dimensional wear coefficient for a similar sample is $\sim 3.8 \times 10^{-6}$ mm^2 N^{-1}. That means that wear under the two conditions is dominated by a severe wear mechanism with a wear rate higher than 10^{-8} mm^2 N^{-1} [52].

In practice, the wear mechanism was significantly more severe than expected and this appears to be due to two reasons. First, the hardness of the pin material was higher in these tests than the disk material and this wear system often results in a more severe wear mode [53]. Second, during the initial time of sliding the true contact area is initially smaller than the apparent contact area due to the nature of the two surfaces [54]. Under these conditions for a load of 5 N, the contact stress of the connecting areas is higher than initially expected and this suggests the true contact stress is probably close to the upper oval in Fig. 10. For these testing conditions, it is therefore reasonable to anticipate a transition towards a severe wear mechanism. Thus, during this initial period the surface of the softer material becomes significantly deformed and this generates extensive debris by adhesion such that the mass loss measured in Fig. 4 is experienced primarily in this initial period.

As the test continues, black particles are produced containing high fractions of oxygen, where these particles are spread over the sliding surface and lead to a decrease in the wear rate [44, 45, 52]. There is some uncertainty regarding the formation process for these fine black particles but they may be produced by a complex mechanical alloying process [52] or through a hydroxide or similar high-oxygen content phase [55]. As the total test duration was not long, the size and the amount of this black debris were not comparable to the plate-like debris and accordingly the total mass loss was due primarily to the loss of the plate-like debris.

Finally, it is necessary to address the apparent disagreement with the Archard relationship given in Eq. 1 since processing by ECAP leads to a higher hardness but also, as shown in Fig. 4 for the samples tested under a load of 23 N, to an increase in the mass loss with increasing numbers of passes in ECAP. This decrease in the wear resistance after processing by ECAP is consistent with very recent results for the Al-1100 and Al-5052 alloys processed by ARB [21], where the lower wear resistance was attributed to the lack of significant strain hardening in the alloys subjected to SPD processing. This conclusion is in agreement with the present results and it is further supported by a recent experimental observation, also for an aluminum alloy, that the strain hardening capability of the alloy is essentially exhausted after two passes of ECAP [56]. The apparent discrepancy may be explained in part by the nature of the microstructure introduced by the ECAP process since processing by ECAP leads not only to a refined grain size but also to the introduction of high energy non-equilibrium grain boundaries [57, 58] and to an increase in both the average grain boundary misorientation angle and the total fraction of high-angle boundaries with increasing numbers of ECAP passes [10]. These microstructural changes are not incorporated in Eq. 1 but they appear to account for the increased mass loss after larger numbers of ECAP passes.

Summary and conclusions

1. An Al-1050 alloy was processed by ECAP leading to a refined microstructure and increased hardness. Samples processed by ECAP were subjected to wear testing under loads of 5 and 23 N.
2. The samples processed by ECAP have similar coefficients of friction to the unprocessed alloy at least for the two loading conditions used in this investigation but the ECAP processing leads to a decrease in the wear resistance and to a mass loss that increases with increasing numbers of ECAP passes.
3. The wear results show good agreement with a wear mechanism map when it is recognized that the true

contact stress of the connecting areas is significantly higher than expected. The map predicts a transition towards the occurrence of a severe wear mechanism.

4. The results suggest the wear tests under both loads are dominated by a severe wear mechanism and the decreasing wear resistance after ECAP is due to the characteristics of grain refinement in the ECAP procedure and the inherent loss of a strain hardening capability.

References

1. Valiev RZ, Estrin Y, Horita Z, Langdon TG, Zehetbauer MJ, Zhu YT (2006) JOM 58(4):33
2. Valiev RZ, Langdon TG (2006) Prog Mater Sci 51:881
3. Zhilyaev AP, Langdon TG (2008) Prog Mater Sci 53:893
4. Saito Y, Tsuji N, Utsunomiya H, Sakai T, Hong RG (1998) Scripta Mater 39:1221
5. Tsuji N, Saito Y, Utsunomiya H, Tanigawa S (1999) Scripta Mater 40:795
6. Horita Z, Fujinami T, Nemoto M, Langdon TG (2000) Metall Mater Trans 31A:691
7. Höppel HW, Kautz M, Xu C, Murashkin M, Langdon TG, Valiev RZ, Mughrabi H (2006) Int J Fatigue 28:1001
8. Horita Z, Furukawa M, Nemoto M, Barnes AJ, Langdon TG (2000) Acta Mater 48:3633
9. Iwahashi Y, Horita Z, Nemoto M, Langdon TG (1998) Acta Mater 46:3317
10. Kawasaki M, Horita Z, Langdon TG (2009) Mater Sci Eng A524:143
11. Valiev RZ, Krasilnikov NA, Tsenev NK (1991) Mater Sci Eng A137:35
12. Valiev RZ, Alexandrov IV, Zhu YT, Lowe TC (2002) J Mater Res 17:5
13. Kim WJ, Sa YK (2006) Scripta Mater 54:1391
14. Estrin Y, Janecek M, Raab GI, Valiev RZ, Zi A (2007) Metall Mater Trans 38A:1906
15. Qiao XG, Gao N, Moktadir Z, Kraft M, Starink MJ (2010) J Micromech Microeng 20:045029
16. Latysh V, Krallics G, Alexandrov I, Fodor A (2006) Curr Appl Phys 6:262
17. Valiev RZ, Semenova IP, Latysh VV, Rack H, Lowe TC, Petruzelka J, Dluhos L, Hrusak D, Sochova J (2008) Adv Eng Mater 10:B15
18. Sato H, Elhadad S, Sitdikov O, Watanabe Y (2008) Mater Sci Forum 584–586:971
19. Abd El Aal MI, El Mahallawy N, Shehata FA, Abd El Hameed M, Yoon EY, Kim HS (2010) Mater Sci Eng A527:3726
20. Kucukomeroglu T (2010) Mater Des 31:782
21. Kim YS, Yu HS, Shin DH (2009) Int J Mater Res 100:871
22. Kim YS, Ha JS, Kim WJ (2004) Mater Sci Forum 449–452:597
23. Gao LL, Cheng XH (2007) Tribol Lett 27:221
24. Gao LL, Cheng XH (2008) Wear 265:986
25. Gao LL, Cheng XH (2008) Mater Sci Eng A473:259
26. Korshunov LG, Noskova NI, Korznikov AV, Chernenko NL, Vil'danova NF (2009) Phys Met Metallogr 108:519
27. Wang ZB, Tao NR, Li S, Wang W, Liu G, Lu J, Lu K (2003) Mater Sci Eng A352:144
28. Stolyarov VV, Shuster LS, Migranov MS, Valiev RZ, Zhu YT (2004) Mater Sci Eng A371:313
29. La P, Ma J, Zhu YT, Yang J, Liu W, Xue Q, Valiev RZ (2005) Acta Mater 53:5167
30. Garbacz H, Gradzka-Dahlke M, Kurzydlowski KJ (2007) Wear 263:572
31. Purcek G, Saray O, Kul O, Karaman I, Yapici GG, Haouaoui M, Maier HJ (2009) Mater Sci Eng A517:97
32. Cheng X, Li Z, Xiang G (2007) Mater Des 28:2218
33. Purcek G, Saray O, Kucukomeroglu T, Haouaoui M, Karaman I (2010) Mater Sci Eng A527:3480
34. Furukawa M, Horita Z, Nemoto M, Langdon TG (2001) J Mater Sci 36:2835. doi:10.1023/A:1017932417043
35. Iwahashi Y, Wang J, Horita Z, Nemoto M, Langdon TG (1996) Scripta Mater 35:143
36. Furukawa M, Iwahashi Y, Horita Z, Nemoto M, Langdon TG (1998) Mater Sci Eng A257:328
37. Oh-ishi K, Horita Z, Furukawa M, Nemoto M, Langdon TG (1998) Metall Mater Trans 29A:2011
38. Nakashima K, Horita Z, Nemoto M, Langdon TG (1998) Acta Mater 46:1589
39. Terhune SD, Swisher DL, Oh-ishi K, Horita Z, Langdon TG, McNelley TR (2002) Metall Mater Trans 33A:2173
40. Salem AA, Langdon TG, McNelley TR, Kalidindi SR, Semiatin SL (2006) Metall Mater Trans 37A:2879
41. Horita Z, Fujinami T, Nemoto M, Langdon TG (2001) J Mater Process Technol 117:288
42. Archard JF (1953) J Appl Phys 24:981
43. Kuo SM, Rigney DA (1992) Mater Sci Eng A157:131
44. Rigney DA (2000) Wear 245:1
45. Zhang J, Alpas AT (1997) Acta Mater 45:513
46. Pramila BN, Biswas SK (1991) Acta Metall Mater 39:833
47. Li XY, Tandon KN (2000) Wear 245:148
48. Tandon KN, Li XY (1997) Scripta Mater 38:7
49. Lim SC, Ashby MF (1987) Acta Metall 35:1
50. Lim SC, Ashby MF, Brunton JH (1987) Acta Metall 35:1343
51. Liu Y, Asthana R, Rohatgi P (1991) J Mater Sci 26:99. doi: 10.1007/BF00576038
52. Hiratsuka K, Muramoto K (2005) Wear 259:467
53. Rigney DA (1994) Wear 175:63
54. Blau PJ (1981) Wear 71:29
55. Kim HJ, Karthikeyan S, Rigney D (2007) Wear 263:849
56. Cetlin PR, Aguilar MTP, Figueiredo RB, Langdon TG (2010) J Mater Sci 45:4561. doi:10.1007/s10853-010-4384-9
57. Wang J, Horita Z, Furukawa M, Nemoto M, Tsenev NK, Valiev RZ, Ma Y, Langdon TG (1993) J Mater Res 8:2810
58. Horita Z, Smith DJ, Nemoto M, Valiev RZ, Langdon TG (1998) J Mater Res 13:446

Effect of grain size on the micro-tribological behavior of pure titanium processed by high-pressure torsion

Chuan Ting Wang [a,b], Nong Gao [b,*], Mark G. Gee [c], Robert J.K. Wood [a], Terence G. Langdon [b,d]

[a] National Centre for Advanced Tribology at Southampton, Engineering Sciences, University of Southampton, Southampton SO17 1BJ, UK
[b] Materials Research Group, Engineering Sciences, University of Southampton, Southampton SO17 1BJ, UK
[c] National Physical Laboratory, Hampton Road, Teddington, Middlesex TW16 5PT, UK
[d] Departments of Aerospace & Mechanical Engineering and Materials Science, University of Southern California, Los Angeles, CA 90089-1453, USA

ARTICLE INFO

ABSTRACT

The micro-wear behavior of commercial pure Ti was investigated before and after processing by high-pressure torsion (HPT) to provide comparisons over a range of grain sizes. The HPT-processed Ti had an average grain size of ~130 nm while the as-received and HPT plus annealed samples had grain sizes of ~8.6 μm and ~607 nm, respectively. The results show all Ti samples have a similar dynamic coefficient of friction but different wear mechanisms. Wear of the coarse grained (CG) Ti showed extensive plastic deformation and wedge formation which produced large wear debris whereas wear of the ultra-fine grained (UFG) Ti was dominated by abrasive wear mechanisms and produced small wear debris. In addition, the UFG Ti showed a more homogenous wear grooving and a lower wear rate than CG Ti which suggests that UFG Ti is more suitable for wear applications.

1. Introduction

Processing by severe plastic deformation (SPD) is defined formally as any method of metal forming, conducted under a hydrostatic pressure, that may be used to impose a very high strain on a bulk solid without introducing any significant change in the overall dimensions of the sample and with the capability of producing exceptional grain refinement [1]. It is now widely established that SPD processing produces ultra-fine grained (UFG) materials possessing unique mechanical and physical properties [2]. Potential industrial applications of SPD-processed materials include precision instruments, biomedical implants and micro-electro-mechanical systems (MEMS) devices [3–5]. However, during the service life of moving contacts, damage is often caused by wear particles that are generated from the interface, especially in the field of electronic engineering and precision instruments.

Considering the inevitability of wear to components moving against each other in close contact, there has been considerable interest in testing the wear behavior of SPD-processed materials [6–13]. Nevertheless, there is conflicting evidence on the effect of SPD processing on the wear resistance of materials, where this is due in part to the different materials studied but primarily it is due to the inherent complexity of wear when two materials contact over a large area.

Some earlier work focused on the nature of the microscopic wear mechanisms and the generation of wear particles in micro- or nano-contacts [14]. An in situ scanning electron microscopy (SEM) wear study via micro- or nano-tribology test systems was one of the most effective methods and several different types of test systems have been developed. An in situ SEM video tape recording (SEM-VTR) tribosystem was developed and used to study the micro wear mechanisms of steel, ceramics and coatings. Several different wear modes, and the transitions between them, were plotted on wear maps [14–16]. Atomic force microscopy (AFM) was also employed to scratch samples in a much lower load range. Recently, a cost effective tribometer was developed which was used to study the micro-scratch behavior of WC/Co hard metals and coatings [17–19]. This test system was subsequently further developed so that it can perform wear tests with a load range between 5 mN and 250 mN, thereby filling the gap between AFM and the traditional wear testers.

Titanium and its alloys are attractive candidate materials for applications from aerospace to sports and biomedical due to their high strength to weight ratio, excellent corrosion resistance and good biocompatibility [20]. Alloys such as Ti–6Al–4V are most often used for biomedical applications, but nevertheless the alloy elements released from Ti alloys may cause long-term health problems [21–23]. Therefore, attempts have been made to produce UFG pure Ti with a comparable high strength to Ti–6Al–4V and a much improved biocompatibility [24–28]. Recent studies also reported the superior osteoblast cell compatibility of UFG pure Ti substrates produced via SPD processing over coarse grained (CG) pure Ti and Ti–6Al–4V substrates, thereby making the UFG pure Ti even more attractive for biomedical applications [27,29].

Recently, attention has been directed to studies of the tribological behavior of Ti processed via SPD [6,25,30,31]. Initially, it was reported that UFG Ti had a lower coefficient of friction than CG Ti under various conditions [25], but this result was not consistent with a later study which revealed a similar coefficient of friction around 0.6 for both CG Ti and UFG Ti [6]. This conflict may be due to the different experimental setups used, as the indenter of the friction tester in one study rotated near the centre of the Ti sample [25] whereas in the other study the indenter reciprocated on the surfaces of the Ti samples [6]. Nevertheless, all studies showed the same trend for the wear mechanism, with the SPD processing inhibiting adhesion and leading to wear by micro-abrasion. Two recent studies reported a similar or slightly worse wear resistance for UFG Ti compared to CG Ti under very low contact pressures, and this was attributed to the formation of an oxide layer which masks the effect of the microstructural change [30,31]. Tribocorrosion tests in a phosphate buffer solution (PBS) demonstrated a better performance for UFG Ti processed by high-pressure torsion (HPT) compared to CG Ti under the tribocorrosion conditions [28]. Furthermore, wear tests performed in a liquid nitrogen environment showed that Ti with the smallest grain size exhibits the best wear resistance due to a higher strength and lower ductility at this very low temperature [32].

The present investigation was initiated to study the micro-tribological behavior of commercial purity (CP) titanium after processing by HPT with and without annealing. The purpose of the study was to understand and compare the scratch behavior of samples having different grain sizes. The coefficient of friction (COF) of SPD-processed material was compared with the as-received material. A worn surface examination by SEM and infinite focus optical microscopy (IFM) was used to identify the nature of the wear mechanisms and also to evaluate the volume loss.

2. Experimental material and procedures

A CP titanium alloy (Grade 2) was used in this investigation with the following impurities in wt.%: 0.015%H, 0.1%C, 0.25%O, 0.03%N and 0.3%Fe.

Prior to micro-scratch testing, some of the materials were subjected to HPT processing using the procedure described in detail elsewhere [33]. For HPT, specimens having diameters of 10 mm were sliced from the as-received billets and ground with abrasive paper to thicknesses of ∼0.8 mm. The HPT processing was conducted at room temperature on a facility having two anvils with circular flat-bottom depressions at the centres. The depression depth was 0.25 mm and the diameter was 10 mm. The processing was performed under a pressure of 3.0 GPa for 10 revolutions. After HPT processing, some of the HPT-deformed samples were annealed at a temperature of 500 °C for 10 min.

Following HPT, all samples including as-received samples were prepared with 4000# SiC abrasive papers followed by polishing with 1 μm diamond paste which gave each sample an average roughness R_a of 15 ± 5 nm. After cleaning with acetone, the samples were subjected to micro-scratch testing using a new micro-scratch tester developed at the National Physical Laboratory in the UK. As shown in Fig. 1, the key feature of this micro-scratch system is the flexure design which was based on a three dimensional cage with an eight-bar kinematic chain. When the probe is brought into contact with the sample surface, a compression force is generated by deflection of these eight bars. At the same time, the normal force capacitance plate measures the deflection of the bars and thereby indicates the extent of bending. The position of the probe is adjusted by applying a feedback signal to a piezoelectric actuator mounted under the flexure to keep the compression force constant. Similarly, the friction force generated during the wear test is measured using the vertical capacitance plate. The micro-scratch system can carry out wear tests with load ranges of 5–250 mN, a stroke length of up to 8 mm and a speed range of 15–220 μm s^{-1} [34].

These scratch tests were performed at room temperature (18 ± 2 °C) under a relative humidity of 50 ± 5%, under loads of 100 or 200 mN for 1, 2, 5, 10, 50, 100 or 200 turns. These two loads were designed to lie within the capacity of the micro-scratch system and to bring sufficient plastic deformation to the samples so that the wear behavior of the different samples would be readily recorded. A diamond indenter with radius of 200 μm was used to create a micro-scratch of 2 mm length on the disk surface. The testing area was located between 2 and 4 mm away from the centres of the disks and the indenter carried out a reciprocating movement on the sample surfaces with a speed of 0.1 mm/s.

The Vickers microhardness, Hv, was measured using a Matsuzawa Seiki MHT-1 microhardness tester with a test weight of 1000 g and a dwell time of 15 s. The microstructures of the samples were investigated by optical microscopy (OM) and transmission electron microscopy (TEM). Specimens for OM were fine ground by 4000# SiC abrasive paper and then etched with a solution of HF:HNO$_3$:H$_2$O = 2:3:10 in volume percentage. The foils for TEM were produced by twin-jet chemical polishing at a temperature of −30 °C in a solution of 5% perchloric, 35% butanol and 60% methanol.
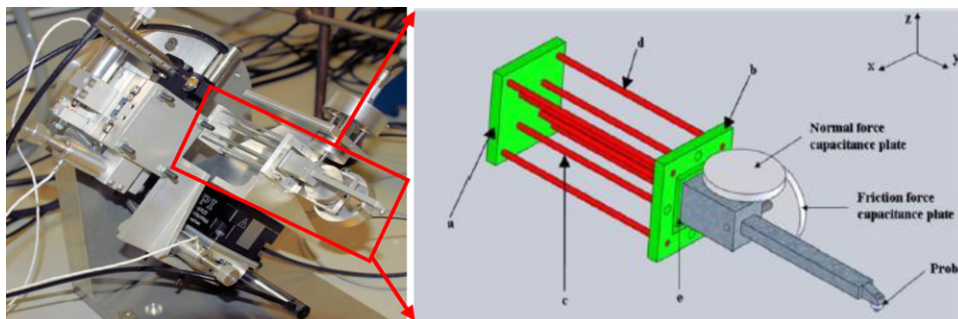
Fig. 1. The overall schematic of micro-scratch test system: (a) the free plate in the flexure element; (b) the mounting plate supported on the piezoelectric actuator; (c) is inner flexure bars; (d) outer flexure bars; (e) the probe lever support [34].

The microstructures of the worn surfaces were analyzed by SEM using a JEOL JSM 6500 instrument. The worn surface profiles were recorded using (IFM) produced by Alicona with a vertical resolution up to 10 nm.

3. Experimental results

3.1. Microstructure and hardness after processing

The microstructure of each sample is shown in Fig. 2. The grain size of Ti in the as-received condition was about 8.6 ± 0.6 μm (Fig. 2a). After HPT processing, large internal stresses were observed within the grains as revealed by extinction contours and the grain boundaries were not well defined. Both bright field images and dark field images were taken to estimate the grain size (Fig. 2c and d). The average grain size of HPT-processed sample was around 130 nm which is similar to previous reports [35,36]. Some of the UFG samples were annealed at 500 °C for 10 min after HPT processing. The grain boundaries then became much better defined with the occurrence of some recrystallization because there were some grains with diameters larger than 1 μm (Fig. 2b). The average grain size of the annealed sample was about 610 ± 50 nm. The microhardness of Ti increased from 182 Hv to about 305 Hv after HPT processing but was reduced to about 256 Hv after annealing due to the recrystallization. The microhardness and microstructure appeared reasonably homogeneous across the disk samples after 10 turns of torsion straining.
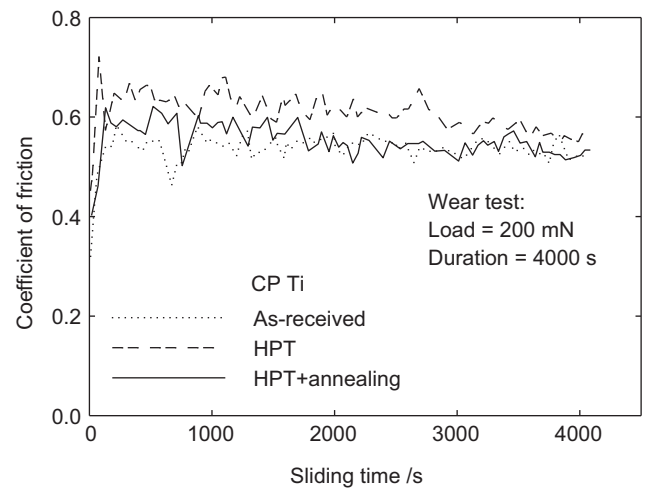
Fig. 3. COF of each Ti sample during micro-scratch under load of 200 mN.

3.2. Coefficient of friction during micro-scratch tests

The dynamic COF of each sample under a load of 200 mN is shown in Fig. 3. It is observed that the friction of the samples was unsteady and independent of the grain size. The average dynamic COF of all the samples was about 0.6 as shown in Table 1, thereby demonstrating that the grain size has no effect on the coefficient of
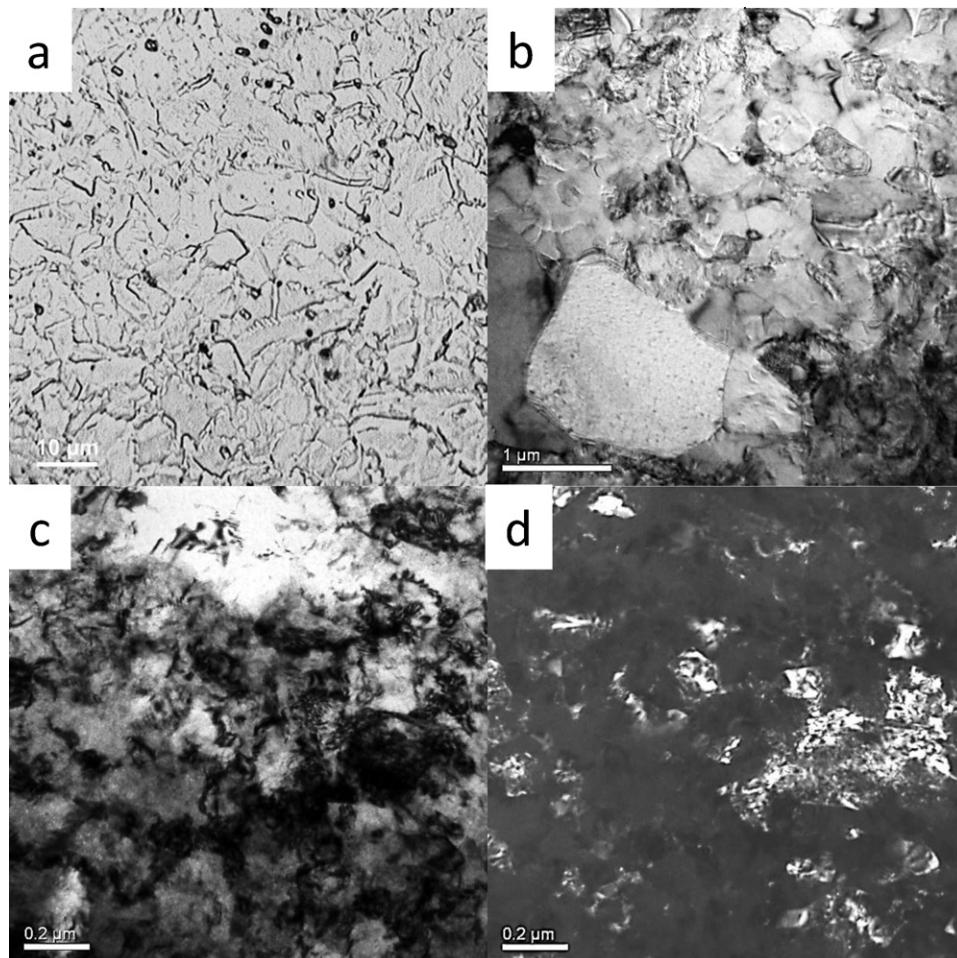
Fig. 2. Microstructure of titanium: (a) as-received, (b) HPT-processed followed by annealing at 773 K for 10 min, (c) bright field TEM image of HPT-processed Ti, (d) dark field TEM image of HPT-processed Ti.

Table 1
Average COF of each sample under 2 load conditions.

	As-received	HPT processed + annealing	HPT processed
Load = 100 mN	0.59 ± 0.01	0.63 ± 0.04	0.62 ± 0.03
Load = 200 mN	0.54 ± 0.01	0.55 ± 0.03	0.60 ± 0.03

friction during micro-scratch testing. Generally, the HPT processed Ti and annealed Ti had slightly higher COF than the CG Ti, and the friction levels decreased slightly with sliding time while the COF of the CG Ti remained constant. After 200 turns of scratching under a load of 200 mN, all samples had similar COF.

3.3. Surface morphology after micro-scratch tests

The appearances of the worn surfaces for the as-received and HPT processed samples are shown in Fig. 4 where the white double arrows denote the sliding directions. Features on the surface were observed due to plastic deformation as material was extruded to the end of the scratch scar from the middle; this wear mode is known as wedge formation or shear-tongue formation [15]. It is clear that much larger shear tongues were formed at the end of the CG Ti (Fig. 4a) compared to the fine-grained sample (Fig. 4c). Furthermore, large flake debris (white arrow in Fig. 4a) was observed in the wear scar of the as-received sample which indicates the operation of adhesion.

At higher magnifications, the difference in the worn surface morphologies for the different samples can be seen. As shown in Fig. 5a, brittle failure (fracture) was observed on the worn surface of the as-received Ti. This means that when the material near the interface was extruded by the indenter, the material undertook plastic deformation and fractured when its limit of ductility was reached. On the worn surface of the HPT-processed sample, multiple grooves parallel to the sliding direction and small debris with diameters around 1 μm were observed (Fig. 5b). The cross-section of the sub-surface damage was studied using optical microscopy and it was found there was no clear evidence for a different deformation behavior between the as-received and HPT-processed samples due to the shallow worn scar.

Fig. 6 shows the topography of the wear scar. It is clear that the worn scar of the as-received sample is very inhomogeneous with material extruded from the scar and piled near the edge to form ridges (Fig. 6a). On the other hand, the wear scar of the

HPT-processed sample has a regular shape with the depth increasing from the edge to the middle of the scar (Fig. 6b). The difference between the as-received sample and the HPT-processed samples was probably caused by their different ductilities. During scratch testing, the surface of the Ti sample was under a force of extrusion and compression. The as-received sample can be easily deformed by the indenter, so that material is extruded, forms large chips, and these large chips pile up and form the high surfaces (Fig. 6a). It is obvious in Fig. 6(a) that the edge of the wear scar of the as-received sample is higher than the normal surface, which means the ridges were formed at the edge of the worn scar and this is another indication of plastic deformation during the scratch test. For the HPT-processed sample, the indenter was unable to penetrate into the sample to the depth of the as-received sample due to the higher strength of the UFG Ti. Furthermore, the HPT-processed sample had lower ductility, so that the debris formed during the scratch test was much smaller and the worn scar showed characteristics of abrasive wear.

3.4. Wear scar profile and volume loss

Five line scans taken perpendicular to the sliding direction were selected randomly from each wear scar and their profiles measured using IFM as shown in Fig. 7. It is observed that the groove shape of the as-received sample was very different at different positions, and the groove of the HPT-processed sample has much better homogenous shape. The profile of the worn scar also shows evidence for ploughing, especially for the as-received sample.

Normally, each worn scar contains ridges and wear grooves. The volume loss (V) can be defined by:

$$V = V_g - V_r \tag{1}$$

where V_g refers to the volume of the worn groove below the original unworn surface and V_r refers to the volume of the ridge formed above the mean surface. The volumes of these parts were measured and plotted against the scratch numbers in Fig. 8. The HPT-processed sample has a much smaller error scatter than the as-received sample because the UFG sample has a more homogeneous scar shape.

Based on a calculation from Eq. (1), there is a negative volume loss for the as-received sample under a load of 100 mN when the scratch number is 10 (Fig. 8b), where this is caused by the ploughing wear mechanism. For the CG sample, ploughing dominated during the first several scratch turns. Therefore, the material
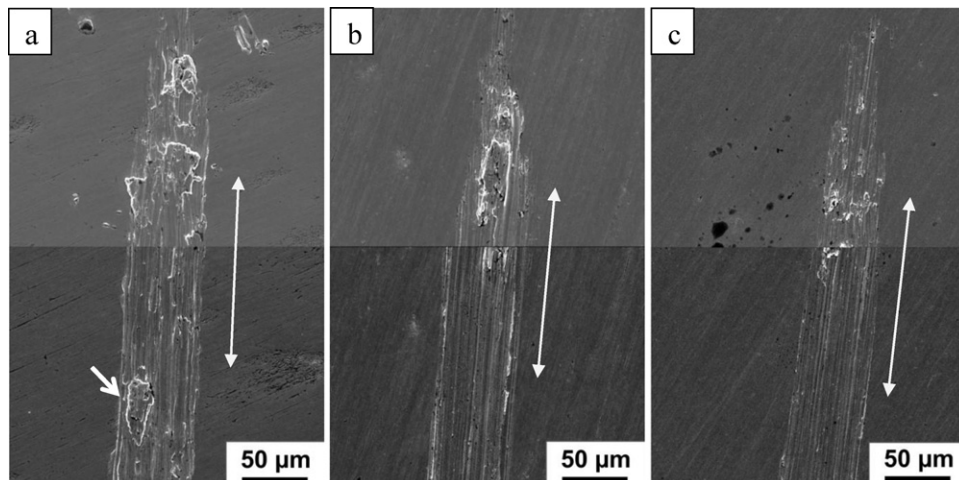
Fig. 4. Worn scar of Ti samples after 50 turns scratch under load of 200 mN with white double arrows showing the sliding directions: (a) as-received sample; (b) HPT + annealing sample; (c) HPT-processed sample.
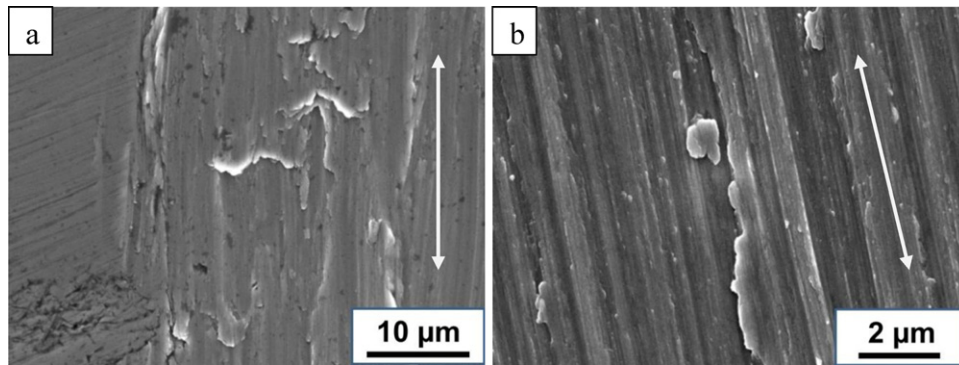
Fig. 5. Surface appearance inside worn scar of Ti samples after 50 turns scratching under load of 200 mN: (a) as-received sample; (b) HPT-processed sample.
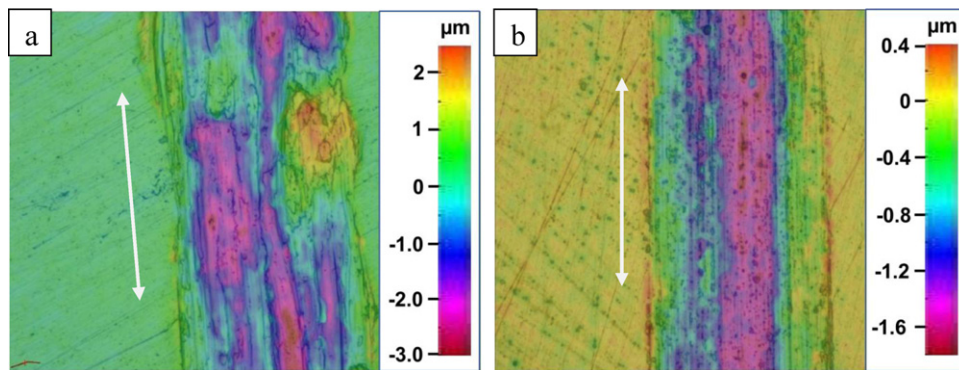
Fig. 6. Worn scar of Ti samples after 50 turns scratch under load of 200 mN: (a) as-received sample; (b) HPT-processed sample.

was extruded from the groove to the edges without falling out, so that no volume loss occurred although grooves were formed. Large debris started to be detached from the sample after several scratches and the volume loss of these samples began to increase. The as-received sample had deeper grooves and wider ridges,

which caused a similar volume loss between the as-received sample and the HPT-processed sample after 50 scratch turns. As shown in Fig. 8(a and c), the volume of ridge remains constant after 10 scratch turns while the volume of the groove increases with the scratch turns. Therefore, when the number of scratch turns exceeds
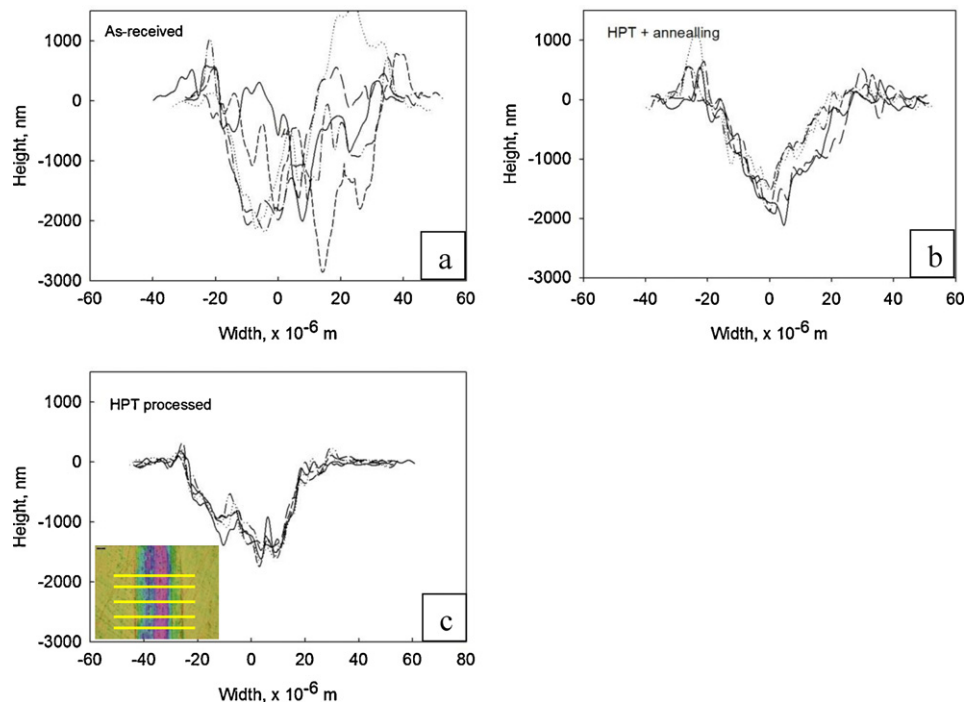
Fig. 7. Worn scar profile of Ti samples after 50 turns scratch under load of 200 mN: (a) as-received sample; (b) HPT + annealing sample; (c) HPT-processed sample.
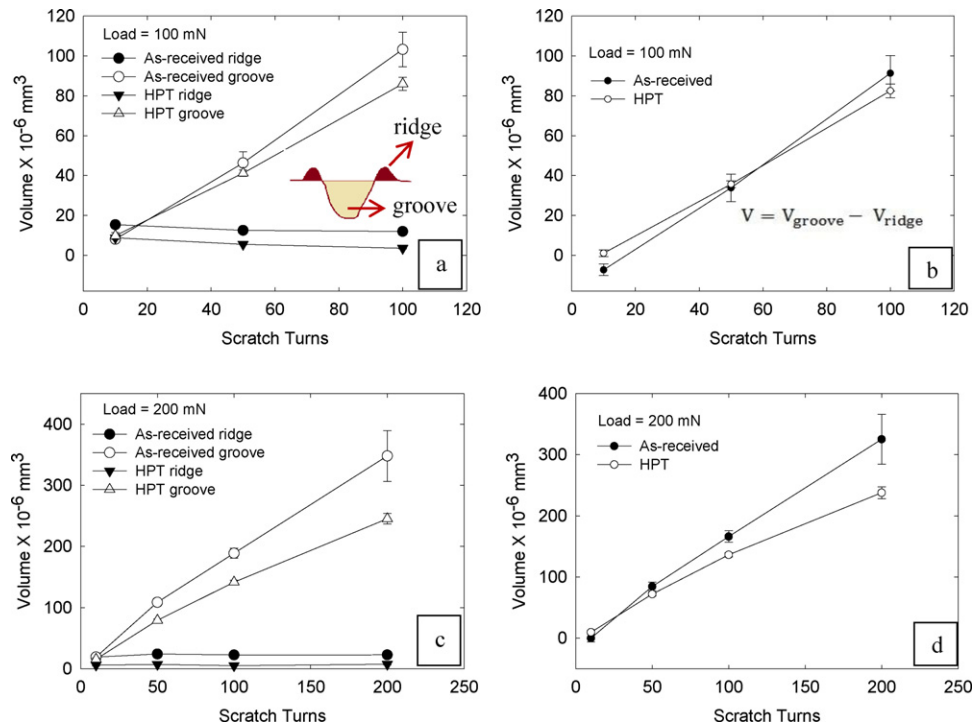
Fig. 8. Volume loss of each sample versus number of scratch turns under load condition of 100 mN and 200 mN: (a and c) volume of ridge (V_r) and groove (V_g); (b and d) volume loss $V = V_g - V_r$.

about 50, the trend becomes clearer and the HPT-processed sample has a lower volume loss than the CG Ti.

4. Discussion

HPT processing was employed to refine the grain size of CP Ti to about 130 nm and to significantly improve the strength of the material. It is worthwhile noting that the hardness of the HPT-processed CP Ti of this study (~305 Hv) is very close to the hardness of the Ti–6Al–4V alloy (~ 330 Hv) which suggests the potential for using UFG Ti as a replacement for the Ti–6Al–4V alloy for biomedical applications. This suggestion is reasonable because it has been demonstrated that CP Ti can be processed by equal-channel angular pressing, another SPD processing technique, at room temperature [37–39].

As shown in earlier studies, there are conflicting results for wear of Ti in the literature due both to the use of different experimental facilities and to the large contact areas which develop during the wear tests and which cause the wear process to be complex. All previous studies compared the different wear behavior between CG materials and UFG materials in a macro-contact range in which the contact occurred at numerous asperities. However, studies have indicated that micro-wear systems may behave in quite different ways from their larger counterparts [40]. Therefore, the importance of investigating the micro-wear behavior of UFG materials is now recognized. In this study, micro-scratch tests were employed for the first time to provide a direct and comprehensive comparison between the wear behavior of CG and UFG Ti and thus to not only simulate the work conditions of micro-components but also to provide information to reveal the relationship between debris formation and the material properties.

During sliding, wear debris is formed on the wear surface via work hardening, phase transitions and third body formation. This debris also affects the wear mechanism through the production of abrasive asperities [41,42]. In this study, it was noticed that different properties of the samples lead to different debris

formation mechanisms during scratching. The occurrence of a phase transition is a possible explanation because there is evidence that the high pressures imposed in HPT processing may produce phase transitions in pure Ti [43,44] and a Ti alloy [45]. However, a further investigation is now needed to explore this possibility. In practice, the ductility and strength of materials affects both debris formation and the size of the debris that is formed.

Previous studies using an in situ tribosystem observed three wear modes: ploughing, wedge formation and cutting [15,46]. The worn surface of the as-received sample in this study showed clear characteristics of ploughing and wedge formation wear whereas the HPT-processed sample exhibited a milder abrasive wear. The wear mechanisms also affected the dynamic coefficient of friction. For the as-received Ti, the large debris formed by wedge formation was pushed out of the wear track as soon as it was formed, and therefore the influence of the debris on the COF was negligible. For the HPT-processed Ti and the annealed Ti, tiny debris formed by abrasion wear was mostly trapped in the wear track, and the rolling of the debris may explain the decreasing COF. In the present study, under loads of 100 and 200 mN, the mean contact pressure P_m between two materials was predicted as 1.18 and 1.49 GPa, respectively. Thus, the contact pressure is quite high but no evidence of oxidation wear was observed.

The specific wear rate, k, is widely used to compare the wear resistance of materials, where this wear rate is defined by:

$$k = \frac{V}{WL} \qquad (2)$$

where V is the volume loss, W is the load and L is the sliding distance. As suggested by Archard's equation, k is inversely proportional to the hardness which shows that materials with higher hardness have better wear resistance [47]. As shown in Fig. 9, the wear rate of Ti decreases with increasing microhardness but this decrease is less than anticipated from Archard's equation. Furthermore, a much smaller error scatter of wear rate was observed for the UFG Ti
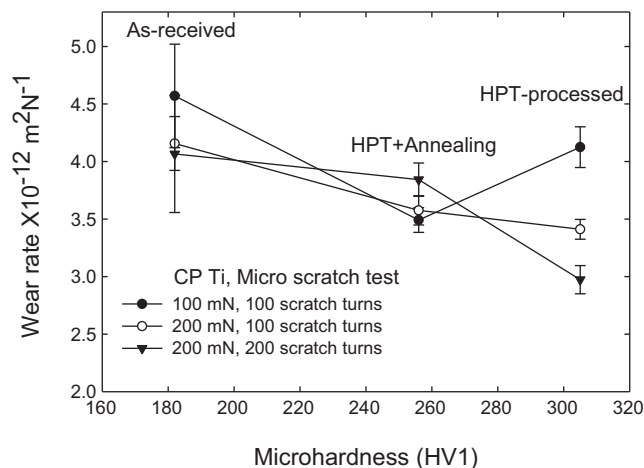
Fig. 9. Specific wear rate versus microhardness of each Ti sample.

samples than the CG Ti samples which indicated a more homogenous wear behavior for UFG Ti compared to CG Ti. For a well-designed wear system, the wear rate of a material is low as well as steady, so that the HPT-processed Ti exhibits a better possibility for wear applications.

5. Conclusions

1. High-pressure torsion was used to introduce significant grain refinement in CP Ti and micro-scratch tests were employed to examine the micro-tribological behavior of samples having different grain sizes.
2. The coefficient of friction of all samples was about 0.6 which shows the grain size of the material has little or no effect on the coefficient of friction during testing.
3. Ploughing and wedge formation were the major wear modes for the coarse-grained samples whereas abrasive was the dominant wear mode for the ultrafine-grained samples. Furthermore, HPT-processed sample have better wear resistance than CG Ti, which indicates that UFG Ti is more suitable for wear applications.

Acknowledgements

References

[1] R.Z. Valiev, Y. Estrin, Z. Horita, T.G. Langdon, M.J. Zehetbauer, Y.T. Zhu, Producing bulk ultrafine-grained materials by severe plastic deformation, JOM 58 (4) (2006) 33–39.
[2] R.Z. Valiev, N.A. Krasilnikov, N.K. Tsenev, Plastic deformation of alloys with submicron-grained structure, Mater. Sci. Eng. A 137 (1991) 35–40.
[3] W.J. Kim, Y.K. Sa, Micro-extrusion of ECAP processed magnesium alloy for production of high strength magnesium micro-gears, Scripta Mater. 54 (2006) 1391–1395.
[4] R.Z. Valiev, I.P. Semenova, V.V. Latysh, H. Rack, T.C. Lowe, J. Petruzelka, L.M. Dluhos, D. Hrusak, J. Sochova, Nanostructured titanium for biomedical applications, Adv. Eng. Mater. 10 (2008) B15–B17.
[5] X.G. Qiao, N. Gao, Z. Moktadir, M. Kraft, M.J. Starink, Fabrication of MEMS components using ultrafine-grained aluminium alloys, J. Micromech. Microeng. 20 (2010) 045029 (9p).
[6] P.Q. La, J. Ma, Y.T. Zhu, J. Yang, W.M. Liu, Q.J. Xue, Dry-sliding tribological properties of ultrafine-grained Ti prepared by severe plastic deformation, Acta Mater. 53 (2005) 5167–5173.
[7] L.L. Gao, X.H. Cheng, Microstructure and dry sliding wear behavior of Cu–10%Al–4Fe alloy produced by equal channel angular extrusion, Wear 265 (2008) 986–991.
[8] G. Purcek, O. Saray, T. Kucukomeroglu, M. Haouaoui, I. Karaman, Effect of equal-channel angular extrusion on the mechanical and tribological properties of as-cast Zn–40Al–2Cu–2Si alloy, Mater. Sci. Eng. A 527 (2010) 3480–3488.
[9] T. Kucukomeroglu, Effect of equal-channel angular extrusion on mechanical and wear properties of eutectic Al–12Si alloy, Mater. Des. 31 (2010) 782–789.
[10] M.I. Abd El Aal, N. El Mahallawy, F.A. Shehata, M. Abd El Hameed, E.Y. Yoon, H.S. Kim, Wear properties of ECAP-processed ultrafine grained Al–Cu alloys, Mater. Sci. Eng. A 527 (2010) 3726–3732.
[11] C.T. Wang, N. Gao, R.J.K. Wood, T.G. Langdon, Wear behavior of an aluminum alloy processed by equal-channel angular pressing, J. Mater. Sci. 46 (2011) 123–130.
[12] C.T. Wang, N. Gao, R.J.K. Wood, T.G. Langdon, Wear behaviour of Al-1050 alloy processed by severe plastic deformation, Mater. Sci. Forum 667–669 (2011) 1100–1105.
[13] N. Gao, C.T. Wang, R.J.K. Wood, T.G. Langdon, Wear resistance of SPD-processed alloys, Mater. Sci. Forum 667–669 (2011) 1094–1099.
[14] H. Kitsunai, K. Kato, K. Hokkirigawa, H. Inoue, The transitions between microscopic wear modes during repeated sliding friction observed by a scanning electron-microscope tribosystem, Wear 135 (1990) 237–249.
[15] K. Kato, Micromechanisms of wear–wear modes, Wear 153 (1992) 277–295.
[16] K. Kato, Microwear mechanisms of coatings, Surf. Coat. Technol. 77 (1995) 469–474.
[17] M.G. Gee, A.D. Gee, A cost effective test system for micro-tribology experiments, Wear 263 (2007) 1484–1491.
[18] L. Winkless, E. Martinot, M.G. Gee, A. Cuenat, Microtribology friction measurements on microtextured silicon, Tribol. Mater. Surf. Interfaces 3 (2009) 165–174.
[19] M.G. Gee, Model scratch corrosion studies for WC/Co hardmetals, Wear 268 (2010) 1170–1177.
[20] M. Geetha, A.K. Singh, R. Asokamani, A.K. Gogia, Ti based biomaterials, the ultimate choice for orthopaedic implants – a review, Prog. Mater. Sci. 54 (2009) 397–425.
[21] Y. Okazaki, E. Gotoh, Comparison of metal release from various metallic biomaterials in vitro, Biomaterials 26 (2005) 11–21.
[22] Y. Li, Wong, J. Xiong, P. Hodgson, C. Wen, Cytotoxicity of titanium and titanium alloying elements, J. Dent. Res. 89 (2010) 493–497.
[23] S. Makihira, Y. Mine, H. Nikawa, T. Shuto, S. Iwata, R. Hosokawa, K. Kamoi, S. Okazaki, Y. Yamaguchi, Titanium ion induces necrosis and sensitivity to lipopolysaccharide in gingival epithelial-like cells, Toxicol. In Vitro 24 (2010) 1905–1910.
[24] V.V. Stolyarov, Y.T. Zhu, I.V. Alexandrov, T.C. Lowe, R.Z. Valiev, Influence of ECAP routes on the microstructure and properties of pure Ti, Mater. Sci. Eng. A 299 (2001) 59–67.
[25] V.V. Stolyarov, L.S. Shuster, M.S. Migranov, R.Z. Valiev, Y.T. Zhu, Reduction of friction coefficient of ultrafine-grained CP titanium, Mater. Sci. Eng. A 371 (2004) 313–317.
[26] H. Garbacz, K.J. Kurzydlowski, Properties of nanotitanium for potential medical applications, Macromol. Symp. 253 (2007) 128–133.
[27] S. Faghihi, F. Azari, A.P. Zhilyaev, J.A. Szpunar, H. Vali, M. Tabrizian, Cellular and molecular interactions between MC3T3-E1 pre-osteoblasts and nanostructured titanium produced by high-pressure torsion, Biomaterials 28 (2007) 3887–3895.
[28] S. Faghihi, D. Li, J.A. Szpunar, Tribocorrosion behaviour of nanostructured titanium substrates processed by high-pressure torsion, Nanotechnology 21 (2010), 485703 (10p).
[29] J.W. Park, Y.J. Kim, C.H. Park, D.H. Lee, Y.G. Ko, J.H. Jang, C.S. Lee, Enhanced osteoblast response to an equal channel angular pressing-processed pure titanium substrate with microrough surface topography, Acta Biomater. 5 (2009) 3272–3280.
[30] H. Garbacz, M. Gradzka-Dahlke, K.J. Kurzydlowski, The tribological properties of nano-titanium obtained by hydrostatic extrusion, Wear 263 (2007) 572–578.
[31] G. Purcek, O. Saray, O. Kul, I. Karaman, G.G. Yapici, M. Haouaoui, H.J. Maier, Mechanical and wear properties of ultrafine-grained pure Ti produced by multi-pass equal-channel angular extrusion, Mater. Sci. Eng. A 517 (2009) 97–104.
[32] A. Jain, B. Basu, B.V. Manoj Kumar, Harshavardhan, J. Sarkar, Grain size–wear rate relationship for titanium in liquid nitrogen environment, Acta Mater. 58 (2010) 2313–2323.
[33] A.P. Zhilyaev, T.G. Langdon, Using high-pressure torsion for metal processing: fundamentals and applications, Prog. Mater. Sci. 53 (2008) 893–979.
[34] M.G. Gee, J.W. Nunn, A. Muniz-Piniella, Micro-tribology experiments on engineering coatings, Wear 271 (2011) 2671–2680.
[35] R.Z. Valiev, A.V. Sergueeva, A.K. Mukherjee, The effect of annealing on tensile deformation behavior of nanostructured SPD titanium, Scripta Mater. 49 (2003) 669–674.
[36] K. Edalati, E. Matsubara, Z. Horita, Processing pure Ti by high-pressure torsion in wide ranges of pressures and strain, Metall. Mater. Trans. A 40A (2009) 2079–2086.
[37] X. Zhao, W. Fu, X. Yang, T.G. Langdon, Microstructure and properties of pure titanium processed by equal-channel angular pressing at room temperature, Scripta Mater. 59 (2008) 542–545.
[38] X. Zhao, X. Yang, X. Liu, X. Wang, T.G. Langdon, The processing of pure titanium through multiple passes of ECAP at room temperature, Mater. Sci. Eng. A 527 (2010) 6335–6339.

[39] Y. Zhang, R.B. Figueiredo, S.N. Alhajeri, J.T. Wang, N. Gao, T.G. Langdon, Structure and mechanical properties of commercial purity titanium processed by ECAP at room temperature, Mater. Sci. Eng. A 528 (2011) 7708–7714.

[40] B. Bhushan, J.N. Israelachvili, U. Landman, Nanotribology–friction, wear and lubrication at the atomic-scale, Nature 374 (1995) 607–616.

[41] T. Sasada, M. Oike, N. Emori, The effect of abrasive grain-size on the transition between abrasive and adhesive wear, Wear 97 (1984) 291–302.

[42] D.A. Rigney, Sliding wear of metals, Annu. Rev. Mater. Sci. 18 (1988) 141–163.

[43] Y. Todaka, J. Sasaki, T. Moto, M. Umemoto, Bulk submicrocrystalline ω-Ti produced by high-pressure torsion straining, Scripta Mater. 59 (2008) 615–618.

[44] Y. Ivanisenko, A. Kilmametov, H. Rösner, R.Z. Valiev, Evidence of $\alpha \to \varpi$ phase transition in titanium after high pressure torsion, Int. J. Mater. Res. 99 (2008) 36–41.

[45] Y.B. Wang, Y.H. Zhao, Q. Lian, X.Z. Liao, R.Z. Valiev, S.P. Ringer, Y.T. Zhu, E.J. Lavernia, Grain size and reversible beta-to-omega phase transformation in a Ti alloy, Scripta Mater. 63 (2010) 613–616.

[46] K. Hokkirigawa, K. Kato, Z.Z. Li, The effect of hardness on the transition of the abrasive wear mechanism of steels, Wear 123 (1988) 241–251.

[47] J.F. Archard, Contact and rubbing of flat surfaces, J. Appl. Phys. 24 (1953) 981–988.

Research Paper

Processing of an ultrafine-grained titanium by high-pressure torsion: An evaluation of the wear properties with and without a TiN coating

Chuan Ting Wang[a,b], Nong Gao[b,*], Mark G. Gee[c], Robert J.K. Wood[a], Terence G. Langdon[b,d]

[a]National Centre for Advanced Tribology at Southampton, Faculty of Engineering and the Environment, University of Southampton, Southampton SO17 1BJ, UK
[b]Materials Research Group, Faculty of Engineering and the Environment, University of Southampton, Southampton SO17 1BJ, UK
[c]National Physical Laboratory, Hampton Road, Teddington, Middlesex TW16 5PT, UK
[d]Departments of Aerospace & Mechanical Engineering and Materials Science, University of Southern California, Los Angeles CA 90089-1453, USA

ARTICLE INFO

ABSTRACT

A commercial purity (CP) Grade 2 Ti was processed by high-pressure torsion (HPT) using an imposed pressure of 3.0 GPa at room temperature. The HPT processing reduced the grain size from $\sim$8.6 μm in the as-received state to ultra-fine grains (UFG) of $\sim$130 nm after HPT. Tensile testing showed the HPT-processed Ti exhibited a good combination of high ultimate tensile strength ($\sim$940 MPa) and a reasonable elongation to failure ($\sim$23%). Physical vapour deposition was used to deposit TiN coatings, with a thickness of 2.5 μm, on Ti samples both with and without HPT processing. Scratch tests showed the TiN coating on UFG Ti had a critical failure load of $\sim$22.5 N whereas the load was only $\sim$12.7 N for the coarse-grained Ti. The difference is explained using a simple composite hardness model. Wear tests demonstrated an improved wear resistance of TiN coating when using UFG Ti as the substrate. The results suggest that CP Ti processed by HPT and subsequently coated with TiN provides a potentially important material for use in bio-implants.

© 2012 Elsevier Ltd. All rights reserved.

1. Introduction

Total joint replacements are now applied worldwide to alleviate the functional deteriorations in human joints caused by degenerative diseases (Geetha et al., 2009). In England, in 2011, there were >80,000 total knee replacements and >75,000 total hip replacements (Leopold, 2011) and predictions suggest these numbers will increase substantially in future years (Kurtz et al., 2007). Based on these reports, it is anticipated there will be an ever increasing demand for bio-implants.

Metallic biomaterials such as stainless steels, Co–Cr alloys and titanium alloys are used extensively in orthopaedic applications due to their high strength, bio-tolerance and excellent corrosion resistance. Nevertheless, there are numerous reports documenting the toxicity of these metal implants. As the metal ions (Ni, Cr, Co, Al, V, etc.) are released from the implants, there are potential health problems such as skin diseases due to Ni toxicity and carcinogenicity due to Co and Cr (Okazaki and Gotoh, 2005, 2008; Li et al., 2010; Makihira et al., 2010). This problem may be avoided through the use of commercial purity (CP) titanium but procedures are then required for improving the strength of the material (Long and Rack, 1998; Elias et al., 2008). Recent reports have demonstrated that ultra-fine grained (UFG) CP Ti, having a comparable high strength to Ti-6Al-4V and a much improved biocompatibility, may be produced using several metal forming procedures based on the imposition of severe plastic deformation (SPD) (Stolyarov et al., 2001a, 2004; Sordi et al., 2012). For example, bulk UFG CP Ti was successfully produced using SPD methods such as equal-channel angular pressing (ECAP) (Valiev and Langdon, 2006) and high-pressure torsion (HPT) (Zhilyaev and Langdon, 2008) and processing both at high temperatures and room temperature.

The results available to date show that processing by HPT generally produces greater grain refinement and improved strengthening by comparison with ECAP (Zhao et al., 2008; Todaka et al., 2008; Edalati et al., 2009; Sabirov et al., 2010, 2011; Zhang et al., 2011). For example, a high ultimate tensile stress (UTS) of ~1400 MPa was achieved in Grade 4 Ti using HPT but with a corresponding significant loss in ductility (Islamgaliev et al., 2008). A corrosion study reported superior corrosion resistance in UFG Ti due to rapid passivation along the grain boundaries (Balyanov et al., 2004). The fatigue life of Ti is enhanced by SPD so that in Grade 4 Ti the fatigue limit after 10^7 cycles was increased to ~590 MPa using ECAP compared with ~350 MPa in the coarse-grained (CG) condition (Semenova et al., 2008, 2009; Estrin and Vinogradov 2010). Recent research on biocompatibility has documented improved pre-osteoblast attachment and rate of growth on UFG pure Ti compared with CG pure Ti and Ti-6Al-4V substrates, where this is attributed to the presence of surface discontinuities, the surface energy, a higher wettability and the presence of stable TiO_2 films which improve the protein adsorption on the surface (Faghihi et al., 2007; Park et al., 2009; Bindu et al., 2009).

Despite these merits, questions remain concerning the long term durability of UFG Ti and specifically the wear resistance. In practice, the sliding motion between the femoral and acetabular metal components will generate metallic debris that may cause pain in the patient and lead ultimately to mechanical failure of the device (Marino and Mascaro, 2004; Diomidis et al., 2012). To address this problem, several studies have been conducted to evaluate the wear behaviour of UFG Ti (Stolyarov et al., 2004; La et al., 2005; Purcek et al., 2009; Faghihi et al., 2010; Alsaran et al., 2011). Initially, friction studies at various temperatures under high load conditions showed that the high strength after ECAP processing improved the load-bearing capacity and reduced the coefficient of friction (COF) of Ti (Stolyarov et al., 2004). Dry sliding tests at room temperature, in both macro and micro contacts,

showed a similar COF for UFG and CG Ti of ~0.6 but the UFG Ti exhibited a ~30% lower wear rate and less tendency for adhesion (La et al., 2005; Wang et al., 2012). When the wear testing was dominated by an oxidation wear mechanism under a very low contact pressure, there was very little difference in the wear rate between UFG and CG Ti because the presence of the oxidation layer effectively masked the strengthening of the UFG structures (Purcek et al., 2009). When testing in an electrolyte, UFG Ti showed a slightly better wear resistance than CG Ti but both materials had relatively high wear rates of the order of $\sim 10^{-13}\,\mathrm{m^3\,N^{-1}\,m^{-1}}$ which suggests that the wear resistance of UFG Ti is not sufficiently good under sliding contacts (Faghihi et al., 2010).

Since UFG pure Ti has many merits including good bioactivity and a limited toxic ion release compared to Ti alloys such as Ti-6Al-4V and other biomaterials (Okazaki and Gotoh, 2005; Latysh et al., 2006; Faghihi et al., 2007; Li et al., 2010), it appears that the use of a surface coating may provide an effective method for increasing the wear resistance to an acceptable level. Earlier experiments showed that the wear resistance of UFG pure Ti may be improved significantly by using a micro-arc oxidation and hydrothermal treatment to form a porous oxide layer with a thickness of ~10 μm on the surface of UFG Ti (Alsaran et al., 2011). This suggests the possibility of combining SPD processing and coating technology to fabricate a coated UFG Ti having high strength and excellent corrosion and wear resistance for use in biomedical applications. Accordingly, the present investigation was initiated to evaluate the feasibility of this approach.

It is important to note that any application of a coating to UFG Ti requires a temperature under 350 °C because of the occurrence of recrystallisation at higher temperatures (Valiev et al., 2003). By comparison with other coating techniques such as chemical vapour deposition (CVD) and thermal oxidation, physical vapour deposition (PVD) allows a much lower processing temperature and may even be conducted at room temperature. Moreover, in PVD it is easy to control the surface roughness which corresponds to the roughness of the substrate surface. There are demonstrations that a TiN coating, introduced via PVD, is effective as a cutting tool coating and biomedical coating due to the dense structure, good interface bonding, high hardness and biocompatibility (PalDey and Deevi, 2003; Hoche et al., 2011). In addition, TiN coatings have excellent bonding with the Ti substrate and good ductility when subjected to impact and scratching (Heinke et al., 1995) and they are widely recognised as good candidate materials for introducing protective layers on bio-implants (Starosvetsky and Gotman, 2001; Piscanec et al., 2004; Balla et al., 2012). An earlier investigation demonstrated a good combination of high strength and reasonable ductility in CP Ti processed by HPT (Wang et al., 2012) and the present study builds on these results by depositing a TiN coating on Ti substrates, both before and after HPT, and evaluating the coating performance using scratch and micro-wear testing.

2. Experimental material and procedures

The experiments were conducted using a Grade 2 CP titanium containing the following impurities in wt.%: 0.015% H, 0.1% C,

0.25% O, 0.03% N and 0.3% Fe. Further information about the material and the processing methods were given earlier (Wang et al., 2012). Briefly, discs were prepared having diameters of 10 mm and thicknesses of ∼0.8 mm and these discs were processed by quasi-constrained HPT (Zhilyaev and Langdon, 2008; Figueiredo et al., 2011, 2012) for 10 revolutions at room temperature under an imposed pressure of 3.0 GPa using a rotation speed of 1 rpm. As noted earlier (Wang et al., 2012), 10 revolutions of HPT produces a very homogeneous microstructure in these Ti samples.

The Vickers microhardness, Hv, was measured using a Matsuzawa Seiki MHT-1 microhardness tester with a test weight of 1000 g and a dwell time of 15 s. Mechanical testing was performed by machining mini-specimens from off-centre positions in the HPT discs using the procedure described earlier (Sakai et al., 2005). These specimens were tested in tension using an Instron testing facility at room temperature operating under conditions of constant cross-head displacement with an initial strain rate of $1.0 \times 10^{-2} \, \text{s}^{-1}$. Due to the small size of the mini-specimens, a special sample holder was designed to fix the samples within the machine.

Using samples both before and after HPT, TiN coatings were deposited on the Ti substrates using PVD in a magnetron sputter ion plating system produced by Teer Coatings Ltd. Prior to the PVD process, all Ti substrates were ground to 1200 grit paper to give an average roughness, R_a, of 230 ± 20 nm. The Ti substrates were then cleaned by Ar plasma ion using a pulsed DC bias, followed by depositing a 100 nm thick Ti layer on the Ti substrates by DC magnetron sputtering. Finally, nitrogen with a carefully controlled flow was introduced into the PVD chamber to produce the TiN coating together with Ti ions from the Ti target. All of these processes were performed at a temperature below 150 °C to avoid recrystallisation of the Ti substrates. Following deposition, the coating had a thickness of ∼2.5 μm. It is important to note that this hard coating can follow the deformation of the Ti substrate under load without producing any stress concentrations and/or cracking.

Scratch tests were performed using a ST3001 scratch tester produced by Teers Coating Ltd. A Rockwell C diamond indenter with 0.2 mm radius and 120° cone angle was used as the scratch tool. The indenter slid on the coating surface as the normal load increased from 0.5 N to 25 N, giving a loading speed per sliding distance of 10 N mm^{-1}. Any failure event, such as a cracking of the coating or delamination, was detected and recorded using an acoustic emission (AE) detector. The critical load, L_c, when the TiN was fully scratched from the substrate was determined through an examination of the scratch track using scanning electron microscopy (SEM). The scratch testing was repeated 5 times for each sample to obtain reliable results. After scratch testing, the surface profiles of the TiN coatings at the critical load were measured using an ultimate focus optical microscope produced by Alicona and operating in line scanning mode

Wear tests were performed on a micro-wear tester available at the National Physical Laboratory and designed specifically for investigating the properties of thin coatings (Gee et al., 2011). The dry sliding tests were conducted under a constant load of 200 mN with a sliding speed of 200 μm s^{-1}. A diamond sphere tip with a radius of 20 μm travelled repeatedly on the coating surface for up to 1400 turns. The initial mean contact

stress, P_{mean}, was estimated as ∼11.2 GPa but this contact stress dropped dramatically when the probe penetrated into the coating. The surface profiles were recorded after wear testing using the ultimate focus optical microscope. Finally, the failure modes and wear mechanisms of the TiN coatings on the Ti substrates were analysed using SEM and energy-dispersive X-ray spectroscopy (EDX) and microstructures were recorded using transmission electron microscopy (TEM).

3. Experimental results

3.1. Microstructure and mechanical properties of Ti substrates

Fig. 1 shows the microstructures and tensile curves of the CP Ti before and after processing by HPT. Optical microscopy gave a grain size of ∼8.6 μm in the as-received state but there was a refined grain size of ∼130 nm after HPT. This reduction in grain size led to an increase in the microhardness from an initial value of ∼182 to ∼305 Hv after HPT (Wang et al., 2012). Examination by TEM showed a high density of dislocations and poorly defined grain boundries after 10 revolutions of HPT where this is characteristic of microstructures produced by HPT (Zhilyaev and Langdon, 2008). The tensile curves shown in Fig. 1 demonstrate that the UTS of Ti increases from ∼660 MPa in the as-received state to ∼940 MPa after HPT but the elongation to failure decreases from ∼40 to ∼23%. This combination of high strength and reasonable ductility in Grade 2 CP Ti after HPT processing makes the UFG pure Ti compatible with the Ti-6Al-4V alloy where the UTS is ∼980 MPa and the elongation to failure is ∼14%.

3.2. The morphology of the coating

The surface morphology of a coating on the as-received Ti substrate is shown in Fig. 2. After deposition, the TiN coating had an average roughness, R_a, of ∼230 nm, which is identical to the initial Ti substrate. It is reasonable to assume the coatings on the CG and UFG Ti have the same thickness because all depositions were conducted together in the same PVD system.
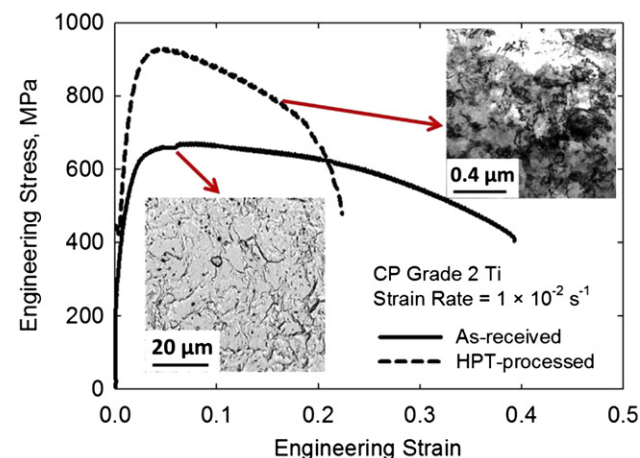
Fig. 1 – Microstructure and tensile curves of Ti substrates.
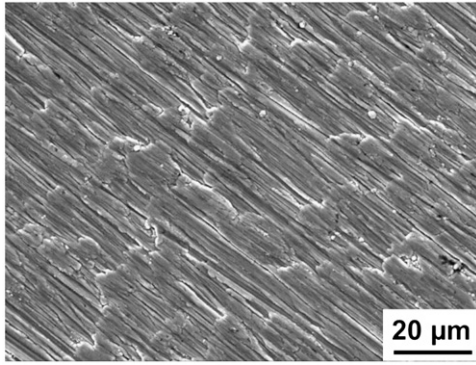
Fig. 2 – Unworn surface of a TiN coating on as-received Ti.
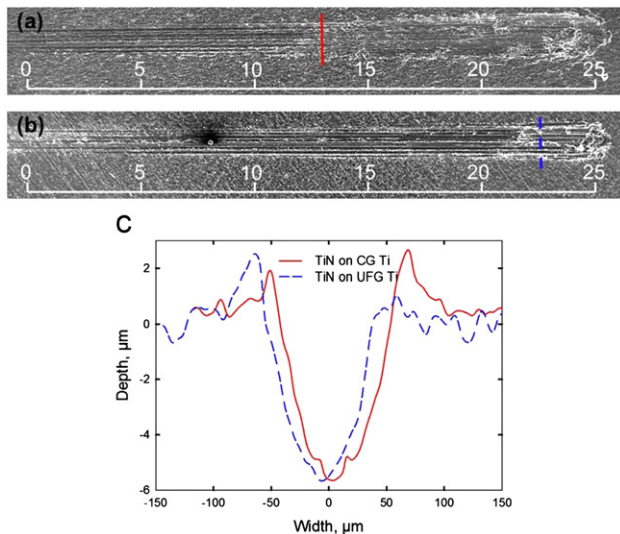
Fig. 3 – SEM images of scratched TiN on (a) CG and (b) UFG Ti substrates, and (c) the cross-section profile of each sample at the critical load.

Fig. 4 – AE signals of TiN on (a) CG and (b) UFG Ti substrates.

3.3. The scratch tests

Since thin coatings are now widely applied in several different conditions, various experimental methods have been proposed to measure the properties of these coatings. The scratch test, conducted using a Rockwell C indenter, is currently accepted as a standard testing method which may be used to provide extensive information on several features of the coatings: examples include the initial cracking load of the coating under which the coating initially cracks and the critical load of the coating, L_c, where the coating is fully removed from the substrate (Stallard et al., 2006). The scratch test also reveals typical failure modes of the coatings which are mostly related to the property of the coating and the adhesion between the coating and the substrate (Bull, 1997).

As shown in Fig. 3, SEM micrographs after scratch testing indicate that L_c of the TiN coating on CG Ti is 12.7 ± 0.2 N whereas L_c for the TiN coating on UFG Ti is 22.5 ± 0.3 N. Similarly, the initial cracking load of the coating is related to a sudden peak in the AE signal, as cracking of the coating produces strain energy which is captured by the AE detector. As shown in Fig. 4, the first cracking of the TiN coating on CG Ti
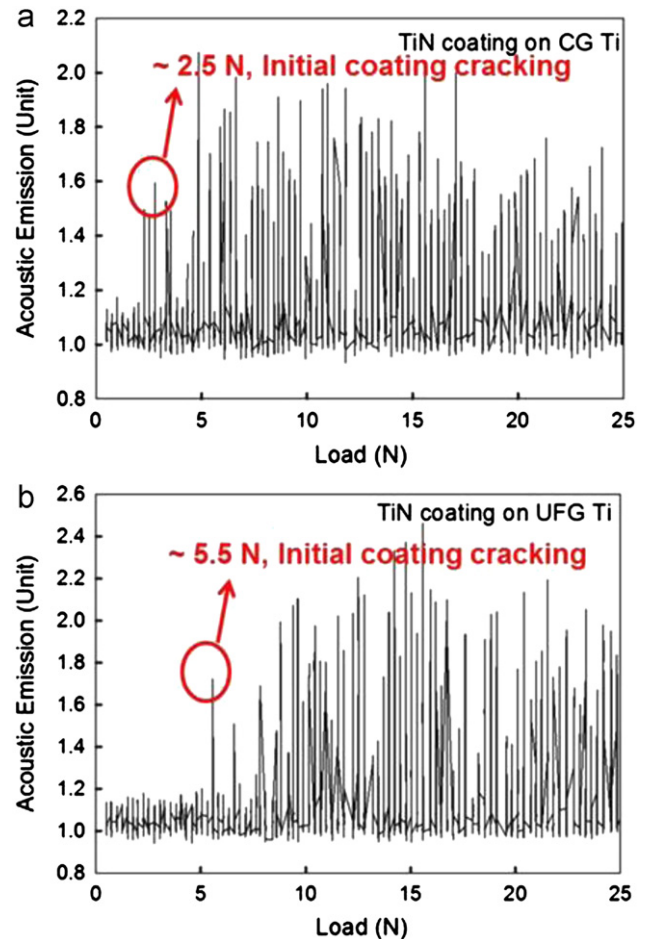
occurs at ~2.5 N while for the TiN coating on UFG Ti a first crack appears at ~5.5 N. In earlier scratch studies, a 2 μm TiN coating gave values for L_c of ~25 N and ~16 N on hot working steel and stainless steel, respectively (Dobrzanski et al., 2005; Guruvenket et al., 2009) and a 2 μm TiN coating on a Ti substrate gave a value for L_c of ~36 N (Stallard et al., 2006). The values for L_c of the TiN coating may vary between different studies because of differences in the interlayer and coating processes.

Using Alicona microscopy after scratch testing, the surface heights of the points along the lines marked in Fig. 3(a) and (b), representing the cross-sectional profiles of the samples, are recorded in Fig. 3(c). It is apparent that the samples have very similar widths and depths when the TiN delaminates from the substrates at the L_c load. The TiN coating delaminated from the substrate when it reached a tensile limit regardless of the substrate and the indenter then penetrates into the material. In practice, the TiN coating on UFG Ti recorded a higher L_c load due to the higher hardness of the ultrafine-grained material. These results demonstrate that a TiN coating with a UFG Ti substrate exhibit a better load-bearing capacity because the hard substrate prevents the indenter from penetrating into the coating.

3.4. The wear tests

Micro-wear tests were employed to examine the wear resistance of the TiN coatings. During the wear tests, a diamond

probe with a radius of 20 μm was brought along the surfaces of the TiN coatings in a reciprocating manner. The COF of all samples showed a steady value of ~0.2 during these tests, as illustrated in Fig. 5. These results confirm that the presence of a TiN coating successfully reduces the COF because earlier experiments gave a relatively high COF of ~0.6 for the uncoated Ti (Wang et al., 2012). Previous wear studies on TiN coatings reported COF values in the range from 0.2 to 1.0 where these values are highly influenced by the counter body and test conditions (Yilbas and Shuja, 2000; Dobrzanski et al., 2005; Guruvenket et al., 2009). A similar COF for a TiN coating was also reported in earlier studies using a similar procedure and contact geometry (Stallard et al., 2006; Jeong et al., 2007).

Fig. 6 shows the wear surface morphologies and cross-sections after 100, 300, 800 and 1400 wear repeats for (a) CG and (b) UFG Ti together with (c) the wear scar profiles. It is apparent that the strength of the substrate has an important effect on the wear of coatings such that the HPT-processed Ti gives better support to the applied coating. Thus, the wear track of a TiN coating on UFG Ti is always shallower and narrower than the same coating on CG Ti. Also, massive deformation of the coating is noted, especially in the coating on the as-received Ti. It can be seen that ridges are formed
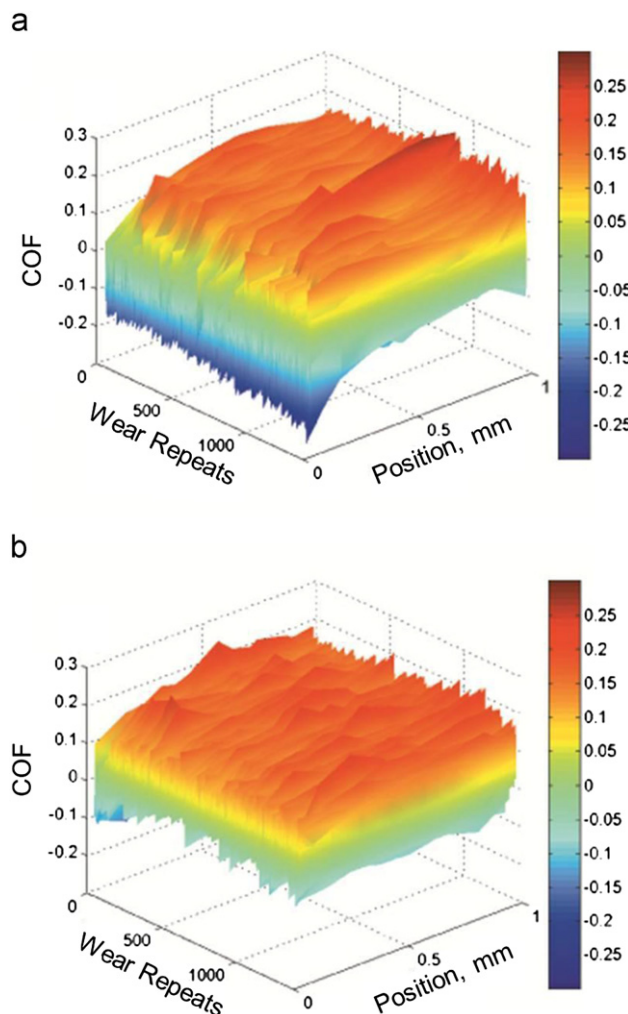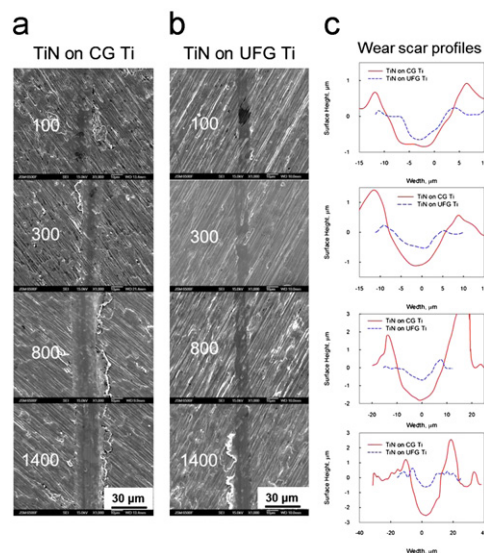
Fig. 6 – Wear surfaces of TiN on (a) CG and (b) UFG Ti samples after different numbers of scratching turns from 100 to 1400 and (c) the relevant wear scar profiles.
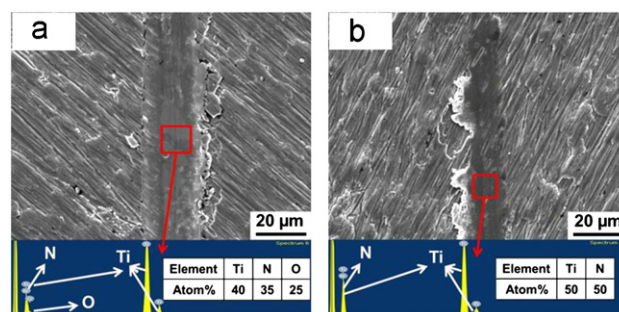
Fig. 7 – Wear surfaces of TiN coating on (a) CG Ti and (b) UFG Ti after 1400 repeats of micro-wear test.

more obviously at the edges of the wear scars for the coated CG Ti. There was no brittle failure of the coatings, by spalling or delamination, thereby confirming a good bonding between the TiN coating and the Ti substrate and also the excellent ductility of the TiN coatings.

Fig. 7 compares the surface morphologies and chemical elements of the TiN coatings on (a) the as-received CG Ti and (b) the UFG Ti after 1400 repeats. Larger volumes of the Ti element were detected by EDX compared to the N element at the bottom of the wear track of the coated as-received sample compared with the HPT sample. This shows the TiN coating on the as-received sample is partly worn through by the indenter whereas 1400 repeats of the wear test penetrated only ~1000 nm into the coated UFG Ti sample. It is estimated from the cross-sections that the wear rates of TiN on as-received Ti is ~$9.1 \times 10^{-14} \, \mathrm{m^3 \, N^{-1} \, m^{-1}}$ whereas on UFG Ti the wear rate is much lower at ~$(1.8 \pm 0.3) \times 10^{-14} \, \mathrm{m^3 \, N^{-1} \, m^{-1}}$. It is difficult to compare these wear rates with earlier studies, where there are reports for TiN coatings of wear rates between 7×10^{-15} and $5 \times 10^{-14} \, \mathrm{m^3 \, N^{-1} \, m^{-1}}$, because these wear test results are highly influenced by testing conditions including the manner of the contact, the counter body, the sliding speed and the load

Fig. 5 – The COF of TiN coatings on (a) CG and (b) UFG Ti during micro-wear testing.

(Takadoum et al., 1997a; Yang and Zhao, 2003; Oeztuerk et al., 2008). Nevertheless, both TiN-coated Ti substrates show wear rates that are two orders of magnitude lower than the uncoated Ti which was studied earlier using the same wear tester and similar wear conditions (Wang et al., 2012). Based on these results, it is reasonable to conclude that, with sufficient strength, good biocompatibility, an absence of the release of toxic elements and a very good abrasion resistance, the TiN-coated UFG Ti makes an excellent candidate material for future total joint replacements.

4.   Discussion

4.1.   A comparison with published data

The results from this investigation demonstrate that processing by HPT is effective in refining the microstructure of pure Ti and achieving a good combination of high strength and reasonable ductility.

The information at present available on the microstructures and mechanical properties of pure Ti processed using various SPD methods, including post-processing, are summarised in Table 1. From Grade 1 to Grade 4 Ti, the level of impurities increases with the grade number so that the strength of Grade 4 is generally the highest. The data in Table 1 demonstrate the possibility of achieving various mechanical properties by combining different SPD methods with additional rolling and/or heat treatments. By comparison with ECAP, processing by HPT is especially effective in refining the grain size without a corresponding significant loss in ductility. This result may be due to the high hydrostatic pressure applied in HPT processing which serves to limit the nucleation and growth of micro-cracks (Lapovok, 2005).

In earlier studies of the processing of pure Ti by HPT, a pressure of 1.5 GPa gave grain refinement to ~200 nm (Stolyarov et al., 1999) and a pressure of 5 GPa gave a grain size of ~120 nm with a transformation from a ductile α-phase with a hexagonal close-packed (HCP) structure to a hard and brittle ω-phase with a simple hexagonal structure (Todaka

et al., 2008). In practice, the amount of the ω-phase increases with increasing strain so that the ductility of the material is reduced (Todaka et al., 2008). This contrasts with the present results using a pressure of 3 GPa where the tensile results in Fig. 1 show that processing by HPT produces both a significantly improved strength and a reasonable ductility.

4.2.   The application to bio-implants

During the service of total joint replacements, there are inevitable sliding contacts between the femoral cup and the tibial or acetabular head during motion of the human body. These contacts generate wear debris and they produce a dimensional loss for the bio-implants that may cause health problems for the patient (Diomidis et al., 2012). In an earlier study, the sliding resistance of both CG and UFG Ti was poor (Wang et al., 2012) However, the deposition of a TiN coating on the Ti substrate provides a direct protection against wear. During scratch testing in the present experiments, the TiN coatings were well adhered to the substrates with no visible evidence for spalling or delamination.

There are several possible reasons for the advantage of a coating but primarily it must be associated with the fundamental properties of the coating such as the thickness and the nature of the interlayer. The interlayer between the coating and the substrate can improve chemical bonding and provide a buffer layer that effectively reduces the stress gradient between the coating and substrate (Voevodin et al., 1995). Although the roughness of the substrate is probably also important, it is not significant in the present study because all substrates had the same polishing history before coating and the coatings were deposited at the same time on different substrates so that their properties are nominally the same. According to other reports (Voevodin et al., 1995), a TiN coating with a thickness of ~2–3 μm corresponds to an optimum scratch resistance, and it contrasts with thicknesses of ~1.5 μm which are too thin so that the coating is worn quickly or ~5 μm where delamination occurs easily (Takadoum and Bennani, 1997b). As shown in Fig. 3, the TiN

Table 1 – Grain size and mechanical properties of pure Ti processed by SPD.					
Ti grades	Processing history	Grain size (nm)	UTS (MPa)	δ%	Ref.
VT1-0	ECAP	300	810	15	(Vinogradov et al., 2001)
Grade 1	ECAP	400	780	14	(Zhao et al., 2008)
Grade 2	ECAP+thermo mechanical treatment (80%)	70	1150	11	(Latysh et al., 2006)
	ECAP+rolling	140	905–937	7–27	(Yapici et al., 2006)
	ECAP(10)+CR (77%)	–	945	14.5	(Stolyarov et al., 2008)
	ECAP	–	750	7	(Zhang et al., 2011)
	ECAP	300	760	21	(Purcek et al., 2011)
	ECAP+CR (70%)	150	1080	32	(Sordi et al., 2012)
Grade 3	ECAP+HPT (1.5 GPa)	200	730	25	(Stolyarov et al., 1999)
	ECAP	280	710	14	(Stolyarov et al., 2001a)
	ECAP+CR (75%)	100	1150	8	(Stolyarov et al., 2001b)
	HPT (5 GPa)	120	950	14	(Sergueeva et al., 2001)
	ECAP(8)+CR (73%)+Annealing (300 °C, 1 h)	~100	1037	12.5	(Stolyarov et al., 2003)
Grade 4	ECAP+drawing	200–600	1280	10	(Sabirov et al., 2011)
	ECAP	300	947	25	(Purcek et al., 2011)
Grade 2	HPT (3 GPa)	130	940	23	This study

Re: CR=cold rolling

coating is detached abruptly from the Ti substrate when the diamond probe penetrates the TiN coating. Under these conditions, the scratch performance of the TiN coating is dictated not only by its own properties but also by the plastic deformation of the substrate. As depicted schematically in Fig. 8, the coating is subjected to a tensile stress as the substrate is deformed by the indenter and it becomes detached from the Ti substrate when it reaches the tensile limit.

4.3. The critical load for failure of the coating

The TiN coating on UFG Ti has a higher critical failure load due to the higher hardness of the substrate which prevents the thin coating from being deformed to the critical level. During the scratch test, the overall profile of the coating-substrate system is analogous to a two-layer composite which may be represented by the following relationship (Korsunsky et al., 1998):

$$H_{C,S} = H_S + \frac{H_C - H_S}{1 + k\beta^2} \tag{1}$$

where $H_{C,S}$ is the apparent hardness of the coating-substrate system, H_S is the hardness of the substrate, H_C is the hardness of the coating, β is the indentation depth and k is a constant obtained from the fitting procedure. During hardness testing, $H_{C,S}$ may be expressed by

$$H_{C,S} = \frac{L}{A} \tag{2}$$

where L is the load and A is the contact area between the indenter and the test surface.

The present study used a spherical indenter so that the contact area A is the front half of the spherical cap defined by

$$A = \pi R \beta \tag{3}$$

where R is the radius of the indenter.

Rewriting Eqs. 1–3, it follows that

$$L_C = \pi R \beta \left(\frac{H_C + k\beta^2 H_S}{1 + k\beta^2} \right) \tag{4}$$

where L_c is the critical load for coating failure.

Assuming that the coating hardness on all substrates are the same and the coating failure occurs at the same depth of penetration, Eq. (4) predicts that the critical load L_c increases with increasing substrate hardness, H_S. This is confirmed by the scratch results reported in this study where the values of L_c are ~12.7 N for the TiN coating on CG Ti and ~22.5 N for the TiN coating on UFG Ti. The experimental results are therefore consistent with a simple composite hardness model.
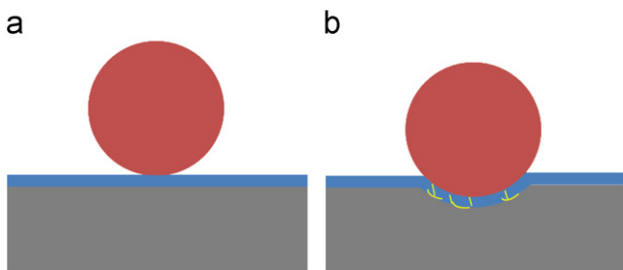
Fig. 8 – Schematic illustration of TiN coating failure during a scratch test: (a) the initial state and (b) the failure of the coating at L_c.

4.4. Implications of this research for practical applications

The results of the micro-wear tests show good deformation behaviour on both substrates. No significant cracking or delamination was observed even when the TiN coating on the CG Ti was worn through after 1400 repeats of sliding. By contrast, there is a report of extensive TiN coating cracking inside the wear track during scratch testing using a 4 μm thick coating on a steel substrate (Hainsworth and Soh, 2003). Thus, the present results confirm the excellent characteristics for TiN coatings on Ti substrates.

The higher strength of UFG Ti by comparison with CG Ti also produces a better wear resistance to the TiN coating under the high contact pressure of the wear test. Typically, the contact pressure for human joints is in the range of ~0.5–20 MPa. For these conditions, the main contact stress lies within the TiN coating and the effect of the substrate on the wear resistance of the TiN coating is negligible. Thus, the higher strength of the UFG substrates provides the bio-implant with both good strength and an improved fatigue life.

In practice, the real contact conditions for bio-implants are not well defined and there may be higher wear rates and more severe wear mechanisms in some patients. For example, in some post-clinical studies there were reports of large wear debris, with a size of ~3–5 μm, in ceramic-on-ceramic bearing contacts associated with the wear regions formed on the implant heads (Nevelos et al., 1999; Hatton et al., 2003). These large wear particles originate from very severe contacts of the implant, such as the presence of a micro-separation between the femoral head/neck and the cup rim (Hatton et al., 2002). As examined in the wear test of this study which employed a high contact stress, the TiN coating on UFG Ti exhibits very good wear resistance under extreme contact conditions because the high strength of UFG Ti inhibits deformation of the coating.

Since most of the abrasion and tribo-corrosion of bio-implants occur at the interface between the head and the cup, it is feasible to fabricate the bio-implant from UFG pure Ti processed by SPD and then apply a hard thin coating to protect the head of the implant. It is anticipated this design will provide the implant with high strength, good fatigue life, good corrosion resistance, together with good wear and tribo-corrosion resistance from the coating. Additional advantages include a lower Young's Modulus (~103 GPa) compared with ceramics, stainless steel and Ti-6Al-4V; and a non-toxic ion release. A design of this type can be extended also to other coatings such as diamond-like carbon or to new materials, such as Ti–Zr, Ti–Nb, and Nb–Zr alloys, which may be employed for the main body of the implant. An advantage of these alloys is that their values for Young's modulus is close to that of human bones (Zhao et al., 2011; Kent et al., 2011; Rubitschek et al., 2012) but the alloys will require additional strengthening using SPD methods.

5. Summary and conclusions

1. Grade 2 commercial purity Ti was processed by high-pressure torsion at room temperature using an imposed pressure of 3.0 GPa. The HPT processing reduced the grain

size from ~8.6 µm to ~130 nm and significantly increased the strength with only a minor loss in ductility.

2. A TiN coating, with a thickness of ~2.5 µm, was deposited on unprocessed Ti and on Ti after processing by HPT. The wear resistance of both materials was excellent.

3. The results show that a TiN coating on ultrafine-grained Ti has an excellent potential for use in bio-implant applications. Advantages of this system include high strength, reasonable ductility, good fatigue life, excellent abrasion resistance and a non-toxic ion release.

Acknowledgements

REFERENCES

Alsaran, A., Purcek, G., Hacisalihoglu, I., Vangolu, Y., Bayrak, O., Karaman, I., Celik, A., 2011. Hydroxyapatite production on ultrafine-grained pure titanium by micro-arc oxidation and hydrothermal treatment. Surface and Coatings Technology 205, S537–S542.

Balla, V.K., Bhat, A., Bose, S., Bandyopadhyay, A., 2012. Laser processed TiN reinforced Ti6Al4V composite coatings. Journal of the Mechanical Behavior of Biomedical Materials 6, 9–20.

Balyanov, A., Kutnyakova, J., Amirkhanova, N.A., Stolyarov, V.V., Valiev, R.Z., Liao, X.Z., Zhao, Y.H., Jiang, Y.B., Xu, H.F., Lowe, T.C., Zhu, Y.T., 2004. Corrosion resistance of ultra fine-grained Ti. Scripta Materialia 51, 225–229.

Bindu, S., Sanosh, K.P., Smetana, K., Balakrishnan, A., Kim, T.N., 2009. An in vivo evaluation of ultra-fine grained titanium implants. Journal of Materials Science and Technology 25, 556–560.

Bull, S.J., 1997. Failure mode maps in the thin film scratch adhesion test. Tribology International 30, 491–498.

Diomidis, N., Mischler, S., More, N.S., Roy, M., 2012. Tribo-electrochemical characterization of metallic biomaterials for total joint replacement. Acta Biomaterialia 8, 852–859.

Dobrzanski, L.A., Polok, M., Adamiak, M., 2005. Structure and properties of wear resistance PVD coatings deposited onto X37CrMoV5-1 type hot work steel. Journal of Materials Processing Technology 164, 843–849.

Edalati, K., Matsubara, E., Horita, Z., 2009. Processing pure Ti by high-pressure torsion in wide ranges of pressures and strain. Metallurgical and Materials Transactions A 40A, 2079–2086.

Elias, C.N., Lima, J.H.C., Valiev, R., Meyers, M.A., 2008. Biomedical applications of titanium and its alloys. JOM 60, 46–49.

Estrin, Y., Vinogradov, A., 2010. Fatigue behaviour of light alloys with ultrafine grain structure produced by severe plastic deformation: an overview. International Journal of Fatigue 32, 898–907.

Faghihi, S., Azari, F., Zhilyaev, A.P., Szpunar, J.A., Vali, H., Tabrizian, M., 2007. Cellular and molecular interactions between MC3T3-E1 pre-osteoblasts and nanostructured titanium produced by high-pressure torsion. Biomaterials 28, 3887–3895.

Faghihi, S., Li, D., Szpunar, J.A., 2010. Tribocorrosion behaviour of nanostructured titanium substrates processed by high-pressure torsion. Nanotechnology 21 (485703), 10.

Figueiredo, R.B., Cetlin, P.R., Langdon, T.G., 2011. Using finite element modeling to examine the flow processes in quasi-constrained high-pressure torsion. Materials Science and Engineering A 528, 8198–8204.

Figueiredo, R.B., Pereira, P.H.R., Aguilar, M.T.P., Cetlin, P.R., Langdon, T.G., 2012. Using finite element modeling to examine the temperature distribution in quasi-constrained high-pressure torsion. Acta Materialia 60, 3190–3198.

Gee, M.G., Nunn, J.W., Muniz-Piniella, A., Orkney, L.P., 2011. Micro-tribology experiments on engineering coatings. Wear 271, 2673–2680.

Geetha, M., Singh, A.K., Asokamani, R., Gogia, A.K., 2009. Ti based biomaterials, the ultimate choice for orthopaedic implants—a review. Progress in Materials Science 54, 397–425.

Guruvenket, S., Li, D., Klemberg-Sapieha, J.E., Martinu, L., Szpunar, J., 2009. Mechanical and tribological properties of duplex treated TiN, nc-TiN/a-SiNx and nc-TiCN/a-SiCN coatings deposited on 410 low alloy stainless steel. Surface and Coatings Technology 203, 2905–2911.

Hainsworth, S.V., Soh, W.C., 2003. The effect of the substrate on the mechanical properties of TiN coatings. Surface and Coatings Technology 163, 515–520.

Hatton, A., Nevelos, J.E., Matthews, J.B., Fisher, J., Ingham, E., 2002. Alumina–alumina artificial hip joints. Part I: a histological analysis and characterisation of wear debris by laser capture microdissection of tissues retrieved at revision. Biomaterials 23, 3429–3440.

Hatton, A., Nevelos, J.E., Matthews, J.B., Fisher, J., Ingham, E., 2003. Effects of clinically relevant alumina ceramic wear particles on TNF-alpha production by human peripheral blood mononuclear phagocytes. Biomaterials 24, 1193–1204.

Heinke, W., Leyland, A., Matthews, A., Berg, G., Friedrich, C., Broszeit, E., 1995. Evaluation of PVD nitride coatings, using impact, scratch and Rockwell-C adhesion tests. Thin Solid Films 270, 431–438.

Hoche, H., Schmidt, J., Gross, S., Trossmann, T., Berger, C., 2011. PVD coating and substrate pretreatment concepts for corrosion and wear protection of magnesium alloys. Surface and Coatings Technol 205, S145–S150.

Islamgaliev, R.K., Kazyhanov, V.U., Shestakova, L.O., Sharafutdinov, A.V., Valiev, R.Z., 2008. Microstructure and mechanical properties of titanium (Grade 4) processed by high-pressure torsion. Materials Science Engineering A. 493, 190–194.

Jeong, S.H., Shin, Y.H., Kim, H.J., Song, S.J., Lee, Y.Z., 2007. A study on scuffing and transition of friction and wear of TiN films using ultrasonic backward radiation. Wear 263, 1386–1389.

Kent, D., Wang, G., Yu, Z., Ma, X., Dargusch, M., 2011. Strength enhancement of a biomedical titanium alloy through a modified accumulative roll bonding technique. Journal of the Mechanical Behavior of Biomedical Materials 4, 405–416.

Korsunsky, A.M., McGurk, M.R., Bull, S.J., Page, T.F., 1998. On the hardness of coated systems. Surface Coatings Technology 99, 171–183.

Kurtz, S., Ong, K., Lau, E., Mowat, F., Halpern, M., 2007. Projections of primary and revision hip and knee arthroplasty in the United States from 2005 to 2030. Journal of Bone & Joint Surgery 89A, 780–785.

La, P., Ma, J., Zhu, Y.T., Yang, J., Liu, W., Xue, Q., Valiev, R.Z., 2005. Dry-sliding tribological properties of ultrafine-grained Ti prepared by severe plastic deformation. Acta Materialia 53, 5167–5173.

Lapovok, R.Ye., 2005. The role of back-pressure in equal channel angular extrusion. Journal of Materials Science 40, 341–346.

Latysh, V., Krallics, G., Alexandrov, I., Fodor, A., 2006. Application of bulk nanostructured materials in medicine. Current Applied Physics 6, 262–266.

Leopold, S.S., 2011. Numbers for breakfast: summary of hip arthroplasty outcomes from the national joint registry for England and wales 8th annual report (2011). Journal of Bone & Joint Surgery 93, 1–3.

Li, Y., Wong, C., Xiong, J., Hodgson, P., Wen, C., 2010. Cytotoxicity of titanium and titanium alloying elements. Journal of Dental Research 89, 493–497.

Long, M., Rack, H.J., 1998. Titanium alloys in total joint replacement—a materials science perspective. Biomaterials 19, 1621–1639.

Makihira, S., Mine, Y., Nikawa, H., Shuto, T., Iwata, S., Hosokawa, R., Kamoi, K., Okazaki, S., Yamaguchi, Y., 2010. Titanium ion induces necrosis and sensitivity to lipopolysaccharide in gingival epithelial-like cells. Toxicology in Vitro 24, 1905–1910.

Marino, C.E.B., Mascaro, L.H., 2004. EIS characterization of a Ti-dental implant in artificial saliva media: dissolution process of the oxide barrier. Journal of Electroanalytical Chemistry 568, 115–120.

Nevelos, J.E., Ingham, E., Doyle, C., Fisher, J., Nevelos, A.B., 1999. Analysis of retrieved alumina ceramic components from Mittelmeier total hip prostheses. Biomaterials 20, 1833–1840.

Oeztuerk, A., Ezirmik, K.V., Kazmanli, K., Uergen, M., Eryilmaz, O.L., Erdemir, A., 2008. Comparative tribological behaviors of TiN-, CrN- and MoN-Cu nanocomposite coatings. Tribology International 41, 49–59.

Okazaki, Y., Gotoh, E., 2005. Comparison of metal release from various metallic biomaterials in vitro. Biomaterials 26, 11–21.

Okazaki, Y., Gotoh, E., 2008. Metal release from stainless steel, Co-Cr-Mo-Ni-Fe and Ni-Ti alloys in vascular implants. Corrosion Science 50, 3429–3438.

PalDey, S., Deevi, S.C., 2003. Single layer and multilayer wear resistant coatings of (Ti,Al)N: a review. Materials Science and Engineering 342, 58–79.

Park, J.W., Kim, Y.J., Park, C.H., Lee, D.H., Ko, Y.G., Jang, J.H., Lee, C.S., 2009. Enhanced osteoblast response to an equal channel angular pressing-processed pure titanium substrate with microrough surface topography. Acta Biomaterialia 5, 3272–3280.

Piscanec, S., Ciacchi, L.C., Vesselli, E., Comelli, G., Sbaizero, O., Meriani, S., De Vita, A., 2004. Bioactivity of TiN-coated titanium implants. Acta Materialia 52, 1237–1245.

Purcek, G., Saray, O., Kul, O., Karaman, I., Yapici, G.G., Haouaoui, M., Maier, H.J., 2009. Mechanical and wear properties of ultrafine-grained pure Ti produced by multi-pass equal-channel angular extrusion. Materials Science and Engineering 517, 97–104.

Purcek, G., Yapici, G.G., Karaman, I., Maier, H.J., 2011. Effect of commercial purity levels on the mechanical properties of ultrafine-grained titanium. Materials Science and Engineering 528, 2303–2308.

Rubitschek, F., Niendorf, T., Karaman, I., Maier, H.J., 2012. Corrosion fatigue behavior of a biocompatible ultrafine-grained niobium alloy in simulated body fluid. Journal of the Mechanical Behavior of Biomedical Materials 5, 181–192.

Sabirov, I., Valiev, R.Z., Semenova, I.P., Pippan, R., 2010. Effect of equal channel angular pressing on the fracture behavior of commercially pure titanium. Metallurgical and Materials Transactions A 41A, 727–733.

Sabirov, I., Perez-Prado, M.T., Molina-Aldareguia, J.M., Semenova, I.P., Salimgareeva, G.K., Valiev, R.Z., 2011. Anisotropy of mechanical properties in high-strength ultra-fine-grained pure Ti processed via a complex severe plastic deformation route. Scripta Materialia 64, 69–72.

Sakai, G., Horita, Z., Langdon, T.G., 2005. Grain refinement and superplasticity in an aluminum alloy processed by high-pressure torsion. Material Science Engineering A 393, 344–351.

Sergueeva, A.V., Stolyarov, V.V., Valiev, R.Z., Mukherjee, A.K., 2001. Advanced mechanical properties of pure titanium with ultra-fine grained structure. Scripta Materialia 45, 747–752.

Semenova, I.P., Valiev, R.Z., Yakushina, E.B., Salimgareeva, G.H., Lowe, T.C., 2008. Strength and fatigue properties enhancement in ultrafine-grained Ti produced by severe plastic deformation. Journal of Materials Science 43, 7354–7359.

Semenova, I.P., Yakushina, E.B., Nurgaleeva, V.V., Valiev, R.Z., 2009. Nanostructuring of Ti-alloys by SPD processing to achieve superior fatigue properties. International Journal of Materials Research 100, 1691–1696.

Sordi, V.L., Ferrante, M., Kawasaki, M., Langdon, T.G., 2012. Microstructure and tensile strength of grade 2 titanium processed by equal-channel angular pressing and by rolling. Journal of Materials Science 47, 7870–7876.

Stallard, J., Poulat, S., Teer, D.G., 2006. The study of the adhesion of a TiN coating on steel and titanium alloy substrates using a multi-mode scratch tester. Tribology International 39, 159–166.

Starosvetsky, D., Gotman, I., 2001. Corrosion behavior of titanium nitride coated Ni–Ti shape memory surgical alloy. Biomaterials 22, 1853–1859.

Stolyarov, V.V., Zhu, Y.T., Lowe, T.C., Islamgaliev, R.K., Valiev, R.Z., 1999. A two step SPD processing of ultrafine-grained titanium. Nanostructured Materials 11, 947–954.

Stolyarov, V.V., Zhu, Y.T., Alexandrov, I.V., Lowe, T.C., Valiev, R.Z., 2001a. Influence of ECAP routes on the microstructure and properties of pure Ti. Material Science Engineering A. 299, 59–67.

Stolyarov, V.V., Zhu, Y.T., Lowe, T.C., Valiev, R.Z., 2001b. Microstructure and properties of pure Ti processed by ECAP and cold extrusion. Material Science Engineering A 303, 82–89.

Stolyarov, V.V., Zhu, Y.T., Alexandrov, I.V., Lowe, T.C., Valiev, R.Z., 2003. Grain refinement and properties of pure Ti processed by warm ECAP and cold rolling. Material Science Engineering A 343, 43–50.

Stolyarov, V.V., Shuster, L.S., Migranov, M.S., Valiev, R.Z., Zhu, Y.T., 2004. Reduction of friction coefficient of ultrafine-grained CP titanium. Material Science Engineering A 371, 313–317.

Stolyarov, V.V., Zeipper, L., Mingler, B., Zehetbauer, M., 2008. Influence of post-deformation on CP-Ti processed by equal channel angular pressing. Material Science Engineering A 476, 98–105.

Takadoum, J., Bennani, H.H., Allouard, M., 1997a. Friction and wear characteristics of TiN, TiCN acid diamond-like carbon films. Surface and Coatings Technology 88, 232–238.

Takadoum, J., Bennani, H.H., 1997b. Influence of substrate roughness and coating thickness on adhesion, friction and wear TiN films. Surface and Coatings Technology 96, 272–282.

Todaka, Y., Sasaki, J., Moto, T., Umemoto, M., 2008. Bulk sub-microcrystalline omega-Ti produced by high-pressure torsion straining. Scripta Materialia 59, 615–618.

Valiev, R.Z., Sergueeva, A.V., Mukherjee, A.K., 2003. The effect of annealing on tensile deformation behavior of nanostructured SPD titanium. Scripta Materialia 49, 669–674.

Valiev, R.Z., Langdon, T.G., 2006. Principles of equal-channel angular pressing as a processing tool for grain refinement. Progress in Materials Science 51, 881–981.

Vinogradov, A.Y., Stolyarov, V.V., Hashimoto, S., Valiev, R.Z., 2001. Cyclic behavior of ultrafine-grain titanium produced by severe plastic deformation. Materials Science and Engineering A 318, 163–173.

Voevodin, A.A., Rebholz, C., Matthews, A., 1995. Comparative tribology studies of hard ceramic and composite metal-DLC coatings in sliding friction conditions. Tribology Transactions 38, 829–836.

Wang, C.T., Gao, N., Gee, M.G., Wood, R.J.K., Langdon, T.G., 2012. Effect of grain size on the micro-tribological behavior of pure titanium processed by high-pressure torsion. Wear 280–281, 28–35.

Yang, Q., Zhao, L.R., 2003. Dry sliding wear of magnetron sputtered TiN/CrN superlattice coatings. Surface and Coatings Technology 173, 58–66.

Yapici, G.G., Karaman, I., Maier, H.J., 2006. Mechanical flow anisotropy in severely deformed pure titanium. Materials Science Engineering A 434, 294–302.

Yilbas, B.S., Shuja, S.Z., 2000. Laser treatment and PVD TiN coating of Ti-6Al-4V alloy. Surface Coatings Technology 130, 152–157.

Zhang, Y., Figueiredo, R.B., Alhajeri, S.N., Wang, J.T., Gao, N., Langdon, T.G., 2011. Structure and mechanical properties of commercial purity titanium processed by ECAP at room temperature. Materials Science and Engineering A 528, 7708–7714.

Zhao, X., Fu, W., Yang, X., Langdon, T.G., 2008. Microstructure and properties of pure titanium processed by equal-channel angular pressing at room temperature. Scripta Materialia 59, 542–545.

Zhao, X., Niinomi, M., Nakai, M., Miyamoto, G., Furuhara, T., 2011. Microstructures and mechanical properties of metastable Ti-30Zr-(Cr, Mo) alloys with changeable Young's modulus for spinal fixation applications. Acta Biomaterialia 7, 3230–3236.

Zhilyaev, A.P., Langdon, T.G., 2008. Using high-pressure torsion for metal processing: fundamentals and applications. Progress in Materials Science 53, 893–979.

Indentation and scratch testing of DLC-Zr coatings on ultrafine-grained titanium processed by high-pressure torsion

Chuan Ting Wang [a,b], Ana Escudeiro [c], Tomas Polcar [a], Albano Cavaleiro [c], Robert J.K. Wood [a], Nong Gao [b,*], Terence G. Langdon [b,d]

[a] National Centre for Advanced Tribology at Southampton, Faculty of Engineering and the Environment, University of Southampton, Southampton SO17 1BJ, UK
[b] Materials Research Group, Faculty of Engineering and the Environment, University of Southampton, Southampton SO17 1BJ, UK
[c] SEG-CEMUC – Department of Mechanical Engineering, University of Coimbra, 3030-788 Coimbra, Portugal
[d] Departments of Aerospace & Mechanical Engineering and Materials Science, University of Southern California, Los Angeles, CA 90089-1453, USA

ABSTRACT

High-pressure torsion was employed to refine the microstructure of grade 2 Ti under an imposed pressure of 3.0 GPa at room temperature. The microhardness of grade 2 Ti increased from 1.82 GPa for the coarse grain state to 3.05 GPa after high-pressure torsion processing, where this value is very close to the hardness of the Ti–6Al–4V alloy. Subsequently, several diamond-like carbon (DLC) coatings with thicknesses of ∼1.4 μm were deposited on as-received Ti, high-pressure torsion processed Ti and Ti–6Al–4V samples via physical vapour deposition. Both indentation and scratch tests showed a much improved adhesion of DLC-7Zr, DLC:H-7Zr and DLC-9Zr coatings with high-pressure torsion processed Ti as the substrate by comparison with the same coatings on coarse-grained Ti. The results suggest that commercial pure Ti processed by high-pressure torsion and coated with a diamond-like carbon coating provides a potential candidate material for bio-implant applications.

© 2012 Elsevier B.V. All rights reserved.

1. Introduction

Human joints might suffer from pain and functional loss due to degenerative diseases, aging and accidents. A total joint replacement is regarded as an effective procedure for treating joint diseases and fractures [1]. A technical survey reported that there is an increasing demand for new and improved implants because of a rapidly growing patient population and increasing numbers of younger patients [2]. The Ti–6Al–4V alloy was designed originally for the aerospace industry but it has been used widely for biomedical applications due to its high strength, good fatigue characteristics, bio-tolerance and excellent corrosion resistance [1]. Despite these attractive qualities, Ti–6Al–4V has significant drawbacks which limit its further capacity to be used as an orthopaedic and dental implant material. For example, the toxic Al and V ions released from Ti–6Al–4V may cause long-term health problems and adverse reactions with body tissues [3,4]. Therefore, there is now an urgent need for exploring the potential for developing other bio-metals.

Pure titanium has excellent properties including high corrosion resistance, low electronic conductivity, a low ion-formation tendency and very good biocompatibility. All these characteristics make it a very good candidate as an implant material.

Nevertheless, pure titanium has a relatively low strength and a very poor wear resistance when it is subjected to sliding and abrasion. Thus, it is generally not suitable for use in artificial joints which seek materials with high strength and good tribological properties. Recently, pure titanium with ultra-fine grain sizes, processed through the application of severe plastic deformation (SPD), appears to offer an alternative possibility for the production of implant materials [5,6]. In severe plastic deformation processing, a high level of straining is imposed on a metal using an extensive hydrostatic pressure and the strain is achieved without changing the overall dimensions of the material [7,8]. Thus, a very large strain may be imposed on materials via repeated severe plastic deformation processing. The ultrafine-grained (UFG) materials produced by severe plastic deformation often possess extraordinary properties, including both high strength and toughness [9], long fatigue life [10,11] and reasonable wear resistance [12,13]. To date, various severe plastic deformation processing methods have been applied successfully for the production of high strength pure Ti [6,14–17]. However, the evidence suggests that severe plastic deformation processing may lead to only a relatively minor improvement in the wear resistance of Ti [5,18]. As an alternative approach, it appears that surface treatments or coatings may be necessary to enhance the service durability of titanium as implant components [19].

The idea of improving wear resistance of Ti alloys via surface treatment has been reported extensively. Surface engineering technologies such as thermal oxidation, ion implantation and

* Corresponding author. Tel.: +44238 0593396; fax: +44238 0593016.
E-mail address: n.gao@soton.ac.uk (N. Gao).

thin coatings can significantly improve the tribological properties of Ti alloys. The high strength of coatings were favourable to maintain the low surface roughness during sliding motion, which also led to less wear loss of the polyethylene counterpart [20,21].

In recent years, attention has moved to surface engineering of ultrafine-grained Ti. High-current-density nitrogen ion implantation was used to enhance the wear resistance of ultrafine-grained Ti and the results demonstrated the potential for forming a hard layer with good wear and corrosion resistance on the surface of ultrafine-grained Ti via ion implantation [22]. However, this method required that the samples were held at the relatively high temperature of 820 K and there is evidence this may be recrystallisation of the ultrafine-grained structure of Ti when the temperature is above ∼620 K [23]. It appears, therefore, that chemical vapour deposition (CVD) and physical vapour deposition (PVD) may be better approaches for this purpose because this permits the use of a lower processing temperature and easier control over the surface roughness. It is important to note that PVD methods such as magnetron sputtering can be controlled at room temperature leading to a much lower internal stress at the interface. For example, a thin and hard TiN coating was deposited on both coarse-grained and ultrafine-grained Ti substrates using PVD at a temperature below 420 K in a recent study [19]. The subsequent wear tests showed that the TiN coating improved the wear resistance of Ti by nearly two orders of magnitude and the ultrafine-grained Ti was a better substrate than coarse-grained Ti due to its higher strength. Therefore, a PVD coating on ultrafine-grained Ti shows significant promise for further exploration in future bio-implant applications.

Diamond-like carbon (DLC) coatings are regarded as other good candidates for the purpose of wear protection because of their excellent mechanical and tribological properties such as high hardness, good wear and corrosion resistance. Moreover, DLC coatings also have a much lower coefficient of friction (COF) which can also reduce the wear of the counter surface during sliding [24]. To date, several studies have explored DLC coatings for bio-implant use [25–27]. Despite the excellent tribological properties of DLC coatings, delamination of the coatings was a major problem which appeared to limit their application as articulating joints [25]. It is reasonable to anticipate that, once removed from the substrate, these DLC coating particles would act as a third body causing severe damage to the substrate or even severe reactions with the tissue. In order to solve these issues, studies have been reported exploring the use of new interlayers to improve the bonding of DLC coatings [28]. Doping with metallic elements, such as Cr [21,29], Ti [30] and W [31], may also improve the adhesion and wear resistance. Recently, zirconium was used as a dopant metal to provide low-toxicity, good tribological behaviour and high corrosion resistance [32–34].

The present investigation was therefore initiated in order to explore the effect of substrate microstructure on the adhesion behaviour and scratch resistance of DLC-7Zr, DLC:H-7Zr and DLC-9Zr coatings deposited on grade 2 pure titanium substrates both with and without high-pressure torsion processing and, in addition, to make a direct comparison with deposition on a Ti–6Al–4V substrate.

2. Experimental materials and procedures

2.1. Materials and processing

The experiments were conducted using grade 2 pure titanium having a composition of 0.015 H, 0.1C, 0.25 O, 0.03 N, 0.3 Fe and balance Ti (wt%) and the Ti–6Al–4V alloy with extra low interstitials. Initially, some of the grade 2 Ti samples were subjected to

high-pressure torsion processing. The samples for high-pressure torsion were machined into disks with a diameter of 10 mm and thicknesses between 0.80 and 0.85 mm. During high-pressure torsion, the disk samples were held in shallow depressions on the faces of two massive anvils, a load was applied and then torsional straining was achieved through rotation of the lower anvil. In high-pressure torsion, the shear strain, γ, at different position of the disk can be estimated using the relationship [35]

$$\gamma = \frac{2\pi NR}{h} \tag{1}$$

where N is the number of rotation revolutions, R is the distance from the centre of the disk and h is the height (or thickness) of the sample. In this study, high-pressure torsion processing was conducted using an imposed pressure of 3.0 GPa for 10 revolutions under quasi-constrained conditions in which there is some restricted outflow of material around the periphery of the disk during the processing operation [36,37]. Additional details on the principles of high-pressure torsion processing are given in earlier reports [38–40].

Microhardness testing of the samples was performed under an indentation load of 1 kg for 15 s. As described earlier [19], tensile testing was conducted at room temperature after high-pressure torsion processing using an initial tensile strain rate of $1.0 \times 10^{-2}\,\mathrm{s}^{-1}$. The microstructures of the materials were examined using a JEM 3010 transmission electron microscope (TEM) operating under an accelerating voltage of 200 kV. A detailed description of these analytical procedures was given in earlier reports [5,19].

2.2. Coating deposition and characterisation

Prior to deposition, the substrates were polished to a roughness less than 50 nm, cleaned in an ultrasonic bath in acetone, ethanol and distilled water for 15 min, and then etched using Ar^+ bombardment for 1 h at a substrate bias voltage of −650 V in order to remove all contaminants and oxides on the substrate surface. The coatings were deposited using dc dual magnetron sputtering in an Ar atmosphere (non-reactive process) and $Ar+CH_4$ (reactive process) to produce non-hydrogenated and hydrogenated coatings, respectively. Two targets were used: titanium was used to deposit an interface layer and a graphite target was used with embedded Zr pellets to prepare functional film. Table 1 summarises the deposition parameters. The work pressure was maintained constant for both reactive and non-reactive sputtering by adjusting the gas flow. A pulsed bias voltage of −50 V and a frequency of 250 kHz were applied. A TiN/TiCN interlayer with a varying composite gradient and a thickness of 450 nm was deposited in order to improve adhesion. The thickness of the functional coating was approximately 1 μm so that the total film thickness was of the order of ∼1.4 μm. To facilitate a detailed description of the results, the coatings were denoted as DLC-XZr and DLC:H-XZr, where X represents the zirconium content.

Table 1
Deposition parameters of DLC-XZr and DLC:H-XZr coatings.

Parameters	DLC-XZr	DLC:H-XZr
Reactive gas flow (%)	–	5
Ar flow (%)	45	40
Base pressure (Pa)	1.5×10^{-3}	
Work pressure (Pa)	0.4	
Substrate bias (V)	−50	
Graphite doped target (W/mm^2)	0.075	

The chemical composition was determined by electron probe microanalysis (EPMA) applying a 10 keV voltage. The coating hardness was measured by depth-sensing indentation using a Berkovich indenter and a load of 5 mN. A series of 32 indentations from two distinct areas were carried out in order to critically evaluate the hardness of the coatings. In addition, the reduced Young modulus was derived from the indentation measurements using the standard method [41]. The Young modulus was calculated using the following parameters: $E_i = 1140$ GPa and $v_i = 0.07$ for the diamond indenter and $v = 0.3$ for the coating [41].

2.3. Rockwell C indentation and scratch test

The coating adhesion to the Ti substrates was evaluated using Rockwell C indentation and scratch testing where these are standard techniques commonly used to quantify the interfacial strength of coating-substrate systems. During the Rockwell C indentation test, a cone-shaped diamond 120° tip (200 μm in radius) was indented perpendicularly onto the coating applying a normal load of 200 N, thereby causing layer damage to the boundary of the indentation. The results of the test were qualitatively evaluated by comparing the optical microscope images of the crack network and the degree of delamination with an adhesion quality chart which classifies the images into six levels from HF1-HF6 [42]. In this classification, HF1 is featured with only a few minor cracks after indentation which indicates a good bonding while at the other extreme HF6 denotes extensive delamination of the coating and very poor adhesion. Adhesion levels from HF1 to HF4 are typically considered as acceptable coating adhesions for use in commercial applications.

The scratch test was performed by using a spherical Rockwell C diamond indenter (200 μm radius) according to standard testing methods [43]. The indenter was slid over the coating surface and the load increased from 2 to 50 N at a speed of 10 N/mm. The lower critical load, L_{c1}, was defined as the load where the first cracks occurred (representing cohesive failure) and the upper critical load, L_{c2}, was defined as the load associated with the first delamination at the edge of the scratch track (representing adhesive failure). In addition, a load L_{c3} was defined as the load under which the coating was totally removed from the substrate. The scratch tests were repeated for three times in order to obtain reliable results. After scratch testing, the cracking or delamination of the coating was observed using optical microscopy along the scratch track. The cross-section profiles of the DLC coatings at the critical load were measured using an ultimate focus optical microscope operating in the line scanning mode.

3. Experimental results

3.1. Mechanical properties of Ti substrates

The results of optical microscopy and TEM showed that high-pressure torsion processing significantly refined the grain size of pure Ti from ~8.6 μm in the as-received state to ~130 nm after high-pressure torsion processing. Due to this grain refinement, the microhardness of pure Ti increased from an initial value of ~1.82 GPa in the coarse-grained state to ~3.05 GPa after high-pressure torsion processing. This latter value for the ultrafine-grained pure Ti is comparable with the hardness of 3.09 GPa for the Ti–6Al–4V alloy used in this study [5].

The tensile testing demonstrated that the ultimate tensile strength (UTS) of Ti increased from ~660 MPa in the coarse-grained state to ~940 MPa after high-pressure torsion with some associated reduction in ductility [19]. This high strength and reasonable ductility of ultrafine-grained pure Ti is compatible

with the Ti–6Al–4V alloy where the UTS is ~980 MPa and the elongation to failure is ~14%.

3.2. Coating characterisation

Table 2 shows the zirconium content, the hardness and the values of the Young modulus of the deposited coatings. It should be noted that the low indentation depth for the indenter (approximately 10% of the coating thickness) made it difficult to ascertain the effect from the substrate material when obtaining these mechanical properties. Details of the coating structure were studied by X-ray diffraction, Raman spectroscopy and X-ray photoelectron spectroscopy and these results were reported elsewhere [33,44]. All of the coatings investigated in this study (with Zr contents of 7–9 at%) exhibited a nanocomposite structure with very small ZrC nanograins (up to ~2 nm) embedded within an amorphous carbon matrix.

3.3. Adhesion performance of the DLC coatings

Table 3 summaries the adhesion results of DLC coating on all three substrates. The Rockwell C indentation tests showed HF3 and HF4 for all samples with only minor delamination and micro-cracking observed around the indentation marks, thereby demonstrating an acceptable adhesion for all tested coatings. The scratch test results showed that the DLC coatings with UFG Ti and Ti–6Al–4V substrates had similar critical loads and these loads were much higher than with the coarse-grained Ti as substrates. Thus, the UFG Ti and Ti–6Al–4V substrates provided better support with their higher hardness and this produced a higher critical load of the DLC coating. These results demonstrate again the important role of substrates for the adhesion of thin DLC coatings.

Optical images of the Rockwell indentations are shown in Fig. 1. It can be seen that the load of 200 N led to radial plastic deformation of the coating which caused circumferential cracking of the film outside the indentation area. Through-thickness cracks were observed on all coatings which may be related to the elastic-plastic boundary of the substrates. The indentation marks had a diameter of ~380 μm on the DLC/coarse-grained Ti samples

Table 2
Summary of coatings chemical composition and mechanical properties.

System	Zr content (at%)	Hardness (GPa)	E (GPa)
DLC-7Zr	7 ± 1	11 ± 2	120 ± 3
DLC:H-7Zr	8 ± 1	13 ± 1	117 ± 4
DLC-9Zr	10 ± 1	12 ± 2	131 ± 3

Table 3
Summary of adhesion results.

Substrate	Coating	Rockwell C		Scratch			
		Ø (μm)	Adhesion	L_{c1} (N)	L_{c2} (N)	L_{c3} (N)	Track width at L_{c3} (μm)
CG Ti	DLC-7Zr	375	HF3	7 ± 2	8 ± 1	13 ± 2	149.7
	DLC:H-7Zr	391	HF4	5 ± 1	7 ± 2	13 ± 1	130.1
	DLC-9Zr	384	HF4	7 ± 1	9 ± 1	15 ± 1	130.7
UFG Ti	DLC-7Zr	282	HF3	8 ± 1	12 ± 1	22 ± 2	113.3
	DLC:H-7Zr	286	HF3	7 ± 2	10 ± 1	20 ± 1	120.9
	DLC-9Zr	287	HF3	10 ± 2	14 ± 1	24 ± 1	123.8
Ti–6Al–4V	DLC-7Zr	277	HF3	9 ± 2	11 ± 1	23 ± 2	139.7
	DLC:H-7Zr	274	HF4	5 ± 1	10 ± 2	19 ± 2	132.1
	DLC-9Zr	282	HF3	11 ± 2	15 ± 1	25 ± 2	126.2

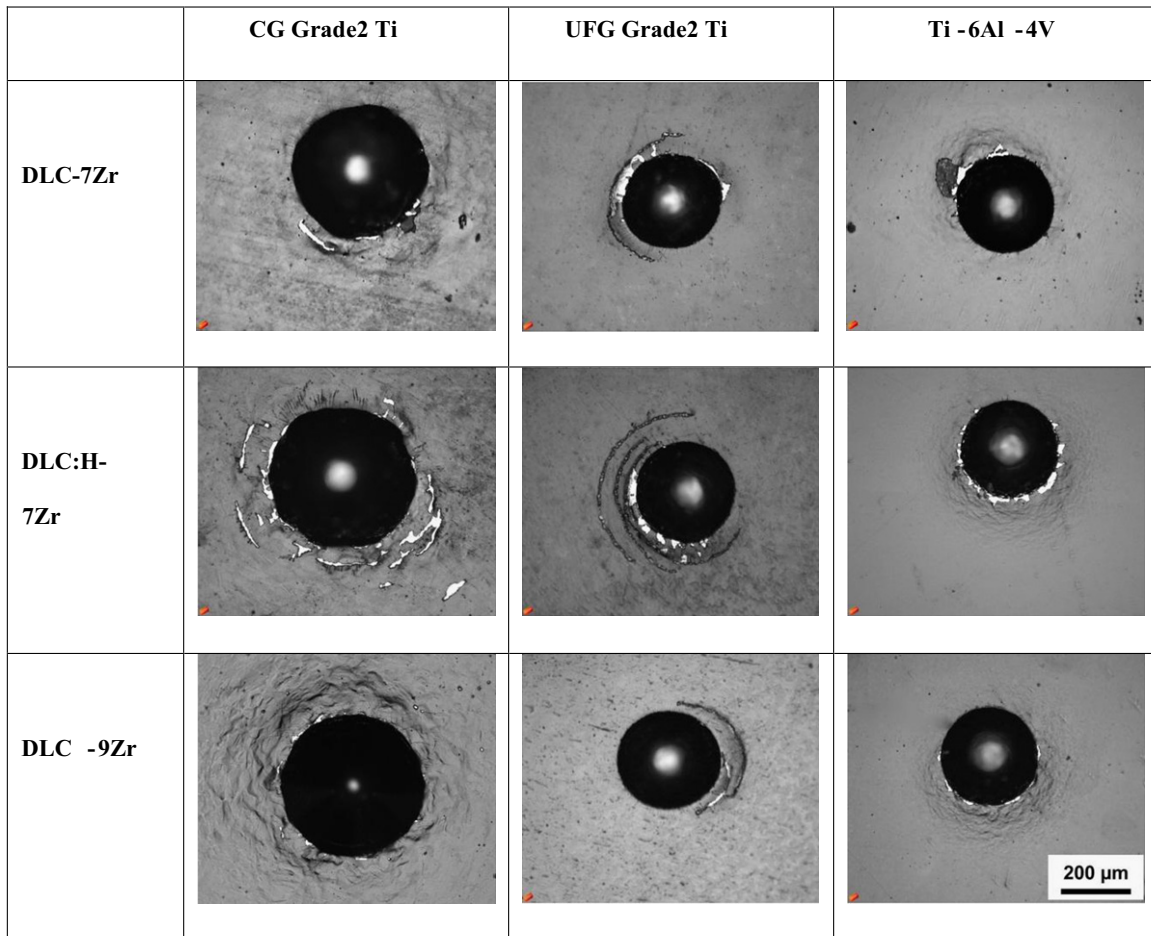|	CG Grade2 Ti	UFG Grade2 Ti	Ti -6Al -4V
DLC-7Zr			
DLC:H-7Zr			
DLC -9Zr			200 µm

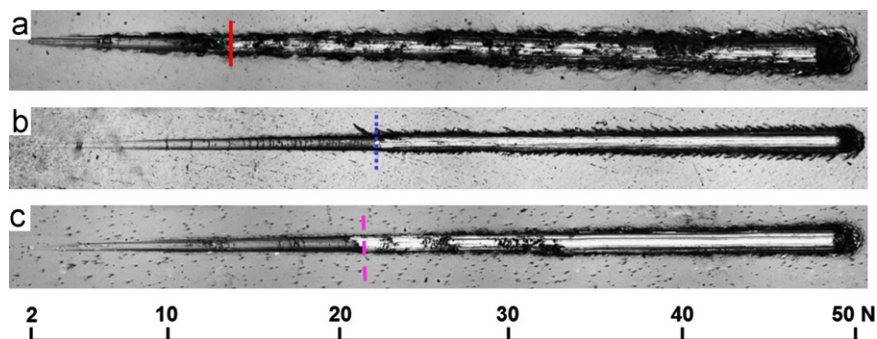**Fig. 1.** Rockwell indentation of DLC on different Ti substrates.

Fig. 2. Scratch tracks of DLC-7Zr coatings on (a) coarse-grained Ti, (b) ultrafine-grained Ti, and (c) Ti–6Al–4V substrates.

which would cause more deformation at the edge and more delamination compared to the DLC/ultrafine-grained Ti and DLC/Ti–6Al–4V samples. This effect was mainly caused by the different hardness of the Ti substrates. Furthermore, the doping of H content led to a decrease in the adhesion strength because all the indents of the DLC:H-7Zr coating showed a higher delamination than DLC-7Zr. It is obvious that the DLC-9Zr coatings with higher Zr content presented the best adhesion behaviour with only small cracks and minor coating delamination. Therefore, it may be possible to further enhance the coating adhesion by increasing the zirconium content. A more comprehensive study of the adhesion of DLC coatings with different Zr content is given elsewhere [44].

The scratch test results matched well with observation from the Rockwell indentations. Fig. 2 shows the scratch tracks of the DLC-7Zr coating on the Ti substrates with increasing loads from 2 to 50 N. Generally, the plastic deformation of the Ti substrates was the main cause for the coating failure. As the diamond stylus was sliding with increasing normal load on the coating surface, the coating followed the deformation of the Ti substrate. The tensile stress both inside the coating and at the interface led to cracking and delamination of the coatings. As shown in Fig. 2(a), the DLC-7Zr coating on coarse-grained Ti failed at an early stage during the scratch test and the indenter caused extensive deformation of the substrate. On the other hand, the DLC-7Zr coatings deposited on ultrafine-grained Ti and Ti–6Al–4V failed at a higher
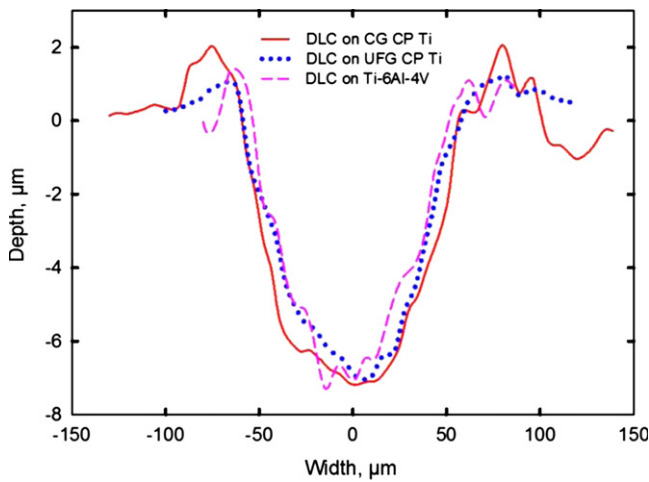
Fig. 3. Cross-section of the scratch tracks in the positions indicated in Fig. 2.

Fig. 4. Critical load of coatings versus the hardness of substrates.

load and the adhesion of the films deposited on both substrates was almost identical (Fig. 2(b) and (c)). The cross-section of the scratch tracks where the substrate was revealed in the scratch track (see the short vertical lines in Fig. 2(a)–(c)) was measured using an ultimate focus optical microscope. Although the coating was deposited onto different substrates, these measurements showed that it always failed when the scratch track was approximately 7 μm deep and 130 μm wide as illustrated in Fig. 3.

4. Discussion

In this study, a grade 2 pure Ti was processed using high-pressure torsion to achieve significant grain refinement and then DLC coatings were successfully deposited on the different Ti substrates and their scratch behaviour was studied. In terms of future bio-medical applications, the results provide a clear demonstration that it is possible to replace the conventional Ti–6Al–4V alloy with ultrafine-grained pure Ti having preferable mechanical properties which may be achieved through high-pressure torsion processing.

Various coating technologies are now available to provide wear resistance for bio-implants. Technologies such as plasma electrolytic oxidation (PEO) and internal oxidation (IO) have been used extensively to process Ti–6Al–4V and other bio-metals but these methods often involve a high processing temperature which may lead to recrystallisation of ultrafine-grained structures [45,46]. When ultrafine-grained materials are chosen as the substrates, the post processing temperature must not exceed the recrystallisation temperature in order to restrict any grain growth of the ultrafine-grained structures. Moreover, the oxidation layers produced through these methods are often very rough and this will entail additional polishing before their use in implants. Thus, PVD methods are regarded as one of the best choices for surface modifying ultrafine-grained materials.

A good adhesion between the thin coating and the substrate is essential for the coating/substrate system. The interposition of a gradient layer (Ti/TiN/TiCN) improves the interface shear strength and the load bearing capacity of the coating [28]. It was observed in this study that, when using ultrafine-grained Ti as the substrate, the load bearing capacity of DLC coatings was improved extensively compared to those with coarse-grained Ti as substrates. A similar trend was observed also on TiN thin coatings on different Ti substrates [19]. The TiN on ultrafine-grained Ti also had a higher critical failure load as it prevented the thin coating
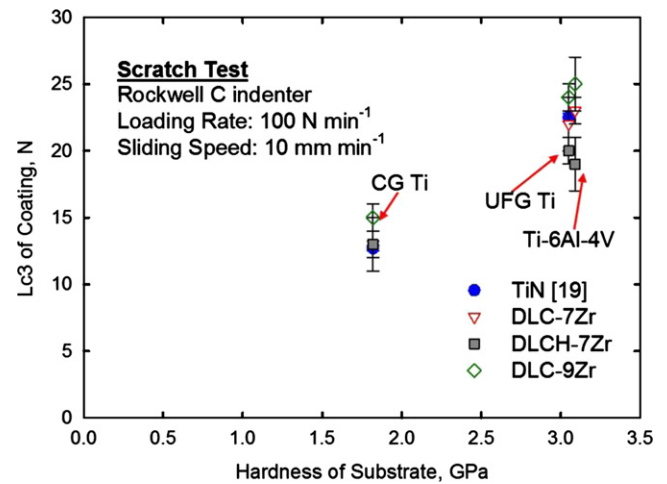
from undergoing deformation. Fig. 4 shows the critical load of the DLC coatings and TiN coating on Ti substrates plotted against the hardness of the substrate. The trend is clear because a harder substrate after high-pressure torsion leads to a higher critical load for the coatings. Therefore, on one hand it is very important to explore better coating parameters such as new interlayer designs and coating compositions in order to achieve a good performance of the coatings. On the other hand, it is also very important to enhance the properties of substrates through surface hardening or grain refinement (i.e. increase the H/E ratio) and thereby give a better support to the thin coatings.

The results from this research showed that the DLC coating failures occurred at the same depth and width of penetration for all three substrates, as is clearly observed in Fig. 3. As the UFG Ti and Ti–6Al–4V had very similar hardness, therefore, the datum points were very close to each other. As shown in Fig. 3, the critical load of all coatings increased with increasing hardness of the substrates. A similar trend was also observed on various TiN coated substrates including stainless steel, high speed steel and WC [47]. An explanation was given by assuming the TiN coating adjusted to the elastic–plastic deformation of the substrates therefore the coating underwent a cohesive–adhesive failure that leads to film delamination. A critical indentation width of 60 μm was observed in that study, where the coating failed whenever it was bent to this width regardless of the substrate material.

By simplifying the coating-substrate system as a two-layer composite, the overall hardness of the coating-substrate system may be represented by the following relationship according to the Burnett–Rickerby model which is based on a volume law of mixtures [47–50]

$$H_{C,S} = \frac{V_C}{V_{total}} H_C + \frac{\chi^3 V_S}{V_{total}} H_S \tag{2}$$

where $H_{C,S}$ is the apparent hardness of the coating-substrate system, H_S is the hardness of the substrate, H_C is the hardness of the coating, χ is a factor by which the plastic zone changes, and the V_C, V_S and V_{total} are the deformation volumes of the coating, substrate and total deformation volume, respectively.

The volumes of the deformation zones are expressed by the following equations:

$$V_C \approx \pi R_C^2 t \tag{3}$$

$$V_S \approx \chi^3 \frac{2}{3} \pi R_S^3 \tag{4}$$

where R_C and R_S are the radii of deformation zone of coating and substrate, respectively. The factor, χ was determined via fitting experimental results by Burnett and Rickerby [48] and addressed as

$$\chi = \left(\frac{E_C H_S}{E_S H_C}\right)^{1/2} \tag{5}$$

where E_C and H_C are the Young's Modulus and hardness of the coating, and E_S and H_S are the Young's Modulus and hardness of the substrate, respectively. R_C and R_S can be obtained through the equation

$$R = r\left(\frac{E}{H}\right)^{1/2} \tag{6}$$

where r is the geometrical length of the indentation volume.

As observed in Fig. 3, the indentation depths of all samples were only around 7 μm, and this depth was obtained after the diamond indenter was removed. In this case, the measured indentation depth was underestimated due to the elastic recovery of materials. Therefore, it is more accurate to recalculate the indentation depth using the measured indentation width considering the sphere shape of the indenter, according to the equation

$$r = \left[\pi\left(R_{ind}^2 - \frac{W^2}{4}\right)\left(R_{ind} - \frac{\sqrt{R_{ind}^2 - \frac{W^2}{4}}}{3}\right)\right]^{1/3} \tag{7}$$

where R_{ind} is the radius of diamond indenter and W is the track width at the critical load point.

Therefore, the overall hardness of this coating-substrate is achieved by rewriting Eqs. (2)–(6)

$$H_{C,S} = \frac{E_C t + \frac{2}{3} r H_S \left(\frac{E_C}{H_C}\right)^{3/2}}{\left(\frac{E_C}{H_C}\right) t + \left(\frac{2}{3}\right) r \left(\frac{E_C}{H_C}\right)^{3/2}} \tag{8}$$

During the scratch testing, the indenter was travelling with an increasing normal load and it was always the front half of the spherical cap in the coating-substrate system. Therefore, the critical load, L_{C3}, is expressed as

$$L_{C3} = H_{C,S} \pi R_{ind} \sqrt{R_{ind}^2 - \frac{W^2}{4}} \tag{9}$$

Thus, Eqs. (8) and (9) clearly emphasise the effect of substrate strength on the scratch behaviour of thin coatings. It further explains that the DLC coatings, with thicknesses around 1 μm, often exhibit high critical loads with hard materials as substrates, such as more than 100 N on Si or glass [51].

The track width of each sample is listed in Table 3 and this can be applied to Eqs. (8) and (9). The comparison between experimental results and the Burnett–Rickerby model is plotted in Fig. 5. It worth noting that as the interlayers had varying compositions and properties and were much thinner than the coatings, thus this analysis simply neglects the properties of the interlayers although in practice the interlayer is important in improving the bonding. This may lead to an underestimation of the model. Moreover, errors may also be introduced due to the ridges formed at the edge of the scratch tracks which made it difficult to measure the track widths.

In this study, the strength and hardness of pure Ti were successfully improved by high-pressure torsion processing. Firstly, this improves the mechanical durability of pure Ti as the main body of bio-implants when they suffer fatigue and shear loadings. Secondly, ultrafine-grained pure Ti is a good substrate for thin coatings and provides improved load bearing capacity of the coating. Therefore, with good strength, fatigue life, excellent bio-compatibility and no toxic release tendency of ultrafine-grained
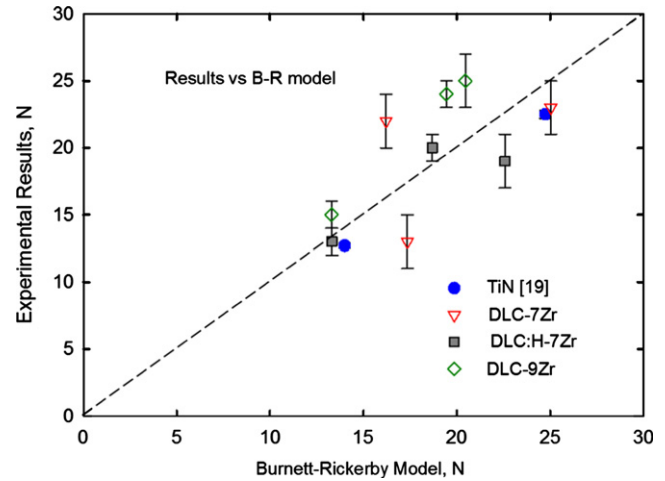

Fig. 5. Comparison of critical load between experimental results and calculation from Burnett and Rickerby model.

pure Ti, and with good wear resistance and an extremely low coefficient of friction of the DLC coatings, the DLC/ultrafine-grained Ti system appears to be an exceptionally strong candidate material for future bio-implant applications.

5. Conclusions

The adhesion behaviour and scratch resistance of three diamond-like carbon coatings deposited on grade 2 pure Ti substrates before and after high-pressure torsion processing were investigated and a comparison was made with a Ti–6Al–4V substrate. The following conclusions are reached:

1. DLC coatings with a gradient TiN/TiCN interlayer show good adhesion on Ti substrates.
2. Hydrogen-free DLC-Zr coatings have better adhesion than hydrogen-doped DLC-Zr coatings, and increase in the percentage of Zr increases the adhesion.
3. The effect of substrate on the performance of the DLC coating under high load was highlighted, showing that coatings with ultrafine-grained pure Ti and Ti–6Al–4V substrates have similar scratch and indentation behaviour. Both are significantly better than the results obtained with coarse-grained Ti substrates.

References

[1] M. Geetha, A.K. Singh, R. Asokamani, A.K. Gogia, Ti based biomaterials, the ultimate choice for orthopaedic implants – a review, Progress in Materials Science 54 (2009) 397–425.
[2] S.S. Leopold, Numbers for breakfast: summary of hip arthroplasty outcomes from the national joint registry for England and wales 8th annual report (2011), Journal of Bone and Joint Surgery 93 (2011) 1–3.

[3] Y. Li, C. Wong, J. Xiong, P. Hodgson, C. Wen, Cytotoxicity of Titanium and Titanium Alloying Elements, Journal of Dental Research 89 (2010) 493–497.

[4] S. Makihira, Y. Mine, H. Nikawa, T. Shuto, S. Iwata, R. Hosokawa, K. Kamoi, S. Okazaki, Y. Yamaguchi, Titanium ion induces necrosis and sensitivity to lipopolysaccharide in gingival epithelial-like cells, Toxicology in Vitro 24 (2010) 1905–1910.

[5] C.T. Wang, N. Gao, M.G. Gee, R.J.K. Wood, T.G. Langdon, Effect of grain size on the micro-tribological behavior of pure titanium processed by high-pressure torsion, Wear 280 (2012) 28–35.

[6] V.L. Sordi, M. Ferrante, M. Kawasaki, T.G. Langdon, Microstructure and tensile strength of grade 2 titanium processed by equal-channel angular pressing and by rolling, Journal of Materials Science 47 (2012) 7870–7876.

[7] R.Z. Valiev, T.G. Langdon, Principles of equal-channel angular pressing as a processing tool for grain refinement, Progress in Materials Science 51 (2006) 881–981.

[8] A.P. Zhilyaev, T.G. Langdon, Using high-pressure torsion for metal processing: fundamentals and applications, Progress in Materials Science 53 (2008) 893–979.

[9] R.Z. Valiev, I.V. Alexandrov, Y.T. Zhu, T.C. Lowe, Paradox of strength and ductility in metals processed by severe plastic deformation, Journal of Materials Research 17 (2002) 5–8.

[10] M. Kautz, H.W. Höppel, C. Xu, M. Murashkin, T.G. Langdon, R.Z. Valiev, H. Mughrabi, An overview: fatigue behaviour of ultrafine-grained metals and alloys, International Journal of Fatigue 28 (2006) 1001–1010.

[11] I.P. Semenova, R.Z. Valiev, E.B. Yakushina, G.H. Salimgareeva, T.C. Lowe, Strength and fatigue properties enhancement in ultrafine-grained Ti produced by severe plastic deformation, Journal of Material Science 43 (2008) 7354–7359.

[12] C.T. Wang, N. Gao, R.J.K. Wood, T.G. Langdon, Wear behavior of an aluminum alloy processed by equal-channel angular pressing, Journal of Materials Science 46 (2011) 123–130.

[13] N. Gao, C.T. Wang, R.J.K. Wood, T.G. Langdon, Tribological properties of ultrafine-grained materials processed by severe plastic deformation, Journal of Materials Science 47 (2012) 4779–4797.

[14] X. Zhao, W. Fu, X. Yang, T.G. Langdon, Microstructure and properties of pure titanium processed by equal-channel angular pressing at room temperature, Scripta Materialia 59 (2008) 542–545.

[15] X. Zhao, X. Yang, C. Wang, X. Wang, T.G. Langdon, The processing of pure titanium through multiple passes of ECAP at room temperature, Materials Science and Engineering A527 (2010) 6335–6339.

[16] I. Sabirov, R.Z. Valiev, I.P. Semenova, R. Pippan, Effect of equal channel angular pressing on the fracture behavior of commercially pure titanium, Metallurgical and Materials Transactions A 41 A (2010) 727–733.

[17] Y. Zhang, R.B. Figueiredo, S.N. Alhajeri, J.T. Wang, N. Gao, T.G. Langdon, Structure and mechanical properties of commercial purity titanium processed by ECAP at room temperature, Materials Science and Engineering A 528 (2011) 7708–7714.

[18] P. La, J. Ma, Y.T. Zhu, J. Yang, W. Liu, Q. Xue, R.Z. Valiev, Dry-sliding tribological properties of ultrafine-grained Ti prepared by severe plastic deformation, Acta Materialia 53 (2005) 5167–5173.

[19] C.T. Wang, N. Gao, M.G. Gee, R.J. Wood, T.G. Langdon, Processing of an ultrafine-grained titanium by high-pressure torsion: an evaluation of the wear properties with and without a TiN coating, Journal of the Mechanical Behavior of Biomedical Materials 17 (2013) 166–175.

[20] A.V. Byeli, V.A. Kukareko, A.G. Kononov, Titanium and zirconium based alloys modified by intensive plastic deformation and nitrogen ion implantation for biocompatible implants, Journal of the Mechanical Behavior of Biomedical Materials 6 (2012) 89–94.

[21] H. Dong, W. Shi, T. Bell, Potential of improving tribological performance of UHMWPE by engineering the Ti6Al4V counterfaces, Wear 225–229 (1999) 146–153.

[22] Z.X. Zhang, H. Dong, T. Bell, The load bearing capacity of hydrogen-free Cr-DLC coatings on deep-case oxygen hardened Ti6Al4V, Surface and Coatings Technology 200 (2006) 5237–5244.

[23] R.Z. Valiev, A.V. Sergueeva, A.K. Mukherjee, The effect of annealing on tensile deformation behavior of nanostructured SPD titanium, Scripta Materialia 49 (2003) 669–674.

[24] V.M. Tiainen, Amorphous carbon as a bio-mechanical coating-mechanical properties and biological applications, Diamond and Related Materials 10 (2001) 153–160.

[25] T.J. Joyce, Examination of failed ex vivo metal-on-metal metatarsophalangeal prosthesis and comparison with theoretically determined lubrication regimes, Wear 263 (2007) 1050–1054.

[26] C.V. Falub, U. Mueller, G. Thorwarth, M. Parlinska-Wojtan, C. Voisard, R. Hauert, In vitro studies of the adhesion of diamond-like carbon thin films on CoCrMo biomedical implant alloy, Acta Materialia 59 (2011) 4678–4689.

[27] R. Hauert, G. Thorwarth, U. Mueller, M. Stiefel, C.V. Falub, K. Thorwarth, T.J. Joyce, Analysis of the in-vivo failure of the adhesive interlayer for a DLC coated articulating metatarsophalangeal joint, Diamond and Related Materials 25 (2012) 34–39.

[28] J. Chen, G.A. Bell, B.D. Beake, H. Dong, Low temperature nano-tribological study on a functionally graded tribological coating using nanoscratch tests, Tribology Letters 43 (2011) 351–360.

[29] A. Pardo, C. Gomez-Aleixandre, J.O. Orwa, A. Cimmino, S. Prawer, Modification of characteristics of diamond-like carbon thin films by low chromium content addition, Diamond and Related Materials 26 (2012) 39–44.

[30] F. Zhao, H. Li, L. Ji, Y. Wang, H. Zhou, J. Chen, Ti-DLC films with superior friction performance, Diamond and Related Materials 19 (2010) 342–349.

[31] A. Czyzniewski, Optimising deposition parameters of W-DLC coatings for tool materials of high speed steel and cemented carbide, Vacuum 86 (2012) 2140–2147.

[32] D.B.N. Lee, M. Roberts, C.G. Bluchel, R.A. Odell, Zirconium: Biomedical and Nephrological Applications, ASAIO Journal 56 (2010) 550–556.

[33] A. Escudeiro, T. Polcar, A. Cavaleiro, a-C(:H) and a-C(:H)-Zr coatings deposited on biomedical Ti-based substrates: tribological properties, Thin Solid Films, http://dx.doi.org/10.1016/j.tsf.2012.12.086, in press.

[34] P. Kumar, P. Dilli Badu, L. Moham, C. Anandan, V.K. William Grips, Wear and corrosion resistance of Zr doped DLC on Ti–13Zr–13Nb biomedical alloy, Journal of Materials Engineering and Performance 22 (2013) 283–293.

[35] R.Z. Valiev, V. Ivanisenko, E.F. Rauch, B. Baudelet, Structure and deformation behaviour of Armco iron subjected to severe plastic deformation, Acta Materialia 44 (1996) 4705–4712.

[36] R.B. Figueiredo, P.R. Cetlin, T.G. Langdon, Using finite element modeling to examine flow processes in quasi-constrained high-pressure torsion, Materials Science and Engineering A528 (2011) 8198–8204.

[37] R.B. Figueiredo, P.H.R. Pereira, M.T.P. Aguilar, P.R. Cetlin, T.G. Langdon, Using finite element modeling to examine the temperature distribution in quasi-constrained high-pressure torsion, Acta Materialia 60 (2012) 3190–3198.

[38] A.P. Zhilyaev, G.V. Nurislamova, B.K. Kim, M.D. Baró, J.A. Szpunar, T.G. Langdon, Experimental parameters influencing grain refinement and microstructural evolution during high-pressure torsion, Acta Materialia 51 (2003) 753–765.

[39] M. Kawasaki, T.G. Langdon, The significance of strain reversals during processing by high-pressure torsion, Materials Science and Engineering A498 (2008) 341–348.

[40] C.T. Wang, N. Gao, R.J.K. Wood, T.G. Langdon, Wear behaviour of Al-1050 alloy processed by severe plastic deformation, Materials Science Forum 667–669 (2011) 1101–1106.

[41] W.C. Oliver, G.M. Pharr, An improved technique for determining hardness and elastic-modulus using load and displacement sensing indentation experiments, Journal of Materials Research 7 (1992) 1564–1583.

[42] N. Vidakis, A. Antoniadis, N. Bilalis, The VDI 3198 indentation test evaluation of a reliable qualitative control for layered compounds, Journal of Materials Processing Technology 143 (2003) 481–485.

[43] J. Stallard, S. Poulat, D.G. Teer, The study of the adhesion of a TiN coating on steel and titanium alloy substrates using a multi-mode scratch tester, Tribology International 39 (2006) 159–166.

[44] A. Escudeiro, T. Polcar, A. Cavaleiro, DLC(H) doped with Zr coatings for orthopaedics applications: adhesion properties, SVC Spring 2013 Bulletin.

[45] J.M. Wheeler, C.A. Collier, J.M. Paillard, J.A. Curran, Evaluation of micromechanical behaviour of plasma electrolytic oxidation (PEO) coatings on Ti–6Al–4V, Surface and Coatings Technology 204 (2010) 3399–3409.

[46] G. Purcek, O. Saray, F. Rubitschek, T. Niendorf, H.J. Maier, I. Karaman, Effect of internal oxidation on wear behavior of ultrafine-grained Nb–Zr, Acta Materialia 59 (2011) 7683–7694.

[47] A. Rodrigo, P. Perillo, H. Ichimura, On the correlation of substrate microhardness with the critical load of scratch adherence for hard coatings, Surface and Coatings Technology 124 (2000) 87–92.

[48] P.J. Burnett, D.S. Rickerby, The mechanical properties of wear resistant coatings.1. modelling of hardness behaviour, Thin Solid Films 148 (1987) 41–50.

[49] P.J. Burnett, D.S. Rickerby, The relationship between hardness and scratch adhesion, Thin Solid Films 154 (1987) 403–416.

[50] A. Rodrigo, H. Ichimura, Analytical correlation of hardness and scratch adhesion for hard films, Surface and Coatings Technology 148 (2001) 8–17.

[51] Y. Huang, Q. Wang, M. Wang, Z. Fei, M. Li, Characterization and analysis of DLC films with different thickness deposited by RF magnetron PECVD, Rare Metals 31 (2012) 198–203.